Quantum noise reduction using squeezed states in LIGO

by

Sheila E Dwyer

B.A., Wellesley College (2005)

Submitted to the Department of Physics
in partial fulfillment of the requirements for the degree of

Doctor of Philosophy in Physics

at the

MASSACHUSETTS INSTITUTE OF TECHNOLOGY

February 2013

Author .....
Department of Physics
January 18th, 2013

Certified by .....
Nergis Mavalvala
Professor of Physics
Thesis Supervisor

Accepted by .....
John Belcher
Associate Department Head for Education

Quantum noise reduction using squeezed states in LIGO

by

Sheila E Dwyer

Submitted to the Department of Physics
on January 18th, 2013, in partial fulfillment of the
requirements for the degree of Doctor of Philosophy in Physics

Abstract

Direct detection of gravitational waves will require earth based detectors to measure strains of the order 10^{-21}, at frequencies of 100 Hz, a sensitivity that has been accomplished with the initial generation of LIGO interferometric gravitational wave detectors. A new generation of detectors currently under construction is designed improve on the sensitivity of the initial detectors by about a factor of 10. The quantum nature of light will limit the sensitivity of these Advanced LIGO interferometers at most frequencies; new approaches to reducing the quantum noise will be needed to improve the sensitivity further. This quantum noise originates from the vacuum fluctuations that enter the unused port of the interferometer and interfere with the laser light. Vacuum fluctuations have the minimum noise allowed by Heisenberg's uncertainty principle, $\Delta X_1 \Delta X_2 \geq 1$, where the two quadratures X_1 and X_2 are non-commuting observables responsible for the two forms of quantum noise, shot noise and radiation pressure noise. By replacing the vacuum fluctuations entering the interferometer with squeezed states, which have lower noise in one quadrature than the vacuum state, we have reduced the shot noise of a LIGO interferometer. The sensitivity to gravitational waves measured during this experiment represents the best sensitivity achieved to date at frequencies above 200 Hz, and possibly the first time that squeezing has been measured in an interferometer at frequencies below 700 Hz. The possibility that injection of squeezed states could introduce environmental noise couplings that would degrade the crucial but fragile low frequency sensitivity of a LIGO interferometer has been a major concern in planning to implement squeezing as part of baseline interferometer operations. These results demonstrate that squeezing is compatible with the low frequency sensitivity of a full scale gravitational wave interferometer. We also investigated the limits to the level of squeezing observed, including optical losses and fluctuations of the squeezing angle. The lessons learned should allow for responsible planning to implement squeezing in Advanced LIGO, either as an alternative to high power operation or an early upgrade to improve the sensitivity. This thesis is available at DSpace@MIT and has LIGO document number P1300006.

Thesis Supervisor: Nergis Mavalvala
Title: Professor of Physics

Acknowledgments

I am grateful to the many people who have made this thesis possible. Thanks to Nergis for her constant enthusiasm and optimism, and the many ways she has supported me over the years. I have also been fortunate to have two other important mentors, Daniel Sigg and Lisa Barsotti, who have taught me a great deal, and made this project fun and successful. Thanks to my committee members, Scott Hughes and Vladan Vuletic. I am grateful for the variety of great teachers and mentors I've had at MIT, in the LSC, and at Wellesley, including Matt Evans, David McClelland, Al Levine, Rick Savage, John Belcher, Hong Liu, Robbie Berg and Glenn Stark.

I'm also very grateful to the CGP at ANU, especially to David McClelland for hosting me and his support for the squeezer project, as well as Michael Stefszky, Sheon Chua, Connor Mow-Lowry, Bram Slagmoden, Jong Chow, Daneil Shaddock, Tim Lam and Thanh Nyguen for making the stay so enjoyable and productive. Likewise, everyone at Hanford was a pleasure to work with and get to know, special thanks go to Mike Landry, Keita Kawabe, and Richard McCarthy for making the squeezing project possible. Thanks to all the students who worked on the squeezer at LHO and MIT, Alexander Khalaidovski, Michael Stefszky, Sheon Chua, Connor Mow-Lowry, Nicolas Smith-Lefebvre, Grant Meadors, and Max Factorovich.

I'd also like to thank my friends and family who have supported me through my time in grad school. A special thanks go to Anne and Jeremey for their companionship and support, to Patrick for all the laughter and joy he has brought to our house, and to my parents for everything. Thanks to my friends at MIT, especially those of you who went through the quals with me, Donnchadha, Uchupol, Thomas, Arturs, Obi, Stephen and Nicolas. My labmates, Chris Wipf, Tim Bodiya, Nicolas Smith-Lefebvre, Eric Oekler, Jeff Kissel, Tomoki Isogait, Patrick Kwee, Adam Libson and Nancy Aggarwal have made MIT LIGO an enjoyable and productive place to work.

Thanks to Marie Woods for her organization and for being able to laugh (and fix it) every time I have created a new administrative difficulty. Thanks to Jeff Kissel and Greg Grabeel for commenting on and proofreading this thesis.

Contents

List of Figures

List of Tables

Chapter 1

Introduction

Einstein used his theory of general relativity to predict the existence of gravitational waves almost a century ago. Direct detection of gravitational waves would provide a new way of observing the universe. Gravitational waves interact incredibly weakly with matter. This means that they are unaffected by passing through the dense ionized gases that obscure violent explosions and the early universe to electromagnetic observations, and could provide rich new insight into events that are currently difficult to observe. The weakness of the interaction with matter also means that direct detection is a tremendous challenge. A passing gravitational wave induces a strain in any object it passes through, alternately stretching and squeezing the object along orthogonal axes by an amount proportional to the length of the object: $h = \Delta L/L$. For the events that earth based detectors aim to observe the expected strains is of the order 10^{-21}. This means that a large part of the effort to detect gravitational waves is aimed at reducing noise in the detectors to improve their sensitivity. LIGO is a network of three detectors, one installed in Livingston Louisiana, and two in Hanford Washington, one of which may move to India. LIGO was planned in phases of increasing sensitivity, Initial, Enhanced and Advanced LIGO. Initial LIGO began in the late 1990s, and achieved its design sensitivity in 2005. Enhanced LIGO was an upgrade of the Initial LIGO interferometers testing some of the technologies planned for Advanced LIGO, with a year long science run ending in late 2010. While Advanced LIGO construction

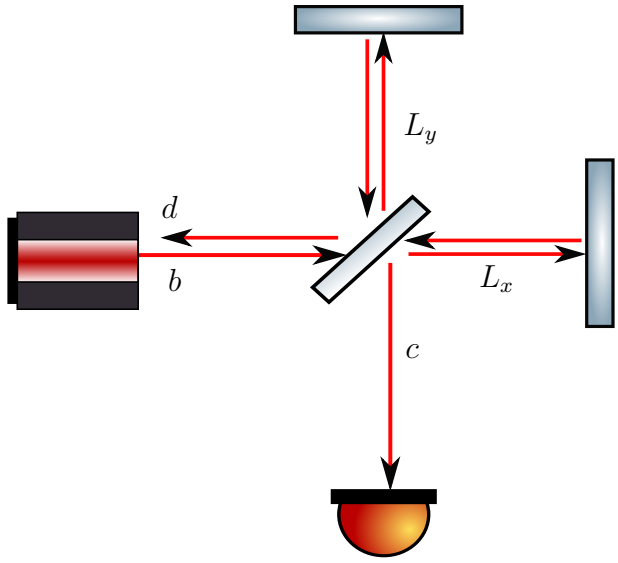

Figure 1-1: Simple Michelson interferometer

began on two interferometers, one at Livingston and one at Hanford, one interferometer was preserved in the Enhanced LIGO configuration for the experiment described in this thesis. Squeezed states were injected into the interferometer, and a reduction in the quantum noise was observed. We investigated technical noise couplings and the limits to the level of squeezing to allow planning for full time implementation of squeezing in an Advanced LIGO or third generation detector.

1.1 Interferometer as a gravitational wave detector

The simple Michelson interferometer illustrated in Figure 1-1 can be used to measure the strain induced by a passing gravitational wave of the correct polarization. Laser light at the frequency ω enters the interferometer where it is split by a beam splitter and sent down two orthogonal arms. The beam-splitter is represented by the transformation from its input fields to its output fields using the convention of [74, p 407]:

$$\mathbf{out} = (\mathbf{BS})\,\mathbf{in} \qquad\qquad \mathbf{BS} = \frac{1}{\sqrt{2}}\begin{pmatrix} 1 & i \\ i & 1 \end{pmatrix} \tag{1.1}$$

In each arm the light acquires a phase shift as it travels to the end mirror and back. We will call the phase shift ϕ_x or ϕ_y; they are proportional to the lengths of the two arms, L_x, L_y. A passing gravitational wave with the optimal polarization changes the phases by [78]:

$$\begin{aligned} \phi_x &= \frac{2\omega L_x}{c}\left(1+\frac{h_+}{2}\right) \\ \phi_y &= \frac{2\omega L_y}{c}\left(1-\frac{h_+}{2}\right) \end{aligned} \tag{1.2}$$

Writing the arm lengths in terms of common and differential parts, $L_x = L_+ + L_-$ and $L_y = L_+ - L_-$ the phases can also be written in terms of common and differential parts:

$$\begin{aligned} \phi_x &= \Phi + \phi & \Phi &= \frac{2\omega}{c}\left(L_+ + \frac{L_- h_+}{2}\right) \\ \phi_y &= \Phi - \phi & \phi &= \frac{2\omega}{c}\left(L_- + \frac{L_+ h_+}{2}\right) \end{aligned} \tag{1.3}$$

And the propagation down the arms and back toward the beam-splitter is represented by:

$$\mathbf{A} = e^{i\Phi}\begin{pmatrix} e^{i\phi} & 0 \\ 0 & e^{-i\phi} \end{pmatrix} \tag{1.4}$$

Now the interferometer output in terms of the input field is:

$$\begin{aligned} \mathbf{out} &= (\mathbf{BS})\mathbf{A}(\mathbf{BS})\mathbf{in} \\ \begin{pmatrix} c \\ d \end{pmatrix} &= e^{i(\Phi+\pi/2)}\begin{pmatrix} \sin\phi & \cos\phi \\ \cos\phi & -\sin\phi \end{pmatrix}\begin{pmatrix} 0 \\ b \end{pmatrix} \end{aligned} \tag{1.5}$$

The photo-current measured by the detectors at the anti-symmetric port (c) and the reflected port is:

$$\begin{aligned} P_{as} &\propto |c|^2 = |b|^2 \cos^2\phi \\ P_{refl} &\propto |d|^2 = |b|^2 \sin^2\phi \end{aligned} \tag{1.6}$$

The differential arm length L_- sets the ratio of the power at the antisymmetric port to the reflected power. The operating point where no light exits the anti-symmetric port is called the dark fringe. The interferometers are operated near this point, so $L_- = (\pi/2 + \Delta_{dc})c/2\omega$. Here Δ_{dc} is an small offset known as the DC offset introduced so that the power at the dark port will have a linear dependence on the gravitational wave strain. Using the small angle approximation, the power at the antisymmetric port is:

$$P_{as} \propto |b|^2 \left(\Delta_{dc}^2 + \frac{2\Delta_{dc}\omega L_+}{c} h_+ \right) \tag{1.7}$$

At this operating point the power at the dark port has a linear dependence on the gravitational wave strain. The goal of a worldwide network of interferometers is to measure a time series of the power at the anti-symmetric port, and find evidence of a passing gravitational wave. Because the strains expected are so small, on the order of 10^{-21}, the noise requirements for gravitational wave interferometers are very stringent. The main limiting noise sources in current gravitational wave detectors are seismic noise, thermal noise, and shot noise. Shot noise is one form of quantum noise, caused by the quantum nature of light. Quantum noise is expected to limit the sensitivity at most frequencies in the next generation of gravitational wave detectors.

1.2 Quantum Noise

1.2.1 Quantized fields

The quantized electric field in a single mode is written in terms of annihilation and creation operators [42]:

$$E(t) = \varepsilon_0 \left(a(t) e^{-i\omega t} + a^\dagger(t) e^{i\omega t} \right) \tag{1.8}$$

The factor ε_0 is a normalization factor with dimensions of electric field, in SI units it is given by $\sqrt{\hbar\omega/\epsilon_0 V}$ where V is the volume of the mode and ϵ_0 is the permitivity of free space [42].

This electric field operator is a Heisenberg picture operator which contains the full time evolution of the system. In free space, or an empty cavity without losses, the annihilation and creation operators here would be Schrödinger picture operators with no time dependence. By allowing the annihilation and creation operators to have time dependence we can take into account interactions, and describe noise on the field. The time dependent annihilation and creation operators we have used are in the rotating frame at the optical frequency ω. Inside of optical cavities the field only resonates when the round trip length (perimeter) of the cavity is an integral number of wavelengths, so the mode frequencies are discreet. The carrier frequency ω is the cavity resonance frequency:

$$\omega = \omega_{a,n} = \frac{2\pi c}{n\lambda} \tag{1.9}$$

where n is an integer. The Hamiltonian for this field is $H = \hbar\omega_a a^\dagger(t)a(t)$. Outside of a cavity, the mode volume becomes infinite and there are a continuum of modes at every frequency.

1.2.2 Noise in the sideband picture

Both classical and quantum noise on an optical field can be understood in terms of sidebands, or in terms of noise quadratures. A field with a carrier frequency ω has noise at the frequency Ω, and can be written as:

$$E(t) = (\bar{E} + \delta E(t))e^{i\omega t} + h.c. \tag{1.10}$$

If the field is amplitude modulated it becomes:

$$(1 + \Gamma\cos\Omega t)\, Ee^{i\omega t} + h.c = Ee^{i\omega t} + \frac{\Gamma E}{2}e^{i(\omega+\Omega)t} + \frac{\Gamma E}{2}e^{i(\omega-\Omega)t} + h.c. \tag{1.11}$$

A phase modulated field becomes:

$$Ee^{i\omega t+\Gamma\cos\Omega t} + h.c. = Ee^{i\omega t} + \frac{i\Gamma E}{2}e^{i(\omega+\Omega)t} + \frac{i\Gamma E}{2}e^{i(\omega-\Omega)t} + h.c. \tag{1.12}$$

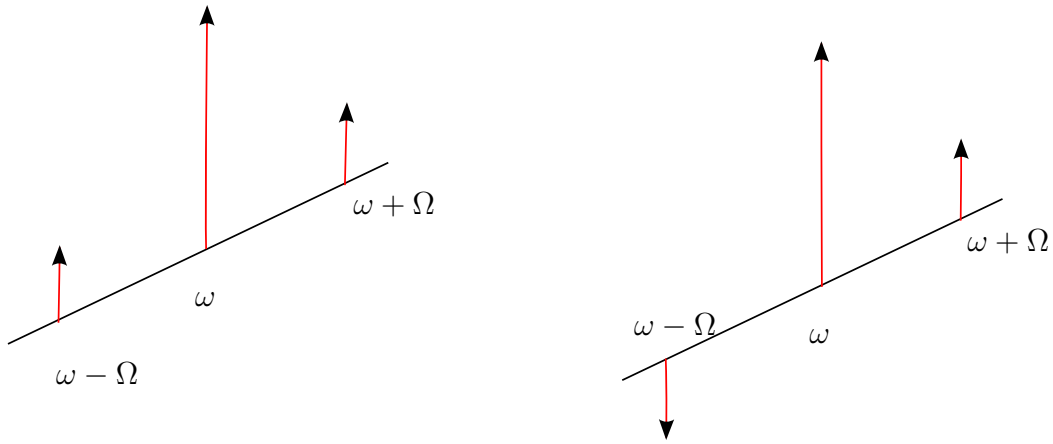

Figure 1-2: Phasors of amplitude noise (left) and phase noise (right) in the sideband picture. In the frame rotating at the carrier frequency ω the carrier is still in these diagrams while the sidebands rotate at Ω, the signal at $\omega + \Omega$ rotating clockwise while the idler at $\omega - \Omega$ rotates counter clockwise. (Sidebands have equal amplitudes)

In both cases the noise can be attributed to symmetric sidebands at the frequencies $\omega \pm \Omega$ around the carrier. The phase relationship between the sidebands and the carrier determines whether the noise is amplitude noise or phase noise. Amplitude noise is described by the real part of $\delta E/\bar{E}$, while phase noise is described by the imaginary part.

We can describe any noisy field as the sum of sidebands at different frequencies by writing the annihilation operator in terms of Fourier components.

$$a(t) = \int_{-\infty}^{\infty} \frac{d\Omega}{\sqrt{2\pi}} \widetilde{a}(\Omega) e^{i\Omega t} \tag{1.13}$$

Using the convention that $a^\dagger(t) = [a(t)]^\dagger$ we have $[a(\Omega)]^\dagger = a^\dagger(-\Omega)$ [17, 40, p 440]. Using Equation 1.8 the quantized electric field in terms of these Fourier components is:

$$E(t) = \frac{\varepsilon_0}{\sqrt{2\pi}} \int_{-\infty}^{\infty} d\Omega \left[\widetilde{a}(\Omega) e^{-i(\omega+\Omega)t} + \widetilde{a}^\dagger(-\Omega) e^{i(\omega+\Omega)t}\right] \tag{1.14}$$

The operators $\widetilde{a}(\Omega)$ and $\widetilde{a}^\dagger(-\Omega)$ represent positive and negative frequency sidebands around the carrier frequency. This would be more apparent if we had not separated out the time dependence at the carrier frequency in Equation 1.8. In that case the translation property

of Fourier transforms would give us Equation 1.14 as:

$$E(t) = \frac{\varepsilon_0}{\sqrt{2\pi}} \int_{-\infty}^{\infty} d\Omega \left[\widetilde{a}(\omega + \Omega) e^{-i\Omega t} + \widetilde{a}^{\dagger}(\omega - \Omega) e^{i\Omega t} \right] \tag{1.15}$$

The limits of the integral sometimes only include positive frequencies, as in the papers introducing the two photon formalism by Caves and Schumaker [9, 72] where the positive and negative frequency components are treated as two different modes then combined (see . In this thesis the transformation to the Fourier domain will be a Fourier transform over all frequencies, following Collet and Gardiner [17, 39].

1.2.3 Quadrature operators and variances

We can also write the field as the sum of two quadratures:

$$E(t) = \varepsilon_0 \left(X_1(t) \cos \omega t + X_2(t) \sin \omega t \right) \tag{1.16}$$

These two quadratures can be written in terms of static and fluctuating parts: $X_{1,2} = \overline{X}_{1,2} + \delta X_{1,2}(t)$. The static part describes the carrier while the fluctuating part describes a modulation. Figures 1-2 and 1-3 show amplitude and phase modulation represented by frequency components and in the plane of the two quadrature operators. Comparing Equations 1.16 and 1.8 the quadrature operators are:

$$X_1(t) = \left(a(t) + a^{\dagger}(t) \right) \tag{1.17}$$

$$X_2(t) = -i \left(a(t) - a^{\dagger}(t) \right) \tag{1.18}$$

We can define an arbitrary quadrature operator [7, p 6]:

$$X(\theta) = X_1(t) \cos \theta + X_2(t) \sin \theta \tag{1.19}$$

$$= a(t) e^{i\theta} + a^{\dagger}(t) e^{-i\theta} \tag{1.20}$$

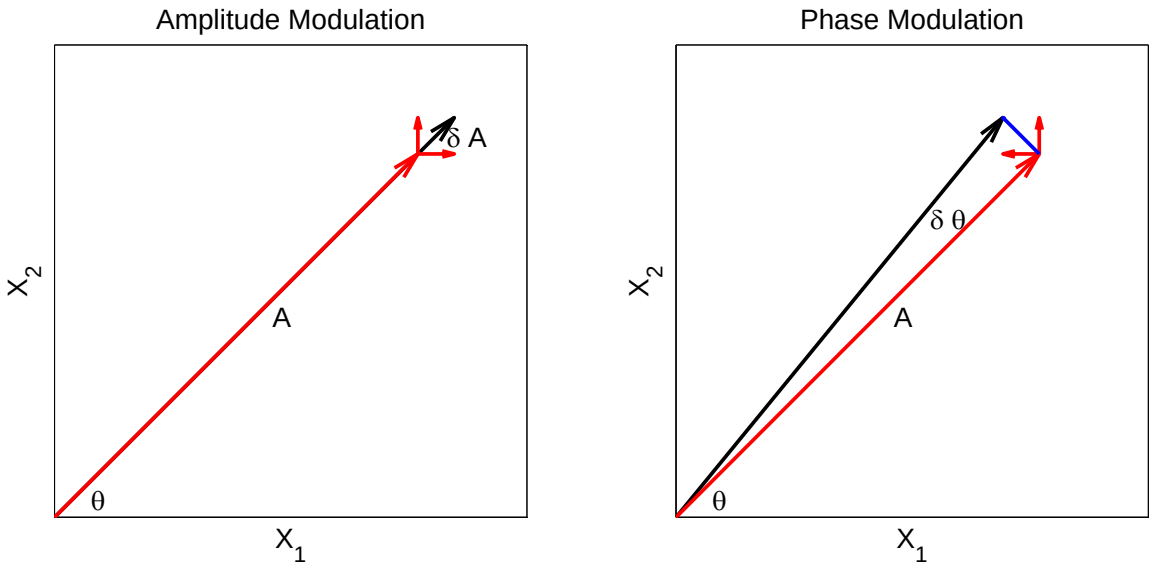

Figure 1-3: The same fields as shown in Figure 1-2 one eighth of a cycle later at $t = \pi/4\Omega$, plotted in the plane of X_1 and X_2 . In this plane, the polar coordinate represents the phase of the field while the radial coordinate is the amplitude. In the rotating frame, the carrier field has a constant phase while upper and lower sidebands rotate around it at Ω in opposite directions. Each of the individual frequency components is shown in red while the total field is shown in black. In the case of amplitude modulation the sidebands add only amplitude noise to the carrier, while in the case of phase modulation the phases are arranged so that only phase noise is added.

If we set θ to the phase of the carrier, then $\delta X(\theta)$ is amplitude noise while $\delta X(\theta + \pi/2)$ is phase noise. The quadrature operators can be written in the frequency domain by taking a Fourier transform:

$$\widetilde{X}_{1,2}(\Omega) = \frac{1}{\sqrt{2\pi}} \int_{-\infty}^{\infty} d\Omega e^{i\Omega t} X_{1,2}(t) \tag{1.21}$$

In the frequency domain the transformation from the annihilation operators to the

quadrature operators is the same as in the time domain:

$$\begin{pmatrix} \widetilde{X}_1(\Omega) \\ \widetilde{X}_2(\Omega) \end{pmatrix} = \begin{pmatrix} 1 & 1 \\ -i & i \end{pmatrix} \begin{pmatrix} \widetilde{a}(\Omega) \\ \widetilde{a}^\dagger(-\Omega) \end{pmatrix}$$
$$\widetilde{\mathbf{X}} = \mathbf{R}\widetilde{\mathbf{a}} \tag{1.22}$$

The arbitrary quadrature operator in the frequency domain is:

$$\widetilde{X}(\Omega, \theta) = \widetilde{a}(\Omega)e^{i\theta} + \widetilde{a}^\dagger(\Omega)e^{-i\theta} \tag{1.23}$$

The quadrature variances are the quantities that we normally measure. Measurements always have a finite bandwidth, W, which is normalized out of the power spectral density [7, p13]:

$$S(\theta, \Omega) = \frac{1}{W}\int_{-w/2}^{w/2}\int_{-\infty}^{\infty} \langle X(\theta, \Omega)X^\dagger(\theta, \Omega')\rangle \, d\Omega' d\Omega$$
$$S(\theta, \Omega) = \langle |\widetilde{X}(\theta, \Omega)|^2 \rangle = V(\theta, \Omega) \tag{1.24}$$

which is the variance of $\widetilde{X}(\Omega)$. This measurement is made by integrating the noise in a frequency band called the resolution bandwidth, which is then normalized out. Equation 1.24 only holds if the noise is constant over the resolution bandwidth of the measurement.

1.2.4 Uncertainty relation

There is an uncertainty relation between orthogonal quadratures of the electromagnetic field. Using the commutation relations for annihilation and creation operators, $\left[a, a^\dagger\right] = 1$, the commutation relation for the single mode quadrature operators is:

$$[X_1, X_2] = 2i \tag{1.25}$$

Which means the uncertainties are governed by:

$$\Delta X_1 \Delta X_2 \geq 1 \tag{1.26}$$

The variance of these quadrature operators are measured in the frequency domain by a power spectral density, the uncertainty relation in the frequency domain is:

$$V(\theta, \Omega) V(\theta + \pi/2, \Omega) \geq 1 \tag{1.27}$$

1.2.5 Vacuum and coherent states

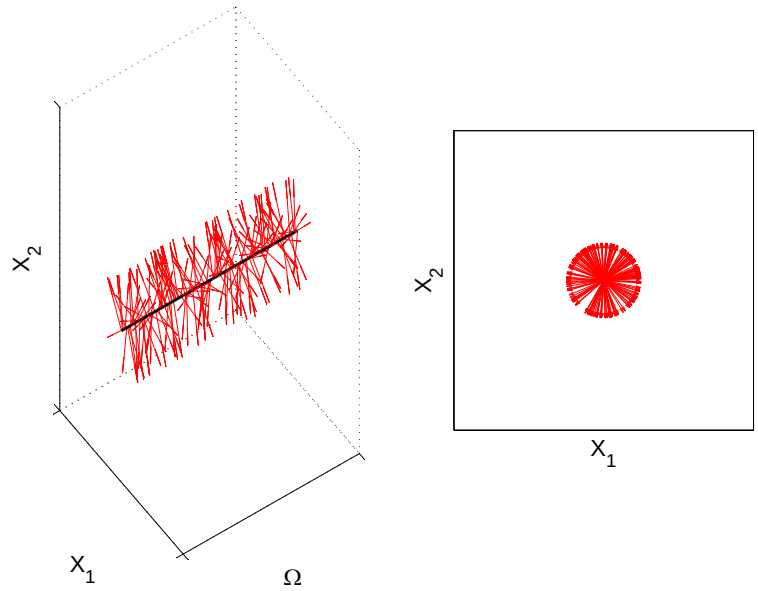

(a) Semiclassical representation of the ground state.

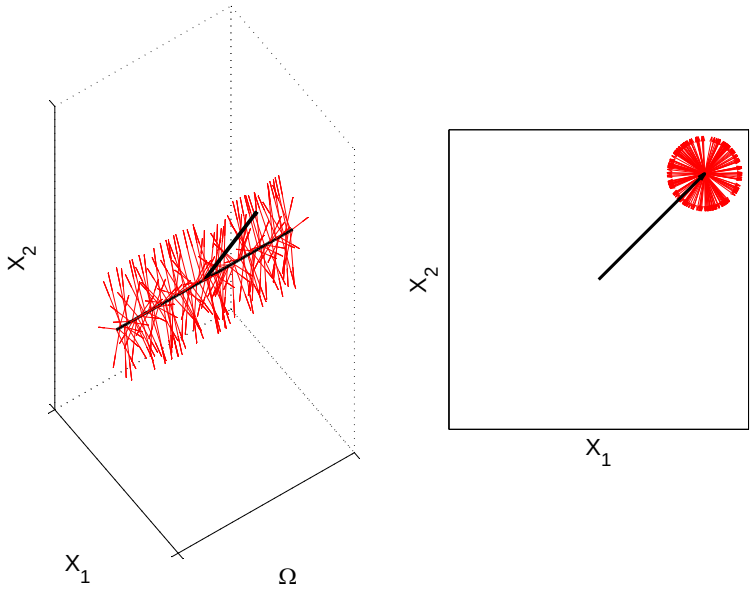

(b) Semiclassical representation of the coherent state.

Figure 1-4: Vacuum fluctuations at every sideband frequency add quantum noise to the electromagnetic field. Coherent amplitude given by solid black arrow.

The ground state and coherent state of the electromagnetic field can be understood as the sum of uncorrelated sidebands. Due to vacuum fluctuations there is a finite probability of having a single photon at each sideband frequency with a random phase, as shown in Figure 1-4a. The total field is the sum of all these sidebands. Since the fluctuations are random and uncorrelated, we would expect a probability distribution for the total field would be a Gaussian centered at the origin in the plane of X_1, X_2, with equal variance in the two quadratures.

The coherent states are eigenstates of the single mode annihilation operator:

$$a\,|\alpha\rangle = \alpha\,|\alpha\rangle \tag{1.28}$$

The ground state is also a coherent state, with eigenvalue 0. We can expand the state α in terms of number states and use the eigenvalue equation to find a recursion relation for the coefficients:

$$\begin{aligned} a\sum_{n=0}^{\infty} c_n\,|n\rangle &= \alpha\sum_{n=0}^{\infty} c_n\,|n\rangle \\ c_{n+1} &= \frac{\alpha}{\sqrt{n}}c_n \end{aligned} \tag{1.29}$$

Using the normalization to find $|c_0|^2 = e^{-|\alpha|^2}$ we have found the coherent states in the basis of number states.

$$|\alpha\rangle = e^{-|\alpha|^2/2}\sum_{n=0}^{\infty}\frac{\alpha^n}{\sqrt{n!}}\,|n\rangle \tag{1.30}$$

For a coherent state $|\alpha|^2 = \langle n\rangle$, so photon number measurements on a coherent state would give a Poisson distribution [46]:

$$P_n = |c_n|^2 = e^{-\langle n\rangle}\frac{\langle n\rangle^n}{n!} \tag{1.31}$$

Using the fact that the number states are generated by: $|n\rangle = a^{\dagger n}/\sqrt{n!}\,|0\rangle$:

$$|\alpha\rangle = e^{-|\alpha|^2/2} \sum_{n=0}^{\infty} \frac{(\alpha a^\dagger)^n}{n!} |0\rangle = e^{-|\alpha|^2/2} e^{\alpha a^\dagger} |0\rangle \tag{1.32}$$

We can write the vacuum state as $|0\rangle = e^{-\alpha^* a}\,|0\rangle$, and then we have [73]:

$$|\alpha\rangle = e^{-|\alpha|^2/2} e^{\alpha a^\dagger} e^{-\alpha^* a} |0\rangle = D(\alpha)\,|0\rangle \tag{1.33}$$

The Baker Hausdorff formula can be used to write the displacement operator $D(\alpha)$ in the more familiar form:

$$D(\alpha) = e^{(\alpha a^\dagger - \alpha^* a)} \tag{1.34}$$

This operator is the generator of the coherent states, it is a displacement operator in the sense that $D^{-1}(\alpha) a D(\alpha) = a + \alpha$. A classical harmonic oscillator starting at rest at the equilibrium position (its ground state) can be put into a excited state by displacing the mass. The quantum coherent states are the closest quantum approximation to these classical states and can also be generated by displacing the ground state, using $D(\alpha)$.

The quadrature variances of a coherent state are:

$$\begin{aligned} V_1 &= \langle\alpha|\, X_1^2\, |\alpha\rangle - \langle\alpha|\, X_1\, |\alpha\rangle^2 = 1 \\ V_2 &= \langle\alpha|\, X_1^2\, |\alpha\rangle - \langle\alpha|\, X_1\, |\alpha\rangle^2 = 1 \end{aligned} \tag{1.35}$$

These are minimum uncertainty states which satisfy the equality of the uncertainty principle: $V_1 V_2 = 1$.

1.2.6 Phase space representation of quantum fields

The plane of X_1 and X_2 from Figure 1-3 is a phase space for a classical field. We would like to represent a quantum state as a distribution in phase space, using the plane of X_1, X_2.

The expectation values for the quadrature amplitudes for a coherent state are:

$$X_1 = \langle\alpha| \frac{a + a^\dagger}{2} |\alpha\rangle = \mathrm{Re}[\alpha] \tag{1.36}$$

$$X_2 = \langle\alpha| \frac{a - a^\dagger}{2i} |\alpha\rangle = \mathrm{Im}[\alpha] \tag{1.37}$$

To represent a state in the plane of X_1, X_2 it is natural to use the basis of coherent states. Coherent states are an over-complete basis, any state can be represented as a linear combination of coherent states but the coherent states are not orthogonal. This means that in this phase space the coherent states will not be points, but will have a finite width, representing the variances of $X_{1,2}$. One quasi-probability distribution we can use is the Q representation:

$$Q(\alpha) = \langle\alpha| \rho |\alpha\rangle / \pi \tag{1.38}$$

where ρ is the density matrix. The Q function is normalized and always positive, $\int Q(\alpha) d^2\alpha = 1$, as a classical phase space probability distribution would be. The Q representation of a coherent state $|\beta\rangle$ is:

$$Q(\alpha) = \frac{1}{\pi} e^{-|\beta-\alpha|^2} \tag{1.39}$$

These are Gaussian states, with a Gaussian quasi-probability distribution centered around β, with equal widths in both quadratures. This quasi-probability distribution for the vacuum or ground state and a coherent state are shown in Figure 1-5. There several similar phase space representations of quantum states, the most commonly used are the P representation and the Wigner function.

1.3 Quantum noise in interferometers

There are two dominant types of quantum noise in an interferometer with movable mirrors, shot noise and quantum radiation pressure noise. Shot noise can be understood by the

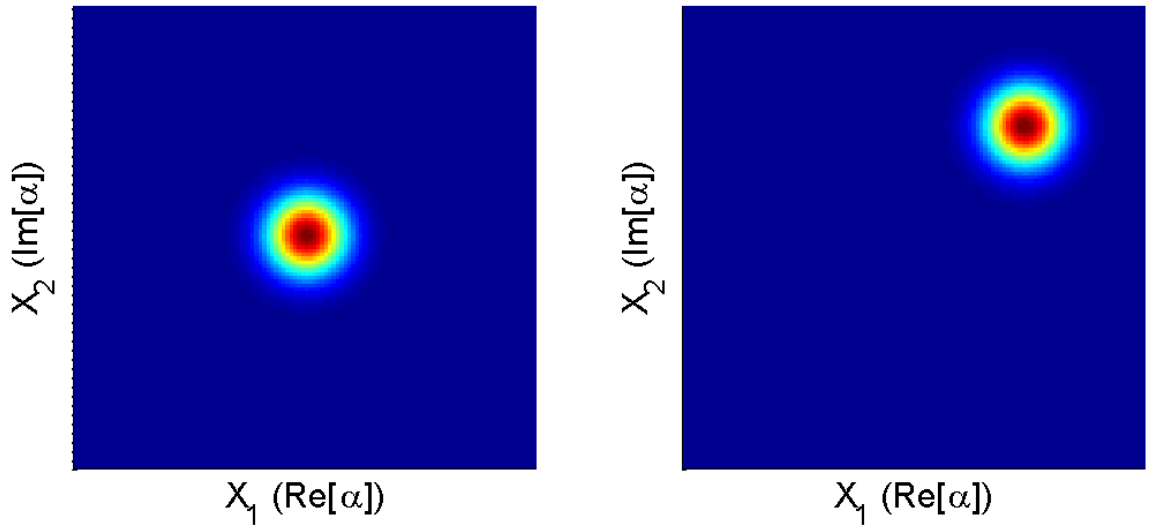

Figure 1-5: Q representation of ground state and coherent state

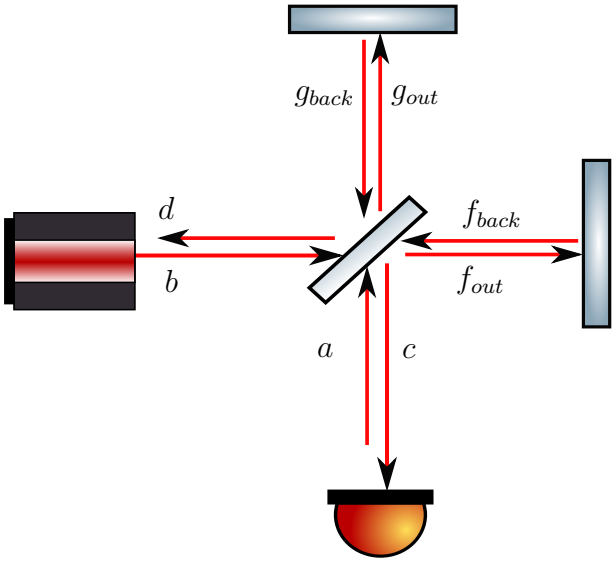

Figure 1-6: Input and output fields of a Michelson interferometer

random arrival times of photons at the photodetector, while radiation pressure noise can be understood as motion of the mirrors caused by fluctuations in the radiation pressure on the mirrors due to amplitude fluctuations in the arms. To understand the quantum behavior of the interferometer, we need to take into account vacuum fields that we ignored in Section 1.1. Figure 1-6 shows a diagram of a gravitational wave interferometer including the input field that enters from the anti-symmetric port. Caves pointed out that both kinds of quantum noise are caused by vacuum fluctuations entering at the dark port [8].

1.3.1 Quantum radiation pressure noise

The fields in the interferometer arms, which cause the radiation pressure on each of the end mirrors are given by:

$$\begin{pmatrix} g_{out} \\ f_{out} \end{pmatrix} = \frac{1}{\sqrt{2}} \begin{pmatrix} 1 & i \\ i & 1 \end{pmatrix} \begin{pmatrix} a \\ b \end{pmatrix} \tag{1.40}$$

The difference between the radiation pressure in the two arms can cause a change in l which can mimic a gravitational wave signal [8]:

$$\begin{aligned} \mathcal{P} &\propto f_{out}^{\dagger} f_{out} - g_{out}^{\dagger} g_{out} \\ &\propto i(b^{\dagger} a - a^{\dagger} b) \end{aligned} \tag{1.41}$$

Since b is the field of the input laser, we can assume that it is in a coherent state with a large amplitude, and replace b by $|\beta| e^{i\theta_b}$. The differential radiation pressure is then:

$$\mathcal{P} \propto |\beta| \left(a e^{i(\pi/2 - \theta_b)} + a^{\dagger} e^{-i(\pi/2 - \theta_b)} \right) = |\beta| X_a(\pi/2 - \theta_b) \tag{1.42}$$

Where $X_a(\theta)$ is the arbitrary quadrature operator for a, the quantum fluctuations that enter at the dark port. The variance of $\mathcal{P}$, which is proportional to the variance of the the quantum fluctuations entering at the dark port, scaled by the laser power $|\beta|^2$, causes the radiation

pressure noise. The radiation pressure noise is filtered by the frequency response of a single pendulum since the mirrors are harmonic oscillators in the restoring force of the earths gravitational field. This means that radiation pressure noise is largest at low frequencies, and falls off at higher frequencies.

1.3.2 Shot noise

Using Equation 1.5 and including the input field a the output fields are given by:

$$\begin{pmatrix} c \\ d \end{pmatrix} = e^{i(\Phi + \pi/2)} \begin{pmatrix} \sin\phi & \cos\phi \\ \cos\phi & -\sin\phi \end{pmatrix} \begin{pmatrix} a \\ b \end{pmatrix} \tag{1.43}$$

The signal on the photo-detector is proportional to $c^\dagger c$:

$$c^\dagger c = a^\dagger a \sin^2\phi + (b^\dagger a + a^\dagger b)\frac{\sin 2\phi}{2} + b^\dagger b \cos^2\phi \tag{1.44}$$

Using the same operating point as in Section 1.1, $\phi = \pi/2 + \Delta_{dc} + \omega L h_+/c$, we can make the small angle approximation for Δ_{dc}. We will also write the operators as the sum of a constant and fluctuating part: $\bar{b} + \delta b$, and $a = \delta a$ since only quantum fluctuations enter from the dark port. Assuming again that the laser is in a coherent state we can replace $\bar{b}$ with $|\beta| e^{i\theta_b}$. Dropping terms that are products of fluctuations we get:

$$c^\dagger c = -\left(\Delta_{dc} + \frac{\omega L h_+}{c}\right)|\beta| X_a(-\theta_b) + \left(\Delta_{dc} + \frac{\omega L h_+}{c}\right)^2 \left(|\beta|^2 + |\beta| \delta X_b(-\theta_b)\right) \tag{1.45}$$

Δ_{dc} is small, $\omega L h_+/c$ is very small, while $|\beta|$ is large; the average signal is of the order $(\Delta_{dc}|\beta|)^2$. We will keep terms that are smaller by one factor of Δ_{dc} or $1/|\beta|$.

$$c^\dagger c = (\Delta_{dc}|\beta|)^2 + \frac{2\omega L h_+}{c}\Delta_{dc}|\beta|^2 - \Delta_{dc}|\beta|\left(X_a(-\theta_b) - \Delta_{dc}\delta X_b(-\theta_b)\right) \tag{1.46}$$

$$c^\dagger c = (\Delta_{dc}|\beta|)^2 + \frac{2\omega L h_+}{c}\Delta_{dc}|\beta|^2 - \Delta_{dc}|\beta| X_a(-\theta_b) \tag{1.47}$$

Since X_a and δX_b will be of the same order of magnitude, the $\Delta_{dc}\delta X_b$ term will be small compared to noise due to fluctuations that enter from the dark port. Comparing Equations 1.47 and 1.42 the fluctuations that cause shot noise are in an orthogonal quadrature to those that cause radiation pressure noise.

To understand how sensor noise limits the sensitivity of a measurement, we need to calibrate the sensor noise in terms of gravitational wave strain.

$$\text{shot noise limited sensitivity} = \frac{\text{quantum noise of } c^\dagger c}{\frac{\mathrm{d}(c^\dagger c)}{\mathrm{d}\, h_+}} \propto \frac{1}{|\beta|} \tag{1.48}$$

The sensitivity of a simple Michelson interferometer to gravitational waves scales with the input power, shown in Equation 1.7, meaning that the shot noise limited sensitivity is inversely proportional to the laser amplitude. By increasing the laser power, the shot noise limited sensitivity can be improved, while increasing the quantum radiation pressure noise. Advanced LIGO has increased the laser power to lower the shot noise limit, and increased the mirror masses to counteract the increased level of radiation pressure noise. The laser power used will test the limits of available technologies, and further increases in laser power and mirror mass will be difficult and expensive.

To increase the effective arm length the LIGO interferometers have Fabry-Perot arms which add a frequency dependence to the calibration of the signal in terms of gravitational wave strain. For an interferometer with Fabry-Perot arms the calibration of power at the antisymmetric port in gravitational wave strain has a frequency dependence [32]:

$$\frac{\text{quantum noise of } c^\dagger c}{\frac{\mathrm{d}(c^\dagger c)}{\mathrm{d}\, h_+}} \propto \frac{1 + i2\Omega\tau_s}{|\beta|} \tag{1.49}$$

where τ_s is the storage time of the arm cavities. This means that the spectrum of quantum noise calibrated in units of gravitational wave strain has a positive slope above the half width of the arm cavities, as shown for Advanced LIGO in Figure 1-7. Once Caves clarified that the vacuum fluctuations at the dark port cause the dominant quantum noise in an interferometer,

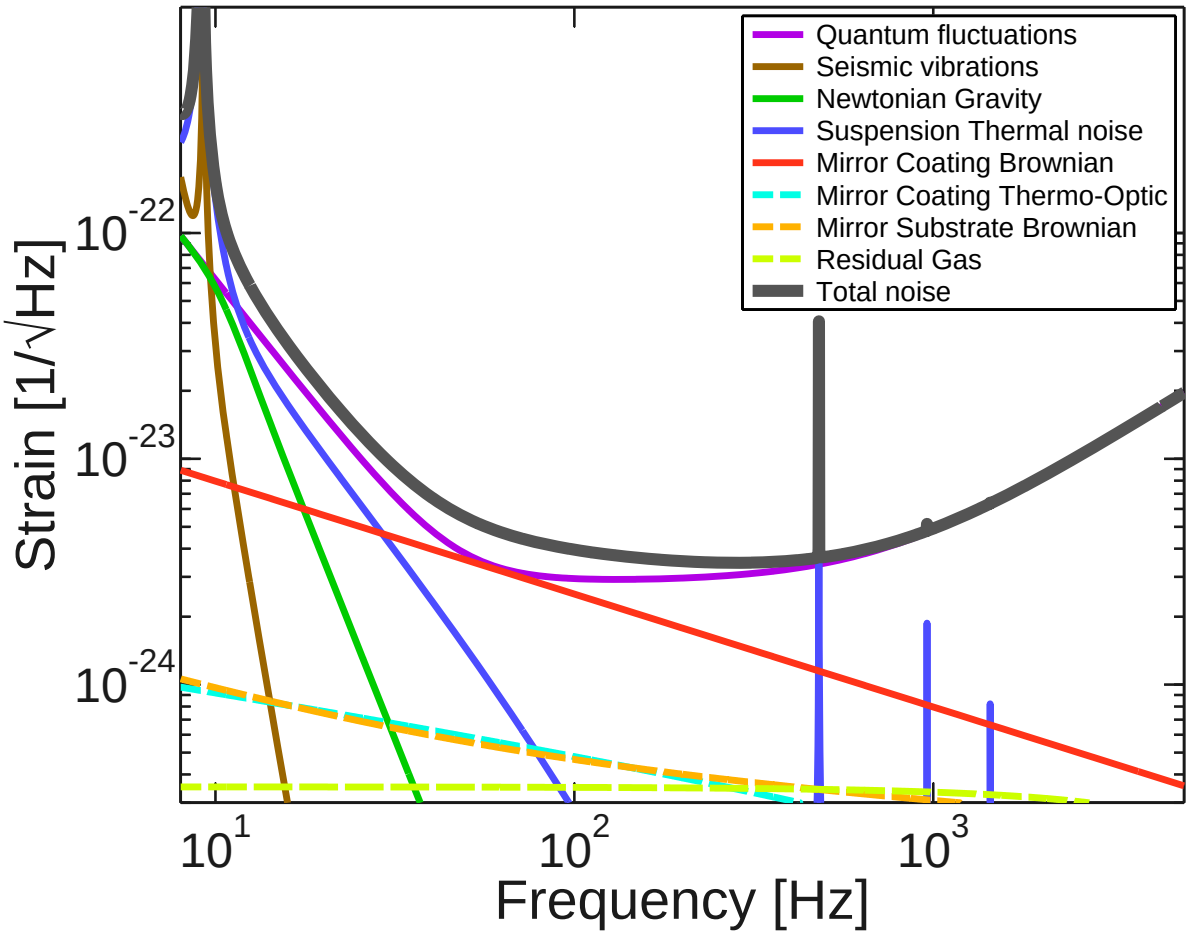

Figure 1-7: Quantum noise limited sensitivity of Advanced LIGO, shown by the purple trace. The shot noise dominates above 100 Hz, calibrated in units of gravitational wave strain the shot noise limit increases with frequency above the arm cavity pole. The gray trace shows the design sensitivity, which is limited by quantum noise at most frequencies in the detection band [53].

he suggested that the noise could be reduced by replacing the vacuum fluctuations with a state with a smaller variance in one quadrature.

1.4 Squeezed States

The uncertainty principle places a minimum on the product of the quadrature variances. For a Gaussian state this is a minimum area in phase space that the state must occupy. However, the uncertainty principle places no minimum on the variance of either quadrature alone, so it is possible to have states with smaller variance in one quadrature than a coherent state, as long as the variance of the orthogonal quadrature is larger. These states are called quadrature squeezed states, and in phase space they resemble a coherent state which has been squeezed.

1.4.1 Two photon coherent states

Yuen considered states that are eigenstates of a linear combination of the annihilation and creation operators [92]:

$$b\,|\beta\rangle = \left(\mu a + \nu a^\dagger\right)|\beta\rangle = \beta\,|\beta\rangle \tag{1.50}$$

where $|\mu|^2 - |\nu|^2 = 1$ and $|\nu/\mu| < 1$. He called these states two-photon coherent states, the coherent states discussed in Section 1.2.5 are a special case when $\nu = 0$. This operator has the same commutation relation as the annihilation and creation operators: $[b, b^\dagger] = (|\mu|^2 - |\nu|^2)[a, a^\dagger] = 1$. By writing a and $a^\dagger$ in terms of b and $b^\dagger$ and using the eigenvalue equation, it is straightforward to find expectation values for the quadrature operators and their variances on these states. We will use the notation:

$$\tanh|\zeta| = \left|\frac{\nu}{\mu}\right| \qquad \frac{\nu}{\mu} = \left|\frac{\nu}{\mu}\right| e^{i\theta} \qquad \zeta = |\zeta| e^{i\theta} \tag{1.51}$$

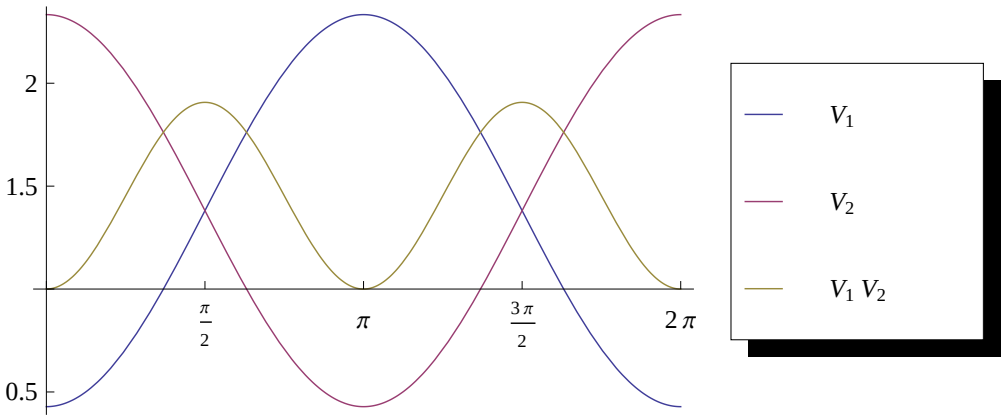

Figure 1-8: Quadrature variances of two photon coherent states with $\beta = 0$ and $\tanh|\zeta| = 0.4$ as θ varies. When the variance of one quadrature is less than one, showing squeezing, the other quadrature has increased variance, called anti-squeezing. When θ is an integral multiple of π, the state is a minimum uncertainty state, and the product of the variances in the two quadratures is one.

As shown in Figure 1-8 these states can have a variance less than the coherent state, and can be minimum uncertainty states. When $\theta = 0$ the variances are:

$$V_1 = \frac{1 - \tanh\zeta}{1 + \tanh|\zeta|} = e^{2|\zeta|} \tag{1.52}$$

$$V_2 = \frac{1 + \tanh\zeta}{1 - \tanh|\zeta|} = e^{-2|\zeta|} \tag{1.53}$$

The decreased noise in one quadrature is called squeezing, while the increased noise in the other we will refer to as anti-squeezing.

1.4.2 Photon statistics

The eigenstates of the generalized number operator $b^\dagger b = m\,|m\rangle$ are generated from the generalized zero state:

$$|m\rangle = \frac{b^{\dagger m}}{\sqrt{m!}}\,|0\rangle_b \qquad\qquad b\,|0\rangle_b = 0 \tag{1.54}$$

An argument exactly analogous to the one leading to Equations 1.30 and 1.31 shows that measurements of the generalized number operator $b^\dagger b$ on the two photon coherent states will result in a Poisson distribution, just like measurements of the number operator on a coherent state [46]. We can write the two photon coherent state in terms of number states following the same procedure used in section 1.2.5 to find a recursion relation [46]:

$$c_n = \frac{\beta c_{n-1} - \nu\sqrt{n-1}c_{n-2}}{\mu\sqrt{n}} \tag{1.55}$$

The normalization $\sum |c_n|^2 = 1$ gives $|c_0| = 1/\sqrt{\cosh|\zeta|}$. The coefficients for the generalized zero state $|0\rangle_b$ are found by setting $\beta = 0$.

$$\begin{aligned} c_{2n+1} &= 0 \\ c_{2n} &= \left(\frac{-\nu}{\mu}\right)^n \sqrt{\frac{(2n-1)!!}{(2n)!!}} c_0 = \left(\frac{-\nu}{2\mu}\right)^n \frac{\sqrt{(2n)!}}{n!\sqrt{\cosh|\zeta|}} \end{aligned} \tag{1.56}$$

This is a state with an even number of photons. The state $|1\rangle_b = b^\dagger |0\rangle_b$, and any odd generalized number state includes only odd photon number states.

1.4.3 Squeezing operator

To find the generator of these states we can follow a procedure similar to the one used to show that the displacement operator generates coherent states:

$$|0\rangle_b = \sum_{n=0}^{\infty} c_0 \left(\frac{-\nu}{2\mu}\right)^n \frac{a^{\dagger 2n}}{n!} |0\rangle = c_0 e^{(-\nu a^{\dagger 2}/2\mu)} |0\rangle \tag{1.57}$$

We can re-write the vacuum state as:

$$|0\rangle = (\cosh|\zeta|)^{-a^\dagger a} e^{(\tanh|\zeta| e^{-i\theta} a^2/2)} |0\rangle \tag{1.58}$$

using the fact that $a\,|0\rangle = 0$. So that our generalized ground state has become:

$$\begin{aligned} |0\rangle_b &= e^{(-\tanh|\zeta| e^{i\theta} a^{\dagger 2}/2)} (\cosh|\zeta|)^{-(a^\dagger a + 1/2)} e^{(\tanh|\zeta| e^{-i\theta} a^2/2)} |0\rangle \\ &= S(\zeta)\,|0\rangle \end{aligned} \tag{1.59}$$

This operator $S(\zeta)$ has been shown [37] to be the same as the unitary squeezing operator:

$$S(\zeta) = \exp\left((\zeta^* a^2 - \zeta a^{\dagger 2})/2\right) \tag{1.60}$$

This is an operator that creates or destroys photons two at a time. The squeezed coherent states are generated by [89]:

$$|\alpha, \zeta\rangle = D(\alpha) S(\zeta)\,|0\rangle \tag{1.61}$$

The squeezed state with $\alpha = \mu\beta - \nu\beta^*$ is equivalent to the two photon coherent state $|\beta\rangle$ [89, p19].

The Q representation quasi-probability distribution of the pure squeezed state $D(\alpha_1)S(\zeta)\,|0\rangle$ is [42]:

$$\begin{aligned} Q(\alpha) = \frac{1}{\pi\cosh|\zeta|} \exp\Bigg(&-|\alpha|^2 - |\alpha_1|^2 + \frac{\alpha_1^*\alpha + \alpha_1\alpha^*}{\cosh|\zeta|} \\ &- \frac{\tanh|\zeta|}{2}\left[e^{i\theta}\left(\alpha_1^{*2} - \alpha^{*2}\right) + e^{-i\theta}\left(\alpha_1^2 - \alpha^2\right)\right]\Bigg) \end{aligned} \tag{1.62}$$

Figure 1-9 shows quasi-probability distributions for a few squeezed states. In phase space these states look similar to the coherent and vacuum states, but they have been squeezed.

1.4.4 Squeezed vacuum state

The term squeezed vacuum state is used to refer to the state $S(\zeta)\,|0\rangle$, which has a equivalent generalized zero state with $\beta = 0$. The quadrature operators are proportional to the electric (X_1) and magnetic (X_2) field amplitudes, and the expectation values for a two photon

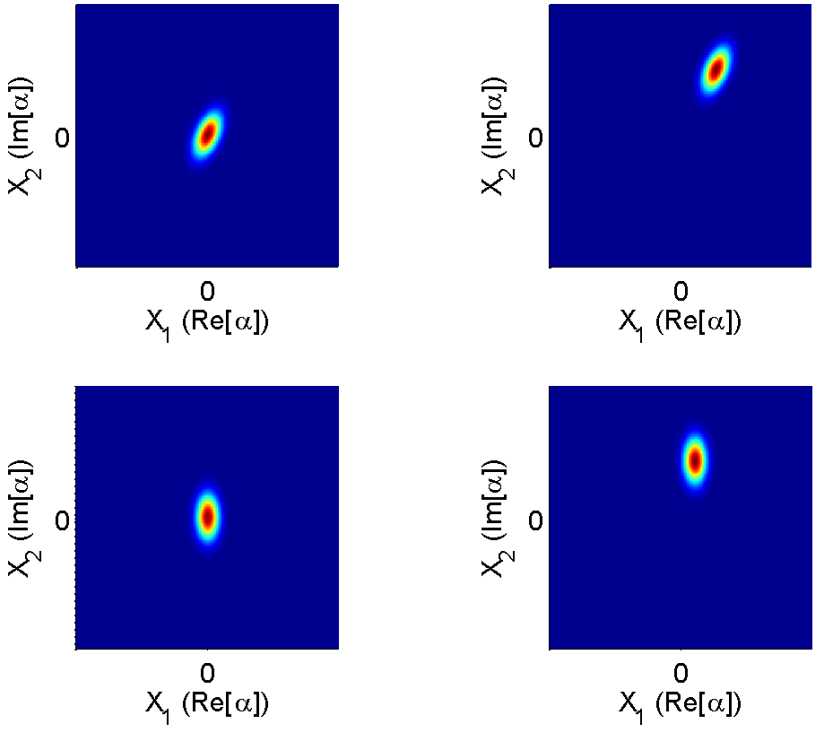

Figure 1-9: Squeezed states

coherent state are:

$$\langle\beta|\, X_1\, |\beta\rangle = 2\,\mathrm{Re}[\mu^*\beta - \nu\beta^*] \tag{1.63}$$

$$\langle\beta|\, X_2\, |\beta\rangle = -2\,\mathrm{Im}[\mu^*\beta - \nu\beta^*] \tag{1.64}$$

when $\beta = 0$ these are zero just as for the ground state. These states are vacuum states in the sense that the average amplitude is zero. We cannot identify a quadrature operator as an amplitude or phase quadrature operator for either the ground state or the squeezed vacuum states, since we do not have the phase of the coherent amplitude to use as a reference.

Although the squeezed vacuum states have zero amplitude, they do contain more photons than the ground state. The average energy of the state is proportional to the photon number

expectation value:

$$\hbar\omega(\frac{1}{2} + \langle\beta|\, a^\dagger a\, |\beta\rangle) = \hbar\omega\left(\frac{1}{2} + |\nu|^2 + (|\mu|^2 + |\nu|^2)|\beta|^2 - 2\,\mathrm{Re}[\nu^*\mu^*\beta^2]\right) \tag{1.65}$$

For a squeezed vacuum state this is $\hbar\omega(|\nu|^2 + 1/2) = \hbar\omega(\sinh^2|\zeta| + 1/2)$. The ground state is the minimum energy state where $\nu = \zeta = 0$. The energy of a squeezed state must be larger than that of the ground state, simply because a squeezed state is different from the ground state. A pure traveling wave squeezed state with 15 dB of squeezing, meaning that $10\log_{10} V = -15$ for one quadrature, has 7.4 photons per second, or 1.4 attoWatts more power than the vacuum fluctuations. For any practical purpose, we can say that there is no power in a squeezed beam. Although these states have higher energy than the vacuum state, we will call them squeezed vacuum states. They are vacuum states in the sense that they have no coherent amplitude. The variance the of the photon number for a squeezed vacuum state is:

$$\langle(a^\dagger a)^2\rangle - \langle a\rangle^2 = \left(|\mu|^2 - |\nu|^2\right)|\nu|^2 = |\nu|^2 \tag{1.66}$$

This is a distribution where the mean is the same as the variance, although it clearly is not a Poisson distribution, as shown in Figure 1-10. For a squeezed state with a coherent amplitude the photon number distribution can be narrower or wider than a Poisson distribution, depending on the squeezing angle.

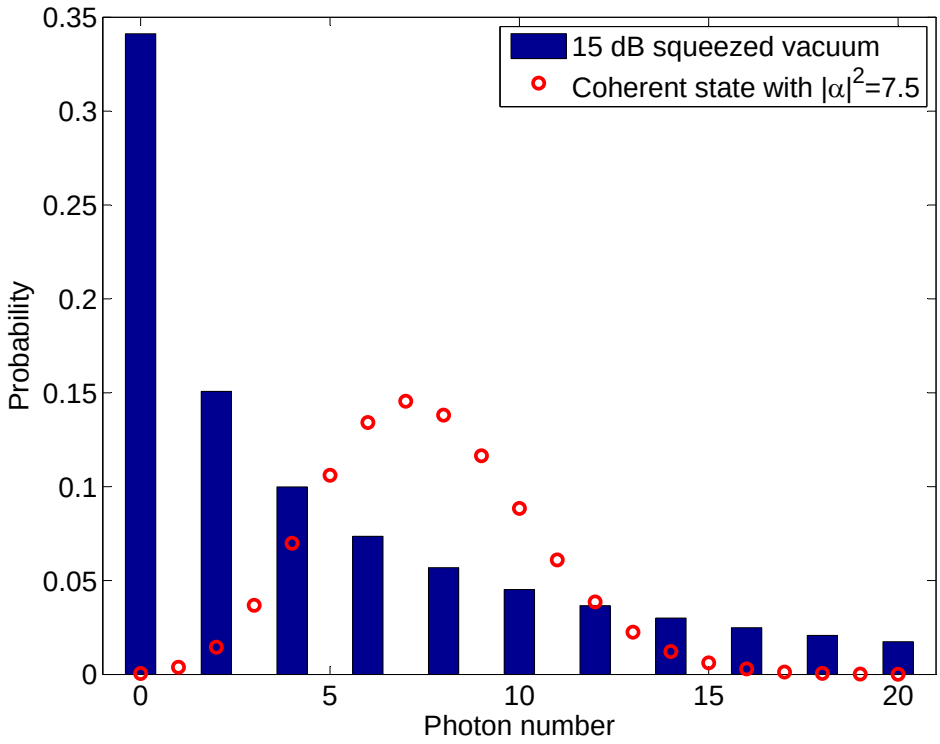

Figure 1-10: Photon statistics of squeezed vacuum. Probability distribution for photon number measurements on a squeezed vacuum state with 15 dB of squeezing. This state has a photon number expectation value of 7.5. For reference the Poisson distribution with a photon number expectation value of 7.5 is shown by the red dots.

Chapter 2

Generation and Detection of Squeezed States

2.1 Second order optical nonlinearity

There are a few methods for generating squeezed states of light, [19, 76], but to date the most reliable method with the highest level of demonstrated squeezing uses nonlinear crystals with a second order nonlinearity in parametric down-conversion. In these crystals the displacement field has a term that is proportional to the square of the electric field [6]:

$$\vec{D} = \varepsilon_0 \left([1 + \chi^{(1)}]\vec{E} + \chi^{(2)}\vec{E}^2 + ... \right) \tag{2.1}$$

This results in a displacement field that can include components at different frequencies than the input fields: a $\chi^{(2)}$ nonlinearity can be used to generate sum and difference frequencies. We use the interactions between a fundamental field at the frequency of the main interferometer laser (ω), with annihilation operator a and a second harmonic field with an annihilation operator b and frequency ($\omega_p \approx 2\omega$). In second harmonic generation the energy of two photons at the fundamental frequency is combined to make one photon at the second harmonic frequency. In optical parametric amplification or optical parametric oscillation,

the energy from one second harmonic (or pump) photon is split into two lower frequency photons, called the signal and idler. We use degenerate optical parametric oscillation (OPO), where the energy of the signal and idler are the same.

The Hamiltonian for these fields inside of a lossless cavity is:

$$H_{cav} = \hbar\omega_a a^\dagger a + \hbar\omega_b b^\dagger b + \frac{i\hbar}{2}\left(\epsilon a^{\dagger 2} b - \epsilon^* a^2 b^\dagger\right) \tag{2.2}$$

Here ω_a is the cavity resonant frequency for the fundamental field, ω_b the cavity resonant frequency for the second harmonic frequency, and ϵ is the nonlinear coupling parameter, which is real when the crystal temperature is optimal. This Hamiltonian describes a two photon processes for the fundamental field, where photons are created or destroyed two at a time. The interaction has the form of the quadratic Hamiltonians that Yuen recognized would generate his two photon coherent states [92].

2.1.1 Lossless optical parametric oscillator

The next several sections will contain a calculation of the squeezing that we can expect under realistic conditions. With a few simplifications we can easily see why the Hamiltonian of Equation 2.2 will produce squeezed states. An optical parametric oscillator (OPO) is a cavity with one of these crystals placed inside, and a strong pump field injected at the second harmonic frequency. In this case we can use the parametric approximation and assume that the pump is in a coherent state with a large amplitude and is not depleted by its interaction with the fundamental field, which will be small. Replacing b with $\beta e^{i\omega_p t}$, assuming that the pump frequency is twice the fundamental field frequency, $\omega_p = 2\omega$ and that both fields are on resonance ($\omega_a = \omega, \omega_b = \omega_p = 2\omega$) and that ϵ is real the Hamiltonian in a lossless cavity becomes:

$$H_{cav} = \hbar\omega a^\dagger a + \frac{i\hbar\epsilon}{2}\left(\beta e^{i2\omega t} a^{\dagger 2} - \beta^* e^{-i2\omega t} a^2\right) \tag{2.3}$$

Moving into the interaction picture where the operators evolve with the time dependence of the background Hamiltonian $\hbar\omega a^\dagger a$ and the states evolve according to the time evolution due to the interaction Hamiltonian:

$$a \to e^{i\omega t} a$$

$$a^\dagger \to e^{-i\omega t} a^\dagger \tag{2.4}$$

$$\frac{i\hbar\epsilon}{2}\left(\beta e^{i2\omega t} a^{\dagger 2} - \beta^* e^{-i2\omega t} a^2\right) \to \frac{i\hbar\epsilon}{2}\left(\beta a^{\dagger 2} - \beta^* a^2\right) = V \tag{2.5}$$

The interaction Hamiltonian V is now time independent and so the time evolution of the state is given by:

$$\hat{U} = e^{-iVt/\hbar} = \exp\left(\frac{\epsilon\beta t a^{\dagger 2} - \epsilon\beta^* t a^2}{2}\right) \tag{2.6}$$

This is just the squeezing operator from Equation 1.60 with $\zeta = \epsilon\beta t$. This cavity squeezes a state that propagates through it, producing a pure squeezed state. As soon as losses are introduced, the state produced will be a mixture of squeezed states and vacuum states, or potentially other fields. Although the lossless cavity provides a simple way to see why second order nonlinearities will create a squeezed state, it is not realistic. If the cavity were truly lossless, the dynamics inside the cavity would have no impact on external fields, and would not be useful in most applications.

2.2 Hamiltonian for field in a cavity with loss

To understand how an OPO creates squeezing of the external field, which can be injected into an interferometer or measured on a homodyne detector, we need to introduce damping through cavity loss. Quantum systems with damping will always evolve to a mixed state, even if they start in a pure state. There are a few approaches to damping in quantum systems; we will follow Collet and Gardiner [17,39] and use the quantum Langevin approach. Once we have equations of motion for the cavity operators, we can use them to relate the

input, output and cavity fields and find the level of squeezing we expect to produce based on cavity parameters. This calculation can be found in many theses and books on quantum optics, [7, 56, 64, 89]. We will set up the basic calculation here in a way that will allow us to take into account experimental realities such as laser noise, cavity length noise, and temperature fluctuations in Chapter 5.

The total Hamiltonian for a cavity with loss is [39]:

$$H = H_{cav} + \sum_j H^j_{bath} + H^j_{int} \tag{2.7}$$

There will be multiple partially reflective mirrors (couplers) where the cavity field interacts with external fields, denoted by the index j. All of these operators are Heisenberg picture operators, that include all of the time evolution information. Once we find equations of motion for these operators we will move back to the rotating frame and use equations for the slowly varying operators introduced in Section 1.2. One way to find the bath and interaction Hamiltonians is to consider the interaction between two coupled cavities and let the length of one of the cavities go to infinity [79]. As the length of the second cavity increases the mode spacing decreases until the fields become a continuum of modes at every frequency. As the length of the cavity goes to infinity the probability of a photon that escapes to the second cavity returning to the first becomes negligible, and the interaction becomes an irreversible loss. H^j_{bath} is the Hamiltonian of all the external modes that couple to the cavity modes through the coupler j,

$$H^j_{bath} = \int_{-\infty}^{\infty} \hbar\omega A^\dagger_j(\omega) A_j(\omega) d\omega + \int_{-\infty}^{\infty} \hbar\omega B^\dagger_j(\omega) B_j(\omega) d\omega \tag{2.8}$$

For each coupler j, $A_j(\omega)$ and $B_j(\omega)$ are bath modes for the fundamental and second harmonic modes respectively. These are continuum modes, and the annihilation and creation operators have units of $\sqrt{\text{photons/frequency}}$. H^j_{int} describes the interaction between cavity

modes and external modes:

$$H_{int}^{j} = i\hbar \int_{-\infty}^{\infty} \sqrt{2\gamma_a^j} \left[A_j^\dagger(\omega) a - a^\dagger A_j(\omega) \right] + \sqrt{2\gamma_b^j} \left[B_j^\dagger(\omega) b - b^\dagger B_j(\omega) \right] d\omega \tag{2.9}$$

Terms like $aA(\omega)$ and $a^\dagger A^\dagger(\omega)$, as well as all interactions between the pump and fundamental fields through the cavity couplers are at frequencies that will be far off resonance in the cavity and have been neglected in the rotating wave approximation. We are considering multiple modes of the external field, but only one mode cavity mode. External fields which are slightly off resonance can excite the cavity mode, just as laser light that is slightly off resonance can excite an atomic transition. $\gamma_{r,g}^j$ is a field decay rate associated with the coupler, given by $\gamma = (1-\sqrt{R})/\tau$ where R is the power reflectivity of the coupler at the appropriate wavelength and $\tau = c/p$ is the cavity round trip time (p is the cavity perimeter) [82]. If the total cavity losses are low, the decay rates can be approximated as $T/2\tau$ where T is the coupler power transmission.

2.3 Equations of motion for nonlinear cavities

Using the Hamiltonian from Equation 2.7, we can use Heisenberg's equation of motion to find equations of motion for the operators. The equations of motion are:

$$\frac{da}{dt} = \frac{i}{\hbar} \left[H_{cav}, a \right] + \sum_j i\hbar \sqrt{2\gamma_a^j} \int_{-\infty}^{\infty} d\omega A_j(\omega) \tag{2.10}$$

$$\frac{db}{dt} = \frac{i}{\hbar} \left[H_{cav}, b \right] + \sum_j i\hbar \sqrt{2\gamma_b^j} \int_{-\infty}^{\infty} d\omega B_j(\omega) \tag{2.11}$$

$$\frac{dA}{dt} = \sum_j -i\omega A_j(\omega) - \sqrt{2\gamma_a^j} a \tag{2.12}$$

$$\frac{dB}{dt} = \sum_j -i\omega A_j(\omega) - \sqrt{2\gamma_a^j} a \tag{2.13}$$

and similarly for the hermitian conjugates of these operators. Defining input and output bath fields as [64]:

$$A_{j,in}(t) = \int_{-\infty}^{\infty} d\omega e^{-i\omega(t-t_0)} A_j(\omega, t) \tag{2.14}$$

$$A_{j,out}(t) = \int_{-\infty}^{\infty} d\omega e^{-i\omega(t-t_1)} A_j(\omega, t) \tag{2.15}$$

and similarly for $B_{j,in}, B_{j,out}$ and hermitian conjugates, where t_0 is an earlier time than t and t_1 is a later time than t. We can integrate Equations 2.12 and 2.13 for $A(\omega)$ and $B(\omega)$ and substitute to solutions back into Equations 2.10 and 2.11. Using the definitions of the input and output baths, we find two equations of motion for each operator $a, a^\dagger, b, b^\dagger$:

$$\dot{a} = -\frac{i}{\hbar}[a, H_{cav}] - \gamma_a^{tot} a + \sum_j i\hbar\sqrt{2\gamma_a^i} A_{j,in} \tag{2.16}$$

$$\dot{a} = -\frac{i}{\hbar}[a, H_{cav}] + \gamma_a^{tot} a - \sum_j i\hbar\sqrt{2\gamma_a^i} A_{j,out} \tag{2.17}$$

where $\gamma_a^{tot} = \sum_j \gamma_a^j$ is the half width at half maximum of the cavity transmission in angular frequency units in the limit that the cavity losses are low. Subtracting Equation 2.16 from Equation 2.17 we can find separate boundary conditions for each coupler, known as the input-output relations:

$$\sqrt{2\gamma_a^j} a = A_{j,in} + A_{j,out} \tag{2.18}$$

The equations similar to Equations 2.16, 2.17, and 2.18 for other operators can be found by substituting $a \to (a^\dagger, b, b^\dagger)$, $A_{j,in} \to (A_{j,in}^\dagger, B_{j,in}, B_{j,in}^\dagger)$ and $A_{j,out} \to (A_{j,out}^\dagger, B_{j,out}, B_{j,out}^\dagger)$. We have followed the convention used in references [17, 64, 89] while different conventions used for the Langevin equations in some references [39, 40, 79] lead to different input-output relations.

The equations of motion with our nonlinear cavity Hamiltonian become:

$$\dot{a} = -\left(\gamma_r^{tot} + i\omega_a\right) a + \epsilon a^\dagger b + \sum_i \sqrt{2\gamma_r^i} A_{in,i} \tag{2.19}$$

$$\dot{a}^\dagger = -\left(\gamma_r^{tot} - i\omega_a\right) a^\dagger + \epsilon^* a b^\dagger + \sum_i \sqrt{2\gamma_r^i} A_{in,i}^\dagger \tag{2.20}$$

$$\dot{b} = -\left(\gamma_g^{tot} + i\omega_b\right) b - \frac{\epsilon^*}{2} a^2 + \sum_i \sqrt{2\gamma_g^i} B_{in,i} \tag{2.21}$$

$$\dot{b}^\dagger = -\left(\gamma_g^{tot} - i\omega_b\right) b^\dagger - \frac{\epsilon}{2} a^{\dagger 2} + \sum_i \sqrt{2\gamma_g^i} A_{in,i}^\dagger \tag{2.22}$$

Making the substitutions $a' = ae^{i\omega t}$, $A' = Ae^{i\omega t}$, $b' = be^{i2\omega t}$, and $B' = Be^{i2\omega t}$ we find equations for the slowly varying envelope operators:

$$\dot{a}' = -\left(\gamma_r^{tot} - i\Delta_a\right) a' + \epsilon a^{\dagger\prime} b' + \sum_i \sqrt{2\gamma_r^i} A'_{in,i} \tag{2.23}$$

$$\dot{a}^{\dagger\prime} = -\left(\gamma_r^{tot} + i\Delta_a\right) a^{\dagger\prime} + \epsilon^* a' b^{\dagger\prime} + \sum_i \sqrt{2\gamma_r^i} A_{in,i}^{\dagger\prime} \tag{2.24}$$

$$\dot{b}' = -\left(\gamma_g^{tot} - i\Delta_b\right) b' - \frac{\epsilon^* a'^2}{2} + \sum_i \sqrt{2\gamma_g^i} B'_{in,i} \tag{2.25}$$

$$\dot{b}^{\dagger\prime} = -\left(\gamma_g^{tot} + i\Delta_b\right) b^{\dagger\prime} - \frac{\epsilon a^{\dagger\prime 2}}{2} + \sum_i \sqrt{2\gamma_g^i} B_{in,i}^{\dagger\prime} \tag{2.26}$$

where $\Delta_a = \omega - \omega_a$ and $\Delta_b = 2\omega - \omega_b$. These primed operators are the slowly varying envelope operators introduced in Section 1.2, from now on we will drop the primes. Ignoring any input fields that include only quantum fluctuations, these are the classical equations of motion given by Drummond [23], and we will use them to calculate the classical behavior of our nonlinear cavities in Section 3.2.

2.4 Optical parametric oscillator equations of motion

Now we will specialize the equations of motion for a generic nonlinear cavity to include only the terms that we need to understand the vacuum squeezing produced by an OPO.

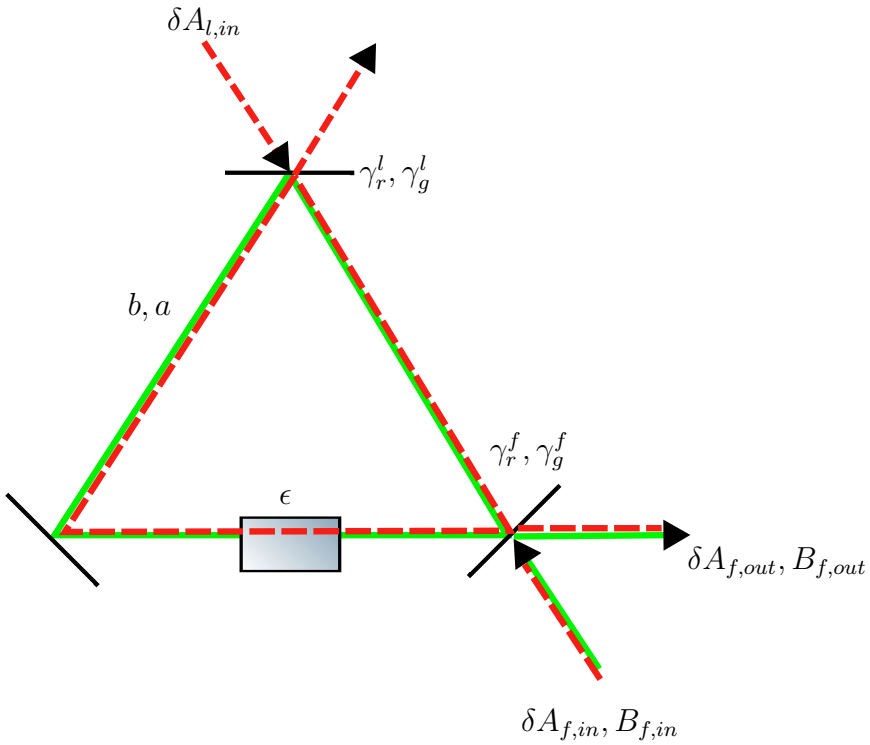

Figure 2-1: Optical parametric oscillator with input and output fields needed to produce vacuum squeezing. Green lines represent the second harmonic field, while dashed red lines represent the vacuum fluctuations or squeezed vacuum fluctuations at the fundamental frequency.

Our OPO uses no coherent input fundamental field and a strong coherent input field at the harmonic frequency, illustrated in Figure 2-1. The green pump field is coupled into the cavity through the same coupler that is the output coupler for the squeezed field, which we will call the front coupler, $\gamma_{r,g}^f$. The cavity losses are represented by another coupler, $\gamma_{r,g}^l$. We can write each of the slowly varying envelope operators as a sum of constant and fluctuating parts, $a = \bar{a} + \delta a(t)$. Since the only inputs at the fundamental frequency are the vacuum fluctuations, the circulating fundamental field has no constant steady state amplitude, only fluctuations $\delta a(t)$. Making the approximation that the pump field is large compared to quantum fluctuations, we can ignore the terms $\epsilon a^2(t)/2 + \sqrt{2\gamma_b^l}\delta B_{l,in}(t)$ in Equation 2.25. This is known as the parametric approximation; using it Equation 2.25 becomes the equation

for a classical field in a cavity without a nonlinear crystal:

$$b = \frac{\sqrt{2\gamma_g^f} B_{in,f}}{\gamma_g^{tot} - i\Delta_b} \tag{2.27}$$

If we set the frequency of the pump field to 2ω then in the rotating frame b is a constant, $\beta = |\beta| e^{i\theta_p}$. Equations 2.23 and 2.24 are now a pair of coupled linear differential equations:

$$\delta\dot{\mathbf{a}} = \gamma_r^{tot} \mathbf{M} \delta\mathbf{a} + \sqrt{2\gamma_r^l}\delta\mathbf{A_{l,in}} + \sqrt{2\gamma_r^f}\delta\mathbf{A_{f,in}} \tag{2.28}$$

where

$$\delta\mathbf{a} = \begin{pmatrix} \delta a \\ \delta a^\dagger \end{pmatrix} \tag{2.29}$$

and similarly for $\delta\mathbf{A_{l,in}}$ and $\delta\mathbf{A_{f,in}}$. The matrix $\mathbf{M}$ is:

$$\mathbf{M} = \begin{pmatrix} -1 + i\dfrac{\Delta_a}{\gamma_r^{tot}} & \dfrac{\epsilon\beta}{\gamma_r^{tot}} \\ \dfrac{\epsilon^*\beta^*}{\gamma_r^{tot}} & -1 - i\dfrac{\Delta_a}{\gamma_r^{tot}} \end{pmatrix} \tag{2.30}$$

The off diagonal elements, due to the nonlinearity, create correlations between the operators and their hermitian conjugates, and are responsible for the squeezing. The normalized nonlinear interaction strength is given by:

$$x = \frac{|\epsilon||\beta|}{\gamma_r^{tot}} \tag{2.31}$$

This is the ratio of the round trip gain to the round trip losses for the fundamental field. When it is 1 or above the cavity can produce a field with a coherent amplitude at the fundamental frequency, known as spontaneous subharmonic generation. We always operate the OPO below this threshold.

The matrix $\mathbf{M}$ contains three terms that describe experimental quantities that can vary

and affect the squeezing produced by the OPO: β, ϵ, and Δ_a. We will write $\mathbf{M}$ as the sum of a constant and fluctuating part: $\mathbf{M} = \overline{\mathbf{M}} + \delta\mathbf{M}(\mathbf{t})$. In Chapter 5 we will consider the impact of the fluctuations on the squeezing produced and measured, but for now we will ignore the fluctuating part, and assume that the interaction is perfectly phase matched so that ϵ is real. Taking a Fourier transform of the time domain slowly varying envelope operators:

$$\widetilde{a}(\Omega) = \frac{1}{\sqrt{2\pi}} \int_{-\infty}^{\infty} a(t) e^{i\Omega t} d\Omega \tag{2.32}$$

Equation 2.28 becomes:

$$i\Omega\delta\widetilde{\mathbf{a}} = \gamma_r^{tot}\overline{\mathbf{M}}\delta\widetilde{\mathbf{a}} + \sqrt{2\gamma_r^l}\delta\widetilde{\mathbf{A}}_{\mathbf{l,in}} + \sqrt{2\gamma_r^f}\delta\widetilde{\mathbf{A}}_{\mathbf{f,in}} \tag{2.33}$$

Using the convention that $c^\dagger(t) = [c(t)]^\dagger$ the Fourier transform of $c^\dagger(t)$ is $c^\dagger(-\Omega)$ [40, p440]. The Fourier domain vectors of operators is:

$$\delta\widetilde{\mathbf{a}} = \begin{pmatrix} \widetilde{a}(\Omega) \\ \widetilde{a}^\dagger(-\Omega) \end{pmatrix} \tag{2.34}$$

and similarly for the operators $a^\dagger, A_{l,in}, A_{f,in}$. Using the translation property of the Fourier transform to translate these frequency components of the slowly varying envelope operators back to frequency components of the Heisenberg picture operators with the full time dependence (moving out of the rotating frame at ω):

$$\begin{pmatrix} \widetilde{a}(\Omega) \\ \widetilde{a}^\dagger(-\Omega) \end{pmatrix} \rightarrow \begin{pmatrix} \widetilde{a}(\omega+\Omega) \\ \widetilde{a}^\dagger(\omega-\Omega) \end{pmatrix} \tag{2.35}$$

The operators represent two symmetric sidebands around the carrier frequency ω, however they should not be confused with separate modes of the field. The intra-cavity operators in

terms of the input operators are:

$$\delta\tilde{\mathbf{a}} = \left(i\Omega\mathbf{I} - \gamma_r^{tot}\mathbf{M}\right)^{-1}\left[\sqrt{2\gamma_r^l}\delta\widetilde{\mathbf{A}}_{\mathbf{l,in}} + \sqrt{2\gamma_r^f}\delta\widetilde{\mathbf{A}}_{\mathbf{f,in}}\right] \tag{2.36}$$

Using the input-output relation, the output field from the front coupler, in terms of the input field, is:

$$\begin{aligned}\delta\widetilde{\mathbf{A}}_{\mathbf{f,out}} &= \sqrt{2\gamma_r^f}\delta\tilde{\mathbf{a}} - \delta\widetilde{\mathbf{A}}_{\mathbf{f,in}} \\ &= \left(2\gamma_r^f\left(i\Omega\mathbf{I} - \gamma_r^{tot}\mathbf{M}\right)^{-1} - \mathbf{I}\right)\delta\mathbf{A}_{\mathbf{f,in}} + 2\sqrt{\gamma_r^l\gamma_r^f}\left(i\Omega\mathbf{I} - \gamma_r^{tot}\mathbf{M}\right)^{-1}\delta\mathbf{A}_{\mathbf{l,in}}\end{aligned} \tag{2.37}$$

2.5 Quadrature variances of intra-cavity and output fields

The variance of the quadrature operators set the noise level of any measurement we will make using these states. Using the transformation $\mathbf{R}$ from Equation 1.22 we can find Equations 2.38 and 2.37 in terms of quadrature operators:

$$\delta\tilde{\mathbf{X}}_{\mathbf{c}} = \left(i\Omega\mathbf{I} - \gamma_r^{tot}\mathbf{R}\mathbf{M}\mathbf{R}^{-\mathbf{1}}\right)^{-1}\left[\sqrt{2\gamma_r^l}\delta\widetilde{\mathbf{X}}_{\mathbf{l,in}} + \sqrt{2\gamma_r^f}\delta\widetilde{\mathbf{X}}_{\mathbf{f,in}}\right] \tag{2.38}$$

$$\delta\widetilde{\mathbf{X}}_{\mathbf{f,out}} = \left(2\gamma_r^f\left(i\Omega\mathbf{I} - \gamma_r^{tot}\mathbf{R}\mathbf{M}\mathbf{R}^{-\mathbf{1}}\right)^{-1} - \mathbf{I}\right)\delta\mathbf{X}_{\mathbf{f,in}} + 2\sqrt{\gamma_r^l\gamma_r^f}\left(i\Omega\mathbf{I} - \gamma_r^{tot}\mathbf{R}\mathbf{M}\mathbf{R}^{-\mathbf{1}}\right)^{-1}\delta\mathbf{X}_{\mathbf{l,in}} \tag{2.39}$$

The variance of these operators, measured by a power spectral density, are given by $V(\Omega) = \langle|\delta\widetilde{X}(\Omega)|^2\rangle$ [7, sec 2.4.1]. A vector of variances for the vacuum state is:

$$\mathbf{V}_{\mathbf{vac}} = \mathbf{V}_{\mathbf{f,in}}(\Omega) = \mathbf{V}_{\mathbf{l,in}}(\Omega) = \begin{pmatrix}\langle|\delta\widetilde{X}_1(\Omega)|^2\rangle \\ \langle|\delta\widetilde{X}_2(\Omega)|^2\rangle\end{pmatrix} = \begin{pmatrix}1 \\ 1\end{pmatrix} \tag{2.40}$$

Since fluctuations in different fields and different quadratures of the vacuum are uncorrelated, cross terms between different inputs are zero. The variance of the resulting fields are given

by

$$\mathbf{V_{out}} = \left(2\gamma_r^f \left(i\Omega\mathbf{I} - \gamma_r^{tot}\mathbf{RMR^{-1}}\right)^{-1} - \mathbf{I}\right) \circ \left(2\gamma_r^f \left(i\Omega\mathbf{I} - \gamma_r^{tot}\mathbf{RMR^{-1}}\right)^{-1} - \mathbf{I}\right)^* \mathbf{V_{inc}}$$
$$+ 4\gamma_r^l\gamma_r^f \left(i\Omega\mathbf{I} - \gamma_r^{tot}\mathbf{RMR^{-1}}\right)^{-1} \circ \left[\left(i\Omega\mathbf{I} - \gamma_r^{tot}\mathbf{RMR^{-1}}\right)^{-1}\right]^* \mathbf{V_l} \quad (2.41)$$

$$\mathbf{V_c} = 2\gamma_r^{tot} \left(i\Omega\mathbf{I} - \gamma_r^{tot}\mathbf{RMR^{-1}}\right)^{-1} \circ \left[\left(i\Omega\mathbf{I} - \gamma_r^{tot}\mathbf{RMR^{-1}}\right)^{-1}\right]^* \mathbf{V_{vac}} \quad (2.42)$$

where $\circ$ indicates the element-wise product and * is used here to mean the element wise complex conjugate.

Assuming that the detunings are zero $\Delta_a = 0$, the temperature is set so that ϵ and therefore x are real, the variances of the circulating fields are given by:

$$\mathbf{V_c} = \frac{2}{\gamma_r^{tot}} \begin{pmatrix} \dfrac{1 + x^2 + \left(\dfrac{\Omega}{\gamma_r^{tot}}\right)^2 + 2x\cos\theta}{\left((1-x)^2 + \left(\dfrac{\Omega}{\gamma_r^{tot}}\right)^2\right)\left((1+x)^2 + \left(\dfrac{\Omega}{\gamma_r^{tot}}\right)^2\right)} \\ \dfrac{1 + x^2 + \left(\dfrac{\Omega}{\gamma_r^{tot}}\right)^2 - 2x\cos\theta}{\left((1-x)^2 + \left(\dfrac{\Omega}{\gamma_r^{tot}}\right)^2\right)\left((1+x)^2 + \left(\dfrac{\Omega}{\gamma_r^{tot}}\right)^2\right)} \end{pmatrix} \quad (2.43)$$

To find the level of squeezing of the intra-cavity field we will find the ratio of the intra-cavity field in the OPO to the variance a field would have if the cavity were empty, meaning that $x \to 0$. The highest levels of squeezing will be observed at measurement frequencies that are small compared to the cavity line-width, so that $\Omega/\gamma_r^{tot} \to 0$. Then the level of squeezing is given by:

$$\frac{V_2(x, \theta = 0)}{V_2(0, \theta = 0)} = \frac{1}{(1+x)^2} \quad (2.44)$$

Even as the normalized nonlinear interaction strength x approaches one, the value at threshold, the maximum amount of squeezing of the intra-cavity field is -3 dB, or 50% reduction in the variance compared to a vacuum state [73, 89].

If we again let the detunings Δ_a be zero, and x be real, we get values for the output field.

$$\mathbf{V_{out}}(\Omega,\theta) = \begin{pmatrix} 1 + \dfrac{4x\eta_{esc}\left(2x + \left(1 + x^2 + \left(\dfrac{\Omega}{\gamma_r^{tot}}\right)^2\right)\cos\theta\right)}{\left((1-x)^2 + \left(\dfrac{\Omega}{\gamma_r^{tot}}\right)^2\right)\left((1+x)^2 + \left(\dfrac{\Omega}{\gamma_r^{tot}}\right)^2\right)} \\ 1 + \dfrac{4x\eta_{esc}\left(2x - \left(1 + x^2 + \left(\dfrac{\Omega}{\gamma_r^{tot}}\right)^2\right)\cos\theta\right)}{\left((1-x)^2 + \left(\dfrac{\Omega}{\gamma_r^{tot}}\right)^2\right)\left((1+x)^2 + \left(\dfrac{\Omega}{\gamma_r^{tot}}\right)^2\right)} \end{pmatrix} \tag{2.45}$$

Here $\eta_{esc} = \gamma_r^f/\gamma_r^{tot}$ is the escape efficiency, the fraction of the round trip power losses that are due to the output coupler. If we let $\theta = 0$ we get the usual results for amplitude squeezing from an OPO [2, 66, 89]:

$$\mathbf{V_{out}}(\Omega,0) = \begin{pmatrix} V_+ \\ V_- \end{pmatrix} = \begin{pmatrix} 1 + \dfrac{4x\eta_{esc}}{(1-x)^2 + (\Omega/\gamma_r^{tot})^2} \\ 1 - \dfrac{4x\eta_{esc}}{(1+x)^2 + (\Omega/\gamma_r^{tot})^2} \end{pmatrix} \tag{2.46}$$

This is a minimum uncertainty state if $\eta_{esc} = 1$, but not otherwise. We can now write Equation 2.45 in a more compact form:

$$\mathbf{V_{out}} = \begin{pmatrix} \cos^2\frac{\theta}{2} & \sin^2\frac{\theta}{2} \\ \sin^2\frac{\theta}{2} & \cos^2\frac{\theta}{2} \end{pmatrix} \begin{pmatrix} V_+ \\ V_- \end{pmatrix} \tag{2.47}$$

Since θ is the phase that determines which quadrature will be squeezed, we will call it the squeezing angle, θ_{sqz}. In this idealized case the squeezing angle is the same as the phase of the pump, but in Chapter 5 we will consider situations where they could be different. In the context of gravitational wave detection, the measurement frequency (10 Hz-10 kHz) will always be well within the cavity line-width of a few GHz, and Ω/γ_r^{tot} can be set to zero.

In ideal limit where $\eta_{esc} \to 1$ and $x \to 1$ the variance of the output field approaches zero. The higher level of squeezing on the output field is possible because the output field

is the sum of the directly reflected field and the leakage field from the cavity. The nonlinear process creates correlations between the leakage cavity field and the directly reflected field, so that the noise of the total field can be reduced.

2.6 Propagation of squeezing

Throughout Chapter 1 we considered the field at a reference plane, and defined operators in that reference plane, where $z = 0$. As the field propagates through space Equation 1.8 becomes:

$$E(t) = \varepsilon_0 \left(a(t) e^{-i(\omega t - kz)} + a^\dagger(t) e^{i(\omega t - kz)} \right) \tag{2.48}$$

Where k is the wavenumber for the field. The equation for the field written in terms of quadrature operators, Equation 1.16, is unchanged at different positions in space, so the quadrature operators at a position z in terms of the annihilation and creation operators are:

$$X_1(z) = a e^{ikz} + a^\dagger e^{-ikz} \tag{2.49}$$

$$X_2(z) = i \left(a e^{ikz} - a^\dagger e^{-ikz} \right) \tag{2.50}$$

The quadrature that is squeezed rotates in the way that a classical phase would rotate as the beam propagates through space:

$$X(\theta, z) = X(\theta + kz, 0) \tag{2.51}$$

Although the squeezed vacuum does not have an amplitude and therefore ca not have a phase in the classical sense because it has no amplitude, as it propagates through space the squeezing angle changes in the same way that the phase of a classical field would.

As the squeezed state propagates it will also experience losses. Any loss can be modeled as a beamsplitter with power reflectivity $\eta_{loss} = 1 - L$. In the quantum treatment of a beamsplitter, we need to consider the fields that enter both ports of the beamsplitter, even

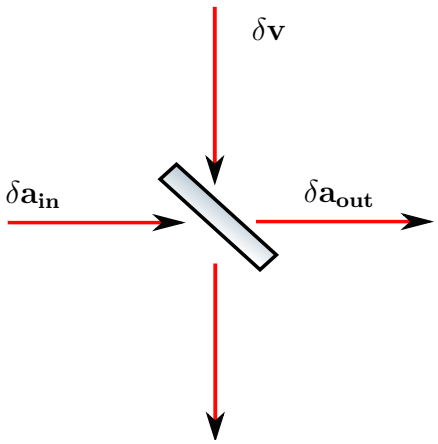

Figure 2-2: Beamsplitter model of loss

when one of the input fields is in the vacuum state. The output field is then:

$$\delta\mathbf{a_{out}} = \sqrt{\eta_{loss}}\delta\mathbf{a_{in}} + i\sqrt{1-\eta_{loss}}\delta\mathbf{v} \tag{2.52}$$

And the variance of the output field is

$$\mathbf{V_{out}} = \eta_{loss}\mathbf{V_{in}} + (1-\eta_{loss})\mathbf{V_{vac}} \tag{2.53}$$

$$V_{out,\pm} = 1 \pm \frac{4\eta_{esc}\eta_{loss}x}{(1\mp x)^2 + (\Omega/\gamma_r^{tot})^2} \tag{2.54}$$

There will be several different sources of loss cascaded in the path from the OPO to the detector, the total propagation loss will be the product of the all of these losses. Even if a pure squeezed state was incident on the lossy optic, it becomes mixed with the vacuum state, meaning that it cannot be a minimum uncertainty state after losses are taken into account.

2.7 Homodyne detection

The requirements for reading out the gravitational wave signal are similar to requirements for detecting squeezing. In both cases we want to measure small audio frequency modulations on an optical frequency wave. There are two important requirements for accomplishing this: the detector noise must be smaller than the modulations we are trying to measure, and the

signals should be demodulated at the laser frequency so that the signals we are trying to measure will be at audio frequencies. Keeping the detector noise below the small signal from a gravitational wave or quantum noise requires both amplifying the signal and keeping other noise sources small. Both amplification and demodulation can be achieved by interfering the signal beam with a local oscillator beam at the same frequency, a technique called homodyne detection. For a thorough discussion of detection techniques see [10]. Figure 2-3 shows a

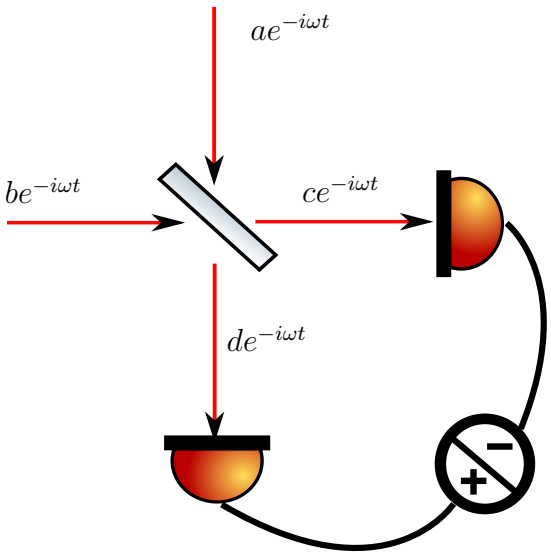

Figure 2-3: Homodyne detector

general schematic of a homodyne detection scheme, with two input fields $ae^{-i\omega t}$ and $be^{-i\omega t}$. The beamsplitter with power reflectivity R transforms the input fields to the output fields:

$$\begin{pmatrix} ce^{-i\omega t} \\ de^{-i\omega t} \end{pmatrix} = \begin{pmatrix} \sqrt{R} & i\sqrt{1-R} \\ i\sqrt{1-R} & \sqrt{R} \end{pmatrix} \begin{pmatrix} ae^{-i\omega t} \\ be^{-i\omega t} \end{pmatrix} \tag{2.55}$$

The photocurrent at each detector becomes:

$$\begin{aligned} I_C &= \varepsilon_0^2 \eta_{PD} \left(|ce^{-i\omega t}|^2 \right) \\ &= \varepsilon_0^2 \eta_{PD} \left(R|a|^2 + i\sqrt{R(1-R)} \left(ba^\dagger - ab^\dagger \right) + (1-R)|b|^2 \right) \end{aligned} \tag{2.56}$$

$$\begin{aligned} I_D &= \varepsilon_0^2 \eta_{PD} \left(|de^{-i\omega t}|^2 \right) \\ &= \varepsilon_0^2 \eta_{PD} \left((1-R)|a|^2 + i\sqrt{R(1-R)} \left(ab^\dagger - a^\dagger b \right) + R|b|^2 \right) \end{aligned} \tag{2.57}$$

where η_{PD} is the quantum efficiency of the photodetector. The optical frequency time dependence $e^{-\omega t}$ has been removed from this measurement, so we can measure operators that are defined in the rotating frame at the laser frequency. The sum and difference photocurrents are:

$$I_{sum} = \varepsilon_0^2 \eta_{PD} \left(I_c + I_D \right) = \varepsilon_0^2 \eta_{PD} \left(|a|^2 + |b|^2 \right) \tag{2.58}$$

$$I_{diff} = \varepsilon_0^2 \eta_{PD} \left(I_c + I_D \right) \tag{2.59}$$

$$= \varepsilon_0^2 \eta_{PD} \left((2R-1)|a|^2 + 2i\sqrt{R(1-R)}(ba^\dagger - ab^\dagger) + (1-2R)|b|^2 \right) \tag{2.60}$$

Homodyne detection can either be balanced, where $R = 1/2$ or unbalanced, and can either use an external local oscillator or use self homodyne in which the same beam has both the signal and the local oscillator.

2.7.1 Balanced homodyne detection with an external local oscillator

The most commonly used method for measuring squeezing in table top experiments is balanced homodyne detection, with an external local oscillator. If a is the signal field whose noise we want to measure, then b is a local oscillator field, in a coherent state with an amplitude much larger than a. In balanced homodyne detection Equation 2.60 becomes:

$$I_{diff} = \varepsilon_0^2 \eta_{PD} i \left(a^\dagger b - a b^\dagger \right) \tag{2.61}$$

The difference photo-current has no dependence on $|a|^2$ and $|b|^2$, which are proportional to the intensity of each beam, and include the intensity noise. At the gravitational wave frequencies where we are interested in measuring squeezing, typical laser beams have intensity noise orders of magnitude larger that the quantum noise we are trying to measure, but the common mode noise subtraction of balanced homodyne detection allows us to make quantum limited noise measurements even when each individual beam has large classical intensity noise. In practice, any beam-splitter will have a reflectivity slightly different than 50%, limiting the suppression of intensity noise that can be achieved with balanced homodyne. For a description of noise reduction in a homodyne detector of this type, see [80].

We can write the local oscillator as a constant and fluctuating part,

$$be^{i\omega t} = \left(|\beta|e^{-i\theta_b} + \delta b(t)\right) e^{i\omega t}$$

. Since our signal field is a vacuum state, there is no constant part and $ae^{i\omega t} = \delta a(t)e^{i\omega t}$. After dropping the small terms $\delta a^\dagger(t)\delta a(t)$ and $\delta b(t)\delta a^\dagger(t)$ Equation 2.61 becomes:

$$\begin{aligned} I_{diff} &= \varepsilon_0^2 \eta_{PD} |\beta| i \left(e^{-i\theta_b}\delta a^\dagger(t) - e^{i\theta_b}\delta a(t)\right) \\ &= \varepsilon_0^2 \eta_{PD} |\beta| \delta X_a(\theta_b - \pi/2) \end{aligned} \tag{2.62}$$

where $\delta X_a(\theta)$ is the arbitrary quadrature operator of a defined by Equation 1.20. So the balanced homodyne measures the arbitrary quadrature operator defined by Equation 1.20 on the signal beam, where the quadrature angle is determined by the phase of the local oscillator. The signal is amplified by the amplitude of the local oscillator. The photocurrent is amplified by a transimpedance gain $\mathcal{R}$, and a power spectral density is measured by a spectrum analyzer [7]:

$$\begin{aligned} S_{diff}(\Omega) &= (\varepsilon_0^2 \eta_{PD} |\beta| \mathcal{R})^2 \left\langle |\delta \widetilde{X}_a(\theta_b - \pi/2, \Omega)|^2 \right\rangle \\ &= (\varepsilon_0^2 \eta_{PD} |\beta| \mathcal{R})^2 V_a(\theta_b - \pi/2, \Omega) \end{aligned} \tag{2.63}$$

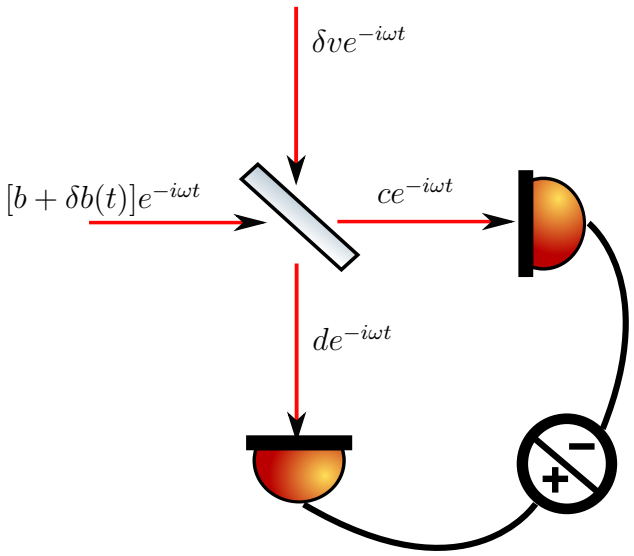

Figure 2-4: Balanced self homodyne

where $V_a(\theta, \Omega)$ is the arbitrary quadrature variance of a defined by Equation 1.24.

2.7.2 Self homodyne detection

Gravitational wave detectors that use a DC readout scheme, like Enhanced and Advanced LIGO, use self homodyne to detect the gravitational wave signal [34, 78]. In self homodyne the input field is $\left[|\beta|e^{i\theta_b} + \delta b(t)\right] e^{-i\omega t}$. The first term is a DC offset due to a small offset of the differential arm degree of freedom from the dark fringe, and acts as the local oscillator. The signal, $\delta b(t)e^{-i\omega t}$, consists of sidebands due to a gravitation wave passing through the detector or due to noise. The sum photo-current, after dropping products of noise terms, becomes:

$$\begin{aligned} I_{sum} &= \varepsilon_0^2 \eta_{PD} \left[|\beta|^2 + |\beta| \left(\delta b(t) e^{i\theta_b} + \delta b^\dagger(t) e^{-i\theta_b}\right)\right] \\ &= \varepsilon_0^2 \eta_{PD} \left[|\beta|^2 + |\beta| \delta X_b(\theta_b)\right] \end{aligned} \tag{2.64}$$

The power spectral density, defined by Equation 1.24 is:

$$S_{sum}(\Omega) = (\varepsilon_0^2 \eta_{PD} |\beta| \mathcal{R})^2 V_b(\Omega, \theta_b) \tag{2.65}$$

This is a measurement of amplitude fluctuations on the signal field, in self homodyne detection there is no freedom to change the relative phase between the local oscillator and change the measurement quadrature. The local oscillator beam used in the interferometer has very low noise, reducing the need for noise rejection.

2.7.3 Balanced self homodyne detection

Enhanced LIGO used balanced self homodyne detection, where the beam-splitter power reflectivity is 50%. The sum photo-current is the gravitational wave readout channel. Since the input to the other port of the beamsplitter is the ground state, with a variance of one, from Equation 2.63 the power spectral density of the difference photo-current in balanced self homodyne is:

$$S_{diff}(\Omega) = (\varepsilon_0^2 \eta_{PD} |\bar{b}| \mathcal{R})^2 \tag{2.66}$$

which is the shot noise level of b, with other types of noise suppressed by the common mode rejection. This channel is known as the nullstream, and can be useful in understanding the contribution of shot noise to the interferometer noise. When $S_{diff}(\Omega) = S_{sum}(\Omega)$, the interferometer is shot noise limited and the coherent state is a good description of b. When squeezing is injected into the interferometer, S_{diff} is unchanged since its noise originates from the vacuum fluctuations at the detection beam splitter, but S_{sum} can have lower noise. A comparison of the two channels gives a real time measurement of the level of squeezing.

2.7.4 Unbalanced homodyne detection with an external local oscillator

To measure squeezing in the interferometer we use unbalanced homodyne detection, illustrated in Figure 2-5. Here a powerful local oscillator is reflected off of a beamsplitter with a large reflectivity, a small fraction of it will be transmitted and interfere with the signal beam which is mostly reflected. A high reflectivity beamsplitter reduces the loss for the

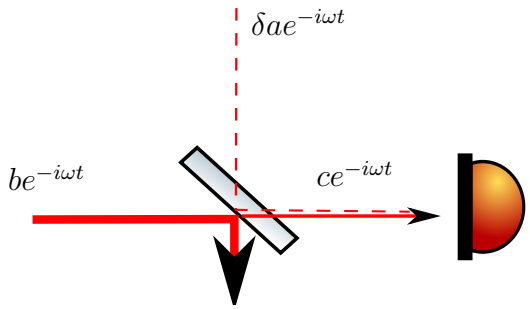

Figure 2-5: Unbalanced homodyne detection

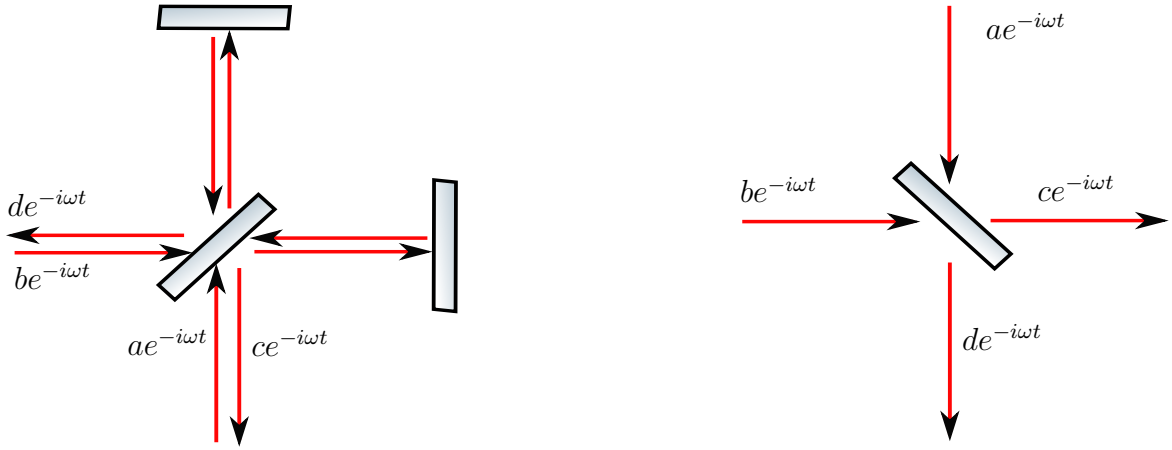

Figure 2-6: Interferometer as a beamsplitter. The main laser input is b, while the dark port input a is either vacuum or squeezed vacuum. d is the reflected field, and c is the field detected to read out the gravitational wave signal.

small signal beam. An interferometer can be simplified and thought of as a beamsplitter, as illustrated in Figure 2-6. Squeezing is injected into the dark port using a Faraday rotator, replacing the vacuum fluctuations in a. From Equation 1.43 the matrix representing the interferometer is:

$$\mathbf{IFO} = e^{i(\Phi + \pi/2)} \begin{pmatrix} \sin\phi & \cos\phi \\ \cos\phi & -\sin\phi \end{pmatrix} \tag{2.67}$$

This matrix is unitary, because of the assumption that there is no loss in the arms. Since it is also symmetric, it is an acceptable description of a beamsplitter although it is different from the convention we used in Equation 1.40. The gravitational wave signal will be in

the amplitude quadrature of c, we will use squeezing to reduce the quantum noise in this quadrature. The output field c from the anti-symmetric port is the input field b to the beamsplitter used in the balanced self homodyne detection described in Section 2.7.3. The sum photo-current is proportional to Equation 1.47:

$$I_c = \varepsilon_0^2 \eta_{PD} c^\dagger c = \varepsilon_0^2 \eta_{PD} (\Delta|\beta|)^2 + \frac{2\omega L h_+}{c} \Delta|\beta|^2 - \Delta|\beta| X_a(-\theta_b) \tag{2.68}$$

This will give a measurement of the variance of the input field, as long as the intensity noise of b is lower than the quantum noise. In the interferometer the output field has much lower intensity noise than a typical laser beam, and so we are able to use that beam as a local oscillator in unbalanced homodyne detection. We can adjust the phase of the injected squeezing to make sure that the quantum noise in the gravitational wave readout is reduced.

2.7.5 Detection losses

The detection process also introduces losses, which have the same effect as propagation losses. Photodiodes are not perfectly efficient; we can think of the photodetector as an ideal photodetector behind a beamsplitter with transmission η_{PD}, the quantum efficiency of the photodiode [7, p 16]. The detector will measure the quantum noise of the field that is in the same spatial mode as the local oscillator, if there is a misalignment of the squeezed beam the measured beam will be a mixture of the squeezed beam and vacuum fluctuations that also interfere with the local oscillator. The misalignment has the same effect as a loss, described by the homodyne efficiency [7, p 20]:

$$\eta_{HD} = \mathcal{V}^2 = \left(\frac{P_{max} - P_{min}}{P_{max} + P_{min}} \right)^2 \tag{2.69}$$

where the fringe visibility $\mathcal{V}$ can be measured by matching the power in the signal and local oscillator beam and measuring the maximum and minimum of the interference fringes.

2.8 Noise reduction due to squeezing

Combining the results from this chapter, the variance of the interferometer readout with squeezing injected is the sum of the variance of the technical noise($V_{tech}(\Omega)$ and the quantum noise ($V(\theta, \Omega)$):

$$V_{tot}(\Omega) = S_{tot}(\Omega) = V_{tech}(\Omega) + V(\theta, \Omega) \tag{2.70}$$

$$= V_{tech}(\Omega) + V_{+}(\Omega)\sin^2\theta_{sqz} + V_{-}(\Omega)\cos^2\theta_{sqz} \tag{2.71}$$

$$V_{\pm}(\Omega) = 1 \pm \frac{4x\eta_{tot}}{(1 \mp x)^2 + (\Omega/\gamma_r^{tot})^2} \tag{2.72}$$

where $\eta_{tot} = \eta_{esc}\eta_{loss}\eta_{HD}\eta_{PD}$. We normally refer to the level of shot noise reduction using logarithmic units:

$$\mathrm{dB}(\Omega) = 10\log_{10}\frac{S(\Omega)\big|_{\text{squeezing}}}{S(\Omega)\big|_{\text{no squeezing}}} \tag{2.73}$$

We often measure an amplitude power spectral density, which is just the square root of the power spectral density, in that case

$$\mathrm{dB} = 20\log_{10}\frac{S^{1/2}(\Omega)\big|_{\text{squeezing}}}{S^{1/2}(\Omega)\big|_{\text{no squeezing}}} \tag{2.74}$$

Chapter 3

Enhanced LIGO squeezing experiment

The potential for squeezing to improve the sensitivity of gravitational wave detectors provided an early motivation for both theoretical and experimental investigations of squeezing. Caves predicted a sensitivity improvement from squeezing in 1981, and Xiao and colleagues first demonstrated an improvement in the sensitivity of an interferometer at 1.6 MHz in a proof of principle experiment 25 years ago [91]. In the last decade as full scale gravitational wave detectors like LIGO and VIRGO have reached their design sensitivities, ongoing work has brought squeezing closer to becoming a feasible technique for gravitational wave astronomy. Table top experiments have shown noise reduction in interferometer configurations more similar to gravitational wave detectors, at measurement frequencies of 5 MHz and above [59, 86]. Squeezing down to approximately 30 kHz was demonstrated in a prototype LIGO interferometer with suspended mirrors in 2007, [43] and another important step towards implementation in full scale detectors was achieved in 2011 with implementation of squeezing down to 1 kHz in the GEO600 detector [15]. GEO has been able to implement squeezing as part of normal operation, study the stability of the level of squeezing, and non Gaussian noise introduced to the interferometer by squeezing.

The most promising astrophysical targets for earth-based gravitational wave detectors are expected to emit at frequencies from 10s of Hz to a few kHz. A variety of noise sources, many driven by acoustic or seismic noise, make precision measurements at these audio and sub-

audio frequencies more difficult than higher frequency measurements. A variety of classical noise couplings had to be overcome to produce squeezing at these low frequencies [58, 80]. Experience has shown that techniques that can successfully improve the performance of a higher frequency interferometer introduce noise couplings that are not acceptable in a LIGO interferometer. To confidently plan to implement squeezing in the astrophysical frequency band below 1 kHz, it was necessary to test squeezing in an interferometer with high sensitivity in this band.

A short window of opportunity to test squeezing in an Enhanced LIGO interferometer opened in late 2011 while construction of Advanced LIGO was underway on two of the LIGO interferometers. One of the interferometers at Hanford, WA was preserved in the Enhanced LIGO configuration, and we were able to use it when the Advanced LIGO schedule allowed. This work is complimentary to the work with squeezing done at GEO600 in the last few years. While we had a shorter window of opportunity, the LIGO interferometers have orders of magnitude better sensitivity in the crucial region around 100 Hz. We were able to use squeezing to achieve the best sensitivity above 250 Hz that has been demonstrated in a gravitational wave detector to date, and understand some of the challenges unique to low frequency squeezing in a full scale gravitational wave interferometer.

3.1 Enhanced LIGO

To sense the incredibly small strains produced by gravitational waves LIGO interferometers have some additional features and additional compelxtiy compared to the simple Michelson interferometer discussed in the introduction. A simplified diagram of the Enhanced LIGO layout is shown in Figure fig:ELIGOlayout. The light source is a Nd:YAG laser, capable of producing 35 W of 1064 nm light. The main laser is prestabilized in frequency and intensity, and filtered by an input mode cleaner to produce a beam with a pure spatial mode for injection into the interferometer.

Because the expected gravitational wave strains are of the order 10^{-21}, the long arms are needed to increase the expected displacements. The LIGO interferometers use 4 km arms,

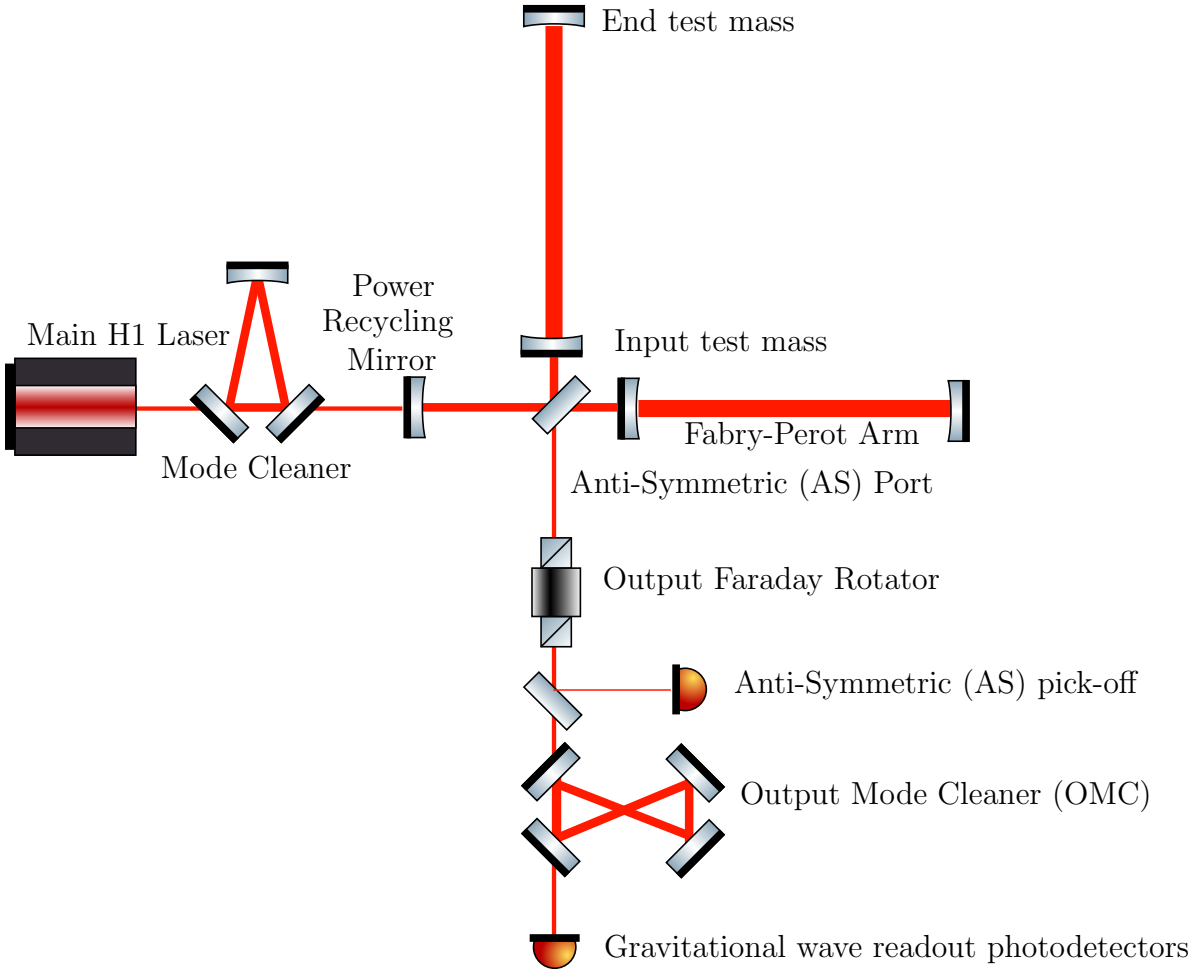

Figure 3-1: Basic layout of Enhanced LIGO, not to scale

each of which is a Fabry-Perot cavity. The Fabry-Perot cavity circulates light for an average of 130 round trips in each arm before leaking out toward the beam-splitter. This means that the phase shift induced by a low frequency gravitational wave will be enhanced by a factor of about 130. The cavities also act as a low pass filter for the gravitational wave signal, with a cavity pole at 85 Hz [32]. The four optics that make up the Fabry-Perot arms are the test masses used to detect gravitational waves, the mirrors closest to the beam-splitter are called input test masses while the high reflectors at the ends of the cavities are known as end test masses. These core interferometer optics are all suspended from vibration isolated platforms, to reduce the coupling of seismic noise to motion of the optics. An active control

system maintains the alignment of these suspended optics [22, 47].

In addition to the arm cavities, LIGO makes use of a power recycling cavity: a nested cavity formed by a partially transmissive power recycling mirror and the two arm cavities. This additional cavity improves the shot noise limited sensitivity by increasing the power at the beamsplitter by a factor of 40, so that with 20 W injected into the interferometer there are 800 W at the beamsplitter and 5 kW in each arm. However, this high power presents several practical challenges [22], including thermal lensing in the input test masses. Advanced LIGO will be capable of increasing the input power by a factor of five, approaching the limits of available technology. Squeezing provides an alternative to high power operation; at some point squeezing will be simpler and lower risk than further increases in input power.

The gravitational wave signal is detected using homodyne detection at the antisymmetric port. The low power (100s of mWs) beam leaving the AS port first passes through an output Faraday isolator (OFI), to prevent scatter from any of the sensors or optics in the readout chain from re-entering the interferometer and creating a parasitic interferometer. After the output Faraday a small amount of the power at the antisymmetric port exits the vacuum system onto the AS table which has several sensors used for alignment sensing and control, and the heterodyne sensing scheme that is used initially to lock the interferometer. This sensing scheme uses RF modulation sidebands for a locking scheme similar to Pound-Drever-Hall (PDH), and at the AS port approximately 2/3 of the optical power was actually from the sidebands at 24.5 MHz. The output mode cleaner(OMC) filters the AS beam to create a quiet local oscillator, rejecting the RF sidebands and any power which is in in the wrong spatial mode [34, 36, 78]. The main results from our experiment were obtained with the Enhanced LIGO interferometer in this configuration, as close as possible to the configuration used during LIGO's flagship S6 science run.

Figure 3-2 shows the strain sensitivity of both the Hanford (H1) and Livingston (L1) Enhanced LIGO detectors. The limiting noise source below 40 Hz is seismic noise. Thermal noise from the mirror suspensions and the optical coating dominates from 40-100 Hz, and shot noise dominates above 200 Hz. Quantum radiation pressure noise is buried orders

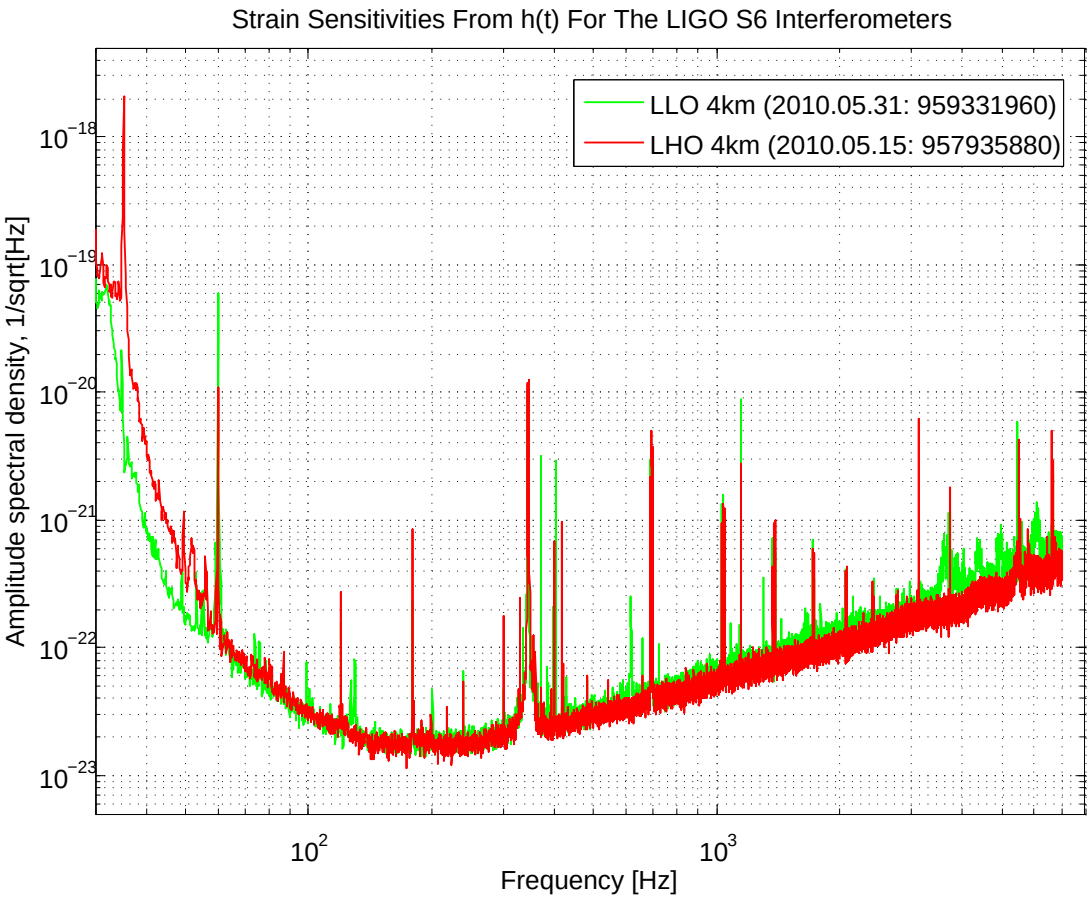

Figure 3-2: Strain sensitivity of enhanced LIGO during S6 science run [16]

of magnitudes below the seismic noise in Enhanced LIGO; no quantum radiation pressure effects were studied during this experiment.

3.2 Squeezed state source

Figure 3-3 shows a simplified layout of the squeezed light source. Both lasers are Nd:YAG non-planar ring oscillators (NPROs). Two frequency stabilization servos (FSS1 and FSS2) keep the pump laser locked to the H1 main laser frequency and the control laser locked at a 29.5 MHz offset. The pump laser is used to pump a second harmonic generator (SHG). This is a standing wave cavity with a periodically poled $KTiOPO_4$ (PPKTP) nonlinear crystal

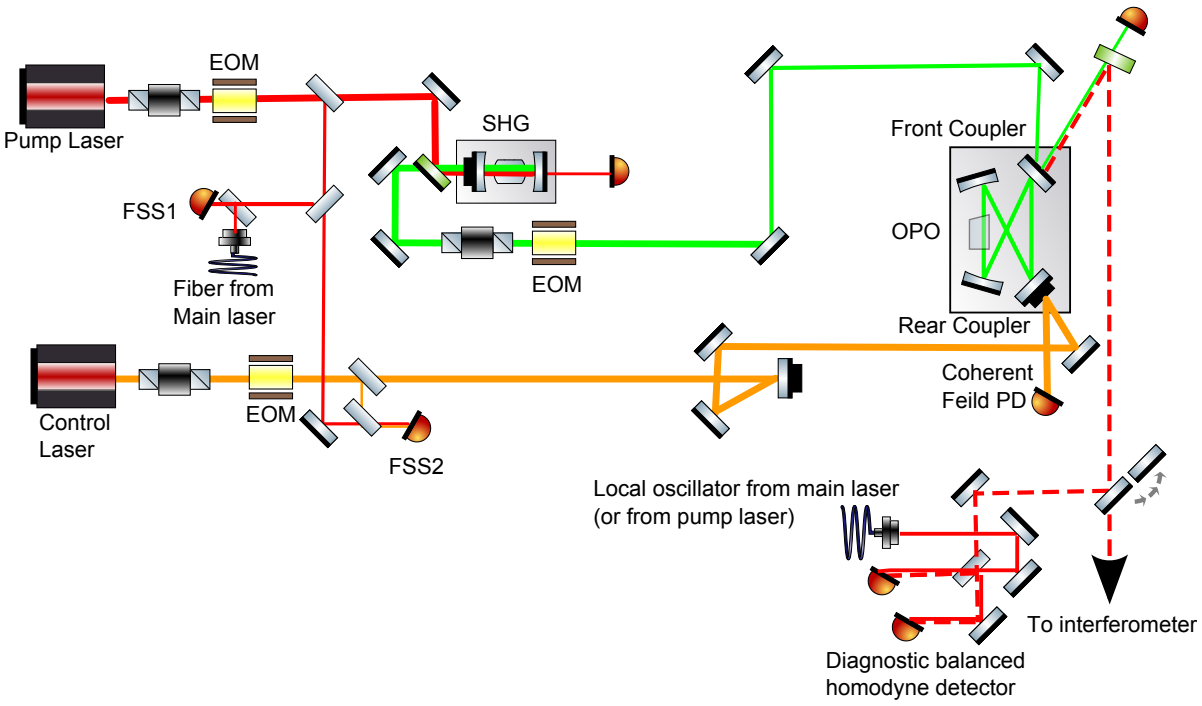

Figure 3-3: Simplified layout of squeezed state source. The pump laser is phase locked to a small amount of light from the main H1 laser. The pump laser is used to pump the second harmonic generator (SHG) which in turn pumps an OPO. A second laser, called the control laser, is offset locked to the pump laser and injected into the OPO through a rear coupler. This field is sensed both in reflection off of the OPO rear coupler and either at the homodyne detector or at the interferometer AS table.

that frequency doubles the fundamental field at 1064 nm to create the second harmonic at 532 nm. The length of the SHG is locked to the pump laser frequency using a Pound-Drever-Hall (PDH) error signal sensed in transmission, and a piezoelectric transducer (PZT) on one of the cavity mirrors as an actuator. The second harmonic beam produced by the SHG is then used to pump the traveling wave OPO, which also contains a PPKTP crystal. The OPO length is locked to the frequency of the second harmonic pump by a PDH signal sensed in reflection off the cavity. The squeezed beam produced by the OPO is separated from the reflected green beam by a dichroic mirror and sent either to a diagnostic balanced homodyne detector or into the interferometer. The homodyne detector was designed and built at the Max Planck Institute for Gravitational Physics in Hannover, Germany. The control laser, used to control the squeezing angle, is injected into a rear coupler of the OPO. Inside the OPO the nonlinear interaction creates a field at the difference frequency between the second harmonic pump and the injected control field, which is 29.5 MHz below the frequency of the cavity resonance. The injected and generated control fields are two symmetric sidebands on the squeezing field, and used to control the squeezing angle. These sidebands are sensed both in reflection off of the OPO rear coupler and at the antisymmetric port (or the diagnostic homodyne detector when it is used). The combination of the two error signals are fed back to the phase of the squeezer lasers to control the squeezing angle, as will be discussed in Chapter 5.

3.2.1 Second harmonic generation in a cavity

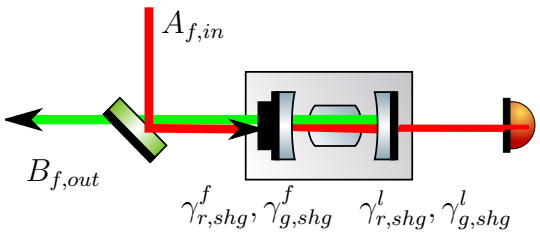

Figure 3-4: Second harmonic generation cavity

Our SHG cavity is based on a design from AEI in Hannover Germany, similar to the SHG

described in [11,85]. It uses a very compact design for mechanical and temperature stability. We can use the equations of motion Equations 2.23-2.26 with the couplers and input and output fields shown in Figure 3-4. Since we are not interested in the quantum behavior of the SHG we ignore the input fields that are quantum fluctuations [7, 44]:

$$\dot{a}(t) = -(\gamma_{r,shg}^{tot} - i\Delta_a(t))a(t) + \epsilon a^\dagger(t)b(t) + \sqrt{2\gamma_{r,shg}^{f}}A_{in,f}(t) \tag{3.1}$$

$$\dot{b}(t) = -(\gamma_{g,shg}^{tot} - i\Delta_b(t))b(t) - \frac{\epsilon a^2(t)}{2} \tag{3.2}$$

Our SHG is resonant only for the infrared field, with an input coupler anti-reflection coated for green so $\gamma_b^{tot} = \gamma_b^{in} = 1/\tau_{shg}$. We can write each of the operators as the sum of a constant and fluctuating part, $\bar{a}+\delta a(t)$. Since we are interested in the steady state power produced by the SHG, we take the time independent part of these equations and set the time derivatives to zero [44, p 84]:

$$0 = -\gamma_{r,shg}^{tot}\bar{a} + \epsilon\bar{a}^\dagger\bar{b} + \sqrt{2\gamma_a^{in}}\bar{A}_{f,in} \tag{3.3}$$

$$0 = -\frac{1}{\tau_{shg}}\bar{b} - \frac{\epsilon\bar{a}^2}{2} \tag{3.4}$$

Using Equation 3.4 and the input-output relations, Equation 2.18, the output second harmonic field in terms of the circulating fundamental field is:

$$\bar{b} = \frac{-\epsilon\bar{a}^2\tau_{shg}}{2} \tag{3.5}$$

$$\bar{B}_{shg}^{out} = \sqrt{2/\tau_{shg}}\bar{b} = -\epsilon\bar{a}^2\sqrt{\frac{\tau_{shg}}{2}} \tag{3.6}$$

The equation for the circulating field in terms of the incident field at the fundamental frequency is nonlinear:

$$\bar{a} = \frac{\sqrt{(2\gamma_{r,shg}^{in})}\bar{A}_{in}}{\left(\gamma_{r,shg}^{tot} + \frac{\epsilon^2\tau_{shg}|\bar{a}|^2}{2}\right)} \tag{3.7}$$

The term $\epsilon^2|\bar{a}|^2\tau_{shg}/2$ is the rate at which the infrared field is lost to conversion to green field, so we can write the ratio of loss through conversion to coupler losses:

$$\alpha_{shg} = \frac{\epsilon^2|\bar{a}|^2\tau_{shg}}{2\gamma_{r,shg}^{tot}} \tag{3.8}$$

The conversion efficiency of an SHG is the ratio of input power at the fundamental frequency to output second harmonic power:

$$\eta_{SHG} = \frac{P_{532}}{P_{1064}} = \frac{2|\bar{B}_{out}|^2}{|\bar{A}_{in}|^2} = \frac{2\gamma_{r,shg}^{in}\tau_{shg}\epsilon^2|\bar{a}|^2}{\left(\gamma_{r,shg}^{tot} + \frac{\epsilon^2|\bar{a}|^2\tau_{shg}}{2}\right)^2} \tag{3.9}$$

We can make the approximation that $\gamma_a^{in} \approx \gamma_a^{tot}$ to get an estimate for the value of $\alpha_{shg} = \epsilon^2|\bar{a}|^2\tau_{shg}/2\gamma_{r,shg}^{tot}$ for our SHG in the configuration that we used it, where the conversion efficiency was around 50%.

$$\eta_{shg} = \frac{4\alpha_{shg}}{(1+\alpha_{shg})^2} \tag{3.10}$$

With the approximation that $\gamma_a^{in} \approx \gamma_a^{tot}$, the ratio α_{shg} becomes the ratio of the intra-cavity loss (all of which is due to conversion) to the input coupler transmission, which is 1 for a critically coupled cavity, which would have 100% conversion efficiency. Our SHG has a value of α_{shg} less than 1. With our conversion efficiency of 50%, $\alpha_{shg} \approx 0.17$. The best SHG conversion efficiency we measured was 60% [81], 50% was a more typical efficiency.

3.2.2 Phase matching

For the nonlinear processes in SHG and OPO to be efficient, the phase relationship between the harmonic and fundamental fields needs to stay fixed (or nearly so) as they propagate. If the index of refraction for the two fields are different, they will acquire different phase shifts as they propagate through the crystal. If the generated field (the second harmonic in SHG or the fundamental field in OPO) becomes out of phase with the propagating field which was generated earlier, they will interfere destructively and energy transfer will not

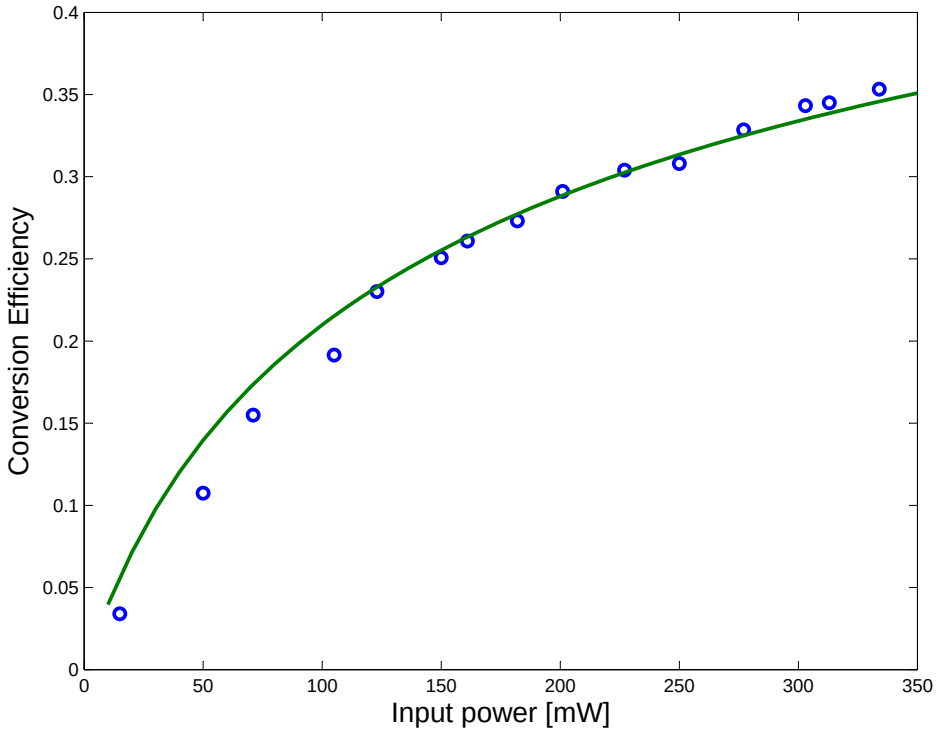

Figure 3-5: Conversion efficiency as a function of input fundamental power. Our measurements are plotted against a numerical solution [67] for the conversion efficiency assuming that the input coupler reflectivity is 90%, the intracavity losses are 2%, and the single pass nonlinear efficiency (harmonic power over fundamental power squared) is 0.17 (1/W)

be efficient. Since low-loss materials usually have normal dispersion, where the index of refraction is a monotonically increasing function of frequency, achieving good phase matching is one of the main challenges of working with nonlinear optics. The condition for a well phase matched interaction can be formulated as momentum conservation from the input (annihilated) photons to the output (created) photons:

$$\sum_i \hbar \mathbf{k}_i = \sum_j \hbar \mathbf{k}_j \tag{3.11}$$

SHG and degenerate OPO are opposite interactions: the inputs to SHG are the outputs of degenerate OPO and vice versa. This means that the phase matching condition for SHG and degenerate OPO are the same. With the fundamental frequency ω_a, the second harmonic or

pump frequency ω_b and the index of refraction for the relevant polarization and frequency given by $n(\omega)$ the phase matching condition becomes

$$\Delta k = \frac{\omega_b n(\omega_b)}{c} - 2\left(\frac{\omega_a n(\omega_a)}{c}\right) = 0 \tag{3.12}$$

From energy conservation we have $\omega_b = 2\omega_a$ so the phase matching condition is:

$$n(\omega_a) = n(\omega_b) \tag{3.13}$$

When the phase matching is not perfect, the strength of the nonlinear interaction depends on the mismatch: $\Delta k L_c$ where the interaction length L_c is the length of the crystal in which the fields interact. For second harmonic generation without depletion, where the interaction is weak enough so that the amplitude of the fundamental field is not affected by the nonlinear interaction, the second harmonic power produced is given by [6, ch 2]:

$$I(\Delta kL) = I_{max}\left(\frac{\sin \Delta k L_c/2}{\Delta k L_c/2}\right)^2 \tag{3.14}$$

where I_{max} is second harmonic power produced with perfect phase matching. There are different methods for achieving phase matching, most of which make use of a crystal's birefringence and use combinations of different polarizations that will have the right indices of refraction for the needed frequencies of light. To generate quadrature squeezing, the correlated photons produced by OPO need to interfere with each other, so we need a phase matching type in our OPO where the two generated fields, called the signal and idler, have the same polarization. We use a phase matching technique known as quasi-phase matching [6, 44, 56].

Figure 3-6 (A) shows a nonlinear interaction with perfect birefringent phase matching, where the generated second harmonic fields add in phase. As illustrated in Figure 3-6 (B), when the phase matching is not perfect and there is a small mismatch Δk, the harmonic field amplitude begins to decrease after a distance called the coherence length of the interaction [6].

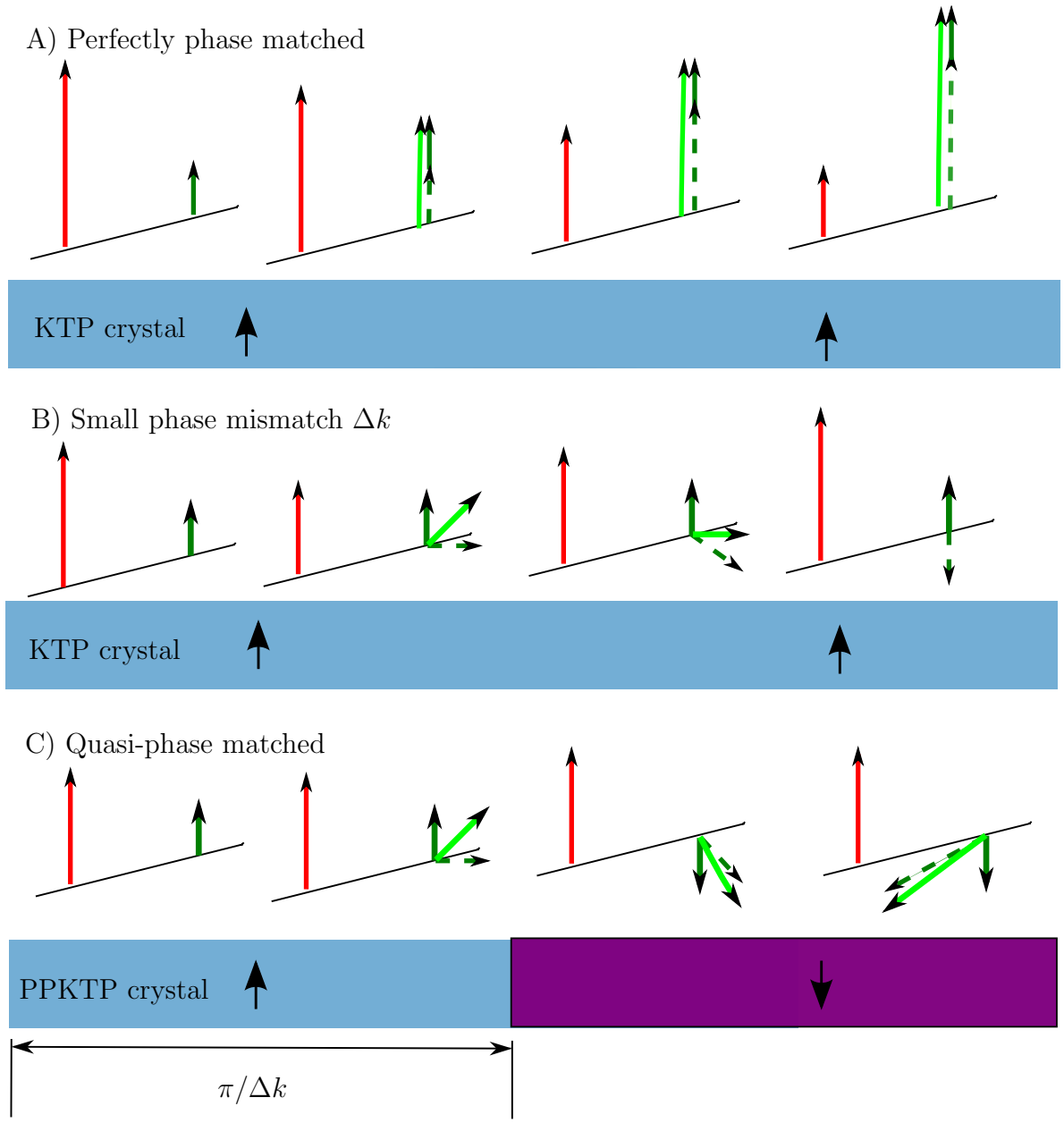

Figure 3-6: A) With perfect phase matching the generated harmonic field (dark green) stays in phase with the propagating harmonic field (dashed), so they add constructively and the total field (light green) grows monotonically. B) When there is a small phase mismatch, the propagating harmonic field acquires a phase shift relative to the fundamental as they propagate. After a distance of $\pi/\Delta k$ the generated harmonic field is out of phase with the propagating field and the harmonic field decreases until its amplitude is zero again at $2\pi/\Delta k$. C) In quasi phase matching, the crystal axis is reversed at $\pi/\Delta k$, or an integer multiple of that distance. This reverses the sign of the nonlinear coupling coefficient, so that there is a π phase shift to the generated field, and the interaction continues to add energy to the generated field. A periodically poled crystal is made up of many of these domains.

This is because the propagating harmonic field has become out of phase with the harmonic field that is being generated, and the interaction is transferring energy back to the fundamental field. In quasi- phase matching the direction of one crystal axis is switched (poled) periodically throughout the length of the crystal. This introduces a π phase shift to the generated harmonic beam. If the poling changes after one coherence length, as in Figure 3-6 (C), the interaction will always add energy to the generated field, and the generated field amplitude grows monotonically as the fields propagate through the crystal. Comparing Figure 3-6 (A) and (C), it is clear that the effective nonlinearity is smaller for a quasi-phase matching than it would be if the same crystal used perfect birefringent phase matching. In practice quasi-phase matching allows for use of large nonlinearities that can not be phase matched using birefringence, like the d_{33} nonlinearity in $KTiOPO_4$ (KTP), so periodically poled crystals make higher effective nonlinearities accessible.

The optimal poling period Λ for quasi-phase matching is:

$$\Lambda = \frac{2\pi}{\Delta k} = \frac{\lambda_r}{2\left(n(\omega_g) - n(\omega_r)\right)} \tag{3.15}$$

where λ_r is the wavelength in vacuum of the fundamental field. In PPKTP we use the d_{33} nonlinearity, so the relevant index of refraction is along the polar (z) axis. The index of refraction of most materials, including KTP, depends on both the temperature and the wavelength of light, we would like to know how the phase mismatch depends on the crystal temperature. Equations for the index of refraction of KTP are given in [28,44,49]. The index of refraction for 1064 nm is 1.830 and for 532 nm is 1.889, so the poling period required is approximately 9 μm. If the poling period is slightly different from the optimal period the phase mismatch is given by:

$$L_c \Delta k_q = 2\pi L_c \left(\frac{2}{\lambda_r} \left[n(\omega_g) - n(\omega_r) \right] + \frac{1}{\Lambda} \right) \tag{3.16}$$

The length of the crystal and the poling period both depend on the temperature of the crystal because of the crystal's thermal expansion, while the indices of refraction also depend on

Table 3.1: Properties of KTP [28]

α_{KTP}	$(6.7 \pm 0.7) \times 10^{-6}[1/^{\circ}C]$
β_{KTP}	$(11 \pm 2) \times 10^{-9}[1/^{\circ}C^2]$
$\left.\frac{dn}{dT}\right\|_{1064\text{ nm},25^{\circ}C}$	$1.4774 \times 10^{-5}[1/^{\circ}C]$
$\left.\frac{dn}{dT}\right\|_{532\text{ nm},25^{\circ}C}$	$2.4188 \times 10^{-5}[1/^{\circ}C]$

Table 3.2: Properies of KTP

temperature. To find the first order temperature dependence we take the derivative [30]:

$$\frac{d(L_c \Delta k_q)}{dT} = 2\pi \left[\frac{dL_c}{dT} \left(\frac{2}{\lambda_r} \left[n(\omega_g) - n(\omega_r) \right] + \frac{1}{\Lambda} \right) + \frac{2L_c}{\lambda_r} \left(\frac{dn(\omega_g)}{dT} - \frac{dn(\omega_r)}{dT} \right) - \frac{L_c}{\Lambda^2} \frac{d\Lambda}{dT} \right] \tag{3.17}$$

Thermal expansion of any length in KTP is given by:

$$L_c(T) = L_{c,0} \left[1 + \alpha_{KTP}(T - 25^{\circ}C) + \beta_{KTP}(T - 25^{\circ}C)^2 \right] \tag{3.18}$$

where α_{KTP} and β_{KTP} are given in Table 3.2, and $L_{c,0}$ is the length at room temperature [28]. This also describes the temperature dependence of the length of the poling period Λ.

Using the same equation for the thermal expansion of the total length and the poling period, we get:

$$\frac{d(L_c \Delta k_q)}{dT} = 2k_r L_{c,0} \left(\alpha_{KTP} \left[n(\omega_g) - n(\omega_r) \right] + \frac{dn(\omega_g)}{dT} - \frac{dn(\omega_r)}{dT} \right) \tag{3.19}$$

where k_r is the wavenumber of the fundamental field in vacuum. In this first order approximation, the temperature dependence of the phase mismatch is independent of the poling period. The phase mismatch, expanded around the peak of the phase matching curve is given by:

$$L_c \Delta k_q = 2k_r L_c \left(\alpha_{KTP} \left[n(\omega_g) - n(\omega_r) \right] + \frac{dn(\omega_g)}{dT} - \frac{dn(\omega_r)}{dT} \right) (T - T_0) \tag{3.20}$$

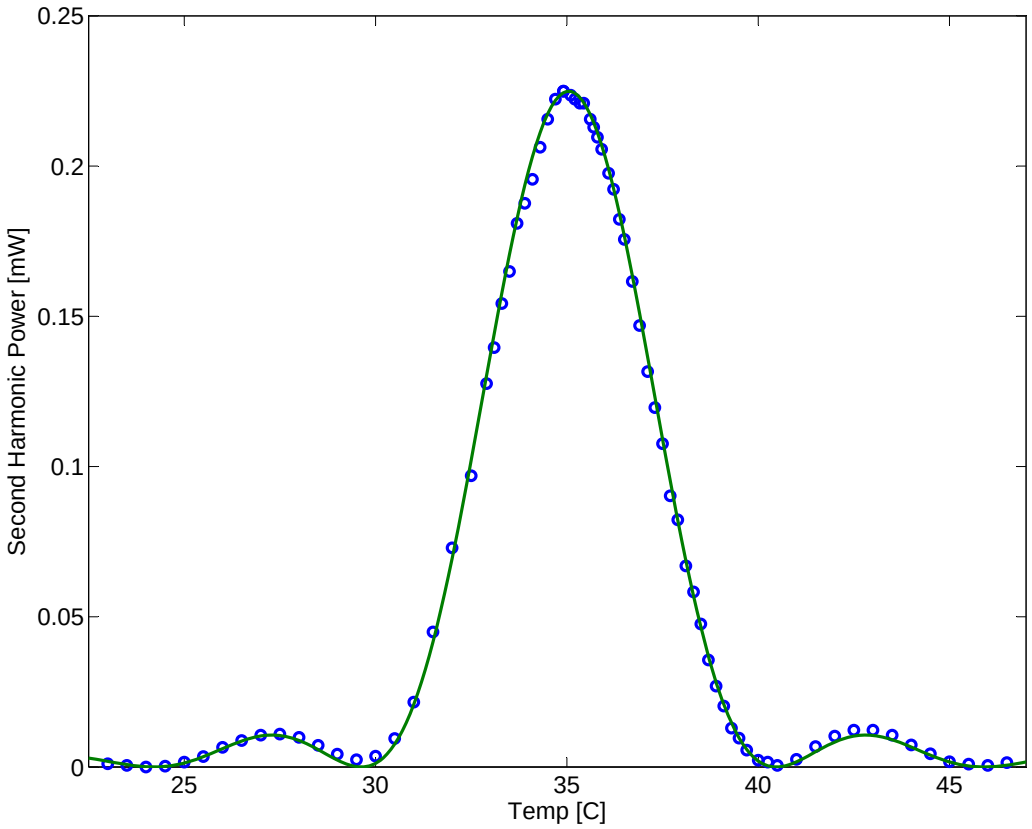

Figure 3-7: Phase matching curve measured with single pass second harmonic generation in PPKTP, with 333mW of incident infrared power. The green curve is a prediction based on Equation 3.19 used in Equation 3.14 and literature values for index of refraction and thermal expansion listed in Table 3.2. The peak height is normalized to fit the data, and the location of the center is set to match the data.

where T_0 is the phase matching temperature. Figure 3-7 shows a measurement of the efficiency of second harmonic generation (in single pass) over a range of crystal temperatures. This measurement was made in single pass to avoid pump depletion and thermal effects present in SHG inside of a cavity, so the resulting curve is in agreement with Equation 3.14.

3.2.3 OPO: Resonant for second harmonic and fundamental fields

Our OPO is based on a design from the Australian National University [12]. Our OPO is resonant for both the fundamental and second harmonic field, unlike many OPO's used for squeezing which are resonant for the fundamental field only [82]. Using a cavity that is

resonant for the pump simplifies our experimental set-up, but doesn't have any significant performance advantage over an OPO that is resonant for the fundamental field only. We can use the second harmonic pump field to generate a PDH signal to lock the length of the OPO and do not need an additional field at the fundamental frequency to sense the cavity length. The sidebands added to the second harmonic beam for the PDH error signal add phase noise to the pump, but this is not a significant limit to the squeezing produced. Because our OPO resonantly enhances the second harmonic field, the incident power needed to reach the threshold for spontaneous sub-harmonic generation is lower than it would be in were single pass. A resonant OPO acts as a filter for fluctuations of the second harmonic field above 15 MHz. An external mode cleaner cavity can also accomplish this filtering, with a narrower linewidth [62]. The resonant cavity also acts as a filter on the spatial mode inside the OPO. To maximize the nonlinear interaction the crystal is placed at the focus of the cavity mode. The second harmonic field in a cavity mode with waist w_0 interacts with the fundamental field in the cavity mode with a waist $\sqrt{2}w_0$. In an empty cavity or an OPO using birefringent phase matching, these modes would be exactly the modes that resonate in the cavity. For a useful discussion of the propagation of Gaussian beams in a nonlinear cavity, see [44, 2.4.8]. Because we use quasi-phase matching, there is a small difference in the waist sizes for the two fields caused by the difference in the index of refraction for 532 nm and 1064 nm, but this difference is small compared to the mode matching errors that could be present without a resonant cavity.

Because we use the second harmonic green pump field to lock the length of the cavity, we need to ensure that the cavity is resonant for the fundamental infrared field when it is locked to the green field, Section3.2.4. This places a requirement on the temperature stability of an OPO that is resonant for the pump, as will be discussed in Chapter 5.

3.2.4 OPO: Dispersion compensation for co-resonance

Because cavity optics have dispersion the phase shift acquired by red and green fields on reflection or transmission off of an optic can be different. This means that a cavity length

that the infared field that would resonate in a cavity is not necessarily at half the frequency of the green field that is resonant in the cavity. We need to make sure that the OPO is resonant for the interferometer carrier frequency (ω) in order to create squeezing that will interfere with the interferometer beam, but injecting a field at the the carrier frequency would add unacceptable low frequency noise couplings [56, 58]. In order to produce squeezing at the frequencies needed for gravitational wave detectors, the cavity length is sensed by a field in a different mode, either the second harmonic field or a 1064 nm field that is shifted in frequency and in a different polarization from the mode that is to be squeezed [51]. In either case, care must be taken that the cavity length that will resonate the field used for locking will also resonate the interferometer carrier frequency. This places a more stringent requirement on the temperature stability of the crystal than the phase matching condition.

For a cavity to be on resonance the phase acquired in one round trip must be an integral multiple of 2π. For the fundamental and second harmonic fields in the OPO this can be written:

$$\phi_{r,rt} = k_r \left[L + (n(\omega_r) - 1)\, L_{c,tot}\right] + \phi_{r,m} = 2\pi h_1 \tag{3.21}$$

$$\phi_{g,rt} = k_g \left[L + (n(\omega_g) - 1)\, L_{c,tot}\right] + \phi_{g,m} = 2\pi h_2 \tag{3.22}$$

where L is the round trip cavity length, $L_{c,tot}$ is the total length of the crystal, $\phi_{r,m}, \phi_{g,m}$ are the totals of the phase shifts from reflection off of each cavity mirror for the red and green fields respectively, k_r and k_g are the wavenumbers in vacuum, and h_1, h_2 are integers. Because $k_g = 2k_r$, there are twice as many cavity lengths that satisfy Equation 3.22 as satisfy Equation 3.21. The PDH lock will adjust the total cavity length to ensure that the condition Equation 3.22 is met, but that does not guarantee that Equation 3.21 will be satisfied. The PDH lock will hold the cavity length at:

$$L = \frac{2\pi h_2 - \phi_{g,m}}{2k_r} - (n(\omega_g) - 1)L_{c,tot} \tag{3.23}$$

At this cavity length the phase of the fundamental field deviates from the red resonance

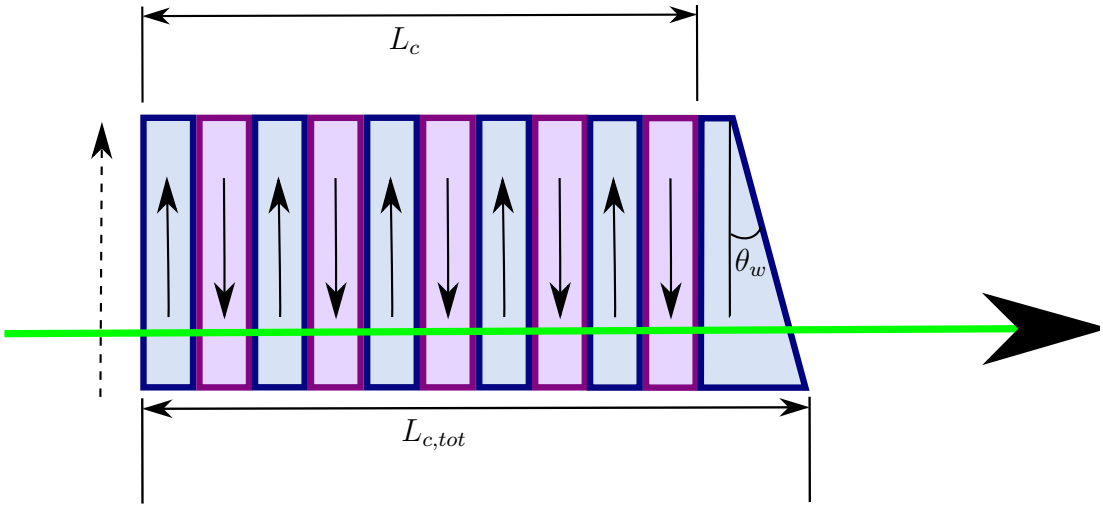

Figure 3-8: Wedged periodically poled crystal. The green arrow shows the direction of the beam propagation; a translation stage allows the crystal position to be adjusted along the direction of the dashed arrow.

condition by the dispersion mismatch:

$$\Delta\phi_{rt} = \phi_{r,m} - \frac{\phi_{g,m}}{2} + [n(\omega_r) - n(\omega_g)]\, k_r L_{c,tot} \tag{3.24}$$

if h_2 is even, or $\pi + \Delta\phi_{r,rt}$ if h_2 is odd. To compensate for this phase shift we need to introduce an adjustable phase shift into the cavity, called dispersion compensation.

An adjustable dispersive medium is used to shift the relative phase of the two fields and ensure that the cavity is co-resonant. This can be accomplished with an anti-reflection coated flat piece of glass called a dispersion plate, which is rotated to adjust the path length. A dispersion plate has the disadvantages of adding additional losses and scatter into the cavity. Instead, we use the crystal as a dispersive medium and adjust the path length of the beam traveling through the crystal to achieve co-resonance. There are two ways to change the path length in the crystal: changing its temperature or adjusting the position of a wedged crystal like the one illustrated in Figure 3-8. In a wedge crystal there is a region of the crystal where the periodic poling stops, here there is no quasi-phase matching. The non-poled region is part of the total crystal length, $L_{c,tot}$ but not part of the interaction length in the crystal, L_c.

To find the temperature dependence of $\Delta\phi_{rt}$ we take its derivative with temperature, use Equation 3.18 for the thermal expansion of lengths and the values from Table 3.2:

$$\frac{d\Delta\phi_{rt}}{dT} = k_r L_{c,tot}\left(\alpha_{KTP}[n(\omega_r) - n(\omega_g)] + \left[\frac{dn(\omega_r)}{dT} - \frac{dn(\omega_g)}{dT}\right]\right) \tag{3.25}$$

$$= \frac{-L_{c,tot}}{2L_c}\frac{d(L_c\Delta k_q)}{dT} \tag{3.26}$$

The temperature dependence of the dispersion mismatch is very similar to that of the phase mismatch, given by Equation 3.19. We can adjust the temperature to optimize only one of

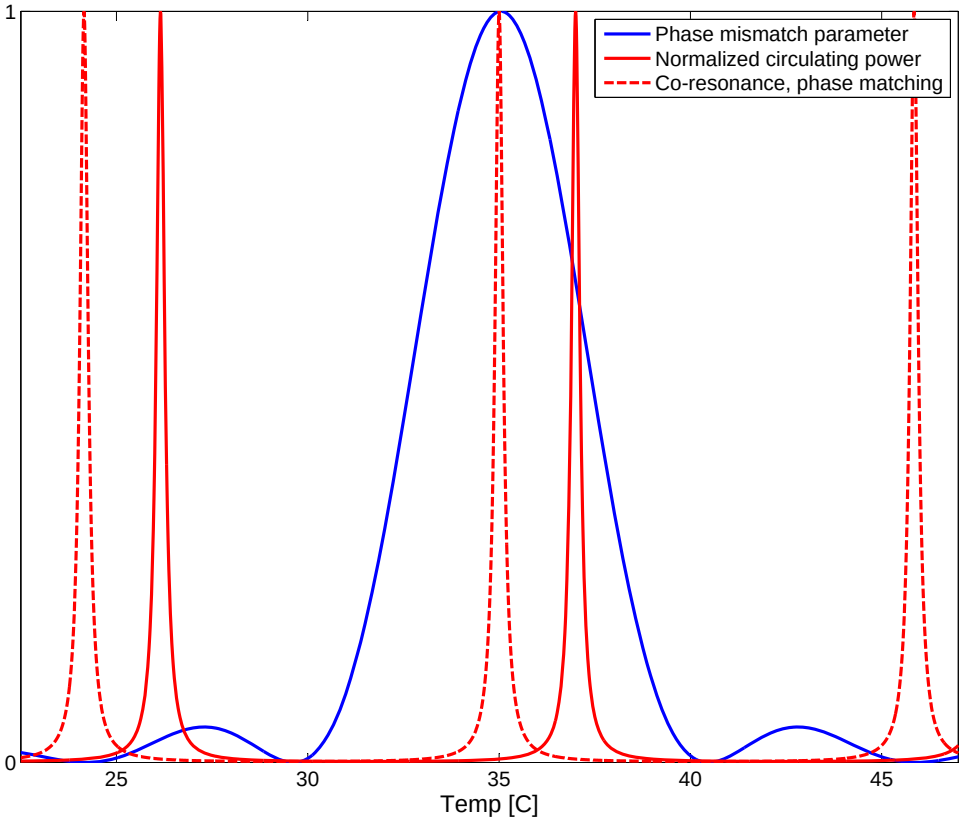

Figure 3-9: Temperature dependence of phase matching and dispersion compensation. The blue curve is the phase mismatch parameter, $\mathrm{sinc}^2\,\Delta k_q L_c$ for PPKTP phase matched at $35°C$. The red curves are calculated assuming that the cavity is locked using the 532 nm pump field, and shows the normalized transmission profile of our OPO for 1064 nm as a function of temperature. The location of the resonance peak relative to the phase matching peak depends on the dispersion of the cavity optics. The dashed red line represents the ideal situation, where the red resonance peak is at the phase matching peak.

these quantities. As shown in Figure 3-9, for a particular crystal position there are a few temperatures for which the cavity will be co-resonant, which will not necessarily be at the same temperature as the peak of the phase matching curve. To produce strong squeezing our OPO needs to be well phase matched and co-resonant. We use the crystal temperature to set the phase matching, and adjust the crystal length to ensure co-resonance. At any temperature, co-resonance occurs when the crystal length is:

$$L_{c,tot} = \frac{(2\pi h + \phi_{g,m}/2 - \phi_{r,m})}{k_r[n(\omega_r) - n(\omega_g)]} \tag{3.27}$$

where h is an integer.

A wedged crystal, like the one shown in Figure 3-8, mounted on a translation stage, allows us to adjust the crystal length once it is already installed in the cavity [48]. At one edge of the crystal the poling stops, and the edge is polished with a wedge. The wedge angle is small ($\theta_w = 1.43°$ in our crystal) so the total crystal length is given by:

$$L_{c,tot} = L_c + y \sin\theta_w \tag{3.28}$$

where L_c is the poled length of the crystal where the interaction is quasi phase matched, and y is the crystal displacement measured from the shorter edge. The dependence of the dispersion mismatch on crystal position is given by:

$$\frac{d\Delta\phi_{rt}}{dy} = (n(\omega_r) - n(\omega_g))\, k_r \sin\theta_w \tag{3.29}$$

Our crystal is 5 mm wide, so we can adjust the total crystal length by about 125 μ m and there are approximately 10 locations in the crystal where the cavity could be co-resonant at any temperature. Since we need to avoid clipping the beams on the edges of the crystal in practice there are between 2 and 5 usable locations in the crystal where the the cavity is co-resonant at a certain temperature. There are occasionally defects in the crystal that lead to higher losses or lower interaction strength at one of these crystal positions. As a function

of crystal position and temperature the dispersion mismatch is given by:

$$\begin{aligned}\Delta\phi_{rt} &= \phi_{r,m} - \frac{\phi_{g,m}}{2} + k_r\left[n(\omega_r) - n(\omega_g) + \left(\frac{dn(\omega_r)}{dT} - \frac{dn(\omega_g)}{dT}\right)(T - 25°C)\right] \\ &\quad \times (L_c + y\sin\theta_w)\,(1 + \alpha_{KTP}(T - 25°C)) \qquad (3.30) \\ &\approx k_r L_c\left(\frac{dn(\omega_r)}{dT} - \frac{dn(\omega_g)}{dT} + \alpha_{KTP}[n(\omega_r) - n(\omega_g)]\right)(T - T_0) \\ &\quad + k_r\sin\theta_w[n(\omega_r) - n(\omega_g)](y - y_0) \qquad (3.31)\end{aligned}$$

where in the approximation T_0 is the phase matching temperature and y_0 is the position where the cavity is co-resonant at the phase matching temperature. Using Equation 3.20 the dispersion mismatch in terms of the phase mismatch is:

$$\Delta\phi_{rt} = -\frac{\Delta k_q L_c}{2} + k_r[n(\omega_r) - n(\omega_g)]\sin\theta_w(y - y_0) \qquad (3.32)$$

Then the crystal position where the cavity is co-resonant for a particular temperature is given by:

$$y_{cr} = -\frac{\Delta k' L_c}{2k_r[n(\omega_g) - n(\omega_r)]\sin\theta_w} + y_o \qquad (3.33)$$

3.2.5 OPO: parametric gain and threshold

The classical dynamics of an OPO, developed in [23], can be used to characterize the strength of the nonlinear interaction. One advantage of an OPO resonant for the pump field is the lower second harmonic power needed to reach a particular value of the normalized nonlinear interaction strength x. The OPO reaches the threshold for spontaneous sub-harmonic generation when the fundamental power generated by the nonlinear interaction each round trip is the same as the power lost through cavity losses. The normalized nonlinear interaction strength, Equation 2.31, is one at threshold:

$$x_{th} = \frac{\epsilon|b|_{th}}{\gamma_r^{tot}} = 1 \qquad (3.34)$$

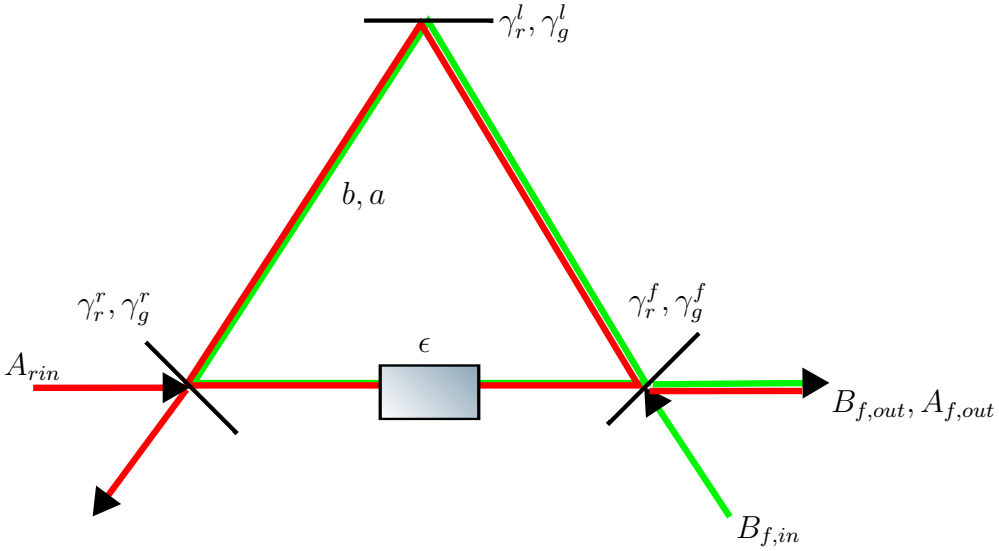

Figure 3-10: Classical OPO with seed. The rear coupler has decay rates γ_r^r and γ_g^r. In Section 2.4 these decay rates were included in the intracavity loss decay rates γ_r^l and γ_g^l but here they will be treated separately.

where P_{th} is the threshold power of the OPO. Because the circulating pump power is proportional to the incident pump power, we can use Equation 3.34 to write an alternative expression for the normalized nonlinear interaction strength:

$$x = \frac{\epsilon |b|_{th}}{\gamma_r^{tot}} \frac{|b|}{|b|_{th}} = \sqrt{\frac{P}{P_{th}}} \tag{3.35}$$

Although we operate the OPO below threshold, we normally use a significant fraction of the threshold power to pump the OPO, so we can use the threshold power to estimate the second harmonic power needed to pump an OPO. As illustrated in Figure 3-10, we characterize the nonlinear interaction strength of the OPO by injecting a coherent seed field $A_{r,in}$ through the rear coupler with decay rate γ_r^r. The classical cavity equations of motion for a degenerate OPO with a coherent seed at the fundamental frequency can be found from Equations 2.23-

2.26, ignoring any inputs that are only quantum fluctuations:

$$\dot{a}(t) = -(\gamma_r^{tot} - i\Delta_a(t))a(t) + \epsilon a^\dagger(t)b(t) + \sqrt{2\gamma_r^r}A_{r,in}(t) \tag{3.36}$$

$$\dot{b}(t) = -(\gamma_g^{tot} - i\Delta_b(t))b(t) - \frac{\epsilon a^2(t)}{2} + \sqrt{2\gamma_g^f}B_{f,in}(t) \tag{3.37}$$

For now we will assume that the cavity is on resonance for the both the pump and seed fields such that the detunings Δ_a and Δ_b vanish. We will also make the parametric approximation from Section 2.4, so that we can drop the second term from Equation 3.37. In the steady state where the field amplitudes are constant these equations become:

$$0 = -\gamma_r^{tot}\bar{a} + \epsilon\bar{a}^\dagger\bar{b} + \sqrt{2\gamma_r^r}\bar{A}_{r,in} \tag{3.38}$$

$$\bar{b} = \frac{\sqrt{2\gamma_g^{out}}}{\gamma_g^{tot}}\bar{B}_{f,in} \tag{3.39}$$

Combining the threshold condition given by Equation 3.34 with Equation 3.39 we can find a value for the incident pump power needed to reach threshold:

$$P_{th} = \hbar\omega_g \left|\bar{B}^{in}\right|^2 = \frac{\hbar\omega_g \left(\gamma_r^{tot}\gamma_g^{tot}\right)^2}{2\epsilon^2\gamma_g^{in}} \tag{3.40}$$

$$\approx \frac{\hbar\omega_g(\gamma_r^{tot})^2\gamma_g^{tot}}{2\epsilon^2} \tag{3.41}$$

where we made the approximation that $\gamma_g^f \approx \gamma_g^{tot}$. One simple way to measure the threshold is to increase the pump power until an infrared beam is produced. A more accurate method is to measure the nonlinear amplification and de-amplification of the coherent seed, known as the nonlinear gain, as a function of the pump power. Measurements of the nonlinear gain are also the best way to estimate the normalized nonlinear interaction strength, x.

To calculate the nonlinear gain we solve Equation 3.38 and its complex conjugate for the

circulating fundamental field:

$$\begin{pmatrix} \bar{a} \\ \bar{a}^\dagger \end{pmatrix} = \frac{\sqrt{2\gamma_r^r}}{\gamma_r^{tot}} \begin{pmatrix} 1 & x^{i\theta_b} \\ xe^{i\theta_b} & 1 \end{pmatrix} \begin{pmatrix} \bar{A}_{r,in} \\ \bar{A}_{r,in}^\dagger \end{pmatrix} \tag{3.42}$$

where $\bar{b} = |\bar{b}|e^{i\theta_b}$. Using the input-output relation, $\bar{A}_{f,out} = \sqrt{2\gamma_r^f}\,\bar{a}$, and setting the phase of the input field so that it is real:

$$\bar{A}_{f,out} = \frac{2\sqrt{\gamma_r^f \gamma_r^r}}{\gamma_r^{tot}} \frac{1 + xe^{i\theta_b}}{1 - x^2} \bar{A}_{r,in} \tag{3.43}$$

where ϕ is again the phase of the circulating pump. The parametric gain is the ratio of the output fundamental power with the pump present to the output fundamental power if there were no pump and therefore no nonlinear interaction:

$$G(x, \theta_b) = \frac{1 + 2x\cos\theta_b + x^2}{(1 - x^2)^2} \tag{3.44}$$

$$G(x, 0) = \frac{1}{(1 - x)^2} \tag{3.45}$$

$$G(x, \pi) = \frac{1}{(1 + x)^2} = g \tag{3.46}$$

where Equation 3.45 describes parametric de-amplification and Equation 3.46 describes amplification, which we will call nonlinear gain g. We measure the nonlinear gain by locking the cavity with the second harmonic field, and sending a small amount of light at the fundamental frequency (the seed) into the cavity through the rear coupler. We then scan the phase of either the seed or the second harmonic field and measure the maximum transmitted power. This is compared to the power transmitted when scanning the cavity with only the seed injected. As shown in Figure 3-11 the threshold for our OPO was near 95 mW. This value increased by about 10% over the course of a year, this may be due to a slow drift in crystal position.

We measure the parametric gain g, to estimate the normalized nonlinear interaction

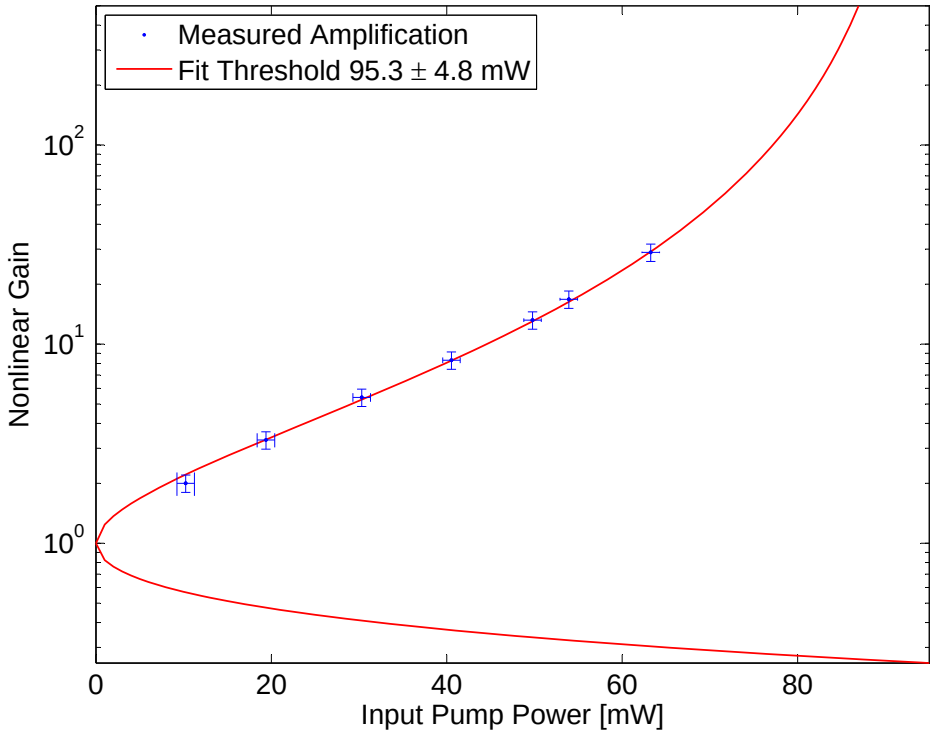

Figure 3-11: Parametric amplification as a function of green power, used to find a value for the threshold of spontaneous subharmonic generation. Parametric amplification is used instead of de-amplification because small offsets cause larger errors in measurements of de-amplification. As the pump power approaches threshold the amplification approaches an asymptote.

strength:

$$x = 1 - 1/\sqrt{G(x,\pi)} = 1 - 1/\sqrt{g} \tag{3.47}$$

Since the parametric gain depends on careful tuning of the crystal temperature, we monitor the parametric gain to adjust the crystal temperature. One could also estimate the normalized nonlinear interaction strength by measuring the power incident on the OPO, using Equation 3.35. This has the disadvantage that misalignment or mode mismatch of the pump beam, errors in the temperature setting, or a drift in the threshold power will all cause errors in the estimate of the normalized interaction strength.

3.2.6 Optimizing nonlinear interaction strength: Phase matching and dispersion compensation in an OPO resonant for the pump

To get the most squeezing from our OPO we need to operate it at the peak of the phase matching and on co-resonance. We can achieve this by maximizing the classical nonlinear gain (and therefore the normalized nonlinear interaction strength) for a fixed pump power. The effect of a phase mismatch is to change the nonlinear coupling constant ϵ, which becomes complex so that the normalized nonlinear interaction strength becomes [45]:

$$x' = xe^{i\Delta k_q L_c/2}\,\mathrm{sinc}(\Delta k_q L_c/2) \tag{3.48}$$

If the co-resonance condition is not satisfied, a detuning is introduced to the fundamental field:

$$\Delta_a = \frac{\Delta\phi_{rt}}{\tau} \tag{3.49}$$

With a detuning and a complex value of the normalized nonlinear interaction strength included, Equation 3.36 and its complex conjugate become:

$$\begin{pmatrix} 0 \\ 0 \end{pmatrix} = \gamma_r^{tot} \begin{pmatrix} 1 - i\Delta_a/\gamma_r^{tot} & |x'|e^{i(\theta_b + \Delta k_q L_c/2)} \\ |x'|e^{-i(\theta_b + \Delta k_q L_c/2)} & 1 - i\Delta_a/\gamma_r^{tot} \end{pmatrix} \begin{pmatrix} \bar{a} \\ \bar{a}^\dagger \end{pmatrix} + \sqrt{2\gamma_r^r} \begin{pmatrix} \bar{A}_{r,in} \\ \bar{A}_{r,in}^\dagger \end{pmatrix} \tag{3.50}$$

Setting the input seed phase to zero we find the output field:

$$\bar{A}_{f,out} = \frac{2\sqrt{\gamma_r^r \gamma_r^f}}{\gamma_r^{tot}} \frac{1 + i\Delta_a/\gamma_r^{tot} + |x'|e^{i(\theta_b + \Delta k_q L_c/2)}}{1 + (\Delta/\gamma_r^{tot})^2 - |x'|^2} \bar{A}_{r,in} \tag{3.51}$$

The ratio of the output power to the output power when there is no pump is:

$$G = \frac{1 + (\Delta_a/\gamma_r^{tot})^2}{(1 + (\Delta_a/\gamma_r^{tot})^2 - |x'|^2)^2} \left| 1 + i\frac{\Delta_a}{\gamma_r^{tot}} + |x'|e^{i(\theta_b + \Delta k_q L_c/2)} \right|^2 \tag{3.52}$$

We scan the phase of either the seed or the second harmonic field and measure the maximum output power, which is produced when:

$$\theta_b + \frac{\Delta k_q L_c}{2} = \tan^{-1}\frac{\Delta_a}{\gamma_r^{tot}} \tag{3.53}$$

The maximum nonlinear gain we measure then is given by:

$$G_{max} = \left(1 - \frac{|x'|}{\sqrt{1 + (\Delta_a/\gamma_r^{tot})^2}} \right)^{-2} \tag{3.54}$$

Since γ_r^{tot} is the half width at half maximum of the cavity transmission profile for the infrared field in angular units, the cavity finesse is $\mathcal{F}_r = \pi/(\tau\gamma_r^{tot})$.

$$G_{max} = \left(1 - \frac{x\,\mathrm{sinc}(\Delta k_q L_c/2)}{\sqrt{1 + (\mathcal{F}_r \Delta\phi_{rt}/\pi)^2}} \right)^{-2} \tag{3.55}$$

The dispersion mismatch $\Delta\phi_{rt}$ is scaled by the infrared cavity finesse in Equation 3.55 meaning that the required temperature stability of the OPO also scales with the cavity finesse. Figure 3-12 shows the nonlinear gain as a function of crystal position and temperature for the parameters of our OPO. We use the nonlinear gain to find the crystal position and temperature that maximizes the nonlinear gain. A practical procedure for doing this is described in Appendix C.

Figure 3-13 shows profiles of the dependence of nonlinear gain on crystal position and temperature around the point where gain is maximized, with the same parameters as Figure 3-12.

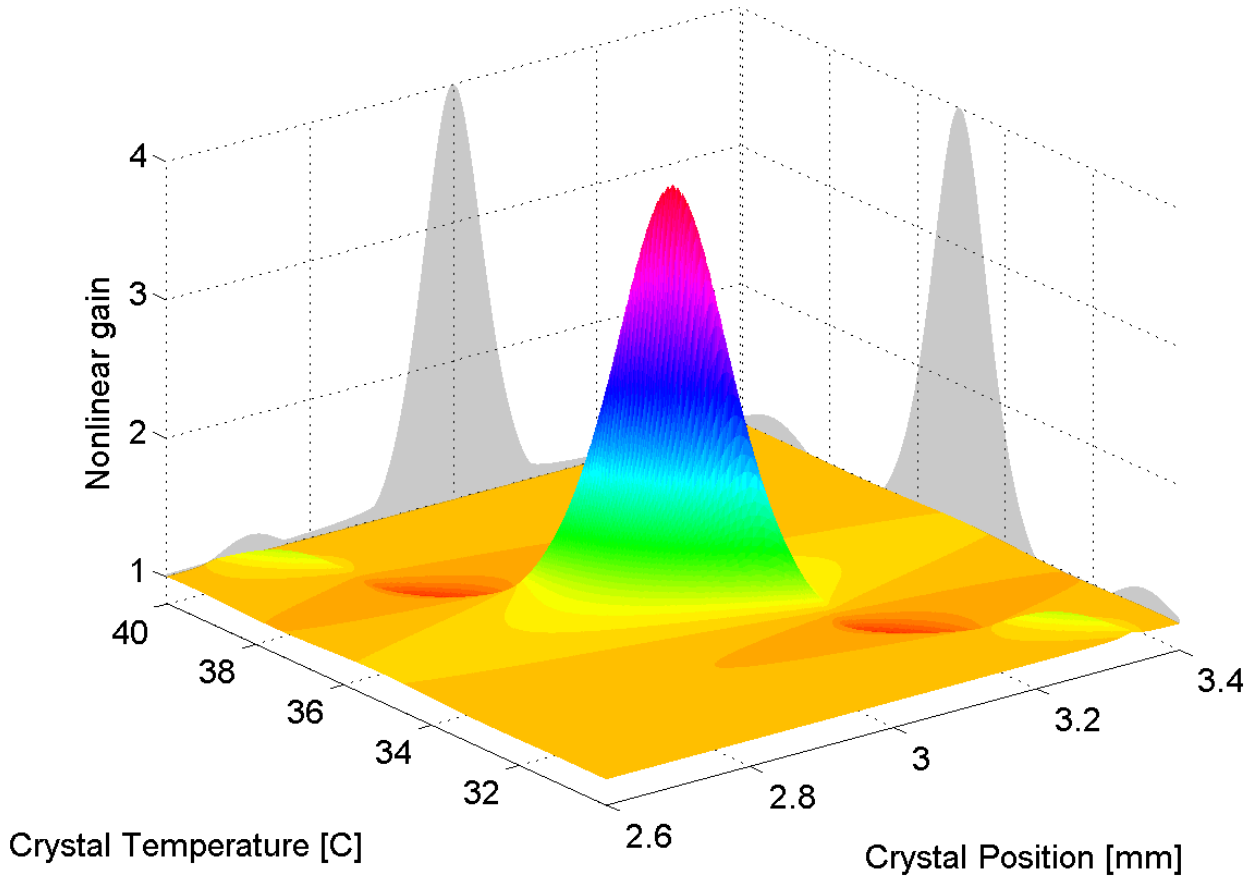

Figure 3-12: Prediction for nonlinear gain as a function of crystal position and temperature for our OPO parameters, and a pump power at one quarter of the threshold value. This pattern is repeated a few times across the width of the crystal, at the same temperatures. The projection on the position axis shows the maximum gain that can be measured at each crystal position once the temperature is optimized.

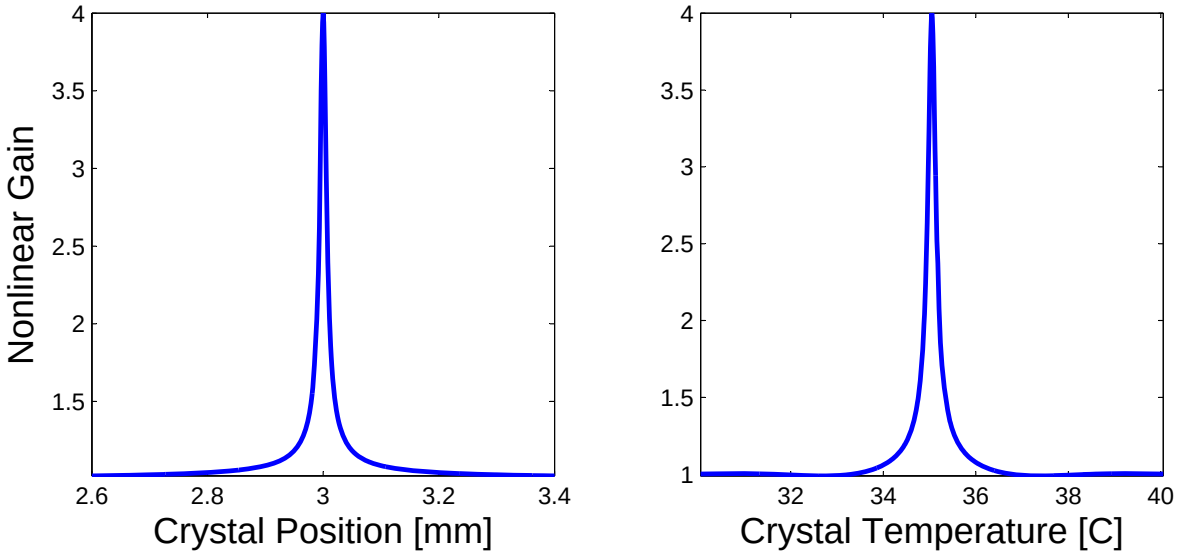

Figure 3-13: Prediction for gain profiles with crystal position and temperature. The left panel shows a cross section of the nonlinear gain when the temperature is set to the phase matching temperature (chosen to be $35°C$ for this example) and the position is varied. The right panel shows a cross section of gain with temperature when the crystal position is set for co-resonance at the phase matching temperature (chosen to be 3mm).

3.2.7 OPO: Escape efficiency

When choosing the front coupler reflectivity for an OPO, the most important factor to consider is the escape efficiency. As was shown in Equation 2.45a lower escape efficiency directly lowers the amount of squeezing produced. The escape efficiency is given by:

$$\eta_{esc} = \frac{\gamma_r^f}{\gamma_r^{tot}} \approx \frac{T_f}{T_f + L_{cav}} \tag{3.56}$$

where the approximation holds for a low loss cavity, T_f is the front coupler infrared power transmission, and L_{cav} is the infrared intra-cavity power losses. In order to keep the escape efficiency of an OPO large, it must be an over-coupled cavity in the infrared, when the front coupler is viewed as the input coupler. This means that any infrared power (as well as any quantum fluctuations) in the cavity will leave through the front coupler.

We measured the intra-cavity losses for our OPO by injecting an infrared field into the front coupler and scanning the cavity through resonance while measuring the reflected power. The ratio of the reflected power on resonance to off resonance is given by:

$$\frac{P_{r,on}}{P_{r,off}} = \frac{\left|\frac{r_{out} - r_l}{1 - r_{out}r_l}\right|^2}{\left|\frac{r_{out} + r_l}{1 + r_{out}r_l}\right|^2} \tag{3.57}$$

where $r_{out} = \sqrt{1 - T_{out}}$ and $r_l = \sqrt{1 - L_{cav}}$. This measurement showed that we had an intra-cavity loss of 0.43% without the crystal installed, this includes a loss of 0.18% from the rear coupler and two high reflectors with 0.05% losses, so the unaccounted for intra cavity losses are 0.2%. With the super-polished crystal used in the final configuration the crystal losses were 0.16%, and the total intra-cavity losses were 0.58%. With our front coupler power transmission of 13.24%, our OPO escape efficiency was 95.9% [27]. Both lowering the intra-cavity losses and increasing the front coupler transmission would increase the escape efficiency. In practice it may be easier to increase the transmission of the front coupler and lower the cavity finesse than to further reduce the intra-cavity losses.

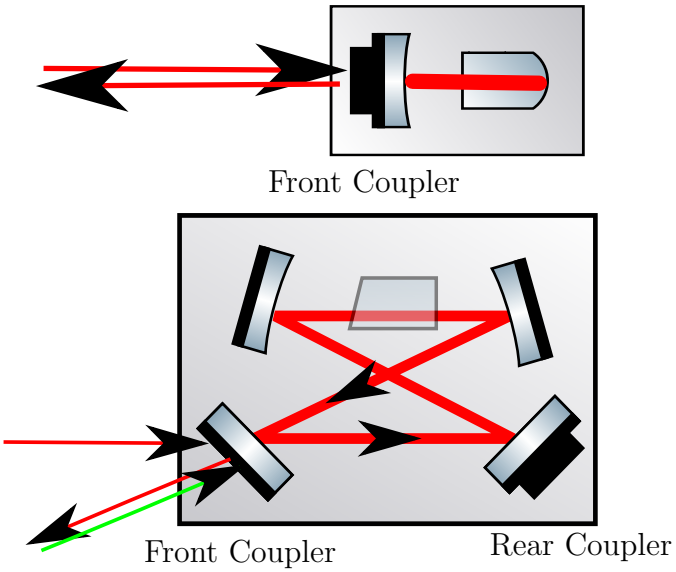

Figure 3-14: Standing wave (top) and traveling wave (bottom) cavity configurations

3.2.8 OPO: Traveling wave cavity

When implementing squeezing on a full-scale gravitational wave detector we need to avoid adding technical noise to the interferometer, which is the subject of Chapter 6. In particular, if stray beam and scattered light from the interferometer are retro-reflected by the squeezed vacuum source back into the interferometer, the squeezer could degrade the interferometer sensitivity instead of improving it as explained in Section 6.2.1. Since the OPO needs to be a highly over-coupled cavity for the infrared field incident on the front coupler, the reflectivity of the cavity to any infrared light incident on the front coupler is nearly unity. This means that almost all stray interferometer light incident on the OPO will be reflected off the input coupler. As shown in Figure 3-14 if the OPO is a standing wave cavity any stray light incident on it will be directly retro-reflected back towards the interferometer. The power in the stray beam can be attenuated using a series of Faraday isolators in the path used to inject squeezing into the interferometer, however the loss introduced by each additional Faraday isolator degrades the squeezing. Instead, we have used a traveling wave design where the stray light is reflected off of the OPO at an angle instead of directly back towards the interferometer. In order to create a parasitic interferometer a second scattering event is

needed that will send the light back into the interferometer. When constructing the path for the green light entering the OPO, it is useful to keep in mind that stray light from the interferometer will counter-propagate along this path and carefully avoid creating places where a second scattering event is likely to occur. Even in the traveling wave configuration a small amount of the circulating power in the OPO is scattered by imperfections of the cavity optics into the counter-propagating mode, so that it will be scattered back towards the interferometer. This effect was measured in an OPO very similar to ours in [12], and will be discussed further in Chapter 6.

The spatial mode of a traveling wave cavity has a small astigmatism, which will cause a small amount of loss due to imperfect mode matching. In Enhanced LIGO the astigmatism of the anti-symmetric port beam was much larger, so the cavity astigmatism was completely negligible.

3.2.9 Complete squeezed vacuum source layout

There are several details of the squeezed vacuum source design that were left out of Figure 3-3 for clarity, but are useful for practical operation. A more complete diagram of the experiment is shown in Figure 3-15.

To prevent any of light at the fundamental frequency from entering the OPO through the second harmonic path, we use several dichroic mirrors to remove residual infrared photons from that beam. A Mach-Zender interferometer in the second harmonic path allows us to intensity stabilize the pump, this reduces thermal fluctuations in the crystal which will limit the long term stability of the squeezer but was not needed for our experiment.

There are a few features that are useful for tuning the performance of the diagnostic balanced homodyne, using the on table local oscillator from the pump laser. The common mode rejection of the local oscillator port on the balanced homodyne detector can be checked and adjusted using the EOM in the on table LO path as an amplitude modulator. The homodyne visibility can be adjusted using the interference of the seed beam with the on table local oscillator with matched powers. The seed beam enters the OPO through the rear

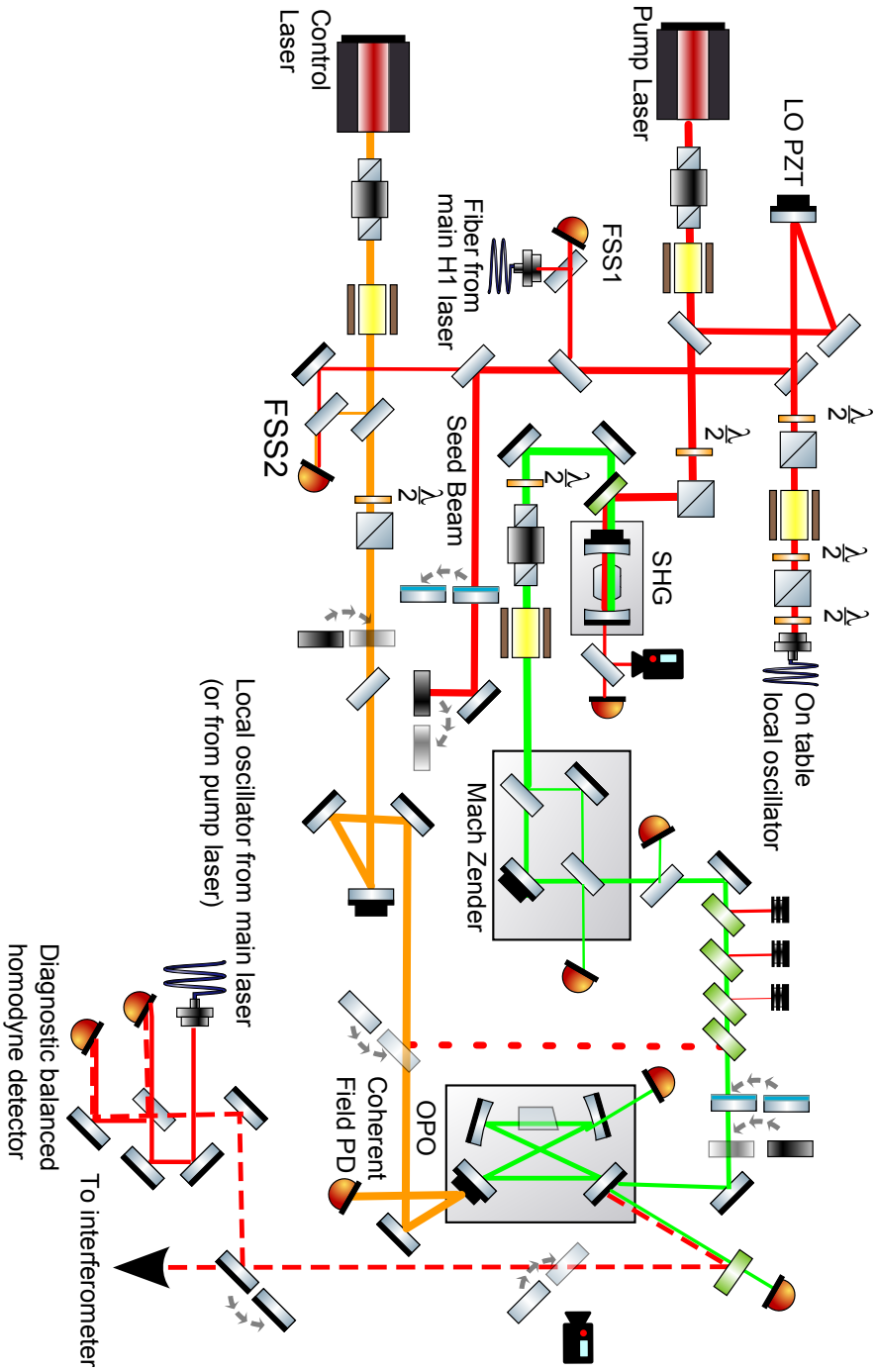

Figure 3-15: Layout of squeezed state source. Flipper mirrors, filters and beam blocks are shown in the positions used for squeezing. To measure parametric gain or the homodyne visibility, the seed beam is unblocked and enters the OPO through the rear coupler. To measure the intracavity losses the flipper mirror in the path towards the rear coupler is inserted, and the seed is sent to the front coupler, shown by the dashed line.

coupler and is blocked during normal operation. To measure the homodyne fringe visibility the OPO temperature is moved away from phase matching, and a filter is inserted in the green path to lower the power so that there will be no nonlinear gain in the OPO and the transmitted seed power will be stable. The transmitted beam, or the transmitted control beam, can also be used for aligning the interferometer injection path.

There is also the option of injecting the seed beam into the OPO through the input coupler, this path is shown by a dashed line in Figure 3-15. This allows us to measure the intracavity loss, which may change depending on the crystal position. If the threshold power changes, a measurement of the intra-cavity loss can help diagnose the cause. If the forward seed is well mode-matched it can also be used as a rough alignment beam which has higher power than the transmitted alignment beams, useful for finding the beam in the initial alignment into the interferometer.

3.2.10 Squeezed vacuum source performance

Our squeezed vacuum source met the requirements of this experiment. Figure 3-16 shows the squeezing measured on the diagnostic homodyne detector, described in Section 2.7.1. In the kHz range, we measured 6 dB of squeezing, and 5 dB at 100 Hz. The level of squeezing was shown to be stable for an hour and a half. We did not have the chance to measure long term performance with the interferometer, so longer term stability was not needed for this experiment; however stable operation for up to 20 hours has been demonstrated in a similar system by Khalaidovski et al [51]. Using the propagation losses in our detection path, we estimate around 10 dB of squeezing produced right outside the input coupler. The squeezer was connected to a digital system to allow remote control.

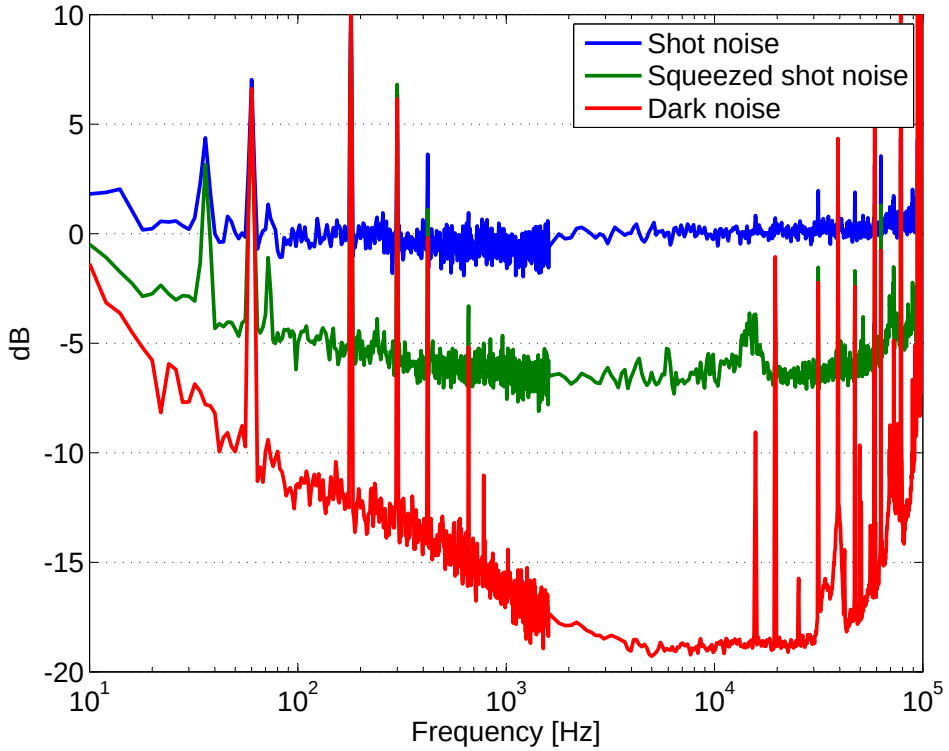

Figure 3-16: Squeezing measured on diagnostic homodyne detector. The red trace shows the electronics noise of the detector.

3.3 Squeezed state injection into Enhanced LIGO

Figure 3-17 shows a schematic of the squeezing injection into Enhanced LIGO. All the components described in Section 3.2 were installed on an optical table, called the squeezed state source or the squeezer. This table was bolted to the ground outside of the vacuum system. An additional in vacuum Faraday isolator in the squeezing injection path, called the injection isolator, reduces the amount of stray light from the interferometer that reaches the squeezer. For this experiment, the output Faraday isolator used in Initial and Enhanced LIGO was replaced with one of the output Faradays that will be used in Advanced LIGO, which allows access to the port used for squeezing injection. For the squeezing experiment the power in the pick-off beam sent to the AS table was reduced to 1% of the power in the AS beam, to reduce the optical loss in the squeezing detection path. A photo-diode

added to the AS table senses the phase between the interferometer carrier beams and the control sidebands on the squeezed beam. The OMC reflects the squeezer control sidebands, and transmits the interferometer carrier and the squeezing to the gravitational wave readout photo-detectors where the improvement in sensitivity is measured. The OMC in the H1 interferometer suffered extra losses in the last part of the Enhanced LIGO science run, which had only a small impact on the sensitivity to gravitational waves, but introduced a 50% loss to the squeezing detection path at the beginning of the squeezing experiment. To reduce the losses, the output mode cleaner from the H1 interferometer was replaced with the Livingston OMC in October 2011.

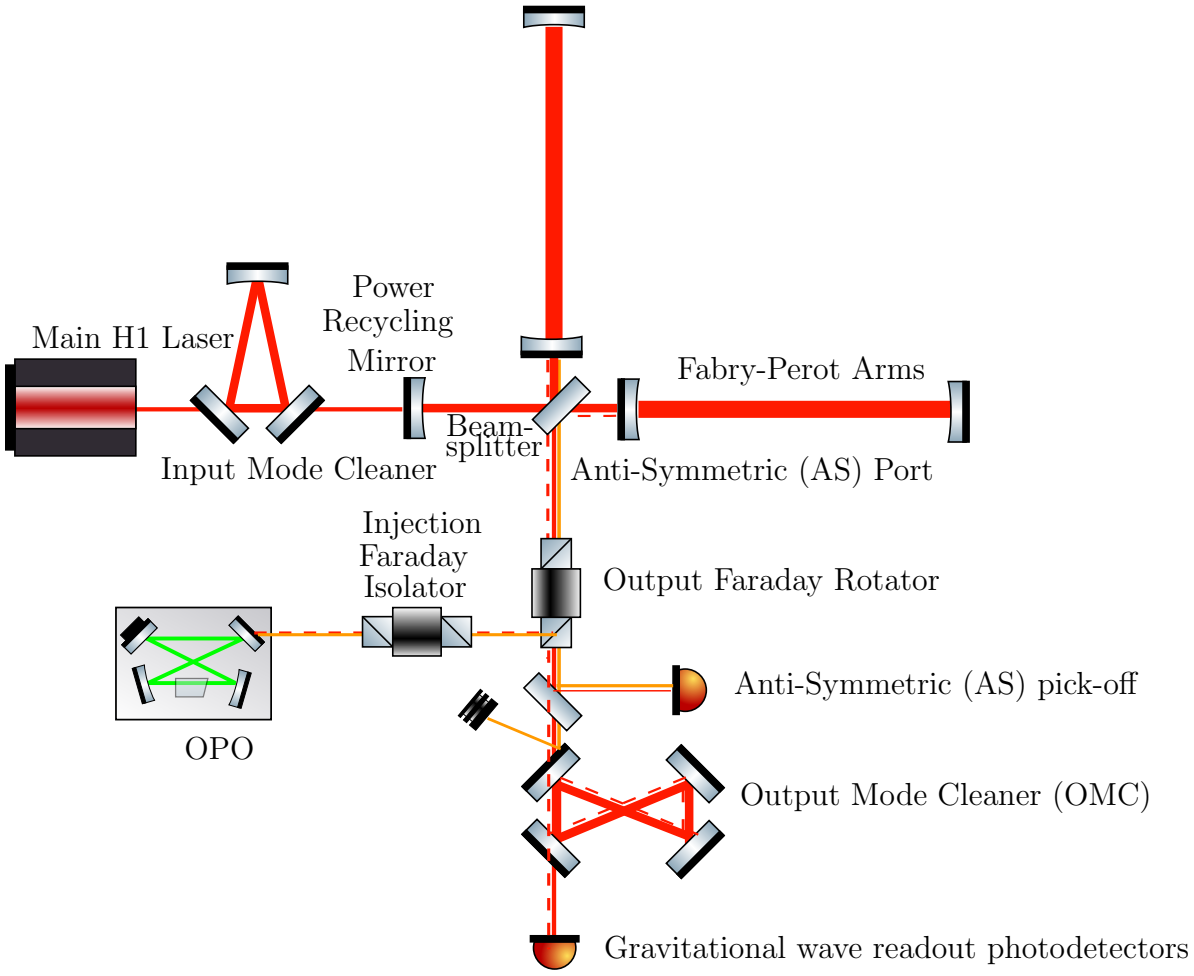

Figure 3-17: Squeezing injection into Enhanced LIGO. The squeezed beam and coherent control sidebands leave the OPO and are injected into the vacuum system, passing through the injection Faraday isolator which mitigates scattered light from the interferometer. The output Faraday is used as a rotator to send the fields from the OPO towards the interferometer beamsplitter. The squeezed field is reflected off of the interferometer arms and returns to the AS port, passing through the output Faraday isolator a second time. A small pick-off sends some of the interferometer light and some of the squeezing control sidebands to a diode on the AS table, which senses the squeezing angle. The output mode cleaner rejects the control sidebands, and transmits the interferometer carrier and squeezed beam to the readout out photo-detectors.

3.3.1 Sensitivity improvement

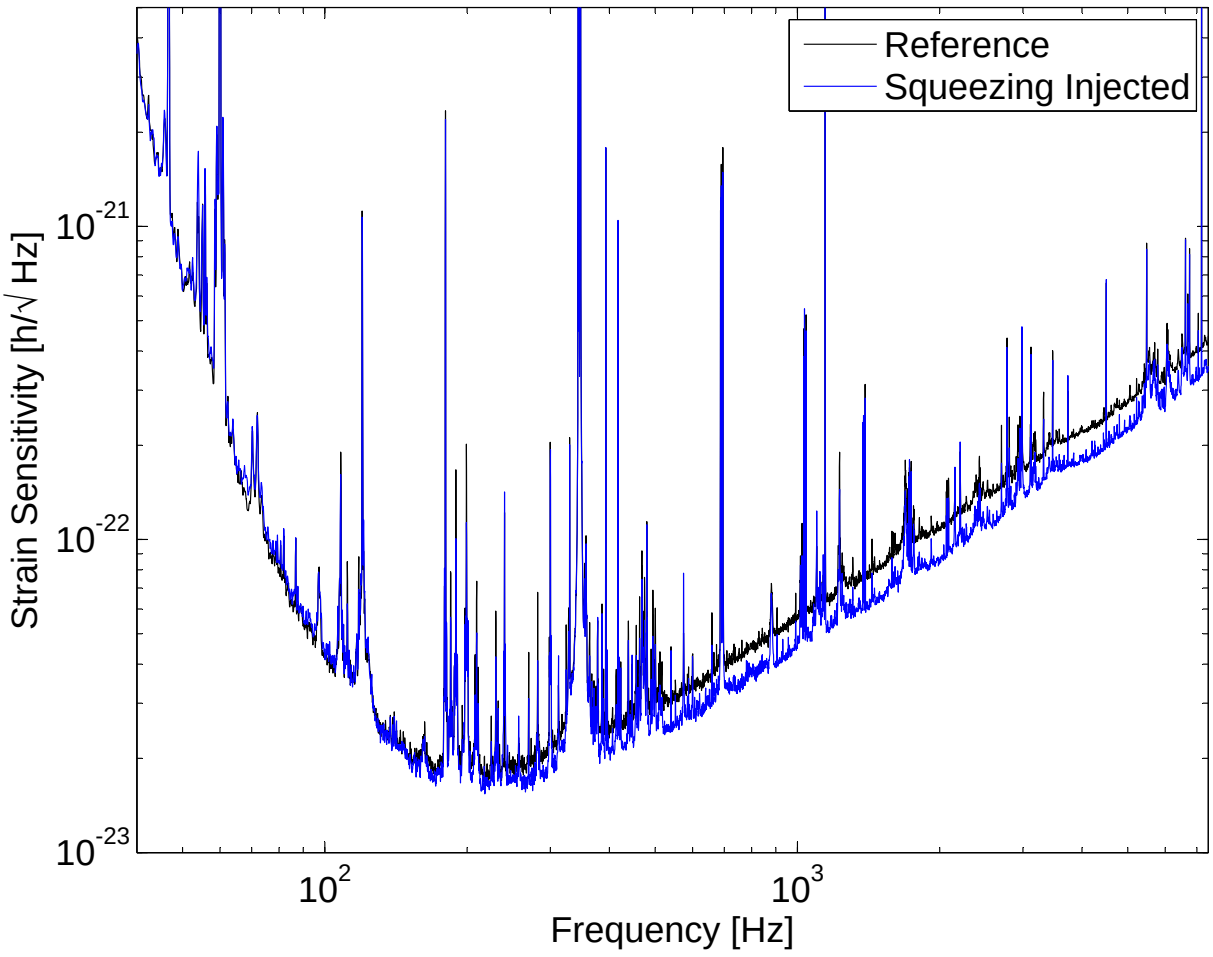

Figure 3-18: Enhanced LIGO sensitivity with squeezing injected. The reference trace shows the sensitivity of H1 without squeezing at the time of our experiment, with 20 Watts of input laser power. The blue trace shows the sensitivity with squeezing injected.

Figure 3-18 shows a comparison of the calibrated sensitivity with squeezing injected and a reference taken just before with the squeezing port blocked. Squeezing reduced the noise by 2 dB at 2 kHz, and improved the sensitivity down to 140 Hz. There are no frequencies at which the injection of squeezed light degrades the sensitivity, demonstrating for the first time that squeezing is compatible with the audio band sensitivity of a full-scale gravitational wave detector. Figure 3-19 shows the same data zoomed in around 200 Hz where Enhanced LIGO has the best sensitivity to gravitational waves. This is the first time that squeezing has been

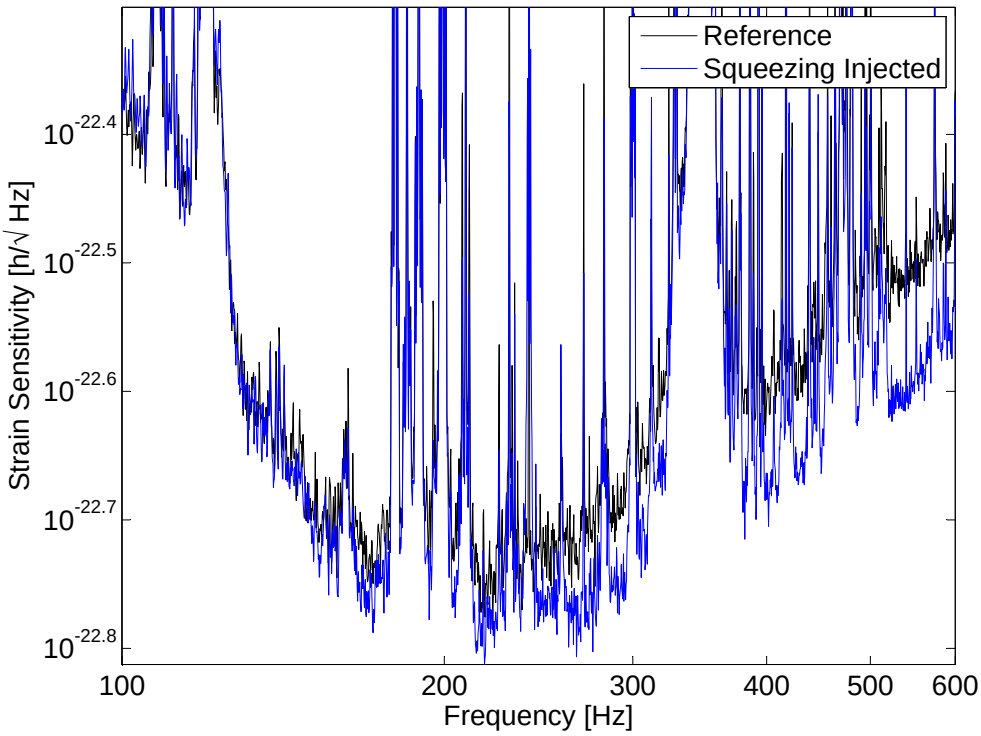

Figure 3-19: Squeezing enhancement in LIGO's most sensitive frequency band. To our knowledge this is the first time squeezing has been shown to improve the sensitivity of an interferometer at these frequencies, which are the most important for detecting neutron star inspirals.

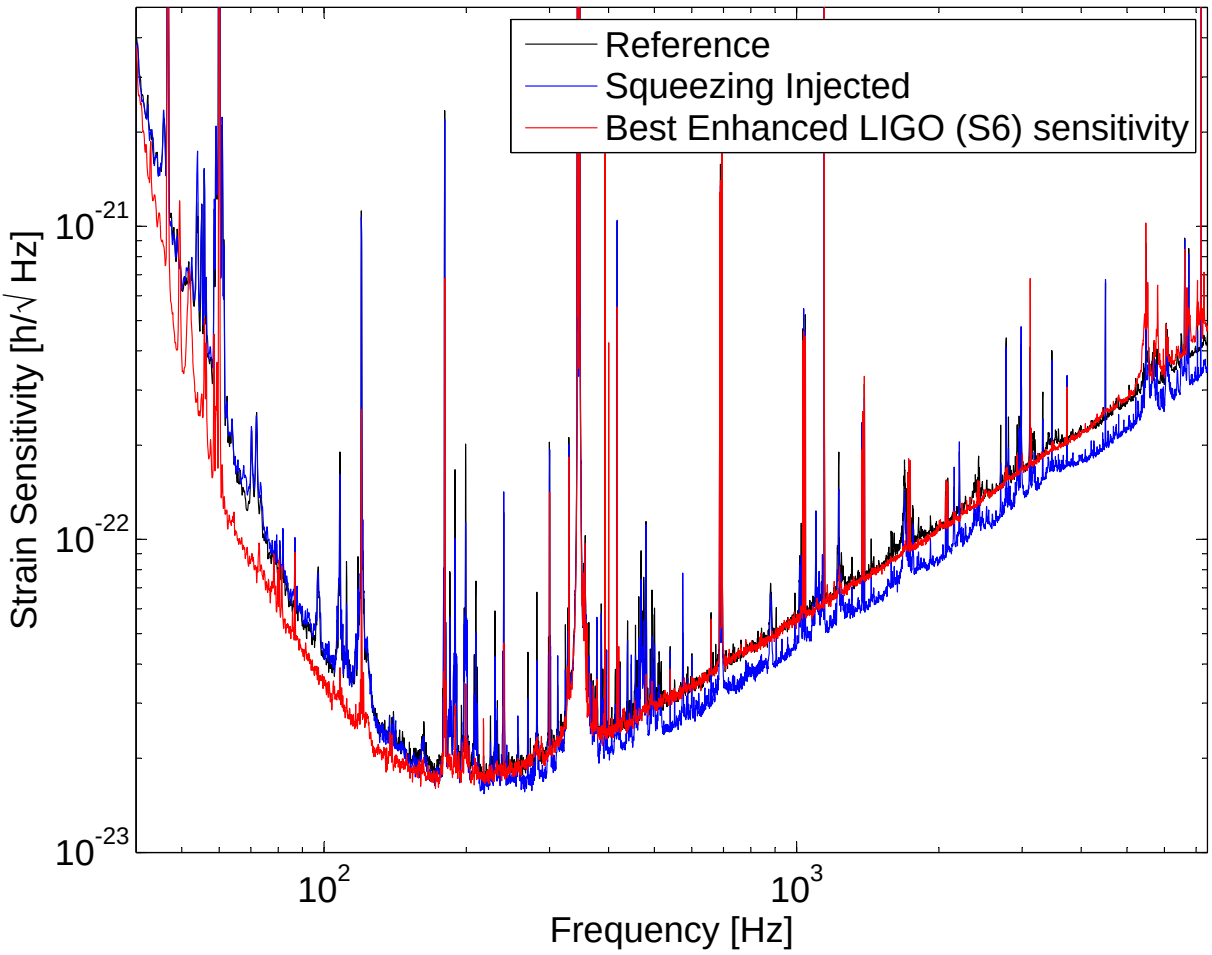

Figure 3-20: Squeezing results compared to Enhanced LIGO's best sensitivity.

observed in a gravitational wave detector at these astrophysically important frequencies. This is the region where acoustically driven noise is expected to be largest, and we see no evidence of added acoustic noise with squeezing. Figure 3-20 shows the data compared to the best sensitivity measured during the sixth LIGO science run. The squeezing result represents the best sensitivity in a gravitational wave detector from 250 Hz to several kHz to-date. The discrepancy below 140 Hz is due to a difference in the seismic environment; the S6 data was taken at an usually quiet time while squeezing and reference trace were taken at a particularly seismically loud time.

Figure 3-21a shows the noise reduction due to squeezing when the interferometer input

power was 16 Watts. This shows that at the best frequencies, we saw 2.25 dB of noise reduction due to squeezing. Figure 3-21b shows that with lower input power we were able to see an improvement from squeezing down to nearly 100 Hz.

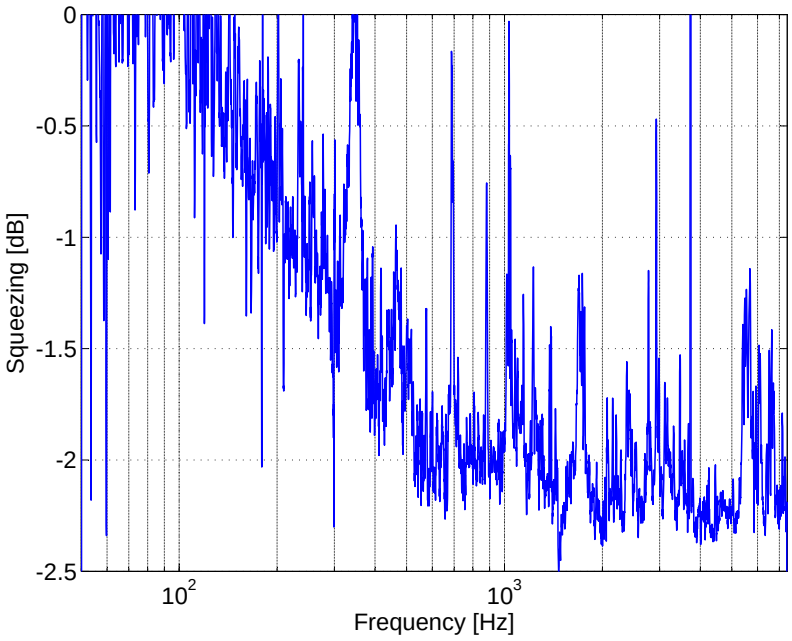

(a) More than 2 dB of squeezing observed with 16 W interferometer input power.

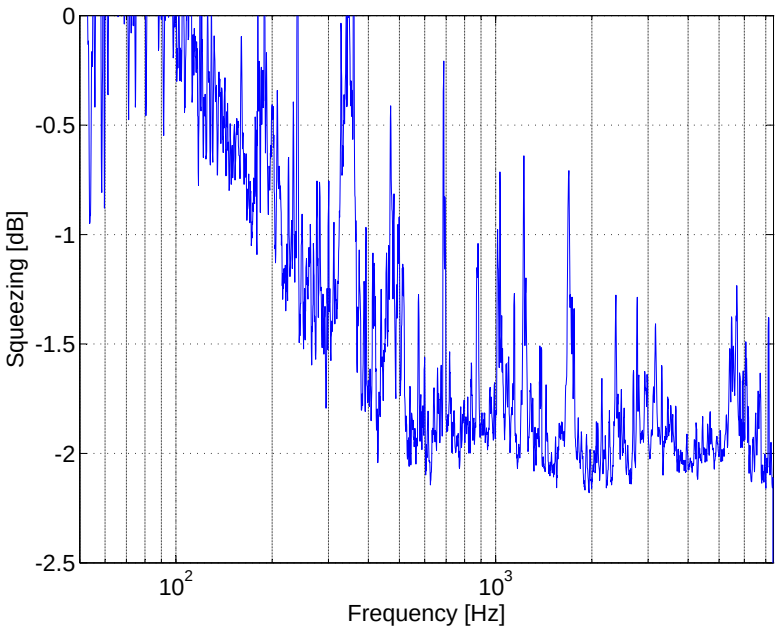

(b) Squeezing observed down to 100 Hz with 8 W input power.

Figure 3-21: Noise reduction due to squeezing, ratios of interferometer sensitivity with squeezing to sensitivity without squeezing, plotted on a log scale.

3.3.2 Astrophysical impact of squeezing enhancement

The true benefit of squeezing will come from improvements in the sensitivity of the detector to realistic sources of gravitational waves.

A commonly used metric for comparing the sensitivity of gravitational wave detectors is the horizon or sight distance for neutron star binary inspirals. This is the distance to which gravitational radiation from a binary of 1.4 $M_\odot$ neutron stars can be detected with a signal to noise ratio of 8, averaged over sky position and binary orientation. The low frequency sensitivity of a detector is most important for detection of inspirals, which emit at lower frequencies for longer times. The horizon distance for an inspiral is proportional to [54]:

$$d_{hor} = \Theta \left[\int df \frac{f^{-7/3}}{S_n(f)} \right]^{1/2} \tag{3.58}$$

where Θ is a constant that depends on the mass of the compact objects, and averaging over the sky positions and binary orientations. The power spectral density $S_n(f)$ is the square of the amplitude spectral densities plotted for example in Figure 3-18. The improvement in inspiral range due to squeezing in the data from Figure 3-21a is shown in Figure 3-22. The nearly 1 Mpc improvement shown is due entirely to squeezing below 1 kHz and represents a 7% increase in the detector's insprial range and a 24% increase in the volume of the universe that the detector can observe. Most of the improvement is due to squeezing below 300 Hz, where the squeezing is demonstrated for the first time in a gravitational wave detector.

Nearby rapidly spinning neutron stars with deformations in their crusts are another promising source for earth-based gravitational wave detectors. In the intermediate frequencies from 300 to 600 Hz, there are 28 known pulsars within 6 kpc [31]. The neutron star equation of state is not well understood, but observations of gravitational radiation from one of these known pulsars would provide new information about the neutron star's asymmetry, possibly caused by strong internal magnetic fields or asymmetries of the crust, and provide insight into this exotic state of matter [31]. At these frequencies the squeezing we observed would provide a 19% improvement in the SNR of any gravitational waves detected from these

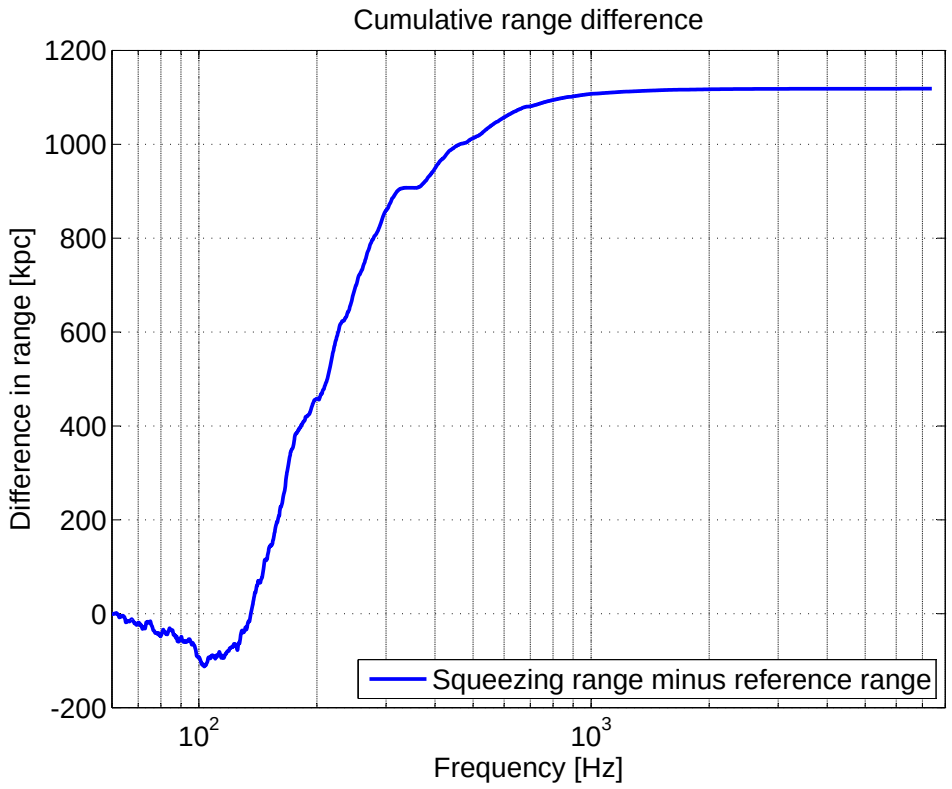

Figure 3-22: Improvement in inspiral range due to squeezing, when interferometer input power was 16 Watts. This plot shows the difference in the cumulative insprial range with and without squeezing, and was calculated based on a script written by Grant Meadors [60]. Most of the nearly 1 Mpc improvement in range came from squeezing below 500 Hz, where the amount of squeezing was small. The small decrease in range at low frequencies was most likely due to non stationarity of the spectrum due to changes in the seismic environment.

pulsars, and reduce upper limits from null detection by 16% [24]. Assuming that neutron stars in this frequency range are isotropically distributed within our galaxy, this represents a factor of two increase in the number of detectable neutron stars for a detector with the level of squeezing we observed.

At the highest frequencies in LIGO's detection band, coalescences and mergers of compact binary systems are a primary astrophysics target. As neutron star binaries lose energy by emitting gravitational waves the frequency of their orbits increase as the radius decreases, until the system reaches the radius of the innermost stable circular orbit, the ISCO. For a binary system of 1.4 $M_\odot$ neutron stars the orbital frequency at ISCO would be 800 Hz, so

the frequency of gravitational radiation would be 1.5 kHz [29]. This means that the 26% increase in the signal to noise ratio due to squeezing at frequencies above 600 Hz can improve observations of this interesting stage of binary evolution.

Coalescing compact binaries are expected to have electromagnetic counterparts. An observation of a single event in both electromagnetic and gravitational radiation could offer more insight than either observation alone would, and increase confidence in an early gravitational wave detection. A real difficulty in triggering searches for electromagnetic counterparts based on a potential observation of gravitational waves is the large area of the sky that must be searched. The sky location of a gravitational wave source is estimated based on the difference in arrival times at different detectors. The timing error for binary coalescence is inversely proportional to the signal to noise ratio, and the solid angle on the sky that needs to be searched for counterparts to a signal detected in a network of two detectors is proportional to the timing error (assuming the detectors have the same timing accuracy) [29]. Since the timing accuracy is weighted towardsthe high frequencies, the improvement may be better than this. This means that the 2 dB noise reduction we saw from squeezing would reduce the area of the sky to be searched by 20%.

We have demonstrated for the first time that squeezing is compatible with operation of a full scale gravitational wave interferometer with good low frequency sensitivity, and shown an improvement in the sensitivity to realistic sources of gravitational waves. While these modest improvements would be beneficial to the astrophysical reach of a gravitational wave detector, the real significance of these results is that they have demonstrated the potential of squeezing in a full scale interferometer. The lessons learned from this experiment allow us to form a detailed plan for achieving a more significant noise reduction in the next generation of interferometric gravitational wave detectors.

Chapter 4

Limits to squeezing noise reduction

Encouraged by the results in the last chapter, demonstrating that squeezing definitely improved the astrophysical reach of a full scale gravitational wave detector, we would like to plan for a larger noise reduction in future detectors like Advanced LIGO. The next two chapters will focus on understanding the factors that limit the noise reduction due to squeezing, and the final chapter will consider the implications of what we have learned for squeezing in Advanced LIGO. The noise variance on the gravitational wave signal is given by Equation 2.71:

$$V_{tot} = V_{tech} + 1 - 4\eta_{tot} x \left(\frac{\cos^2 \theta_{sqz}}{(1+x)^2} - \frac{\sin^2 \theta_{sqz}}{(1-x)^2} \right) \tag{4.1}$$

Since we will only be considering squeezing at gravitational wave frequencies, the measurement frequencies are all small compared to the line-width of the OPO and we have ignored the frequency dependence of the level of squeezing produced by the OPO. All of the effects that limit the squeezing can be described by only four factors, V_{tech}, η_{tot}, x and θ_{sqz}. If the detector is dominated by technical noise, squeezing the quantum noise will have no effect on the total noise. Optical losses limit the degree of squeezing by mixing a squeezed state with the noisier vacuum state. Fluctuations of the squeezing angle also reduce the broadband level of measured squeezing by adding noise from the anti-squeezed quadrature into the measured quadrature. Since we have enough second harmonic power available in our set

up to reach threshold, x was not a significant limit in our experiment.

While some of the factors that affect the level of squeezing are fixed, for example the finite transmission of an optical element, many of them can be adjusted to maximize squeezing, like the crystal temperature and position, the OPO length and input power, and the alignment of the beam from the squeezer into the interferometer. Ideally the experiment is operated at the point that maximizes the signal to noise ratio with respect to all of these adjustable parameters. As with any locally maximized function, fluctuations of the independent variables will lead to a degradation of the level of squeezing. If the fluctuations are slow compared to the measurement time, the level of measured squeezing will fluctuate over time, causing a non stationary spectrum. Fluctuations of variables which have been optimized will always degrade the mean level of squeezing, if the fluctuations are faster than the measurement time the only evidence will be a lower level of squeezing. For this reason there is a good deal of overlap between the mechanisms that degrade the level of squeezing and the long term stability of the squeezing; the same fluctuations that limit the stability when they happen slowly compared to the measurement time limit the level of squeezing when they happen faster than the measurement time. Although the next two chapters are focused on the level of squeezing, much of this will be applicable to investigations of the long term stability.

4.1 Technical noise

Noise sources other than quantum noise add in quadrature with the quantum noise, potentially masking any reduction in quantum noise. In a balanced homodyne detector the technical noise includes electronics noise, amplitude noise from the local oscillator due to a small imbalance between the two photo-diodes of the homodyne detector, and any amplitude noise from a coherent field entering from the squeezing port. For a discussion of the different sources of phase noise in a homodyne detector see [82].

When the interferometer is used to detect squeezing, seismic and thermal noise are the main limiting technical noise sources. Understanding and reducing these noise sources will

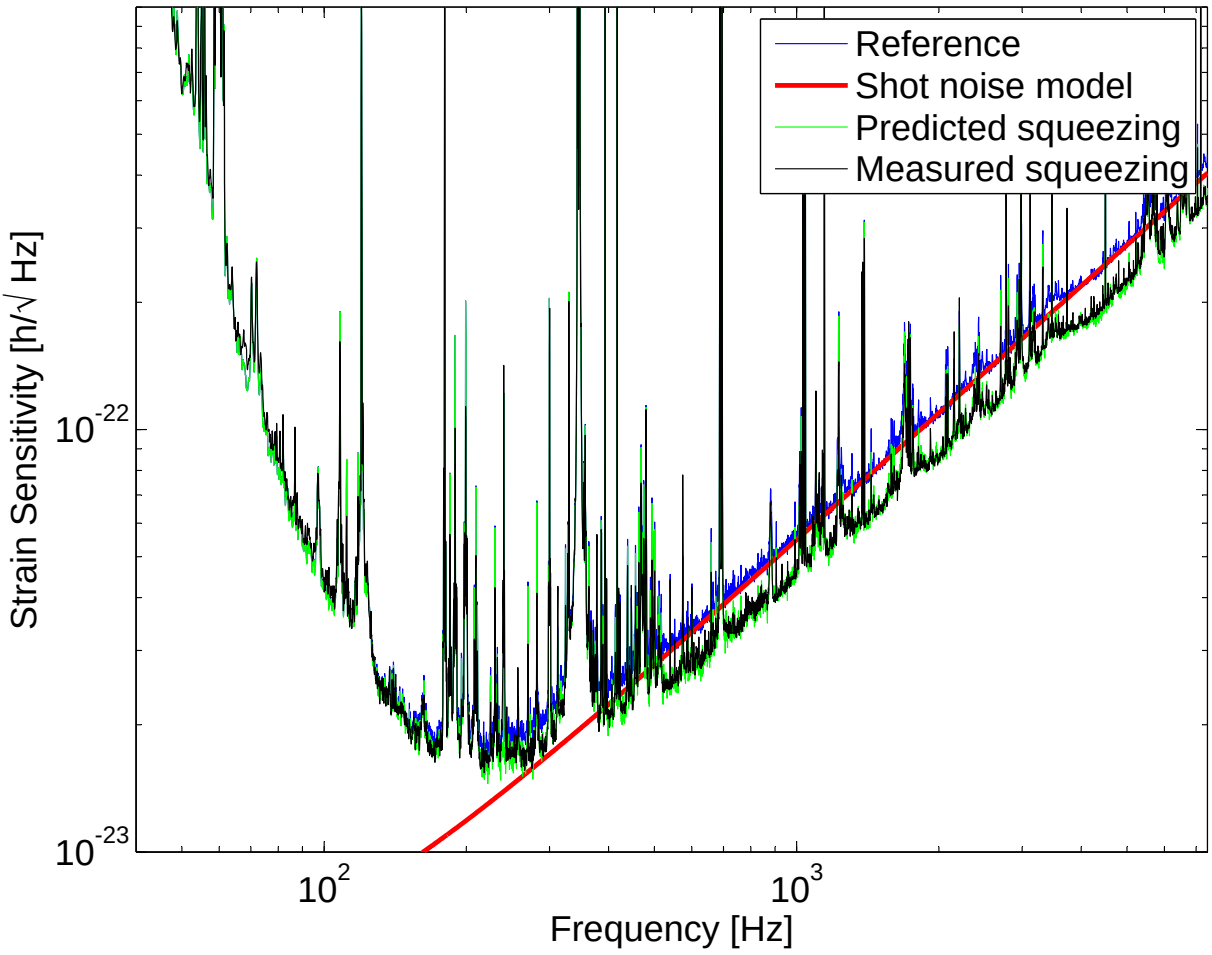

Figure 4-1: Squeezing with technical noise. The blue curve shows the reference trace, without squeezing injected. A model of shot noise for this data, with a zero at 100 Hz and the overall level set to match this data, is shown by the green line. An estimate of technical noise can be made by subtracting the shot noise model from the reference trace. The shot noise model, reduced by 2.1 dB, added in quadrature with the technical noise estimate, was used to make a prediction of the spectrum with squeezing injected, shown in red. This is an accurate prediction of the measured squeezing spectrum, shown in black. Technical noise added to the interferometer by the squeezer would cause the measurement to deviate from the prediction.

be important to improve the sensitivity of the interferometer, but to understand how they limit the squeezing we simply need to know the level of noise. This can be found easily by comparing the measured spectrum of the interferometer with either a model or a measurement of the shot noise level. The null-stream channel provides a measurement of the shot noise level even when squeezing is injected into the interferometer, as discussed in Section 2.7.3. By subtracting the shot noise in quadrature from the entire spectrum, we get an estimate of the total interferometer technical noise, which generally will have a frequency dependent spectrum. At frequencies where the interferometer technical noise is near the shot noise level or above it, it will degrade the squeezing. As long as there is some frequency in the spectrum where the technical noise is well below the shot noise, the maximum squeezing measured should indicate the level of shot noise reduction due to squeezing. A prediction for the spectrum with squeezing can be constructed by applying that maximum level of squeezing to the model of shot noise (or measurement), and adding the squeezed shot noise model in quadrature with the estimated interferometer technical noise. If this prediction matches well with the measured spectrum with squeezing injected, as in Figure 4-1, the technical noise is well understood and the squeezer is not adding significant technical noise to the interferometer. If the squeezer is adding additional technical noise to the interferometer, the improvement (or degradation) due to squeezing is unlikely to be flat in frequency. The extra noise added by squeezing will cause a discrepancy between the predicted and measured spectrum with squeezing.

4.2 Optical Losses

The term η_{tot} is called the total efficiency, and is often referred to as total losses. Sometimes the detection efficiency $\eta_{det} = \eta_{loss}\eta_{HD}\eta_{PD}$ is distinguished from the escape efficiency, so that the total efficiency becomes $\eta_{det}\eta_{esc}$. Figure 4-2a shows how detection efficiency affects the quantum noise as the squeezing angle changes. Viewed on a log scale, small losses have a dramatic effect on the squeezing. Figure 4-2b shows the measured squeezing as a function of injected squeezing for different detection efficiencies. For every detection efficiency the

Viewport	99.8%
Injection Faraday Isolator	94%
Output Faraday Rotator in output direction	94%
Pick off for AS table	98.8%
total	87%
total assuming output Faraday losses are symmetric	82%

Table 4.1: Measurements of power transmission of individual elements, illustrated in 3-17. [27]

measured squeezing approaches a limiting value, further increases in the generated squeezing do not improve the measured squeezing. Gravitational wave detectors are certainly in this loss limited regime but detection efficiencies have not been reliably above 50%.

4.2.1 Independent measurements of optical losses in H1 experiment

As discussed in Section 3.2.7, our OPO escape efficiency was 96%, with approximately equal contributions from crystal losses, rear coupler losses, and unidentified losses. Our detection efficiency varied from 40-46%. Table 4.1 shows measurements of optical losses between the squeezer and the OMC made before installation, the product of these values was in agreement with losses measured after installation by injecting a coherent beam. In the final configuration the transmission of the output mode cleaner for a well mode matched beam was 82%.

The largest uncertainty in our measurements of the detection efficiency come from uncertainty in the mode matching and alignment of the squeezed beam to the output mode cleaner. The mode matching was 80% with the interferometer unlocked, but the AS beam mode matching to the OMC differed by nearly 30% from an unlocked interferometer to a locked full power interferometer. The mode matching to the OMC could change due to thermal lensing on the input test masses. We measured the total transmission from the squeezer to the OMC photo-diodes to be 52% by locking the OMC length and alignment to the beam from the squeezer. We were able to see that the throughput was as expected

with the interferometer locked on RF with low power by injecting a large coherent beam from the squeezer with a frequency offset from the interferometer beam, aligning the OMC to the interferometer beam using quadrant photodiodes, and measuring the transmission of the squeezer beam through the OMC. We were only able to make this measurement with the original H1 OMC, not the Livingston OMC used for the second half of the squeezing experiment due to a camera alignment problem. The consistency between the throughput measurements with an interferometer locked on RF and an unlocked interferometer indicate that our technique for aligning the squeezed beam to the interferometer beam was adequate.

Combining the 52% propagation efficiency with our 96% escape efficiency and a lower limit of 95.4% on the quantum efficiency of the photodetectors [35], we predict a total efficiency of around 47%. During our experimental run the interferometer alignment varied from day to day, so that the detection efficiency varied as well. The detection efficiency would also have varied on a time scale of a few Hz, since the squeezer had no auto alignment system.

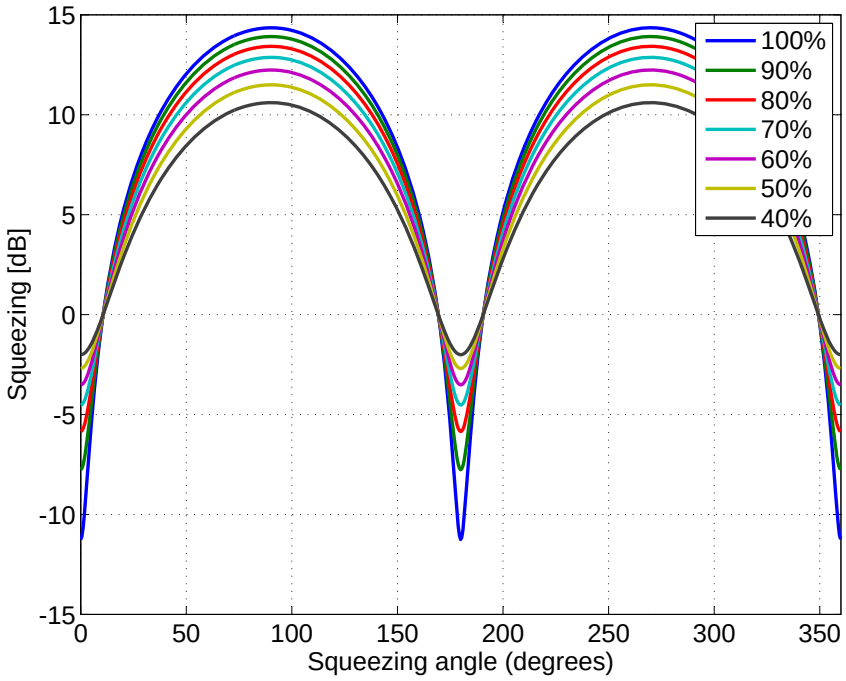

(a) Measured quantum noise as squeezing angle is changed for different detection efficiencies

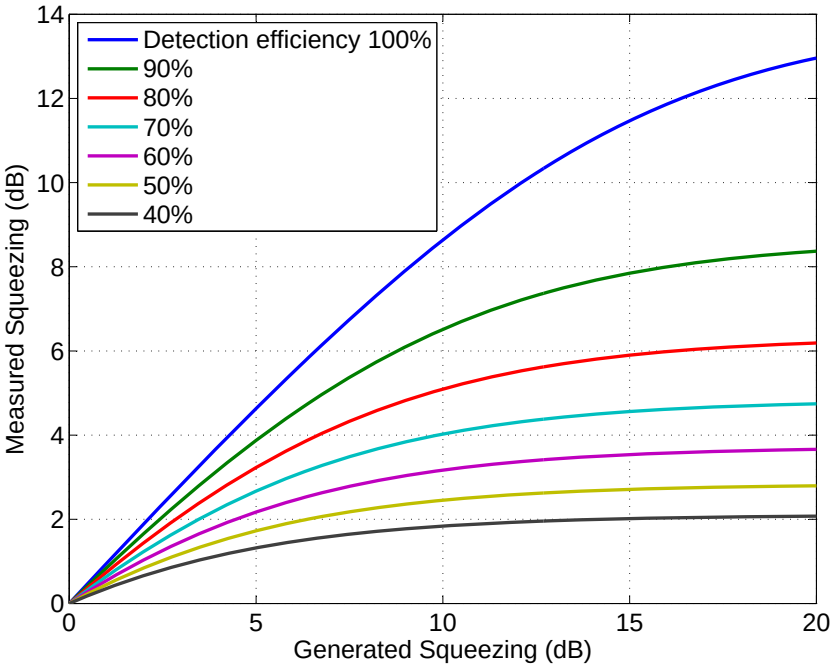

(b) Measured squeezing as a function of injected squeezing with different detection efficiencies, assuming 96% escape efficiency.

Figure 4-2: Squeezing with losses

4.3 Squeezing angle fluctuations

While we have locking loops that control the average squeezing angle, there are remaining fluctuations, sometimes called squeezing angle phase noise. These squeezing angle fluctuations mix some of the quantum noise from the orthogonal quadrature into the measurement. This degrades the broadband level of squeezing by an amount that depends on the total rms squeezing angle fluctuations that are faster than the measurement time. If the mean squeezing angle is θ_{sqz} with Gaussian fluctuations with standard deviation of $\widetilde{\theta}_{sqz}$, then the measured level of squeezing is:

$$V_{tot}(\theta_{sqz},\widetilde{\theta}_{sqz}) = V_{tech} + \frac{1}{\tilde{\theta}_{sqz}\sqrt{2\pi}}\int_{-\infty}^{\infty} dx e^{-x^2/2\widetilde{\theta}^2_{sqz}} \left(V_+ \sin^2(\theta_{sqz}+x) + V_- \cos^2(\theta_{sqz}+x)\right) \tag{4.2}$$

$$= V_{tech} + \frac{1}{\tilde{\theta}_{sqz}\sqrt{2\pi}}\int_{-\infty}^{\infty} dx e^{-x^2/2\widetilde{\theta}^2_{sqz}}$$

$$\times \left(V(\theta_{sqz})\cos^2 x + V(\theta_{sqz}+\pi/2)\sin^2 x + \frac{V_+ - V_-}{2}\sin 2\mu \sin 2x\right) \tag{4.3}$$

$$= V_{tech} + e^{-\widetilde{\theta}^2_{sqz}}\left(V(\theta_{sqz})\cosh\left(\widetilde{\theta}^2_{sqz}\right) + V(\theta_{sqz}+\pi/2)\sinh\left(\widetilde{\theta}^2_{sqz}\right)\right) \tag{4.4}$$

If we use the small angle approximation we have [2, 33, 84]:

$$V_{tot}(\theta_{sqz},\widetilde{\theta}_{sqz}) = V_{tech} + V(\theta_{sqz})\cos^2\widetilde{\theta}_{sqz} + V(\theta_{sqz}+\pi/2)\sin^2\widetilde{\theta}^2_{sqz} \tag{4.5}$$

Figure 4-3 shows the effect of squeezing angle fluctuations at frequencies well above the cavity line-width, which is largest at frequencies well inside the cavity line-width. While there are noise sources that cause high frequency squeezing angle fluctuations, like the control sidebands and quantum phase fluctuations at high frequencies, the dominant sources of squeezing angle fluctuations are driven by seismic, acoustic and thermal fluctuations which are large at frequencies in LIGO's measurement band and below. This means that $\tilde{\theta}_{sqz}$

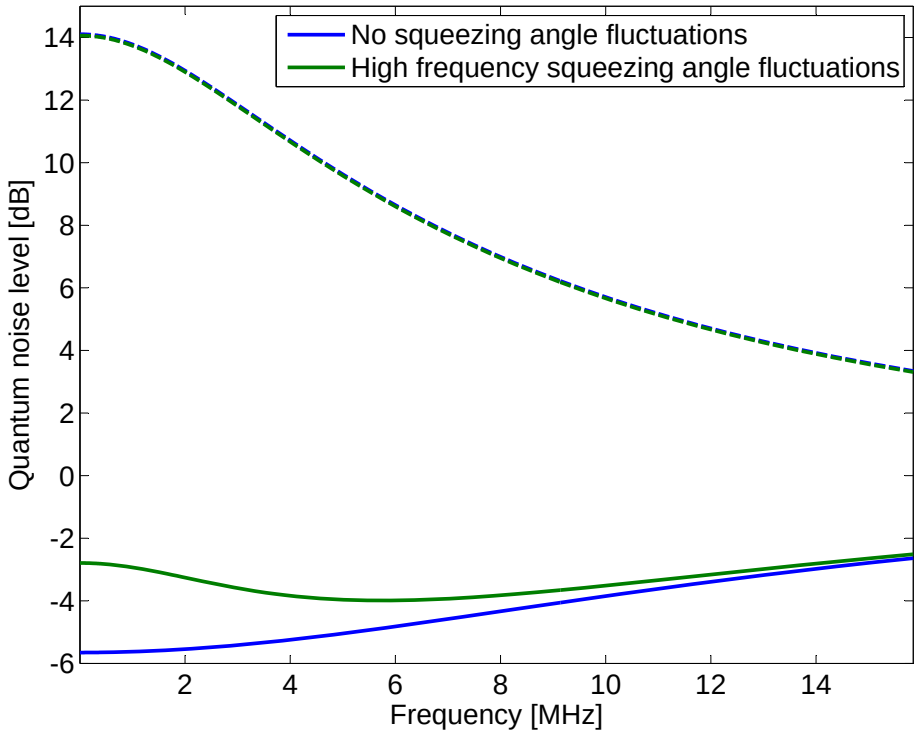

Figure 4-3: Squeezing level predicted for an OPO with a 12 MHz linewidth (HWHM), operated at half of the threshold power and 75% detection efficiency. The dashed lines show the level of anti-squeezing, which is nearly identical with and without squeezing angle fluctuations. The blue traces have no squeezing angle fluctuations, while the green traces have 100 mradians of RMS squeezing angle fluctuations all at frequencies above 15 MHz. Squeezing angle fluctuations do not have a large effect on the level of anti-squeezing but they do degrade the level of squeezing, especially at low measurement frequencies where the maximum anti-squeezing is produced.

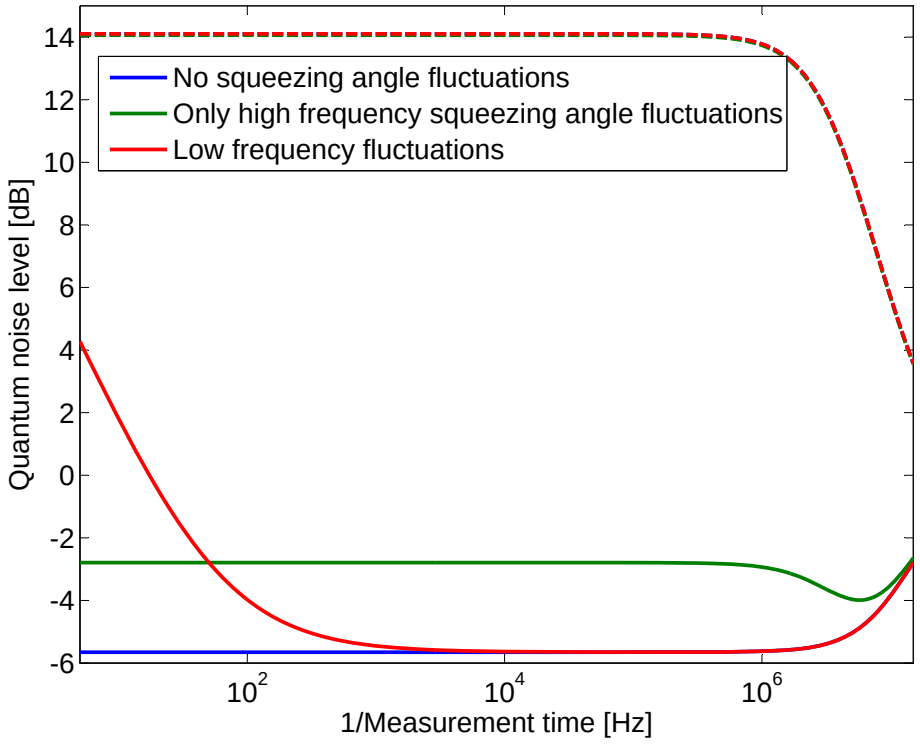

Figure 4-4: Squeezing with frequency dependent squeezing angle fluctuations, and same parameters used in Figure 4-3. The blue and green traces are the same as in Figure 4-3, plotted on a log frequency scale, if the measurement frequency is the inverse of the measurement time. The red curves are calculated with squeezing angle fluctuations that have an amplitude spectral density inversely proportional to frequency. The rms squeezing angle fluctuations above 50 Hz are the same in the low frequency and high frequency case, so the level of squeezing measured at 50 Hz is the same.

depends on the measurement time:

$$\widetilde{\theta}_{sqz}(f) = \left[\int_{1/t_m}^{\infty} S_\theta(f)\,\mathrm{d}\,f\right]^{1/2} \tag{4.6}$$

where if $S_\theta(f)$ is the power spectral density of squeezing angle phase noise, and t_m is the measurement time. Figure 4-4 shows the impact of squeezing angle fluctuations with a spectrum that is inversely proportional to frequency. Because spectra are normally taken with averaging, the inverse of the measurement time is usually lower than the lowest frequency included in the spectrum. Squeezing angle fluctuations are a more important concern for

squeezing used in gravitational wave detectors than in other applications of squeezing, both because of the low measurement frequencies and the long measurement times. As shown in Figure 4-5b, the effect of phase noise is more important with higher levels of squeezing, meaning that squeezing angle fluctuations will become a more important concern in future gravitational wave detectors planning for 6 dB or more of squeezing noise reduction.

4.4 Nonlinear interaction strength

Currently available crystals and laser sources allow us to reach a normalized nonlinear interaction strength of $x = 1$ easily with planning. This means that in practice the strength of the nonlinearity does not limit to the level of squeezing. Since the variances $V_{\pm}$ are odd functions of the nonlinear interaction strength, so the mean level of squeezing is determined by the mean value of x, and unaffected by fluctuations. However, if the value of x does drift over time the level of squeezing will also drift causing a non-stationary spectrum. An intensity stabilization on the second harmonic pump beam may be needed to stabilize the level of squeezing in the long term, both to reduce fluctuations of x and to reduce squeezing angle fluctuations caused by temperature changes as discussed in Section 5.2.2.

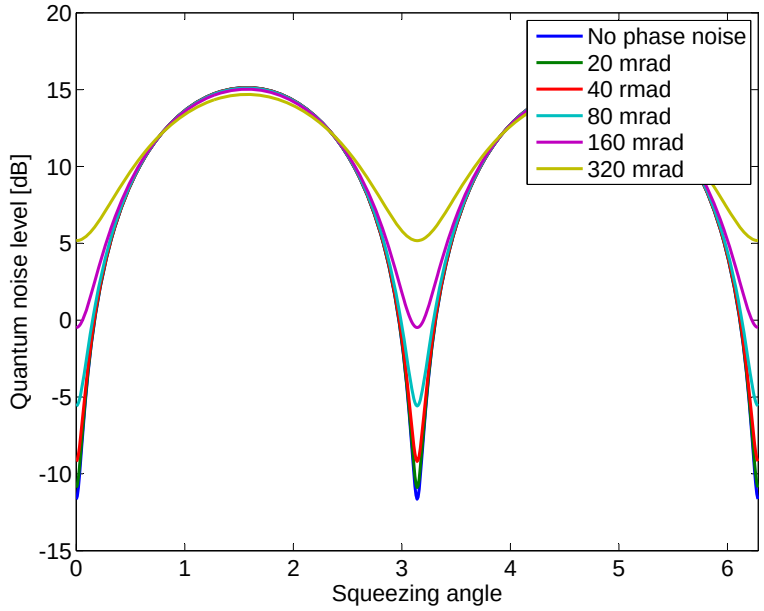

(a) Prediction for squeezing produced by our OPO, with different amounts of phase noise.

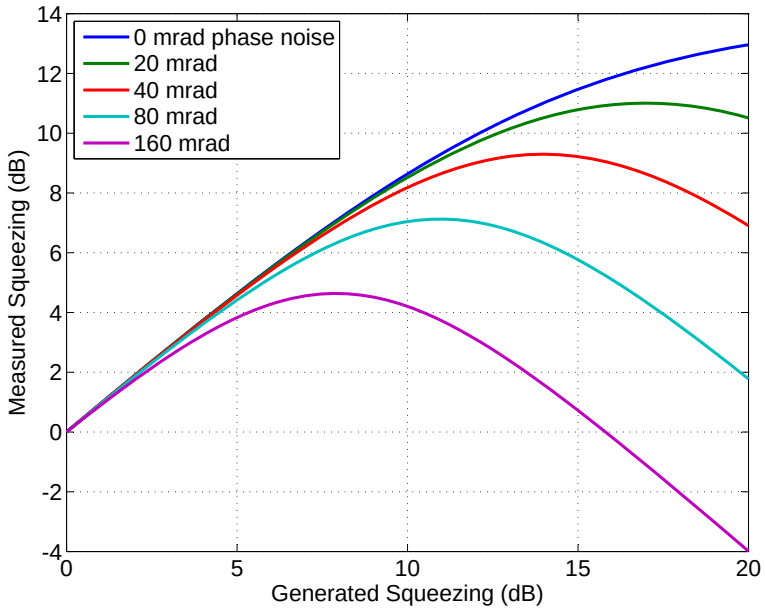

(b) Measured squeezing as a function of injected squeezing with different amounts of phase noise in detection.

Figure 4-5: Squeezing with phase noise

4.5 Measurements of total losses and total phase noise

The limits to squeezing can be studied in a bottom up way- considering each mechanism for degradation separately and calculating or measuring how it affects the squeezing, or by a top down approach- where the measured noise is used to estimate the factors that limit squeezing. Ideally the two approaches agree, and the level of squeezing is fully understood, but discrepancies can help identify unexpected sources of degradation. The technical noise can be estimated using the method illustrated in Figure 4-1. The classical nonlinear gain can be measured before squeezing is injected and used to estimate the normalized nonlinear interaction strength, which should not be an important limit to the squeezing. The remaining factors that can limit squeezing, η_{tot} and $\tilde{\theta}_{sqz}$ can be measured by the method illustrated in Figure 4-6. A measurement of the squeezing and anti-squeezing at a series of different nonlinear gains can be used to fit for the total losses and total squeezing angle fluctuations, as long as the alignment and loop gains are kept the same for all of the measurements. The results of a measurement using this method with Enhanced LIGO are shown in Figure 4-7. This is a standard technique for characterizing the performance of a squeezer and detector [2, 55, 61, 84], here we are using it to characterize the performance of the interferometer as a squeezing detector.

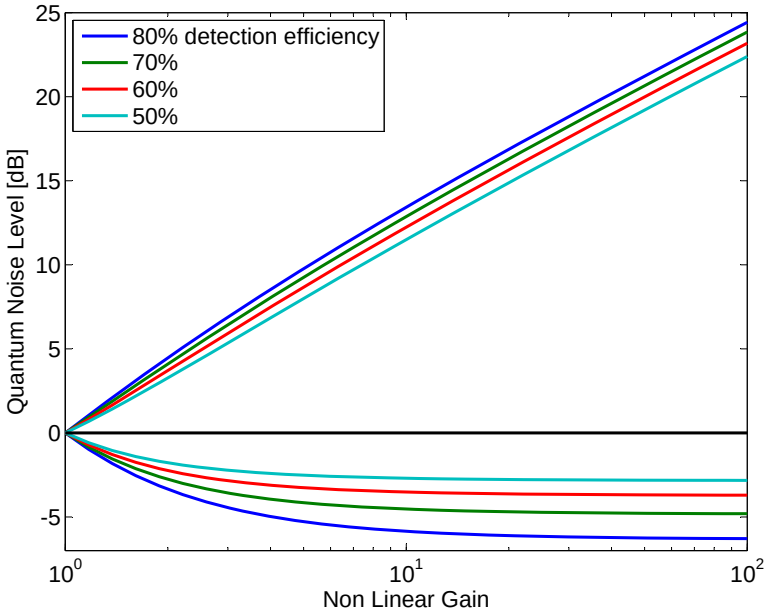

(a) Quantum noise as a function of nonlinear gain without phase noise.

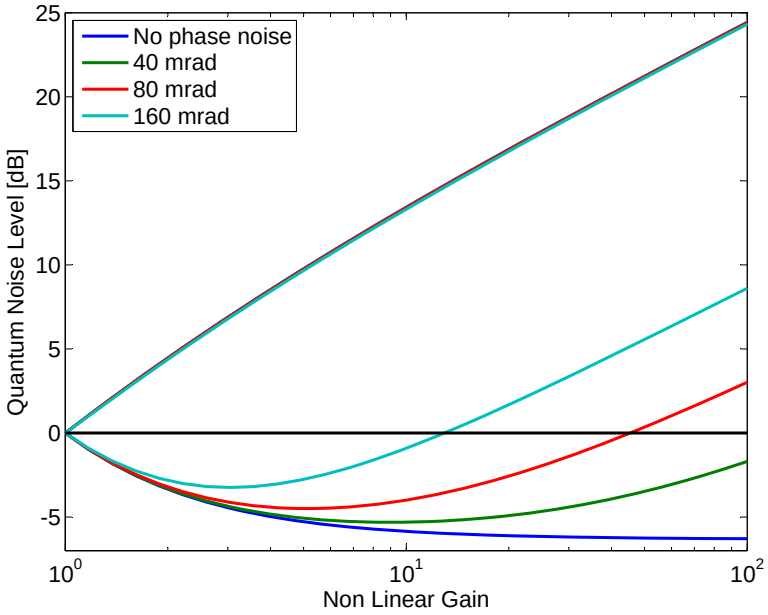

(b) Quantum noise as a function of nonlinear gain with 80% detection efficiency.

Figure 4-6: Method for distinguishing between losses and phase noise. The level of anti-squeezing is relatively unaffected by phase noise, but does depend on the detection efficiency. The level of squeezing, especially at high nonlinear gains, depends strongly on the level of phase noise.

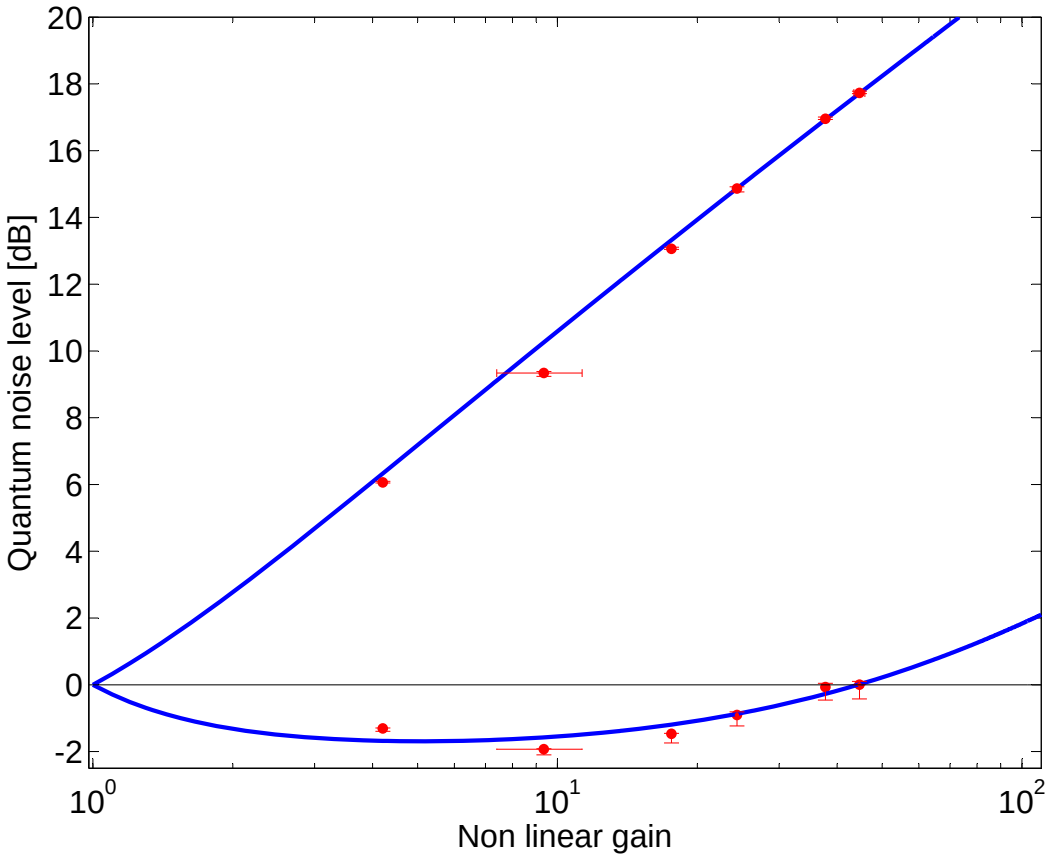

Figure 4-7: Measurement of total efficiency and total phase noise of squeezing during the Enhanced LIGO squeezing experiment. The blue line shows a fit to the red points with total efficiency, $38.5 \pm 8.3\%$, and squeezing angle fluctuations of 81.0 ± 13.6 mrad.

Chapter 5

Squeezing angle fluctuations

In the last chapter we used Equation 4.1 for the squeezing produced in an idealized situation, without cavity length noise, laser noise, or temperature fluctuations, to characterize the squeezing actually measured in the interferometer. We saw that the limits in the idealized situation explain the limits to the measured squeezing. In this chapter we will consider ways in which the actual experiment deviates from the assumptions made in Section 2.5 to arrive at Equation 4.1. In this chapter we will only consider the impact that realistic fluctuations in our experiment have on the quantum noise reduction that squeezing can achieve. Any noise couplings that can add classical noise to the interferometer we consider technical noise which will be addressed in the next chapter. The control of squeezing angle fluctuations in a gravitational wave detector has some unique requirements. We will describe the control scheme and an unexpected noise coupling that it introduced. We will see that the dominant impact of all these experimental realities can be approximated as fluctuations of the squeezing angle, so that Equation 4.1 remains a good approximation to the measured variance even with these realities taken into account.

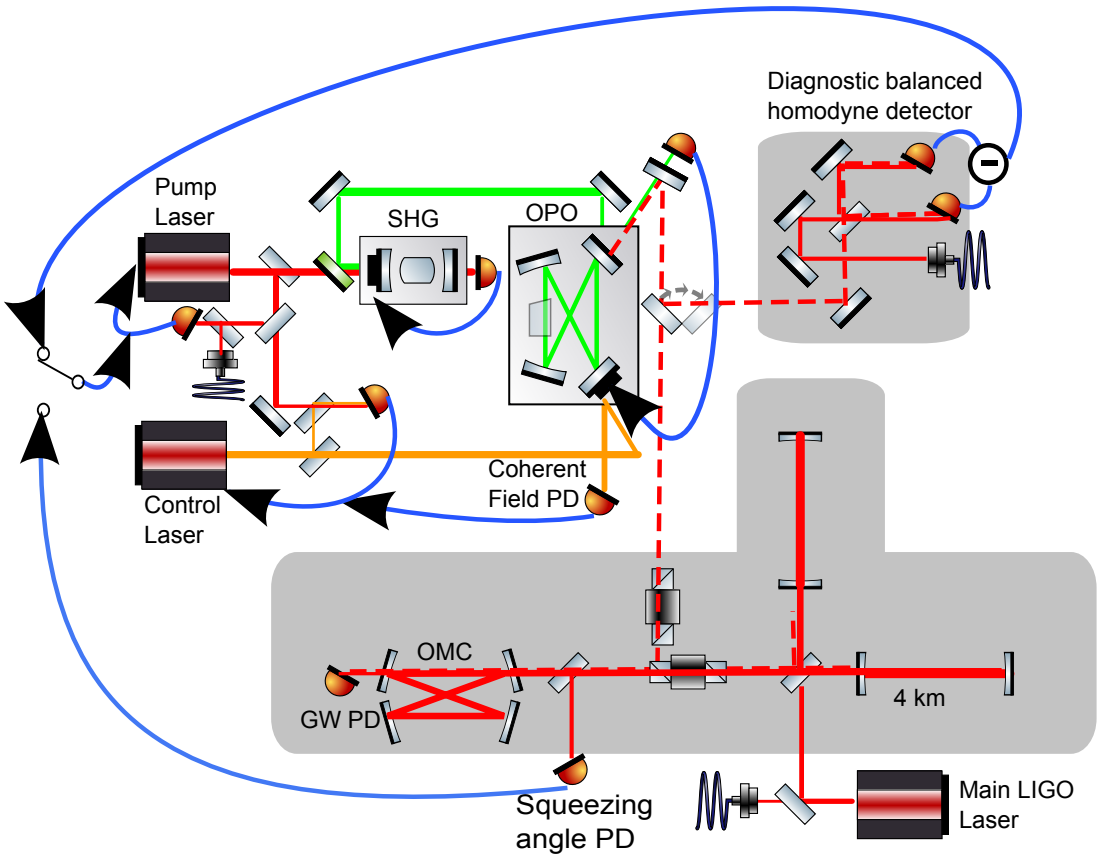

Figure 5-1: Diagram of the control scheme for H1 squeezing experiment

5.1 Introduction to squeezed vacuum source control scheme

The squeezer control scheme is designed to control several degrees of freedom, including the frequency and phase of the two lasers, the lengths of the two cavities, and the phase of the squeezed state relative to the local oscillator at the detector. Although there are six control loops, four of them are used in a hierarchical arrangement to control a single degree of

freedom, the squeezing angle. Figure 5-1 shows a simplified layout of the squeezing experiment in Enhanced LIGO and illustrates the control scheme used to reduce squeezing angle fluctuations, a variation on the control scheme described in [11]. The pump laser is locked with a bandwidth of 240 kHz to the interferometer's carrier frequency through a fiber, while the control laser is offset locked 29.5 MHz above the pump laser frequency with a 470 kHz bandwidth. The pump laser pumps a second harmonic generator (SHG) similar to the one described in [11]; the generated 532 nm field pumps an OPO similar to the one described in [12]. These cavity lengths are each controlled with bandwidths of 6 and 9 kHz respectively by Pound-Drever-Hall locking actuating on a cavity mirror attached to a piezo-electric transducer (PZT). The control laser is injected into the OPO where the nonlinear process generates a second sideband symmetric about the carrier frequency. The phase relationship between the injected and generated sidebands is the same as the phase relationship between the correlated audio frequency sidebands generated by the OPO, and is sensed in reflection off the OPO at the coherent field photo-detector. The phase of the control laser is then locked to the phase of the squeezed state with a 90 kHz bandwidth servo by actuating on the lock point of the auxiliary laser phase locked loop and a path length PZT. The phase of the coherent control sidebands are now a proxy for the squeezed angle. In normal operation, the squeezed state and coherent sidebands are injected into the interferometer, reflect off the Fabry- Perot arm cavities and interfere with the anti-symmetric port beam. A pickoff mirror sends a small amount of power to the squeezing angle photo-detector, which senses the phase between the coherent sidebands and the interferometer carrier, which is indirectly a measure of the squeezed quadrature. This signal is fed back to the phase between the main squeezing laser and the interferometer laser with a bandwidth of 10 kHz, using a voltage controlled oscillator. The output mode cleaner rejects the coherent sidebands and transmits the squeezed field and the interferometer carrier to the gravitational wave photo-detector where the reduction in quantum noise is measured by homodyne detection. Alternatively, the diagnostic homodyne detector can be used to measure the squeezing and generate the coherent squeezing angle control error signal to characterize the squeezer performance without

the interferometer.

5.2 Factors that can shift squeezing angle

To understand how experimental realities can limit the squeezing produced by an OPO we will expand the calculation from Section 2.4 to include laser noise, cavity length fluctuations, and temperature fluctuations. We will follow the general approach used by McKenzie [57], to show that first order couplings of these noise sources to the field produced by the OPO (technical noise) can be eliminated when there is no coherent field at the fundamental frequency, [56, Chapter 5]. We will start with the assumption that there is no coherent field at the fundamental frequency, and so we will not find the first order couplings of these noise sources to the variance calculated in [56]. When we consider the second order couplings of these noise sources to the variance we will see that we can approximate them as first order couplings to the squeezing angle. In Section 2.4 we found the time domain equations for the cavity fields. In this section we will not assume that the second harmonic field is in a coherent state and allow it to have noise:

$$\dot{b} = -(\gamma_r^{tot} - i\Delta_b)b + \sqrt{2\gamma_g^f}B_{in,f} \tag{5.1}$$

$$\delta\dot{\mathbf{a}} = \gamma_r^{tot}\mathbf{M}\delta\mathbf{a} + \sqrt{2\gamma_r^l}\delta\mathbf{A_{l,in}} + \sqrt{2\gamma_r^f}\delta\mathbf{A_{f,in}} \tag{5.2}$$

$$\mathbf{M} = \begin{pmatrix} -1 + i\dfrac{\Delta_a}{\gamma_r^{tot}} & \dfrac{\epsilon b}{\gamma_r^{tot}} \\ \dfrac{\epsilon^* b^\dagger}{\gamma_r^{tot}} & -1 - i\dfrac{\Delta_a}{\gamma_r^{tot}} \end{pmatrix} \tag{5.3}$$

Assuming that the three main noise sources, laser phase noise, laser amplitude noise, and cavity length noise, are incoherent we will calculate each effect separately and can add them in quadrature to find the total squeezing angle fluctuations.

5.2.1 OPO Cavity length noise

The cavity length is locked to the frequency of the second harmonic field, so the average detuning for that field vanishes. Although the cavity length noise is suppressed by the PDH lock, residual length noise remains, causing the detuning to have a fluctuating component:

$$\Delta_b = 2\omega \frac{\delta L(t)}{\bar{L}} \equiv 2\Delta(t) \tag{5.4}$$

where Δ is the detuning at the fundamental frequency. Since cavity length fluctuations are driven by acoustic and seismic motion they will be at frequencies far below the cavity linewidth and we can ignore any frequency dependence in the squeezing spectrum. We can instead simply calculate the effect of a static length detuning Δ on the squeezing angle to understand the impact of fluctuations. From Equation 5.1 the circulating field becomes:

$$b = \frac{\sqrt{2\gamma_g^{out}} B^{in}}{\gamma_b^{tot}} \frac{1}{1 - i2\Delta/\gamma_b^{tot}} \tag{5.5}$$

If we keep only terms that are first order in Δ/γ_g^{tot} the detuning causes only a phase shift of the circulating field, so we can expect that a detuning will cause a shift of the squeezing angle. The change in the cavity length also causes a phase shift for the infrared fields, so we will use the full cavity equations of motion with the static detuning included to find the effect on the squeezing. Now $\mathbf{M}$ from Equation 5.3 becomes:

$$\mathbf{M} = \gamma_r^{tot} \begin{pmatrix} -1 + i\frac{\Delta}{\gamma_r^{tot}} & \frac{x e^{i\theta_b}}{1 - i2\Delta/\gamma_g^{tot}} \\ \frac{x e^{-i\theta_b}}{1 + i2\Delta/\gamma_g^{tot}} & -1 - i\frac{\Delta}{\gamma_r^{tot}} \end{pmatrix} \tag{5.6}$$

Following the procedure of Section 2.4 using this matrix gives an expression for the variances of the output fields with a detuning included. A plot of the resulting variances for the parameters of our OPO is shown in Figure 5-2. At $\theta_b = 0$ the variance in the squeezed

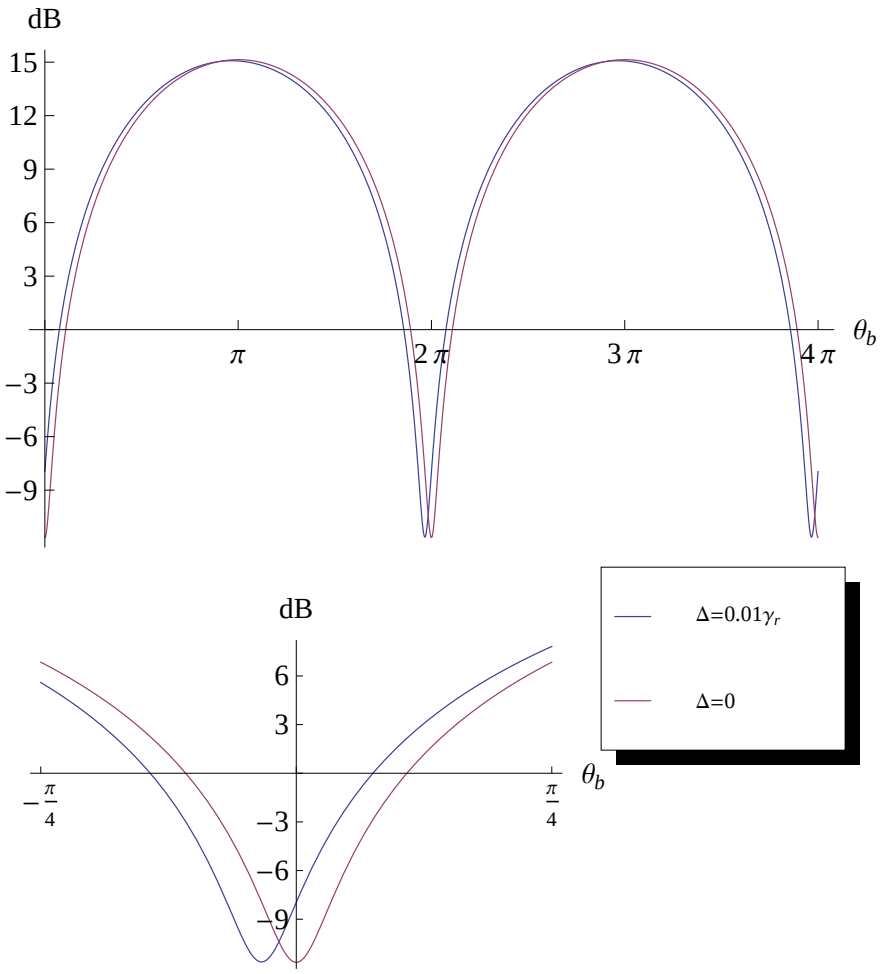

Figure 5-2: Quadrature variance of output field as incident pump phase varies for a cavity on resonance (purple) and slightly detuned (blue). The maximum level of squeezing is almost unchanged by small detunings, although the squeezing angle is shifted relative to the phase of the input field. Δ is the detuning from the OPO resonance for the fundamental field.

quadrature to second order in the detuning is:

$$V_{sqz} = V_- + \frac{4\eta_{esc}x}{(1-x^2)^2}\left[\frac{4(1-x+2x^2)}{(\gamma_g^{tot})^2} + \frac{4}{\gamma_g^{tot}\gamma_r^{tot}} + \frac{x+3}{(1+x)(\gamma_r^{tot})^2}\right]\Delta^2 \qquad (5.7)$$

From Figure 5-2 it is clear that the effect of the detuning is a phase shift,and that the maximum level of squeezing with no detuning can nearly be recovered if the pump phase is adjusted to compensate for the detuning. To find the first order approximation for the shift in the squeezing angle due to a cavity detuning we make an expansion at the point where

the variance is linear with the incident pump phase, $\theta_b = \pi/2$. We can find the first order shift in the squeezing angle by taking derivatives at this point:

$$\frac{d\theta_{sqz}}{d\Delta} = \frac{\frac{dV}{d\Delta}\Big|_{\phi=\pi/2,\Delta=0}}{\frac{dV}{d\phi}\Big|_{\phi=\pi/2,\Delta=0}} = \frac{2}{\gamma_g^{tot}} + \frac{2}{\gamma_r^{tot}(1+x^2)} \tag{5.8}$$

The squeezing angle fluctuations caused by a cavity length change $\delta L(t)$ are :

$$\delta\theta_{sqz}(t) = \left(\frac{1}{\gamma_g^{tot}} + \frac{1}{\gamma_r^{tot}(1+x^2)}\right)\frac{2\omega\delta L(t)}{\bar{L}} \tag{5.9}$$

Although the impact of a detuning on the noise level is second order, we can approximate the effect as a linear coupling to the squeezing angle, which allows us to use linear controls to mitigate the effect.

5.2.2 Crystal temperature fluctuations

The amplitude fluctuations of the second harmonic field, as well as environmental temperature changes, can cause temperature fluctuations of the nonlinear crystal. A change in crystal temperature will cause a change in the nonlinear coupling parameter and the co-resonance condition, as discussed in Section 3.2.6. The detuning for the fundamental field is given by the dispersion mismatch (Equation 3.31) over the cavity round trip time:

$$\begin{aligned}\Delta_a = \frac{\Delta\phi_{rt}}{\tau} &= \frac{1}{\tau}\Bigg[k_r L_c\left(\alpha\left[n(\omega_g) - n(\omega_r)\right] + \frac{dn(\omega_g)}{dT} - \frac{dn(\omega_r)}{dT}\right)(T - T_0) \\ &\qquad + k_r(n(\omega_r) - n(\omega_g))\sin\theta_w(y - y_0)\Bigg] \qquad (5.10)\\ &\equiv \frac{\upsilon(T - T_0) + \Upsilon(y - y_0)}{\tau} \qquad (5.11)\end{aligned}$$

where τ is again the cavity round trip time, and we approximate the total crystal length by the length of the poled region in the crystal. Ideally the temperature setting is adjusted for co-resonance, so the constant part of the detuning is zero. If the crystal position is optimized,

$y = y_0$, and the average temperature is set for co-resonance then

$$\Delta_a = \frac{\upsilon \delta T(t)}{\tau} \tag{5.12}$$

The nonlinear coupling parameter depends on the phase mismatch [45, 57]:

$$\epsilon = \epsilon_0 e^{-i\Delta k_q L_c/2} \operatorname{sinc}\left(\frac{\Delta k_q L_c}{2}\right) \tag{5.13}$$

where ϵ_0 is the nonlinear coupling parameter for perfect quasi-phase matching. The argument of the exponential will have the same impact on the squeezing as a phase shift of the second harmonic circulating field would have. From Equation 3.20:

$$\frac{L_c \Delta k_q}{2} = \upsilon(T - T_0) = \upsilon \delta T(t) \tag{5.14}$$

Temperature fluctuations will all be at low frequencies compared to the cavity linewidth, so can once again ignore the frequency dependence. Assuming that the crystal position is optimal a temperature fluctuation δT away from the optimal temperature will change the matrix $\mathbf{M}$ that describes the OPO to:

$$\mathbf{M} = \begin{pmatrix} -1 + i\dfrac{\upsilon \delta T}{\gamma_r^{tot}\tau} & x \operatorname{sinc}(\upsilon \delta T) e^{i(\theta_b - \upsilon \delta T)} \\ x \operatorname{sinc}(\upsilon \delta T) e^{-i(\theta_b - \upsilon \delta T)} & -1 - i\dfrac{\upsilon \delta T}{\gamma_r^{tot}\tau} \end{pmatrix} \tag{5.15}$$

As shown in Figure 5-3 a temperature shift also causes a shift in the squeezing angle, and only a small change in the maximum level of squeezing that can be measured. The squeezing angle fluctuations are the dominant effect, we can calculate the linear coupling of temperature fluctuations to squeezing angle by taking derivatives around the point $\theta_b = \pi/2$ and $T = T_0$, the optimal temperature:

$$\frac{d\theta_{sqz}}{dT} = \frac{\left.\frac{dV}{dT}\right|_{\phi=\pi/2,\delta T=0}}{\left.\frac{dV}{d\phi}\right|_{\phi=\pi/2,\delta T=0}} = \upsilon\left(\frac{2}{\gamma_r^{tot}\tau(1+x^2)} - 1\right) \tag{5.16}$$

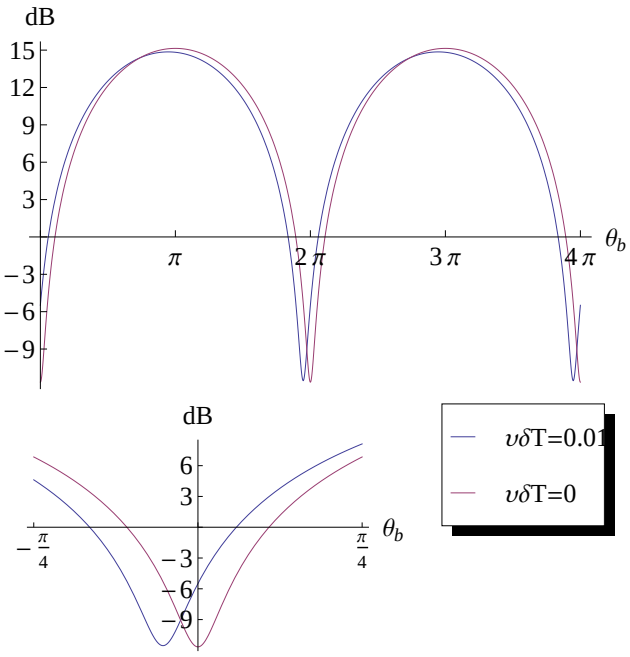

Figure 5-3: Quadrature variance of output field as a function of incident pump phase, with a temperature offset.

5.2.3 Second harmonic field amplitude fluctuations

Fluctuations in the circulating second harmonic power can directly change the normalized nonlinear interaction strength, and can also cause fluctuations in the crystal temperature. Without the temperature effect, the amplitude fluctuations are not an important limit to the squeezing. Using the equations of motion, a static increase in the circulating amplitude simply increases the level of squeezing, as shown in Figure 5-4. The mean level of squeezing is determined by the mean circulating amplitude, so amplitude fluctuations would degrade the long term stability but not the level of squeezing if there were no temperature effects.

Absorption in the crystal means that the temperature fluctuations are driven by fluctuations in the circulating second harmonic power [51]. The crystal absorbs some of the second harmonic power, causing localized heating where the beam passes through. The amount of localized heating is not measured by the temperature sensor, which is on or near the crystal surface, so our temperature control servo does not correct for the localized heating [57]. The second harmonic power absorbed by a crystal with a low absorption coefficient α_{KTP} will

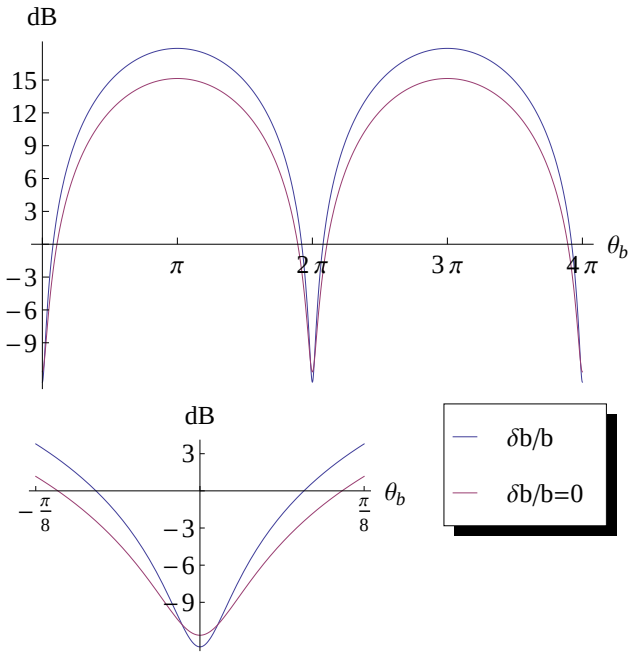

Figure 5-4: Quadrature variance of output field as a function of incident pump phase, with a change in pump amplitude ignoring temperature effects.

be:

$$P_{abs} = P_{circ}(1 - e^{-\alpha_{KTP} L_{c,tot}}) = P_{circ}\alpha_{KTP} L_{c,tot} \tag{5.17}$$

Writing the circulating power in terms of the linearized operators:

$$P_{circ} = \bar{P}_{circ} + \delta P_{circ}(t) = \bar{P}_{circ}\left(1 + \frac{\delta P_{circ}(t)}{\bar{P}_{circ}}\right) \tag{5.18}$$

$$= 2\hbar\omega\left(\bar{b}^{\dagger} + \delta b^{\dagger}(t)\right)\left(\bar{b} + \delta b(t)\right)$$

$$= 2\hbar\omega|\bar{b}|^2\left(1 + 2\,\mathrm{Re}\left[\frac{\delta b(t)}{\bar{b}}\right]\right) \tag{5.19}$$

The absorption of the constant part of the power can be compensated for by changing the setting of the temperature controller, however the fluctuations will not be compensated by

the temperature controller.

$$\delta\widetilde{P}_{abs}(t) = 4\alpha_{KTP}L_{c,tot}\hbar\omega|\bar{b}|^2\,\mathrm{Re}\left[\frac{\delta\widetilde{b}}{\bar{b}}\right] \tag{5.20}$$

In the frequency domain the temperature change due to a change in the circulating power will be [45]:

$$\delta\widetilde{T} = \frac{\tau_T}{C\rho V}\left(\frac{1}{1+s\tau_T}\right)\delta\widetilde{P}_{abs} \tag{5.21}$$

where C is the specific heat and ρ is the density of the crystal, V is the mode volume in the crystal, and τ_T is the thermal relaxation time of the crystal which is much smaller than the cavity line-width. The transfer function from incident to circulating amplitude fluctuations is:

$$\mathrm{Re}\left[\frac{\delta\widetilde{B}}{\bar{B}}\right] = \frac{1}{1+s/\gamma_r^{tot}}\,\mathrm{Re}\left[\frac{\delta\widetilde{b}}{\bar{b}}\right] \tag{5.22}$$

We can now write the crystal temperature fluctuations in terms of the amplitude fluctuations of the input field using Equations 5.21 and 5.20:

$$\delta\widetilde{T} = \frac{\tau_T 4\alpha_{KTP}L_{c,tot}\hbar\omega|\bar{b}|^2}{C\rho V}\left(\frac{1}{1+s\tau_T}\right)\left(\frac{1}{1+s/\gamma_g^{tot}}\right)\mathrm{Re}\left[\frac{\delta\widetilde{B}}{\bar{B}}\right] \tag{5.23}$$

$$= \left(\frac{1}{1+s\tau_T}\right)\left(\frac{1}{1+s/\gamma_g^{tot}}\right)\frac{2\tau_T\overline{P}_{abs}}{C\rho V}\,\mathrm{Re}\left[\frac{\delta\widetilde{B}}{\bar{B}}\right] \tag{5.24}$$

While amplitude fluctuations can be at high frequencies, due to either classical or quantum noise on the second harmonic field, the thermal relaxation time will be of the order of hundred of Hertz and so the thermal effect will only be important at low frequencies. Because of the thermal effect an intensity stabilization of the second harmonic pump beam could be helpful in a squeezer, [51]. Because of a difference in the control electronics (locking to a zero crossing rather than using an offset to adjust the locking point) our squeezer is immune to

the second noise coupling mechanism mentioned in [51]. Another approach to controlling the temperature would be to sense the co-resonance condition using an addition field in the OPO, as was demonstrated in [57]. This scheme would have to be modified for use in a gravitational wave detector to avoid introducing a coherent field at the interferometer frequency, but could be feasible if the sensing beam were offset in frequency by an FSR from the interferometer frequency and injected into the OPO in the counter propagating direction.

5.2.4 Phase noise of incident second harmonic field

Motivated by our control scheme we will only consider phase fluctuations of the second harmonic pump, assuming that frequency fluctuations are small enough to be treated as phase fluctuations. Pump phase fluctuations have long been understood to limit the squeezing produced by an OPO [41, 68, 90] and the quantum noise of the pump laser phase has been considered as an ultimate limit to the squeezing that can be produced by an OPO [21]. The impact of a static phase shift of the circulating field is simply a shift of the squeezing angle:

$$\begin{aligned}\mathbf{M} &= \begin{pmatrix} -1 & xe^{i\theta_b}(1+i\delta\theta_b) \\ xe^{-i\theta_b}(1-i\delta\theta_b) & -1 \end{pmatrix} \\ &= \begin{pmatrix} -1 & xe^{i(\theta_b+\delta\theta_b)} \\ xe^{i(\theta_b+\delta\theta_b)} & -1 \end{pmatrix} + \mathcal{O}[(\delta\theta_b)^2] \end{aligned} \tag{5.25}$$

However, the pump phase noise can be at high frequencies. The phase noise driven by acoustic or seismic noise should be well within the cavity linewidth, but there can also be high frequency phase noise due to quantum noise and the control sidebands used to lock the OPO and SHG lengths. The assumption that the fluctuations will be small compared to the cavity line-width that simplified the calculations in the previous sections cannot be used indiscriminately for phase fluctuations.

With the operators written in terms of constant and fluctuating parts, $b(t) = \bar{b} + \delta b(t)$

the equation of motion for the circulating pump field Equation 5.1 becomes:

$$\dot{\delta b}(t) = -\gamma_g^{tot}(\bar{b} + \delta b(t)) + \sqrt{2\gamma_g^f}(\bar{B}_{f,in} + \delta B_{f,in}(t)) \tag{5.26}$$

The time independent part of this equation can be solved for the static part of the circulating field:

$$\bar{b} = \frac{\sqrt{2\gamma_b^f}}{\gamma_g^{tot}}\bar{B}_{f,in} \tag{5.27}$$

The time dependent part is:

$$\dot{\delta b}(t) = -\gamma_g^{tot}\delta b + \sqrt{2\gamma_g^f}\delta B_{f,in}(t) \tag{5.28}$$

$$\frac{\dot{\delta b}(t)}{\bar{b}} = -\gamma_g^{tot}\frac{\delta b(t)}{\bar{b}} + \gamma_g^{tot}\frac{\delta B_{f,in}(t)}{\bar{B}_{f,in}} \tag{5.29}$$

To first order the real part of the relative fluctuations $\delta b/\bar{b}$ are relative amplitude fluctuations, while the imaginary parts are phase fluctuations. We can separate Equation 5.29 into real and imaginary parts, and label the imaginary parts $\delta\theta_b(t)$ and similarly for the input field:

$$\dot{\delta\phi^b}(t) = -\gamma_g^{tot}\delta\theta_b(t) + \gamma_g^{tot}\delta\theta_B(t) \tag{5.30}$$

Moving into the frequency domain we have:

$$\widetilde{\delta\theta_b} = \frac{1}{1 + s/\gamma_g^{tot}}\widetilde{\delta\theta_B} \tag{5.31}$$

Where s is $i2\pi f$, and f is the frequency of the fluctuation. This transfer function has a pole at the green cavity linewidth, γ_g^{tot}, so high frequency fluctuations of the second harmonic pump are filtered by the resonant cavity. Increasing the green finesse would lower the pole frequency and further reduce the high frequency phase fluctuations. When the OPO is not resonant for the pump field, an additional mode cleaner cavity is sometimes used to reduce the pump phase fluctuations [88]. The justification given for the use of an external mode

cleaner is that it reduces phase noise due to the control sidebands, which are normally at several MHz, often tens of MHz. The evidence cited for the impact of these phase fluctuations on the squeezing is relevant to phase fluctuations at frequencies much smaller than the cavity line-widths [33, 84] and shouldn't be directly applied to the MHz control sidebands.

Gea-Banacloche has calculated the impact of white noise phase fluctuations on squeezing produced in an OPO using the full cavity equations of motion [41]. To find the impact of an arbitrary spectrum of phase fluctuations on the squeezing we would need to solve the equations of motion for the cavity field of an OPO with phase noise included Equation 2.28:

$$\delta\dot{\mathbf{a}}(t) = \gamma_r^{tot}[\bar{\mathbf{M}} + i\delta\theta_b(t)\mathbf{M}_\phi]\delta\mathbf{a}(t) + \sqrt{2\gamma_r^l}\delta\mathbf{A}_{\mathbf{l,in}}(t) + \sqrt{2\gamma_r^f}\delta\mathbf{A}_{\mathbf{f,in}}(t) \tag{5.32}$$

Where:

$$\overline{\mathbf{M}} = \begin{pmatrix} -1 & xe^{i\theta_b} \\ xe^{-i\theta_b} & -1 \end{pmatrix} \qquad \mathbf{M}_\phi = \begin{pmatrix} 0 & xe^{i\theta_b} \\ -xe^{-i\theta_b} & 0 \end{pmatrix} \tag{5.33}$$

In the frequency domain this becomes:

$$i\Omega\delta\widetilde{\mathbf{a}} = \gamma_r^{tot}\overline{\mathbf{M}}\delta\widetilde{\mathbf{a}} + \gamma_r^{tot}\mathbf{M}_\phi\delta\widetilde{\theta}_b * \delta\widetilde{\mathbf{a}} + \sqrt{2\gamma_r^l}\delta\widetilde{\mathbf{A}}_{\mathbf{l,in}} + \sqrt{2\gamma_r^f}\delta\widetilde{\mathbf{A}}_{\mathbf{f,in}} \tag{5.34}$$

where $*$ is the convolution. I won't try to solve this for any spectrum of fluctuations, but we can get a general idea about the impact of high frequency pump phase fluctuations by considering the control sidebands. Assuming that spectrum of phase fluctuations is a delta function at the control sideband frequency s,

$$\delta\widetilde{\mathbf{a}}(\Omega) = (i\Omega\mathbf{I} - \gamma_r^{tot}\mathbf{M})^{-1}\left(\gamma_r^{tot}\mathbf{M}_\phi\widetilde{\theta}_{rms}\delta\mathbf{a}(s) + \sqrt{2\gamma_r^l}\delta\widetilde{\mathbf{A}}_{\mathbf{l,in}} + \sqrt{2\gamma_r^f}\delta\widetilde{\mathbf{A}}_{\mathbf{f,in}}\right) \tag{5.35}$$

where $\widetilde{\theta}_{rms}$ is the RMS fluctuations due to the control sidebands. The noise of the cavity field $\delta\mathbf{a}$ is frequency dependent, at high enough measurement frequencies the noise will just be the same as the noise of a vacuum state, so clearly modulations at frequencies well outside

the cavity line-width will have a reduced impact on the squeezing produced.

5.2.5 Relative phase of local oscillator

The relative phase between the local oscillator and the squeezed field can also cause fluctuations in the squeezing angle. Since this relative phase sets the homodyne angle, fluctuations at all frequencies directly cause squeezing angle fluctuations. There is no frequency dependence to the impact of local oscillator phase fluctuations on the measured squeezing, even phase noise well outside of the measurement bandwidth contribute to the squeezing angle fluctuations.

5.3 Squeezing angle control

Although the squeezer has control loops that suppress cavity length fluctuations and laser frequency noise, the squeezing angle at the readout detector needs to be controlled as well to compensate for changes in path length, crystal temperature fluctuations, and pump phase noise. To control the squeezing angle, we need a sensor that can sense the squeezing angle fluctuations that are not compensated by our other locking loops.

We relied on a coherent locking technique, similar to those described in [44] and [11]. This technique uses a second laser, offset in frequency from the interferometer and pump lasers by Ω_c, as a proxy for the squeezing angle. This laser is then injected into the OPO through a rear coupler, which has a small amount of transmission for 1064 nm, $T_r = 0.15\%$ and decay rate γ_r^r. In earlier parts of this thesis the decay rate of the rear coupler has been included in γ_r^l. Because this field will experience the same nonlinear gain as the squeezed field in the OPO and the same path length fluctuations as the squeezed field as they travel toward the detector we can use it to measure the same disturbances that will cause squeezing angle fluctuations. The coherent control field must be small enough that that parametric

approximation holds, so the green field is un-depleted:

$$\frac{\epsilon c_+^2(t)}{2} \ll \gamma_g^{tot} b(t) \tag{5.36}$$

If this condition is not satisfied the nonlinear interaction could couple noise from the coherent control beam to the field at the fundamental frequency. Once injected into the OPO, the coherent control beam is amplified and deamplified by the nonlinear interaction. A second sideband is generated at the difference frequency between the injected sideband at $\omega + \Omega_c$ and the second harmonic field, which is at the frequency $\omega - \Omega_c$. The relative phase between the injected and generated fields will be the same as the relative phase between the correlated sidebands that create the quadrature squeezing. The relative phase between these sidebands will be affected by fluctuations in the cavity length, crystal temperature, or second harmonic field in the same way as the audio frequency sidebands that create squeezing. These sidebands will propagate out of the OPO, and travel along the same path as the squeezing to the detector acquiring the same phase shift as the squeezed field. At the detector, the phase relationship between these fields and the local oscillator can be used to measure which quadrature is squeezed, as shown in Figure 5-5. If the injected and generated sidebands had the same amplitudes, they would add noise only in the anti-squeezed quadrature.

Two degrees of freedom need to be controlled with this control scheme, first the relative phase of the injected field entering the OPO relative to the phase of the generated field which we will call $\psi = \phi_+ - \phi_-$, where ϕ_+ and ϕ_- are the phases of the upper and , we sensed in reflection off the rear coupler, we will call this degree of freedom the coherent locking field phase. The second degree of freedom is the phase of the injected field relative to the local oscillator. Ideally the phase relative to the local oscillator $\phi = \phi_+ - \phi_{ifo}$ is sensed at the readout detector, which we will call the squeezing angle error signal. A balanced homodyne detector with an external local oscillator can be used to measure this error signal as demonstrated in [11,87] because the homodyne detector common mode rejection suppresses the amplitude noise introduced by the coherent fields. In a gravitational wave detector, the squeezing is detected with unbalanced homodyne detection (Section 2.7.4) which doesn't have

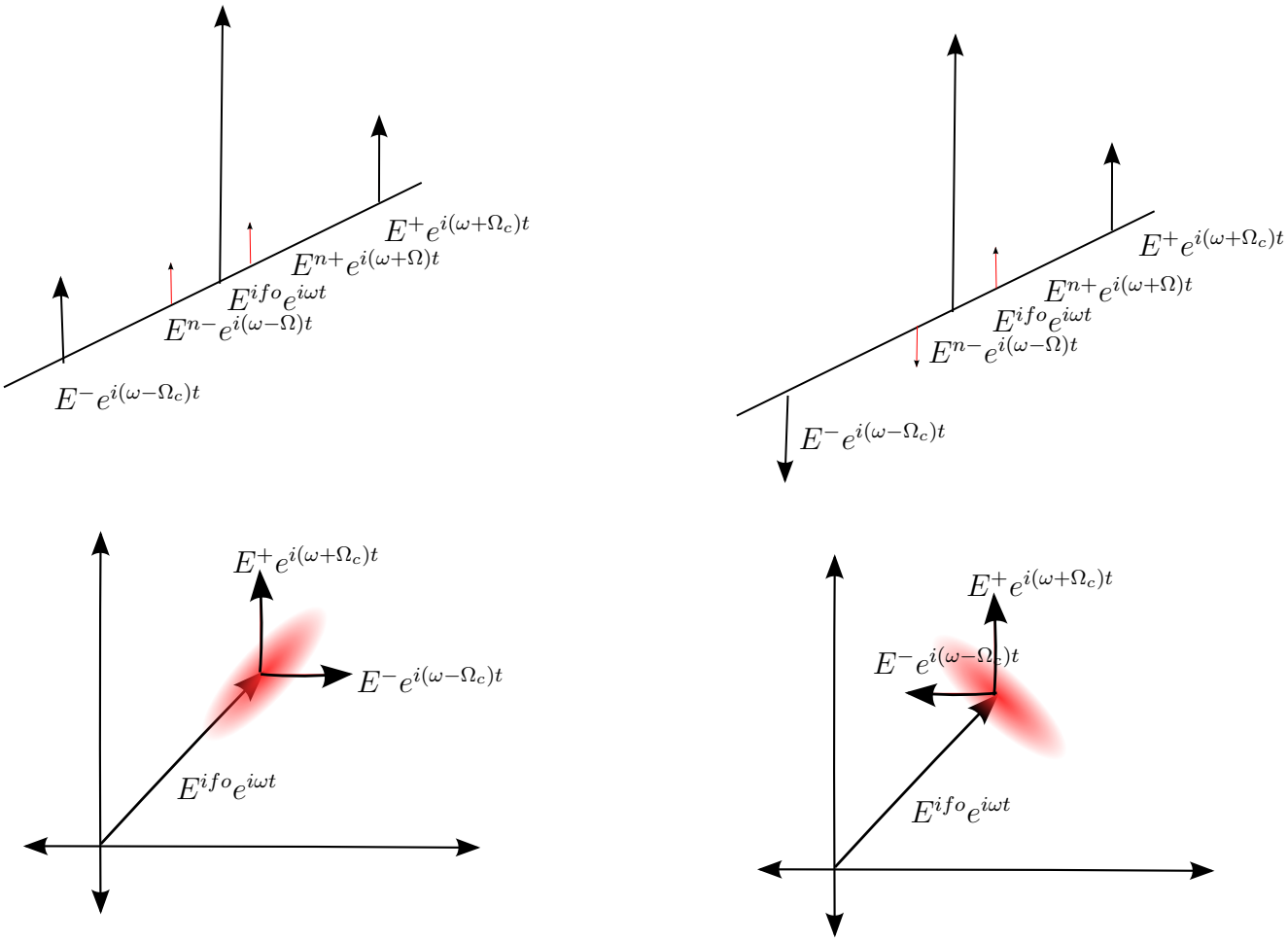

Figure 5-5: Phase relationship between the coherent control sidebands (E^{+} and E^{-}) and the local oscillator(E^{ifo}), is related to the phase relationship between the noise sidebands (E^{n+} and E^{n-}) and the local oscillator. This means that the coherent sidebands can be used to sense the squeezing angle.

the intrinsic amplitude noise rejection of a balanced homodyne. The output mode cleaner removes the control sidebands from the interferometer beam before it reaches the readout detector, removing both the amplitude and phase noise they could add to the readout. This means that the error signal for squeezing angle control is sensed elsewhere; we have used the beam on the anti-symmetric port, although other choices like the reflection off of the output mode cleaner are possible. The output mode cleaner acts as a spatial filter for the anti-symmetric port beam, removing higher order modes and only transmitting the squeezed beam which is well aligned to the interferometer beam. Because we sense the error signal

for the squeezing angle control before the output mode cleaner, the higher order modes will also contribute to our error signal.

5.4 Squeezing angle control with higher-order modes

The squeezing angle control error signal is generated by the beat between the interferometer field and the coherent squeezing angle control fields, both of which can have misalignments. Assuming that at the photo-detector both fields are mostly in the TEM_{00} mode with a small component in the TEM_{ij} higher-order mode we can write the total field at the photo-detector as

$$\begin{aligned} E(x,y,z,t) &= E^{ifo} + E^{+} + E^{-} \\ &= \sum_{ij} \{ (a_{00}^{ifo} u_{00}(x,y,z) + a_{ij}^{ifo} u_{ij}(x,y,z)) e^{i\phi_{ifo}} \\ &+ (a_{00}^{+} u_{00}(x,y,z) + a_{ij}^{+} u_{ij}(x,y,z)) e^{i(\Omega_c t + \phi_+)} \\ &+ (a_{00}^{-} u_{00}(x,y,z) + a_{ij}^{-} u_{ij}(x,y,z)) e^{i(-\Omega_c t + \phi_-)} \} e^{i\omega t} + c.c. \end{aligned} \tag{5.37}$$

Here $u_{ij}(x,y,z)$ is the spatial mode function for the mode, and the phases ϕ_{ifo}, ϕ_+ and ϕ_- are chosen so that a_{00}^{ifo}, a_{00}^{+} and a_{00}^{-} are real. The photocurrent will be

$$I_{PD} \propto \int_{-\infty}^{\infty} |E(x,y,z_{PD},t)|^2 dxdy \tag{5.38}$$

Since the mode functions are orthogonal:

$$\int_{-\infty}^{\infty} u_{ij}(x,y) u_{kl}(x,y) dxdy = \delta_{ik}\delta_{jl} \tag{5.39}$$

Since this photocurrent will be demodulated at Ω_c we can also ignore terms at zero frequency and terms at $2\Omega_c$. We could also demodulate this signal at $2\Omega_c$ to obtain an error signal for the coherent locking field control loop, instead of using the beam reflected off of the rear

coupler. Terms that remain at Ω_c are

$$\begin{aligned} I_{PD} \quad \propto \quad & \Big[a_{00}^{ifo} a_{00}^{+*} e^{i(\phi_{ifo} - \phi_+)} + a_{00}^{ifo*} a_{00}^{-} e^{i(\phi_- - \phi_{ifo})} \\ & + a_{ij}^{ifo} a_{ij}^{+*} e^{i(\phi_{ifo} - \phi_+)} + a_{ij}^{ifo*} a_{ij}^{-} e^{i(\phi_- - \phi_{ifo})}\Big] e^{-i\Omega_c t} + c.c. \end{aligned} \tag{5.40}$$

We can assume that the higher-order modes are small compared to TEM_{00} modes, and write

$$\gamma_{ij}^{ifo} = \left|\frac{a_{ij}^{ifo}}{a_{00}^{ifo}}\right| \qquad\qquad \gamma_{ij}^{clf} = \left|\frac{a_{ij}^{+}}{a_{00}^{+}}\right| = \left|\frac{a_{ij}^{-}}{a_{00}^{-}}\right|$$

Because of the Gouy phase shift there is a difference between the phase of the higher order modes and the 00 modes:

$$a_{ij}^{ifo} = \gamma_{ij}^{ifo} a_{00}^{ifo} e^{i\phi_{ij}^{ifo}} \qquad\qquad a_{ij}^{clf} = \gamma_{ij}^{clf} a_{00}^{clf} e^{i\phi_{ij}^{clf}} \tag{5.41}$$

A common misalignment will cause the same Gouy phase shift in the two beams, but there may also be relative misalignments that cause a relative phase shift:

$$\phi_{ij} = \phi_{ij}^{ifo} - \phi_{ij}^{clf} \tag{5.42}$$

The ratio of the amplitudes of the two squeezing angle control sidebands is the same in all spatial modes:

$$\alpha = \left|\frac{a_{00}^{-}}{a_{00}^{+}}\right| = \left|\frac{a_{ij}^{-}}{a_{ij}^{+}}\right| \tag{5.43}$$

Now the photocurrent can be written

$$\begin{aligned} I_{PD} \propto & \cos(\phi_{ifo} - \phi_+ - \Omega_c t) + \alpha \cos(\phi_- - \phi_{ifo} - \Omega_c t) \\ & + \Sigma_{ij} \gamma_{ij}^{ifo} \gamma_{ij}^{clf} \left[\cos(\phi_{ifo} - \phi_+ - \Omega_c t + \phi_{ij}) + \alpha \cos(\phi_- - \phi_{ifo} - \Omega_c t - \phi_{ij})\right] \end{aligned} \tag{5.44}$$

The coherent field locking loop controls the phase between these two fields, $\psi \equiv \phi_+ - \phi_-$. We will also write $\phi \equiv \phi_+ - \phi_{ifo}$. The photo-current can now be written

$$\begin{aligned} I_{PD} \propto & \left[\cos\left(-\phi - \Omega_c t\right) + \alpha \cos\left(\phi - \psi - \Omega_c t\right)\right. \\ & \left. + \Sigma_{ij} \gamma_{ij}^{ifo} \gamma_{ij}^{clf} \left(\cos\left(-\phi + \phi_{ij} - \Omega_c t\right) - \alpha \cos\left(-\Omega_c t + \phi - \psi - \phi_{ij}\right)\right)\right] \end{aligned} \tag{5.45}$$

This photocurrent is demodulated by signals $\cos\left(\Omega_c t - \theta_{dm}\right)$(for the I phase) and $\sin\left(\Omega_c t - \theta_{dm}\right)$ (for the Q phase), and low passed to get rid of the 2ω terms.

$$\begin{aligned} I_{err} \quad \propto \quad & \cos\left(-\phi + \theta_{dm}\right) + \alpha \cos\left(\phi - \psi + \theta_{dm}\right) \\ & + \Sigma_{ij} \gamma_{ij}^{ifo} \gamma_{ij}^{clf} \left[\cos\left(-\phi + \phi_{ij} + \theta_{dm}\right) + \alpha \cos\left(\phi - \psi - \phi_{ij} + \theta_{dm}\right)\right] \end{aligned} \tag{5.46}$$

$$\begin{aligned} Q_{err} \quad \propto \quad & \sin\left(-\phi + \theta_{dm}\right) + \alpha \sin\left(\phi - \psi + \theta_{dm}\right) \\ & + \Sigma_{ij} \gamma_{ij}^{ifo} \gamma_{ij}^{clf} \left[\sin\left(-\phi + \phi_{ij} + \theta_{dm}\right) + \alpha \sin\left(\phi - \psi - \phi_{ij} + \theta_{dm}\right)\right] \end{aligned} \tag{5.47}$$

5.4.1 Error signals without higher order modes

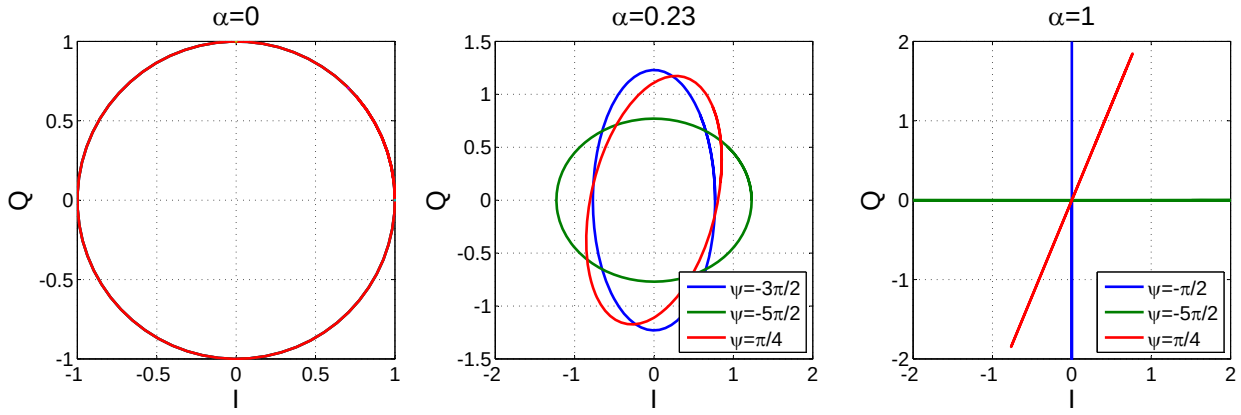

Figure 5-6: Error signals with I and Q demodulation phases without higher order modes as the phase ϕ rotates and ψ is held constant.

The misalignment terms will be small compared to the error signal due to the u_{00} modes, so we can calculate them as small perturbations around the error signals without higher

order modes. Without any misalignments the demodulated signals are simply

$$I_{err} \propto \cos\left(-\phi + \theta_{dm}\right) + \alpha \cos\left(\phi - \psi + \theta_{dm}\right) \tag{5.48}$$

$$Q_{err} \propto \sin\left(-\phi + \theta_{dm}\right) + \alpha \sin\left(\phi - \psi + \theta_{dm}\right) \tag{5.49}$$

If there were no nonlinear gain in the OPO there would be no generated sideband, the error signal would simply be a beat note, and would map out a circle in I and Q as ϕ changes. In the other extreme, if the two sidebands have equal amplitudes ($\alpha = 1$) the error signal becomes a line in the I-Q plane similar to a Pound-Drever-Hall error signal which could be zeroed in either quadrature by adjusting the demodulation phase. Our error signal is an intermediate case where $\alpha \approx 0.23$ [75]. This means that the error signals trace out an ellipse in the plane of I and Q as ϕ changes, and the orientation of the ellipse is determined by θ_{dm} and ψ. If the I quadrature is used for locking, then when the squeezing angle control loop is locked $I_{err} = 0$. To observe amplitude squeezing at the detectors ψ and ϕ need to be tuned correctly.

From Figure fig:CohControlSidebands the squeezing angle in terms of the phases of the control sidebands and local oscillator is:

$$\theta_{sqz} \;\; = \frac{\phi_+ - \phi_{ifo} - (\phi_{ifo} - \phi_-)}{2} = \phi - \frac{\psi}{2} \tag{5.50}$$

The squeezing angle is $\frac{\pi}{2}$ for amplitude squeezing and 0 for phase squeezing, which gives us the relations $\phi = \frac{\psi+\pi}{2}$ for squeezing measured at the readout detector and $\phi = \frac{\psi}{2}$ for anti squeezing measured at the readout detectors. If we substitute our relations for ψ into the expressions for I_{err} and Q_{err} we find

Squeezing	Antisqueezing
$\theta_{sqz} = \frac{\pi}{2}$	$\theta_{sqz} = 0$
$\phi = \frac{\psi+\pi}{2}$	$\phi = \frac{\psi}{2}$
$I_{err} \propto (1-\alpha)\cos(\phi - \theta_{dm})$	$I \propto (1+\alpha)\cos(\phi - \theta_{dm})$
$Q_{err} \propto (1-\alpha)\sin(\theta_{dm} - \phi)$	$Q \propto (1+\alpha)\sin(\theta_{dm} - \phi)$
Squeezing angle locked using I_{err}	
$I = 0$	$I = 0$
$\phi = \pi/2 + \theta_{dm}$	$\phi = \pi/2 + \theta_{dm}$
$\psi = 2\theta_{dm}$	$\psi = 2\theta_{dm} + \pi$
$Q = -(1-\alpha)$	$Q = -(1+\alpha)$

The second panel of Figure 5-6 shows a plot of the error signals with ϕ rotating for a value of α similar to the one produced by our squeezed light source. When the ellipse is aligned with the semi major axis along the axis of the locking quadrature, the demodulation phases should be set for squeezing. This means that we could hope to tune our squeezing angle by minimizing the signal in the unlocked quadrature. However, misalignment of the squeezing beam relative to the interferometer beam can complicate this picture.

5.4.2 Effect of a misalignment on locking point

The coherent locking field control loop will keep ψ constant, and is not affected by relative misalignments, but misalignments will cause a change in the locking point of the local oscillator loop, $\Delta\phi$. If the demodulation phase is optimized without any misalignments, ($\psi = 2\theta_{dm}$), the demodulated signals including the effects of misalignment are:

$$\begin{aligned} I &\propto (1+\alpha)\left[\cos(\phi - \theta_{dm}) + \Sigma_{ij}\gamma_{ij}^{ifo}\gamma_{ij}^{clf}\cos(\phi - \theta_{dm} - \phi_{ij})\right] \\ Q &\propto (1-\alpha)\left[\sin(\theta_{dm} - \phi) + \Sigma_{ij}\gamma_{ij}^{ifo}\gamma_{ij}^{clf}\sin(\theta_{dm} - \phi + \phi_{ij})\right] \end{aligned} \tag{5.51}$$

We can assume that $\gamma_{ij}^{ifo}\gamma_{ij}^{clf} \ll 1$ and so when we lock and $I_{err} = 0$, then $\phi \approx \pi/2 + \theta_{dm} + \Delta\phi$ where $\Delta\phi$ is a small angle.

$$\begin{aligned} I &\propto -(1+\alpha)\left[\sin\Delta\phi + \Sigma_{ij}\gamma_{ij}^{ifo}\gamma_{ij}^{clf}\sin\left(\Delta\phi - \phi_{ij}\right)\right] \\ &\propto -(1+\alpha)\left[\sin\Delta\phi + \Sigma_{ij}\gamma_{ij}^{ifo}\gamma_{ij}^{clf}\left(\sin\Delta\phi\cos\phi_{ij} - \cos\Delta\phi\sin\phi_{ij}\right)\right] \end{aligned} \tag{5.52}$$

Now we can use the locking condition $I = 0$ and the small angle approximation to first order in $\Delta\phi$ to find an equation for the locking point error:

$$\begin{aligned} \Delta\phi &= \frac{\sum_{ij}\gamma_{ij}^{ifo}\gamma_{ij}^{clf}\sin\phi_{ij}}{(1+\sum_{ij}\gamma_{ij}^{ifo}\gamma_{ij}^{clf}\cos\phi_{ij}}) \\ &\approx \sum_{ij}\gamma_{ij}^{ifo}\gamma_{ij}^{clf}\sin\phi_{ij} \end{aligned} \tag{5.53}$$

This will lead to a change in the squeezing angle equal to the lock point error $\Delta\phi$ unless one of the other phases is adjusted to compensate for it.

5.4.3 Squeezing angle fluctuations due to beam jitter lock point errors

If there were no alignment jitter but only static misalignments, the locking point for the squeeze angle would no longer be the point that minimizes the signal in the unlocked quadrature, but the maximum level of squeezing could be measured if the demodulation phase was tuned to compensate for the misalignment (ignoring losses). If there were no static misalignments but only beam jitter the phase noise added by fluctuations of the locking point will reduce the amount of squeezing observed, but this is a second order effect. If one of the beams has a static misalignment, the effect will become first order, for example:

$$\begin{aligned} \Delta\theta_{sqz}(t) &= (\sin(\bar{\phi}_{ij} + \delta\phi_{ij}(t))\delta\gamma_{ij}^{ifo}(t)(\bar{\gamma}_{ij}^{clf} + \delta\gamma_{ij}^{clf}(t)) \\ &\approx \bar{\gamma}_{ij}^{clf}\delta\gamma_{ij}^{ifo}(1+\bar{\phi}_{ij})\delta\phi_{ij}(t) \end{aligned} \tag{5.54}$$

Static misalignment of one beam will increase the phase noise added by the fluctuations of the other beam. If all of the jitter were due to motion of one optic, which should have a fixed Gouy phase, the phases ϕ_{ij} would be static, but it is likely that there are multiple optics at different Gouy phases that contribute to the beam jitter. Since we do not know which optics cause the jitter, we do not know what these phases are, and how large their fluctuations are.

5.4.4 Evidence for alignment coupling to squeezing angle

We discovered this alignment coupling to the squeezing angle using the technique described in Section 4.5. Limits on the total phase noise can be obtained using single measurements at high gain of both the maximum and minimum quantum noise obtained. The anti-squeezing value can be used to find a value for total efficiency while the minimum quantum noise measured can be used to understand the phase noise. We saw that the locking point for the squeezing angle loop that minimized the quantum noise changed when interferometer alignment changed, and that the total phase noise also varied with alignment.

We also made an intentional misalignment of one of the mirrors in the squeezing injection path, and saw that we needed to adjust the locking point after the alignment change to minimize noise.

5.4.5 Independent measurement of spectrum of squeezing angle fluctuations

One can also make a measurement of the total spectrum of the squeezing angle fluctuations. This is possible by band-passing the interferometer spectrum at frequencies where the technical noise is small, and measuring the RMS noise power in that band. This gives a time series of the quantum noise variance. By tuning the squeezing angle so that the variance has a linear dependence on the squeezing angle, we can make a measurement of the squeezing

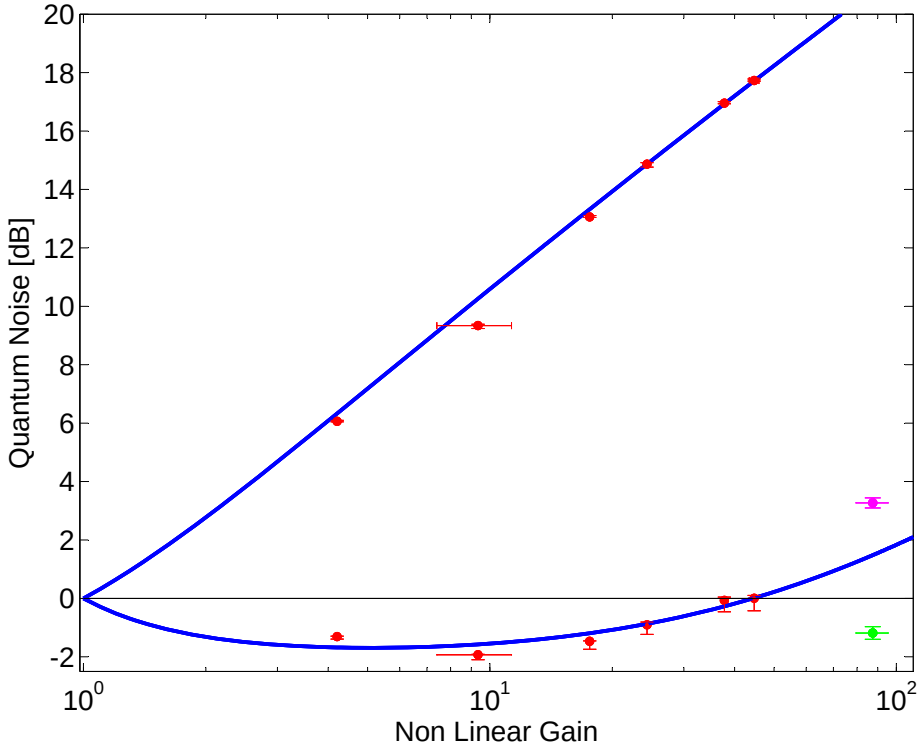

Figure 5-7: Changes in interferometer alignment change total squeezing angle phase noise. The red points and blue fit are the same data as shown in Figure 4-7, the green and magenta points were measured at a different time. After measuring the phase noise of 109 ± 9 mrad represented by the magenta point assuming that the total efficiency was $42\% \pm 7\%$, the interferometer alignment was adjusted slightly. The change in interferometer alignment meant that the error point for the squeezing angle control loop (demodulation phase) had to be adjusted to find the minimum quantum noise, represented by the green point with 37 ± 6 mrad of phase noise.

angle fluctuations. The derivatives of the variance are:

$$\frac{dV}{d\theta_{sqz}} = (V_+ - V_-)\sin 2\theta_{sqz} \tag{5.55}$$

$$\frac{d^2V}{d\theta_{sqz}^2} = 2(V_+ - V_-)cos2\theta_{sqz} \tag{5.56}$$

The variance should be linear in the squeezing angle around $\theta = \frac{\pi}{4}$, where the slope is:

$$\frac{dV}{d\theta} = (V_+ - V_-) = 8\eta_{tot}x\frac{1+x^2}{(1-x^2)^2} \tag{5.57}$$

This slope increases as x approaches 1, so this measurement will have the best signal to noise ratio at high nonlinear gains. By taking a spectrum of the variance time series and calibrating it in terms of squeezing angle fluctuations, we can directly measure a spectrum of squeezing angle fluctuations. This method provides an out of loop sensor for the squeezing angle fluctuations, which can be compared to the spectrum of squeezing angle fluctuations measured by the squeezing angle sensor.

As shown in Figure 5-8 the squeezing angle fluctuations measured in this way are larger than the fluctuations measured by the coherent locking squeezing angle sensor. An in loop sensor can measure noise lower than the actual noise if the control loop is imposing the sensor's noise on the degree of freedom being controlled. As shown in Figure 5-8 the sensor noise of the coherent locking squeezing angle sensor is below the error signal at these frequencies, so sensor noise is not causing the discrepancy between the in loop and out of loop sensors. This means that the sensor we are using to lock is not accurately measuring the squeezing angle, due to locking point errors. The out of loop sensor in Figure 5-8 shows an RMS squeezing angle fluctuation below 9 Hz of 39 mrad, while the in loop sensor has 1.6 mrad. These low frequency locking point errors are an important, and possibly dominant, source of squeezing angle noise in our experiment. The interferometer alignment jitter is mostly in the range 10-1 Hz [77], so the alignment jitter coupling to squeezing angle is a plausible explanation for these locking point errors.

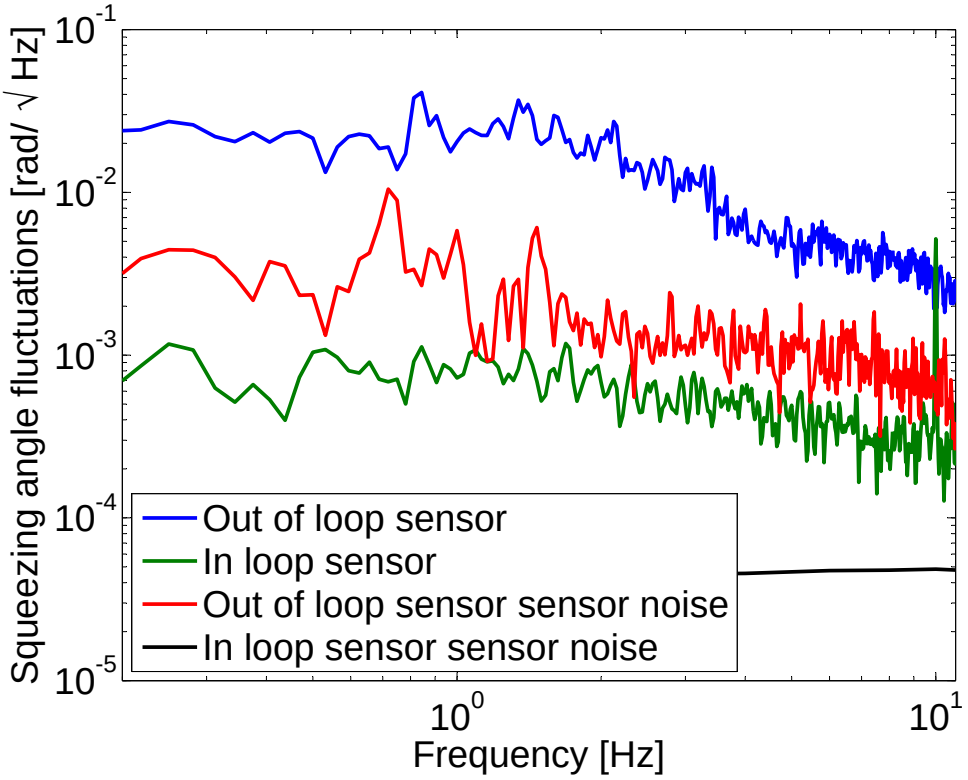

Figure 5-8: Spectrum of squeezing angle fluctuations. The blue trace is a spectrum of the variance of the interferometer spectrum in a frequency bin that is quantum noise limited, calibrated in units of squeezing angle fluctuations. This is an out of loop sensor for the squeezing angle fluctuations, the sensor noise for this out of loop sensor was measured when no squeezing was injected into the interferometer. The in loop sensor is derived from the squeezing angle control sidebands, and is not sensor noise limited as shown by the black trace. This means that the error signal derived from the squeezing angle control sidebands is not a completely accurate measurement of the squeezing angle fluctuations.

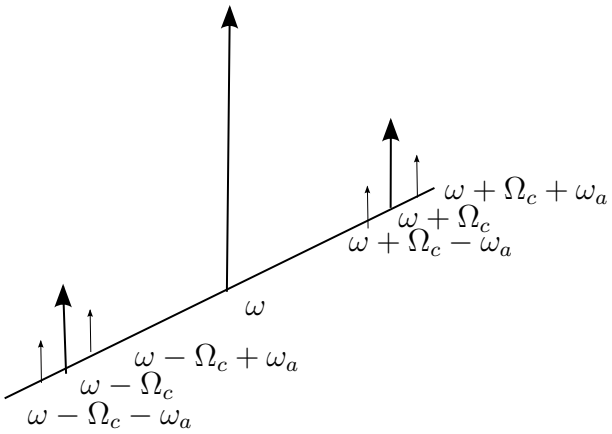

Figure 5-9: Audio frequency sidebands on squeezing angle control sidebands due to audio frequency squeezing angle fluctuations

5.5 Squeezing angle control with Fabry Perot Arms

The interferometer's Fabry-Perot arms limit the bandwidth coherent squeezing angle control. The 4 km arm cavities have a free spectral range of 37 kHz, and are resonant for the interferometer carrier frequency, so they will also be resonant for light that is offset in frequency from the carrier by an integer multiple of 37 kHz. The offset frequency for the squeezing angle control sidebands should be chosen so that they are anti-resonant and reflect off the arms. Fluctuations of the squeezing angle will put sidebands at the audio frequency of the fluctuations, ω_a onto the coherent control sidebands, illustrated in Figure 5-9. These audio frequency sidebands can become resonant in the arm cavities, which causes a phase shift relative to the coherent sideband at Ω_c. This means that the arm cavity resonances add resonances to the squeezing angle sensor, which can cause instabilities in the control loop. Figure 5-10 shows the resonances added to the squeezing angle sensor by the arm cavity resonances. By shifting the offset frequency Ω_c, we can shift the location of the resonances by the same amount. With no filtering these resonances limit the squeezing angle control bandwidth to 10 kHz, with a notch filter this can be improved slightly. However there will be a series of these resonances in the response function every 37kHz, meaning that coherent squeezing angle control will never have a high bandwidth in a km scale interferometer with Fabry-Perot arms.

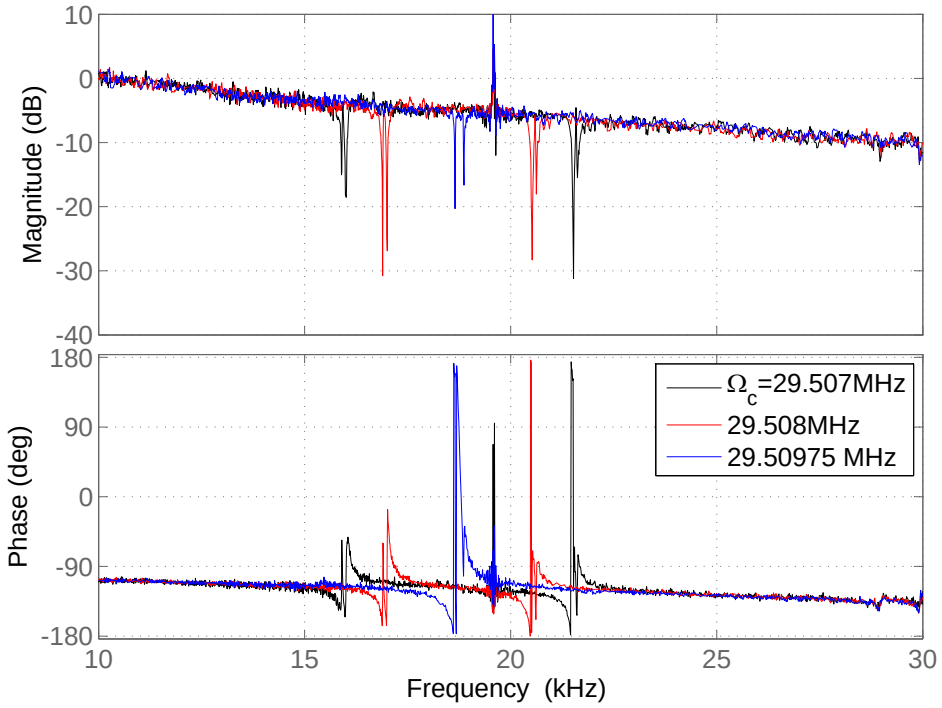

Figure 5-10: Arm cavity resonances appear in response function of coherent squeezing angle control sensor. The sum of the frequencies of the pair of resonances is the free spectral range of the arm cavities.

5.6 Squeezing angle fluctuations due to interferometer control sidebands

Phase fluctuations of the local oscillator beam which are outside the bandwidth of the squeezing angle control will directly add squeezing angle fluctuations. Radio frequency sidebands on the interferometer are used to sense and control the interferometer length and alignment, these can add phase noise to the interferometer beam at the readout photo-detectors, which is the local oscillator for squeezing detection. While these control sidebands should be mostly amplitude modulation sidebands at the anti-symmetric port, there is a small amount of phase modulation due to the interferometer contrast defect and due to an imbalance between the two sidebands.

5.6.1 Contrast Defect

A small mismatch in the reflectivity of the two arms means that there is a small amount of light, called the contrast defect light, at the interferometer carrier frequency at the dark port independent of the interferometer offset. The contrast defect field is (for the most part) 90 degrees out of phase with the interferometer leakage field due to the offset. This means that the amplitude sidebands on the carrier light are phase modulation sidebands on the contrast defect light; a not to scale illustration is shown in Figure 5-11. The phase noise on the contrast defect in turn adds phase noise to the total field. From the left side of Figure 5-11 we see that the contrast defect shifts the phase of the entire carrier field by $\theta_1 \approx A_{cd}/A_{leak}$ where A_{cd} is the amplitude of the contrast defect light and A_{leak} is the amplitude of the field due to the DC offset. If x is the component of the control sidebands that adds phase noise to the total carrier field, $\theta_1 \approx x/A_{SB}$. The maximum phase excursion is

$$\delta\theta_1 \approx x/A_{carr} = \frac{A_{SB}A_{cd}}{A_{carr}^2} \tag{5.58}$$

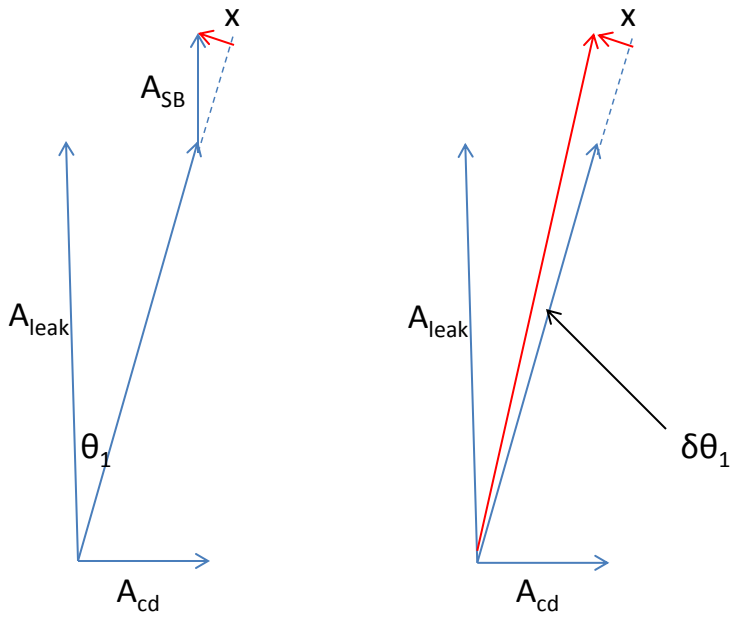

Figure 5-11: Illustration of RF sidebands and contrast defect adding phase noise to the carrier, not to scale. A_{cd} is the amplitude of the contrast defect light, A_{leak} is the amplitude of the light due to the interferometer DC offset which is the local oscillator for the self-homodyne used to detect gravitational waves, A_{SB} is the amplitude of both the sidebands transmitted through the OMC.

The powers in each sideband P_{SB} are measured before the OMC, which has a power transmission of

$$T_{SB} = \left| \frac{t_{in} t_{out}}{1 - \rho r_{in} r_{out} e^{i\left(\frac{2\pi f_{SB}}{f_{FSR}}\right)}} \right|^2 = 2.35 \times 10^{-4} \tag{5.59}$$

for the sidebands, where $t_{in,out}$ and $r_{in,out}$ are the amplitude transmittance and reflectance of the OMC input and output couplers respectively, f_{FSR} is the free sprectal range, f_{SB} is the sideband frequency (24.5 MHz) and ρ is the intra-cavity loss. The rms phase noise added is

$$\widetilde{\theta}_{CD} = \sqrt{\frac{2 T_{SB} P_{SB} P_{CD}}{P_{carr}^2}} \tag{5.60}$$

This gives 3.0 ± 0.2 mrad of phase noise due to the contrast defect rotating the control sidebands into the phase quadrature.

5.6.2 Sideband Imbalance

If the amplitudes of the two amplitude modulation sidebands are not exactly the same they will add some phase modulation to the field. The maximum phase excursion is:

$$\theta_I = \frac{A_2 - A_1}{A_{leak}} \tag{5.61}$$

where now we are ignoring the contrast defect field, and $A_{1,2}$ are the amplitude in the two sidebands. The RMS phase noise due to sideband imbalance is:

$$\begin{aligned} \widetilde{\theta}_I &= \frac{(\sqrt{P_2} - \sqrt{P_1})\sqrt{T_{SB}}}{\sqrt{8P_{CR}}} \\ &\approx \sqrt{\frac{T_{SB} dP_{SB}^2}{8 P_{leak} \overline{P}}} \end{aligned} \tag{5.62}$$

where $P_{2,1}$ are the powers in the 2 sidebands, $dP = P_2 - P_1$ and $\bar{P} = (P_2 + P_1)/2$. This gives 0.96 ± 0.3 mrad RMS phase noise due to sideband imbalance. The phase noise due to sideband imbalance and that due to contrast defect add in quadrature to give a total of 2.8 mrad phase noise from the interferometer control sidebands, an insignificant contribution to our total phase noise.

5.7 Conclusion

Phase noise will not be an important limit to the level of squeezing achieved in a gravtiational wave interferometer until the losses are reduced significantly, and frequency dependent squeezing is available (see Section 7.4). However, the squeezing angle fluctuations can be studied, using the error signals, measurements of the total squeezing angle fluctuations made at high gain, and spectra of the fluctuations made by measuring fluctuations in the noise

power at a squeezing angle near $\pi/4$. This will allow us to find solutions now to reduce the most important sources of squeezing angle fluctuations, so that squeezing angle fluctuations do not become an obstacle to achieving a high level of squeezing once the interferometer losses are low enough.

Chapter 6

Technical noise added to interferometer by squeezing

6.1 Introduction

One concern in planning to implement squeezing on a full scale gravitational wave detector is the possibility that the squeezer could add noise and degrade the interferometer sensitivity at some frequencies, either due to increased radiation pressure noise, or technical noise that the squeezer introduces. While squeezing at GEO600 and the 40 meter interferometer at Caltech have demonstrated squeezing at frequencies above 900 Hz and 4 kHz respectively, both of these interferometers have orders of magnitude less sensitivity than Enhanced LIGO at the crucial region around 100 Hz [15, 43]. Past experience has shown that techniques that work well on interferometers at higher frequencies, such as an out of vacuum output mode cleaner, can add unacceptable levels of environmental coupling to a full-scale LIGO interferometer [50]. Testing a squeezer on an Enhanced LIGO interferometer gave us the opportunity to demonstrate that squeezing is compatible with good low frequency sensitivity, and to measure the environmental couplings in a regime that is as close as possible to the Advanced LIGO sensitivity.

The results shown in Section 3.3 show that in the final configuration squeezing did not

add noise at any frequencies in the Enhanced LIGO spectrum. This is the most convincing argument we have that squeezing is compatible with an interferometer with good low frequency sensitivity. However, Advanced LIGO will be about a factor of ten more sensitive once it reaches design sensitivity, so we have characterized three main sources of technical noise added by the squeezer. Our measurements and estimates show that an out of vacuum squeezer should not add technical noise to an Advanced LIGO interferometer.

6.2 Noise coupling mechanisms

The noise coupling mechanism of most concern for Advanced LIGO is backscatter, where light scattered out of the interferometer reflects off of the squeezer and is scattered back into the interferometer creating a spurious interferometer. Fields at the interferometer carrier frequency that originate from the squeezer and resonate in the OPO, which we call seeding, can also enter the interferometer and add noise. Lastly any amplitude noise on the small amount of coherent locking field that passes through the output mode cleaner could potentially add noise to the detector.

6.2.1 Backscatter

Due to imperfections in the Faraday isolator, a small amount of light from the anti-symmetric port of the interferometer is sent towards the squeezing table. A second Faraday isolator was installed in the squeezing path to isolate the squeezer from this light, but a small amount of light is transmitted through the Faraday towards the squeezer. The OPO is in a traveling wave configuration, as discussed in 3.2.8, so the direct reflection of the scattered light will not return to the interferometer [12]. However, imperfections in optics in the squeezing injection path, and especially inside the OPO, can cause a small amount of light to be scattered back towards the interferometer, where it interferes with the signal field and adds noise. The two fields at the photo-detectors are $E_{sig}e^{i\phi_{sig}}$ and $E_{sc}e^{i(\phi_{sig}+\phi_{sc})}$, where ϕ_{sc} is the phase due to

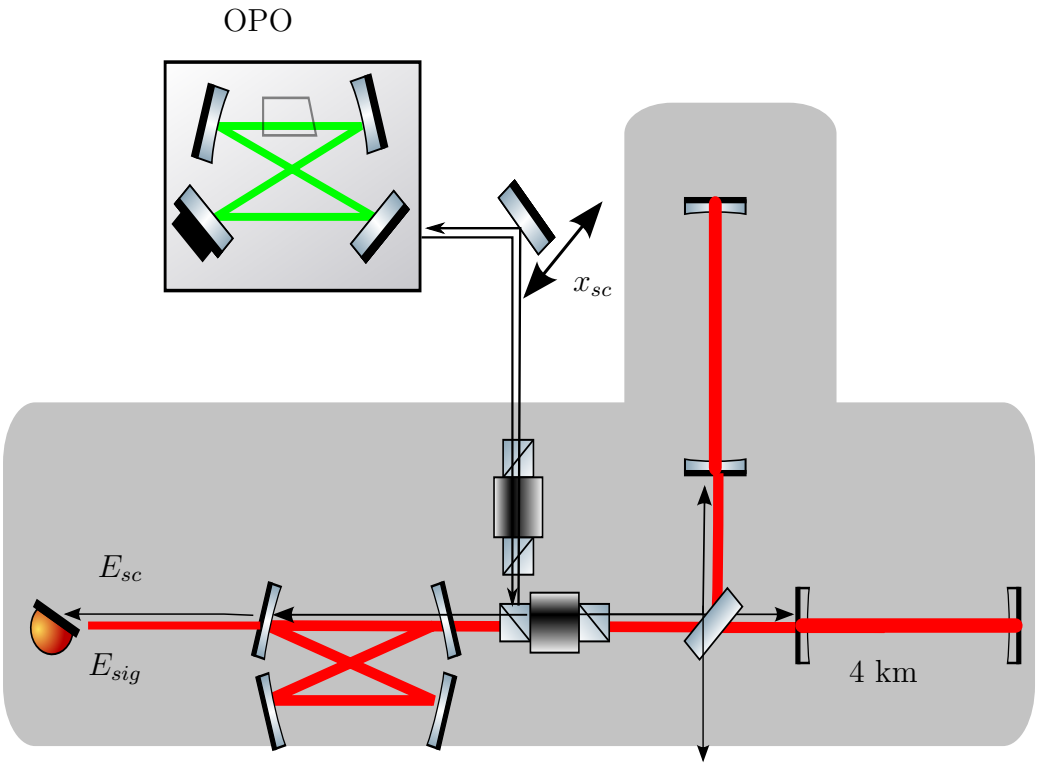

Figure 6-1: Squeezing injected into Enhanced LIGO interferometer. Black arrows represent scattered light, E_{sc} and E_{sig} are the amplitudes of the fields due to scattering and the signal field at the gravitational wave readout photo-detector. Path length changes in the scattering path (x_{sc}) will add noise to the interferometer's signal.

the scattering path. The intensity at the photo-detector (for E_{sc}, E_{sig} both real) is given by

$$\begin{aligned} I_{PD} &= \frac{c}{4\pi}|E_{sig}e^{i\phi_{sig}} + E_{sc}e^{i\phi_{sc}}|^2 \\ &\approx \frac{c}{4\pi}\left(|E_{sig}|^2 + 2E_{sig}E_{sc}\cos\phi_{sc}\right) \end{aligned} \tag{6.1}$$

dropping higher order terms in E_{sc} because $E_{sc} \ll E_{sig}$. Integrating over the photo-detector area the relative intensity noise due to scattering is:

$$RIN_{sc}(t) = 2\sqrt{\frac{P_{sc}}{P_{sig}}}\cos\phi_{sc}(t)$$

Fluctuations in the phase of the scattered light ϕ_{sc} are either due to path length changes as the squeezer table and optics move relative to the suspended interferometer $\phi_{sc}(t) = 4\pi\frac{x_{sc}(t)}{\lambda}$, or due to changes in the length of the OPO. The ground motion can have amplitudes larger than a wavelength at low frequencies, so path length changes cause a large slowly varying term $\underline{\phi}_{sc} = 2k\underline{x}_{sc}(t)$ [65]. At higher frequencies, in the gravitational wave detection band, the phase fluctuations are small, and we can use the small angle approximation:

$$\begin{aligned} RIN_{sc}(t) &= 2\sqrt{\frac{P_{sc}}{P_{sig}}}\cos\left(2k\underline{x}_{sc}(t) + \delta\phi_{sc}(t)\right) \\ &= 2\sqrt{\frac{P_{sc}}{P_{sig}}}\left(\cos 2k\underline{x}_{sc}(t)\cos\delta\phi_{sc}(t) - \sin 2k\underline{x}_{sc}(t)\sin\delta\phi_{sc}(t)\right) \\ &\simeq 2\sqrt{\frac{P_{sc}}{P_{sig}}}\left(\cos 2k\underline{x}_{sc}(t) - \delta\phi_{sc}(t)\sin 2k\underline{x}_{sc}(t)\right) \end{aligned} \tag{6.2}$$

A worst case expression for the noise fluctuating with $\delta\phi_{sc}(f)$ comes from setting $\sin 2k\underline{x}_{sc}(t) = 1$, in the frequency domain this gives:

$$RIN_{sc}(f) = 2\sqrt{\frac{P_{sc}}{P_{sig}}}\delta\phi_{sc}(f) \tag{6.3}$$

We could also use an average over many cycles of $\tilde{x}(t)$ to get an amplitude spectral density:

$$RIN_{sc}(f) = \sqrt{\frac{2P_{sc}}{P_{sig}}}\delta\phi_{sc}(f) \tag{6.4}$$

When the motion is not small compared to the wavelength, the coupling becomes nonlinear and up-conversion of low frequency motion can cause noise in the gravitational wave band.

When the amplitude of the motion is larger than one wavelength, $\underline{x}_{sc}(t) = \Gamma\cos\omega_l t$ the coupling is nonlinear, and causes fringe wrapping:

$$RIN_{sc}(t) = 2\sqrt{\frac{P_{sc}}{P_{sig}}}\cos\left(\frac{4\pi}{\lambda}\Gamma\cos\omega_l t\right) \tag{6.5}$$

6.2.2 Seeding of the OPO

In addition to light scattered out of the interferometer any other light at the interferometer carrier frequency that originates from the squeezer will add technical noise to the gravitational wave readout. The main laser on the squeezer table is tuned to the interferometer frequency, and care must be taken in constructing a squeezer to avoid scattering this light into the OPO or towards the interferometer. For this reason the squeezer was built using as many super-polished optics as possible, in a clean-room to avoid contamination from dust, and multiple dichroic beam splitters were used to remove the field at the fundamental frequency from the second harmonic pump. Any light that does enter the OPO will be on resonance in the cavity, and will either be parametrically amplified or de-amplified depending on its phase. Similar to backscattering the relative intensity noise due to seeding is given by:

$$RIN_{sd}(t) = 2\sqrt{\frac{P_{sd}}{P_{sig}}}\cos\phi_{sd}(t)$$

where P_{sd} is the power due to unwanted light and $\phi_{sd}(t)$ is the phase difference of this light from the interferometer signal. The seeding could have multiple paths so the total phase might be complicated, but it will propagate through the OPO and through the squeezing injection path. Backscattered light double passes the squeezing injection path, while seeding of the OPO single passes that path, so some motion is common to both kinds of spurious interferometers.

6.2.3 Backscatter and seeding from a nonlinear cavity

The backscatter and seed fields both resonate in the OPO, and will experience parametric amplification and de-amplification. In units of $\sqrt{photons/second}$, the amplitude of the seed

traveling wave field leaving the OPO, $\bar{A}_{sd,out}$ is given by [44, p 86]:

$$\bar{A}_{sd,out}(\theta) = \frac{1 + xe^{i\theta_{sd}}}{1 - x^2} \frac{2\sqrt{\gamma_r^f \gamma_r^{sd}}}{\gamma_r^{tot}} \bar{A}_{sd,inc} \tag{6.6}$$

$$P_{sd,out}(\theta) = \frac{1 + 2x\cos\theta_{sd} + x^2}{(1 - x^2)^2} \frac{4\gamma_r^f \gamma_r^{sd}}{(\gamma_r^{tot})^2} P_{sd,inc} \tag{6.7}$$

where θ_{sd} is the phase between the seed field and the pump field, $P_{sd,inc}$ is the power in the cavity mode incident on the OPO from the noise field and $\gamma_{sd,in}$ is the decay rate of the coupler through which seeding enters the cavity. The relative phase between the seed light and the pump in the OPO depends on the path through which the seeding couples into the OPO, and is not controlled. Assuming that over long enough times the phase will drift over multiple fringes we can average over θ_{sd} to approximate the noise field exiting the cavity:

$$P_{out} = \frac{1 + x^2}{(1 - x^2)^2} \frac{4\gamma_r^{out} \gamma_r^{sd}}{(\gamma_r^{tot})^2} P_{in} \tag{6.8}$$

A more realistic assumption may be that the relative phase has a Gaussian distribution with a mean $\bar{\theta}_{sd}$ and standard deviation $\tilde{\theta}_{sd}$, then the power in the beam due to seeding will be:

$$P_{out}(\phi) = \frac{4\gamma_r^{out} \gamma_r^{sd} P_{in}}{(\gamma_r^{tot})^2 (1 - x^2)^2} \left(1 + 2x \int \frac{1}{\sqrt{2\pi}\tilde{\theta}_{sd}} e^{-\left(\frac{(\theta - \bar{\theta}_{sd})^2}{2\tilde{\theta}_{sd}^2} \right)} \cos\theta \mathrm{d}\theta + x^2 \right) \tag{6.9}$$

In the case of backscatter the scattered field from the interferometer first couples into the reverse propagating cavity mode through the output coupler, where it is resonantly enhanced. The amplitude of the counter-propagating field (in units of $\sqrt{photons}$) is:

$$\bar{a}_{cp} = \frac{\sqrt{2\gamma_r^f}}{\gamma_r^{tot}} \bar{A}_{sc,inc}$$

The nonlinear crystal in the OPO is the most likely scattering source, the 0.16% loss it introduces into the cavity is a combination of scattering and absorption losses. The scatter

from a transmissive optic is characterized by the bidirectional scatter distribution function (BSDF), which includes scatter from both surfaces and the bulk [83, p 21]. The power transmittance of scattering a normally incident beam into the counter-propagating mode is

$$T_{bs} = BSDF(\theta_s = 0)\Omega_{1/e}$$

where $\Omega_{1/e} = \lambda^2/\pi\omega_0^2$ is the solid angle of the beam with waist ω_0 at the optic. T_{bs} is the product of two transmissions, the fraction of the power in the counter-propagating mode that is scattered out of that mode, and the fraction of that scattered power that enters the co-propagating mode. The product of the two rates is given by $\gamma_{bs}^2 = T_{bs}/\tau^2$. The circulating backscattered field in the cavity mode co-propagating with the squeezed field experiences the nonlinear gain and is given by:

$$\bar{a}_{bs} = \frac{1 + xe^{i\theta_{sc}}}{1 - x^2}\frac{2\gamma_{bs}}{\gamma_r^{tot}}\bar{a}_{cp} = \frac{1 + xe^{i\theta_{sc}}}{1 - x^2}\frac{2\gamma_{bs}\sqrt{2\gamma_r^f}}{(\gamma_r^{tot})^2}\bar{A}_{sc,inc}$$

where θ_{sc} is the phase between the circulating backscattered field and the pump field. Since the output fields are related to the circulating fields by $\bar{A}_{bs,out} = \sqrt{2\gamma_r^f}\bar{a}_{bs}$ the backscattered field and powers are given by:

$$\bar{A}_{bs,out} = \frac{1 + xe^{i\theta_{sc}}}{1 - x^2}\frac{4\gamma_{bs}\gamma_r^{out}}{(\gamma_r^{tot})^2}\bar{A}_{sc,inc} \tag{6.10}$$

$$P_{bs,out}(\phi) = \left(\frac{1 + 2x\cos\theta_{sc} + x^2}{(1 - x^2)^2}\right)\frac{16(\gamma_r^f)^2\gamma_{bs}^2}{(\gamma_r^{tot})^4}P_{sc,inc} \tag{6.11}$$

This reduces to the usual result for backscatter in a mode cleaner cavity [38, 69] if there is no nonlinear gain ($x = 0$), and we assume that the finesse is high and the cavity is critically coupled so that ($\gamma_r^{tot} = 2\gamma_r^f = 2\pi/(\mathcal{F}_r\tau)$):

$$\left|\frac{P_{bs,out}}{P_{sc,inc}}\right|_{MC} = \frac{\gamma_{bs}^2}{\gamma_{out}^2} \tag{6.12}$$

$$\left|\frac{P_{bs,out}}{P_{sc,inc}}\right|_{MC} = BRDF(\theta_i)\Omega_{1/e}\left(\frac{\mathcal{F}_r}{\pi}\right)^2 \tag{6.13}$$

where $BRDF(\theta_i)$ is the bidirectional reflectance distribution function and is similar to BSDF for a reflective optic with angle of incidence θ_i. For our OPO the output coupler is the dominant loss, so $\gamma_{tot} \approx \gamma_{out}$, and the ratio of backscattered power to power incident on the OPO is given by:

$$R_{OPO} = \frac{P_{bs,out}(\phi)}{P_{sc,inc}} = \frac{16\gamma_{bs}^2}{(\gamma_r^{tot})^2}\left(\frac{1+2x\cos\theta_{sc}+x^2}{(1-x^2)^2}\right) \tag{6.14}$$

$$= 16\frac{T_{bs}}{T_f^2}\left(\frac{1+2x\cos\theta_{sc}+x^2}{(1-x^2)^2}\right) \tag{6.15}$$

where T_f is the power transmission of the front coupler.

6.2.4 Phase of the scattered light

There are two relative phases that determine the level of backscatter noise in the interferometer, ϕ_{sc} is the phase between the interferometer signal field and the backscattered field at the readout photo-detectors, while θ_{sc} is the relative phase between the pump and the scattered field inside the OPO, which determines the level of parametric amplification or de-amplification. The path length between the OPO and the point where light leaves the interferometer arms, ϕ_{pl}, as well as the OPO length L_{opo} contribute to both of these phases as well as the squeezing angle θ_{sqz}.

The length noises are dominated by low and audio frequency fluctuations, while the cavity poles are at 10s of MHz, so we find expression for the phases ignoring the frequency dependence of the cavity transfer functions. The squeezing angle is given by:

$$\theta_{sqz} = \theta_b + \left(\frac{2}{\gamma_g^{tot}} + \frac{2}{\gamma_r^{tot}(1+x^2)}\right)\frac{\omega\delta L_{OPO}}{\overline{L}} + \phi_{pl} \tag{6.16}$$

The control system adjusts θ_b to maintain θ_{sqz} as $\phi_{ifo} + \pi/2$ so that the light at the dark port will be amplitude squeezed. The phase that determines whether the scattered light is

amplified or de-amplified is:

$$\theta_{sc} = \theta_b - 2\left(\phi_{ifo} + \phi_{pl} + \frac{\omega\delta L}{\gamma_r^{tot}\overline{L}}\right) \tag{6.17}$$

One of the three phases can be set to zero, if we set $\phi_{ifo} = 0$, then $\theta_{sc} = \pi$. The fluctuations in θ_{sc} should be of the same order as the fluctuations of the squeezing angle. We can use Equation 6.15 and replace θ_{sc} with a Gaussian distribution with mean of π and a small standard deviation $\tilde{\theta}_{sc}$ to find an expression for the reflectivity of our OPO for light scattered out of the interferometer:

$$R_{OPO} = \frac{16T_{bs}}{T_{out}^2}\left(\frac{1 - 2xe^{-\tilde{\theta}_{sc}^2/2} + x^2}{(1-x^2)^2}\right) \tag{6.18}$$

The amount of backscattered power from a nonlinear cavity, normalized to the amount of backscatter from the same cavity without nonlinear gain, plotted in Figure 6-2, is simply the parametric amplification and de-amplification of the nonlinear cavity. This is to be expected since backscatter is simply another mechanism for coupling a classical seed field into the cavity.

6.2.5 Amplitude noise of coherent locking field

Amplitude fluctuations of the coherent locking field may add intensity noise to the squeezing readout, either on a balanced homodyne detector or on the interferometer readout. Because the coherent field is detuned in the OPO, length fluctuations of the OPO and phase noise of the coherent field both impose amplitude noise on the coherent field. The ratio of the field incident on a cavity to the transmitted field is given by:

$$\frac{E_{trans}}{E_{inc}} = \frac{t_{in}t_{out}}{1 - g_{rt}e^{2\pi\phi_{rt}(t)}}$$

where $t_{in,out}, r_{in,out}$ are the amplitude transmittances of the input and output couplers, g_{rt} is the round trip cavity gain, and $\phi_{rt}(t)$ is the phase acquired in one round trip. Since

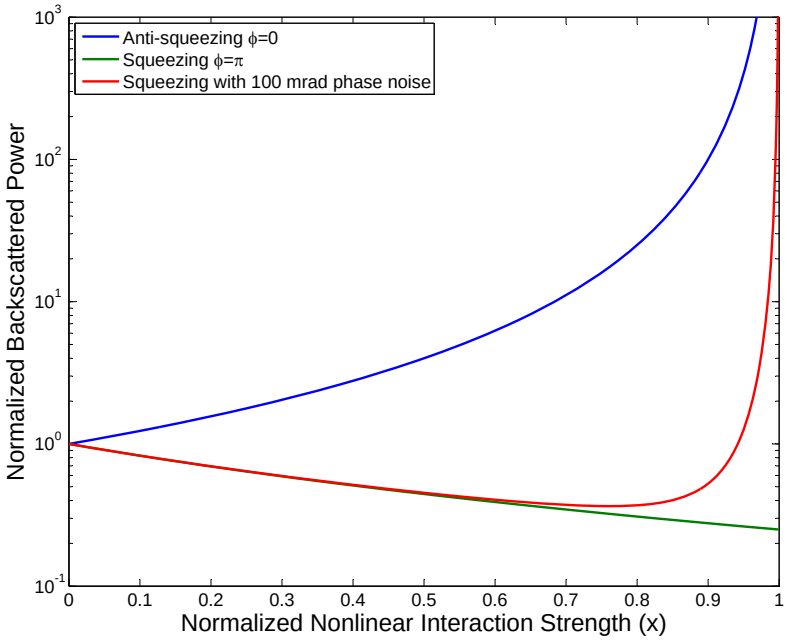

Figure 6-2: Backscatter expected from a nonlinear cavity, normalized to the amount of backscatter expected from the same cavity when there is no nonlinear interaction. The blue and green curves show the backscatter expected for anti squeezing and squeezing respectively, while the red curve shows the backscatter expected from squeezing with 100 mrad phase noise included.

the OPO is a nonlinear cavity, g_{rt} includes the nonlinear gain. For the nonlinear gain and offset frequency used in our experiment, the generated coherent sideband had 5% of the power that the injected sideband had, so we will only calculate the amplitude noise from the dominant, injected sideband. Since the length of the cavity is locked to the phase of the green pump, and the phase of the coherent field is also locked to the phase of the green pump, ϕ_{rt}, should be fixed by the ratio of the offset frequency f_{offs} to the free spectral range f_{FSR} with small fluctuations due to the residual laser phase and the cavity length fluctuations,

$\Delta\phi_{aux}(t), \Delta L(t)$,

$$\begin{aligned}\phi_{rt}(t) &= 2\pi\left(\frac{f_{offs}}{f_{FSR}} + \frac{\Delta L(t)}{\lambda}\right) + \Delta\phi_{aux}(t) \\ &= \bar{\phi}_{rt} + \Delta\phi_{rt}(t)\end{aligned}$$

This means that the power transmission is given by:

$$T(t) = \left|\frac{E_{trans}}{E_{inc}}\right|^2 \tag{6.19}$$

$$= \frac{t_{in}^2 t_{out}^2}{1 - g_{rt}^2 - 2g_{rt}\left(\cos\bar{\phi}_{rt}\cos\Delta\phi_{rt}(t) - \sin\bar{\phi}_{rt}\sin\Delta\phi_{rt}(t)\right)} \tag{6.20}$$

Making the small angle approximation for $\Delta\phi_{rt}(t)$.

$$T(t) = \frac{t_{in}^2 t_{out}^2}{1 - g_{rt}^2 - 2g_{rt}\cos\bar{\phi}_{rt}}\left(\frac{1}{1 + \frac{2g_{rt}\Delta\phi_{rt}(t)\sin\bar{\phi}_{rt}}{1 - g_{rt}^2 - 2g_{rt}\cos\bar{\phi}_{rt}}}\right) \tag{6.21}$$

$$\approx \frac{t_{in}^2 t_{out}^2}{1 - g_{rt}^2 - 2g_{rt}\cos\bar{\phi}_{rt}}\left(1 - \frac{2g_{rt}\Delta\phi_{rt}(t)\sin\bar{\phi}_{rt}}{1 - g_{rt}^2 - 2g_{rt}\cos\bar{\phi}_{rt}}\right) \tag{6.22}$$

Based on the ratio of transmitted coherent field to the incident field on the OPO, and the ratio of the generated to injected sideband power, we can infer that g_{rt} for the coherent control laser is 0.4. The phase $\bar{\phi}_{rt}$ is small, as is $\Delta\phi_{rt}(t)$, so we can make the approximation 6.22. Fluctuations in the round trip phase $\Delta\phi_{rt}$ cause power fluctuations on the transmitted beam given by:

$$\frac{\delta P_{trans}(f)}{\bar{P}_{trans}} = \frac{2g_{rt}\sin\bar{\phi}_{rt}}{1 - g_{rt}^2 - 2g_{rt}\cos\bar{\phi}_{rt}}\Delta\phi_{rt}(f) \tag{6.23}$$

The diagnostic homodyne detector must be carefully aligned to have good common mode rejection for both the coherent locking field and the local oscillator, a description of alignment methods is given in [80]. In the gravitational wave detector, the coherent field is rejected by the output mode cleaner(OMC), and only a small fraction of it actually reaches the detector,

so the amplitude noise is largely suppressed. The relative intensity noise at the gravitational wave readout photo-detector is given by:

$$RIN_{output}(f) = \frac{\delta P_{trans}(f)\eta_{prop}T_{OMC}(\Omega_c)}{P_{sig}} \tag{6.24}$$

$$= \frac{RIN_{trans}(f)P_{trans}\eta_{prop}T_{OMC}(\Omega_c)}{P_{sig}} \tag{6.25}$$

$$= \frac{P_{inc}\eta_{prop}T_{OMC}(\Omega_c)}{P_{sig}} \frac{2t_{in}^2 t_{out}^2 g_{rt}\sin\bar{\phi}_{rt}}{(1-g_{rt}^2-2g_{rt}\cos\bar{\phi}_{rt})^2}\Delta\phi_{rt}(f) \tag{6.26}$$

where P_{inc} is the power incident on the rear coupler of the OPO, η_{loss} is the propagation efficiency, and $T_{OMC}(\Omega_c)$ is the transmission of the control sidebands at the offset frequency Ω_c through the OMC given by Equation 5.59. Fluctuations due to OPO length noise, control laser phase noise, as well as the amplitude noise of the control laser before it enters the OPO need to be summed in quadrature, so the relative intensity noise at the output PD from intensity noise on the coherent control field is:

$$\begin{aligned} RIN_{output}(f) &= \frac{P_{inc}\eta_{prop}T_{OMC}(\Omega)t_{in}^2 t_{out}^2}{P_{sig}(1-g_{rt}^2-2g_{rt}\cos\bar{\phi}_{rt})} \times \\ &\left[\left(\frac{2g_{rt}\sin\bar{\phi}_{rt}}{(1-g_{rt}^2-2g_{rt}\cos\bar{\phi}_{rt})}\right)^2\left[\frac{\Delta L(f)}{\lambda}^2+\Delta\phi_{aux}^2(f)\right]+\delta RIN_{inc}^2\right]^{1/2} \end{aligned} \tag{6.27}$$

6.3 Measurements and estimates of technical noise introduced to Enhanced LIGO by squeezing injection

6.3.1 Amplitude noise from coherent locking field

In our experiment the amplitude noise introduce by the coherent control field was too small to measure. Using Equation 5.59 for $T_{OMC}(\Omega_c)$, and 6.25, and the values in Table 6.1 we predict that the relative intensity noise due to amplitude noise from the coherent control field will be 4×10^{-12}, almost 4 orders of magnitude below shot noise. This should only become a concern if the squeezing angle error signal is derived after the OMC, in which case

RIN_{trans} in transmission of the OPO	3×10^{-5} (peak)
P_{trans} coherent control field leaving OPO	56 μW
Detection efficiency η_{det}	0.45
OMC finesse	360
coherent control offset frequency Ω	29.5 MHz
$T_{OMC}(\Omega)$ power transmission of OMC	1.6×10^{-4}
P_{sig} power in signal field	30mW

Table 6.1: Values used to estimate level of noise due to coherent control field amplitude fluctuations.

more of the coherent field will need to be transmitted.

6.3.2 Linear couplings of environmental noise

Spurious interferometers due to backscatter or seeding could linearly couple environmental noise from motion on the squeezer table into the interferometer spectrum. Although the change in path length between the squeezer and the interferometer is often several microns at low frequencies (0.1 to 0.4 Hz), the motion in LIGO's sensitive frequency band from 50 Hz-8 kHz is much smaller than one wavelength [65]. No matter which noise coupling mechanism is responsible, we can use the same techniques to characterize the linear coupling, identify contributions from individual optics, damp their motion, and reduce the noise.

Coherences between appropriate environmental sensors and the gravitational wave read out channel (DARM) characterize the coupling of noise from the sensor location into the interferometer. An accelerometer mounted on the squeezing table initially revealed coherences from 200-300 Hz, which were later eliminated, as shown in Figure 6-3.

By increasing the level of motion, and monitoring the noise power spectrum, we can characterize both incoherent and coherent couplings. By closely watching a spectrum of DARM while bowing individual optics gently enough that neighboring optics were not also moved, we were able to identify particular features in the spectrum with single optics and damp their motion. After damping identified resonances, the spectrum with squeezing injected appears identical to the spectrum without squeezing, and the noise at specific frequencies was reduced by at least a factor of ten, as shown in Figure 6-4.

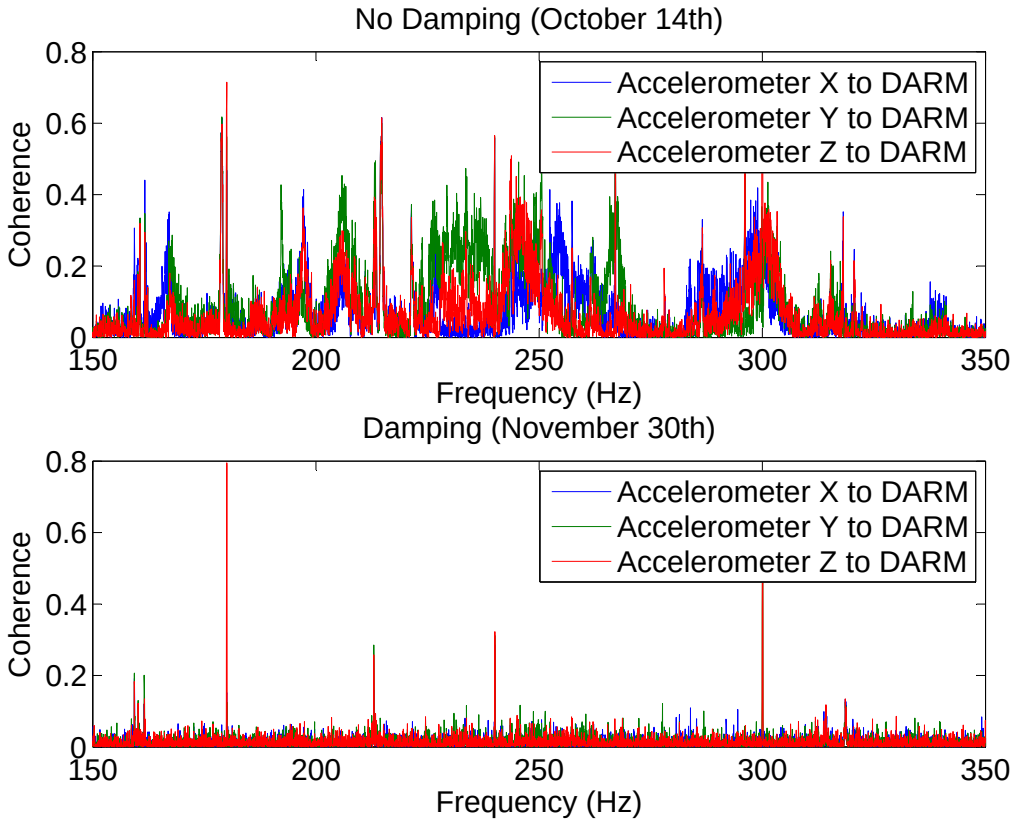

Figure 6-3: Coherence between accelerometers mounted on the squeezer table and the differential arm degree of freedom. The two measurements were made with similar environmental conditions, as measured by the accelerometers. The upper panel shows coherence between 150-300 Hz which was not present when the squeezer was blocked with a black glass beam dump, indicating that the coupling mechanism involved the squeezer [70]. Damping the resonances of individual optics identified as responsible for adding noise, as well as other improvements, reduced the coherence as shown in the lower panel.

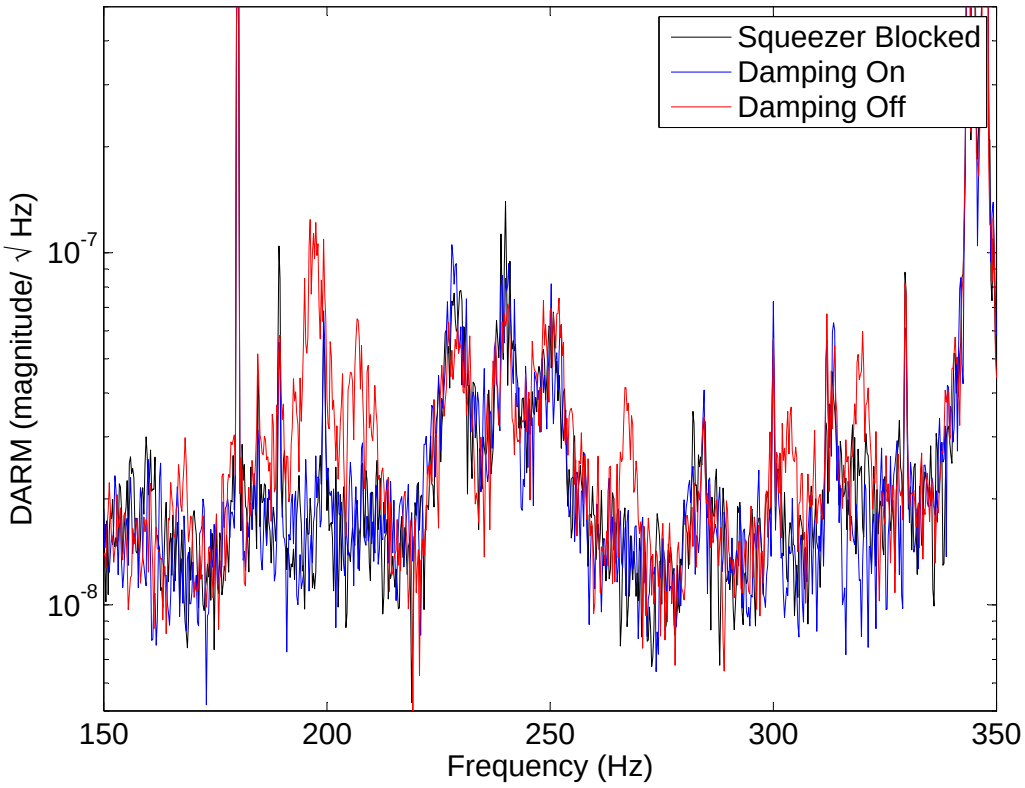

Figure 6-4: Noise in interferometer readout (differential arm degree of freedom DARM) without squeezing injected, and with unoptimized squeezing injected with and without damping material, showing that with mechanical resonances damped squeezing adds no extra noise at these frequencies.

The level of technical noise introduced by the squeezer in the final configuration for the H1 experiment was below the normal level of interferometer noise. In order to estimate the level of noise added, we increased the table motion at specific frequencies until we added measurable noise, and extrapolated to the level of noise for normal table motion. This technique measures noise that is small compared to the interferometer noise, but does not measure at every frequency and could miss noise in a narrow frequency band caused by a mechanical resonance.

Different optic mounts have slightly different resonant frequencies, and all of these optics can contribute to the total motion $\delta x_{sc}(f)$. Using accelerometers we measured the increase

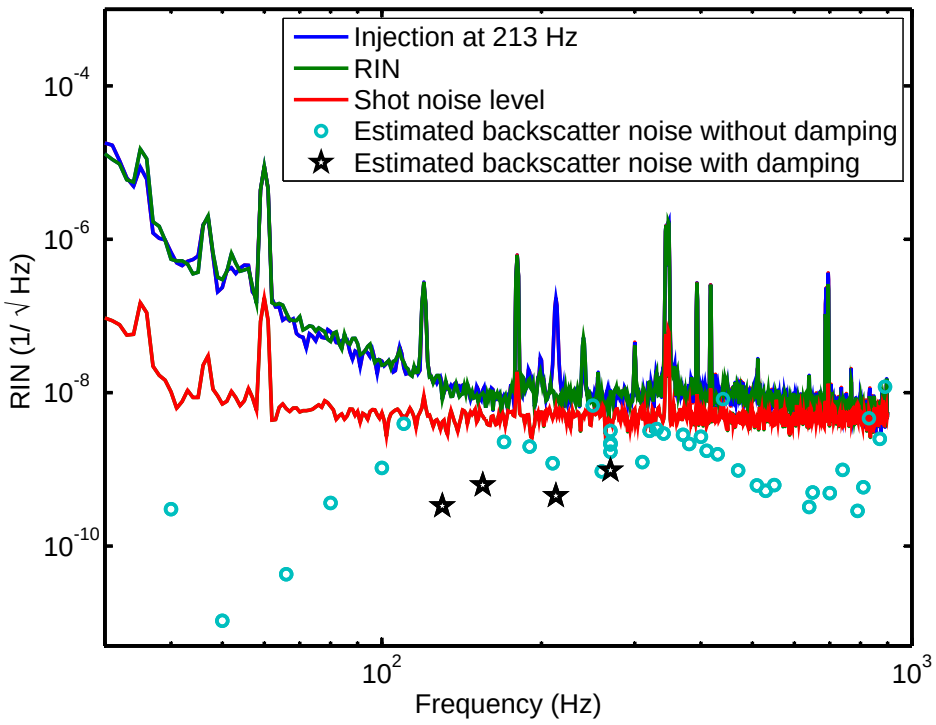

Figure 6-5: Method of estimating level of backscatter noise. The blue and red traces show the relative intensity noise (RIN) at the gravitational wave readout detector under normal conditions and with the squeezer table motion increased at a single frequency. The green trace is the difference photo-current between the two OMC photo-detectors, which is a measure of shot noise at high frequencies. The light blue circles and black stars are inferred by measuring the noise with injection and comparing table motion as measured by accelerometers with and without an injection.

in table motion with injections from the shaker, and assumed that the transfer function from the table motion to $\delta x_{sc}(f)$ is linear. Multiple excitation amplitudes at the same frequency were used to confirm that the coupling from table motion to noise on the interferometer output was linear. Assuming only that the accelerometer signal at a particular frequency is proportional to the motion at that frequency we can compare measurement taken with the injection off and on:

$$\frac{RIN_{off}}{RIN_{on}} = \frac{\delta x_{sc,off}(f)}{\delta x_{sc,on}(f)} = \frac{\delta x_{accel,off}(f)}{\delta x_{accel,on}(f)}$$

Spectra were also recorded with the shaker on and a black glass beam dump on blocking

the squeezer port, to check that the squeezer was the dominant mechanism for adding noise from the shaker, rather than electromagnetic couplings or other motion in the corner station. The resulting estimate of the level of noise is shown in Figure 6-5.

Frequency (Hz)	$RIN_{ifo}/RINsc$	$RIN_{shot}/RINsc$
75	143 (lower limit)	NA
130	24.5	12.5
155	15.9	7.89
213	14.0	1.97
270	11.0	4.43

Table 6.2: Level of noise added to interferometer by squeezing injection at several frequencies.

6.3.3 Frequency offset measurement of power from spurious interferometers

To more fully understand the level of noise we added to the interferometer, we would like to know how much backscattered and seed power reached the gravitational wave photodetectors. One easy way to measure the power due to backscatter inside the OPO and seeding of the OPO is to introduce a frequency offset between the squeezer pump laser and the interferometer carrier and lock the OPO to the pump frequency. Light at the squeezer pump frequency that seeds the OPO enters the interferometer and creates a beat note at the offset frequency, where it can be easily distinguished from other noise sources. Light scattered from the interferometer into the OPO and backscattered will interact with the second harmonic beam through the nonlinear gain and some photons will be generated with twice the frequency offset of the squeezing pump laser. Figure 6-6 shows the resulting spectrum. When the offset frequency is Ω the total field at the detector is a sum of the signal field E_{carr} and the noise field E_n, and the photo current is

$$I_{PD} \propto |E_{carr}|^2 + 2E_{carr}E_n^* \cos\Omega t + ... \tag{6.28}$$

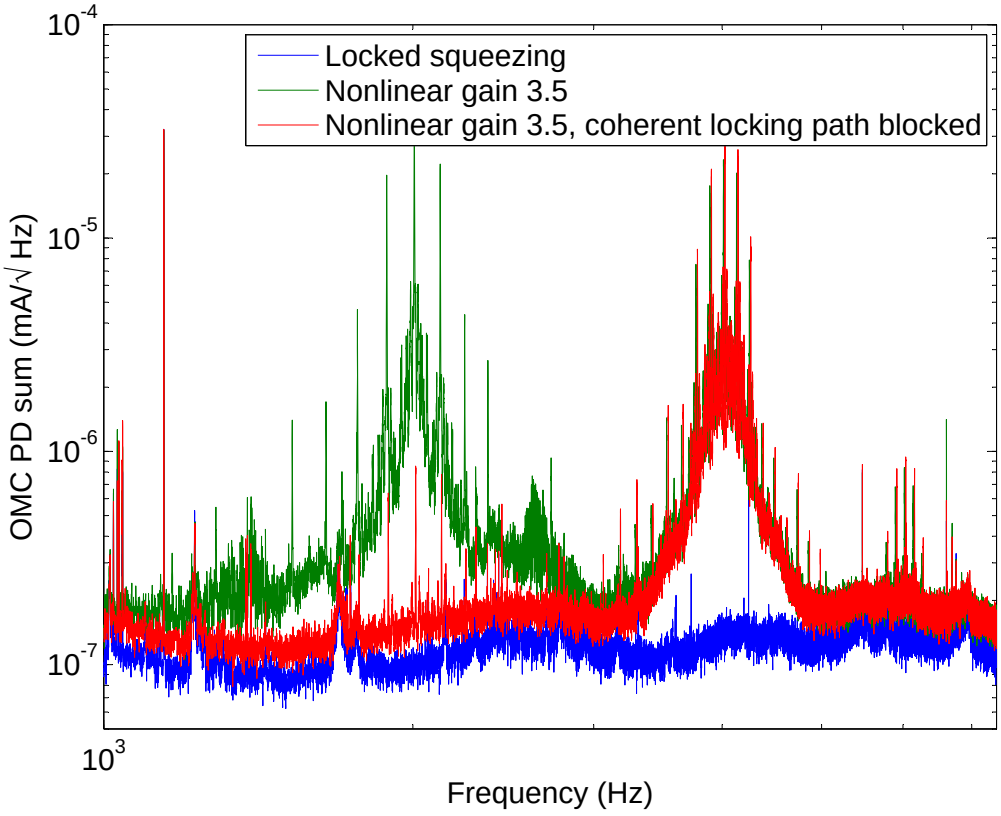

Figure 6-6: Method of distinguishing backscatter inside OPO from other spurious interferometers. The blue trace is a reference spectrum with squeezing injected and the squeezing angle controlled, while the other traces have a 2 kHz offset between the interferometer carrier frequency and the squeezing pump laser. Since the squeezing angle is rotating at 2 kHz, the added anti-squeezing raises the noise floor at all frequencies. The beat between the interferometer carrier and light at the squeezer main laser frequency is shifted up to 2 kHz, while some of the light scattered into the OPO from the interferometer is unconverted by the nonlinear process to 4 kHz. The red trace shows the result with seeding blocked.

when the noise field is small. We can measure the ratio of the area of the peak due to interference (I_n) to the average DC photo-current (I_c):

$$\frac{I_n}{I_c} = \frac{2\int E_c E_n^* \mathrm{d}A}{\int |E_c|^2 \mathrm{d}A} = 2\sqrt{\frac{P_n}{P_c}} \tag{6.29}$$

By monitoring this spectrum while blocking different paths on the table and locking and

Nonlinear gain	$\sqrt{\frac{P_{sd}}{P_{sig}}}$	P_{sd}(pW)
1.1	3.8×10^{-6}	0.34
3.5	1.5×10^{-6}	0.051
9.47	1.9×10^{-5}	0.080

Table 6.3: Inferred powers at OMC PDs due to seeding at the main laser frequency, before addition of notch.

unlocking control loops, we were able to identify and eliminate our seeding. The cable driving the electro-optics modulator in the phase lock loop for the control laser had a small amount of RF pick-up at the offset frequency of 29.5 MHz. This small signal added sidebands to the control field, one of which is at the pump laser frequency. As shown in Table 6.3 with this method we were easily able to identify less than a picoWatt of seed power reaching the interferometer readout photo-detectors. In the initial configuration, this seeding added some noise to the interferometer spectrum, limiting the amount of power we were able to use in the coherent control field without introducing noise, and therefore limiting the signal to noise of our squeezing angle control scheme [13,26]. Once a notch was added to eliminate the pickup, we were able to turn the power up and get a better signal to noise for the squeezing angle control loops without introducing noise [25].

We can use the peak at twice the offset frequency, to calculate the amount of backscattered power from the OPO. We use the steady state cavity equations of motion, with the assumption that the detuning is small compared to cavity decay rates[1], [44, p 66], where a_s is the amplitude of the signal field circulating in the cavity, in this case the back scattered field from the interferometer, and a_i is the idler generated light at twice the frequency offset.

$$\begin{pmatrix} a_s \\ a_i \end{pmatrix} = \frac{1}{(\gamma_r^{tot})^2 - \epsilon^2|b|^2} \begin{pmatrix} \gamma_r^{tot} & \epsilon\bar{b} \\ \epsilon\bar{b}^* & \gamma_r^{tot} \end{pmatrix} \begin{pmatrix} 2\gamma_{bs}\bar{a}_{cp} \\ 0 \end{pmatrix} \tag{6.30}$$

ϵ is the nonlinear coupling constant, and $\bar{b}$ is the pump amplitude. Solving this for the ratio

[1]The factor of 2 difference in the off diagonal terms from the reference is intentional. When using the approximation that these are two different modes, it is necessary to use two mode Hamiltonian given in [42,89]

of the circulating idler and signal amplitudes we get the simple result:

$$\left|\frac{a_i}{a_s}\right| = \frac{\epsilon|\bar{b}|}{\gamma^{tot}} = x$$

This is just the normalized nonlinear interaction strength, related to the parametric amplification g by $x = 1 - 1/\sqrt{g}$ [2]. We can also find expressions for the amplitudes and powers of the output field scattered back towards the interferometer:

$$\bar{A}_{s,out} = \sqrt{2\gamma_r^f}\, a_s = \frac{1}{1-x^2}\frac{4\gamma_r^f \gamma_{bs}}{(\gamma_r^{tot})^2}\bar{A}_{sc,inc} \tag{6.31}$$

$$\bar{A}_{i,out} = \sqrt{2\gamma_r^f}\, a_i = \frac{xe^{-i\theta}}{1-x^2}\frac{4\gamma_r^f \gamma_{bs}}{(\gamma_r^{tot})^2}\bar{A}_{sc,inc} \tag{6.32}$$

$$P_{out,s} = \left(\frac{1}{1-x^2}\right)^2 \frac{16(\gamma_r^f)^2\gamma_{bs}^2}{(\gamma_r^{tot})^4} P_{sc,inc} \tag{6.33}$$

$$P_{out,i} = \left(\frac{x}{1-x^2}\right)^2 \frac{16(\gamma_r^f)^2\gamma_{bs}^2}{(\gamma_r^{tot})^4} P_{sc,inc} \tag{6.34}$$

Comparing this to Equation 6.18 and gives the ratio of the idler backscattered power measured during the frequency offset measurement to the backscattered power during normal operation:

$$\frac{P_{out,i}}{P_{out,bs}} = \frac{x^2}{1 - 2xe^{-\tilde{\theta}^2/2} + x^2} \tag{6.35}$$

$$\frac{P_{out,i}}{P_{out,bs}}(\tilde{\theta} = 0) = \left(\frac{x}{1-x}\right)^2 \tag{6.36}$$

Table 6.4 summarizes the results of frequency offset measurements at different nonlinear gains, the amount of backscattered power inferred from each if there were no nonlinear gain in the cavity, and the amount of backscatter we would expect assuming that the phase noise is around 100 mrad. This measurement may be the easiest and most reliable way to characterize scatter from inside the OPO, which was the dominant backscatter mechanism in our experiment. However, this method does not measure backscatter off of optics outside the OPO, and it does not give us information about the phase θ_{sc} that determines if the

Nonlinear gain	$P_{out,i}(fW)$	$P_{bs}(x=0)$	$P_{out,bs}$(fW)
9.47	170	110	42
3.5	47	130	63
3.5	46	130	61
1.1	0.13	60	55
1.1	0.07	32	30

Table 6.4: Power at OMC PDs due to backscatter. $P_{out,i}$ is the power at twice the offset frequency measured in the offset test, $P_{bs}(x=0)$ is the inferred level of backscatter from the cavity if there were no nonlinear gain, $P_{out,bs}$ is the predicted level with locked squeezing injected into the interferometer and 100 mrad phase noise in θ_{sc}. The measurements taken at low nonlinear gains are less accurate because of the very small amount of measured power.

backscattered field will be amplified or de-amplified in the OPO.

6.3.4 Fringe wrapping measurement of backscattered power

Fringe wrapping provides a more direct way to measure the total backscattered power under normal operating conditions, both from the OPO and from other optics. We used a longitudinal piezoelectric in the injection path to modulate the path length by many wavelengths while keeping the squeezing angle locked. This method has the disadvantage (compared to the offset measurement) that an extra PZT has to be installed in the injection path which can cause misalignments when an excitation is applied. The backscattered light double passes the modulated mirror, while seeding that originates on the squeezer table reflects off the mirror once. This means we are modulating the phase of backscattered light with twice the modulation depth as on table seed light:

$$RIN(t) = 2\sqrt{\frac{P_{sc}}{P_{sig}}}\cos\left(\frac{4\pi\Gamma}{\lambda}\cos\omega_l t\right) + 2\sqrt{\frac{P_{sd}}{P_{sig}}}\cos\left(\frac{2\pi\Gamma}{\lambda}\cos\omega_l t\right)$$

In the frequency domain this will produce a distinct shelf in the spectrum, as shown in Figure 6-7, which can be fit to find the amount of backscattered power. Figure 6-7 shows the noise contribution that one would expect from fringe wrapping with both seeding and backscatter present. When the seed power is equal to or less than the backscattered power, the fringe

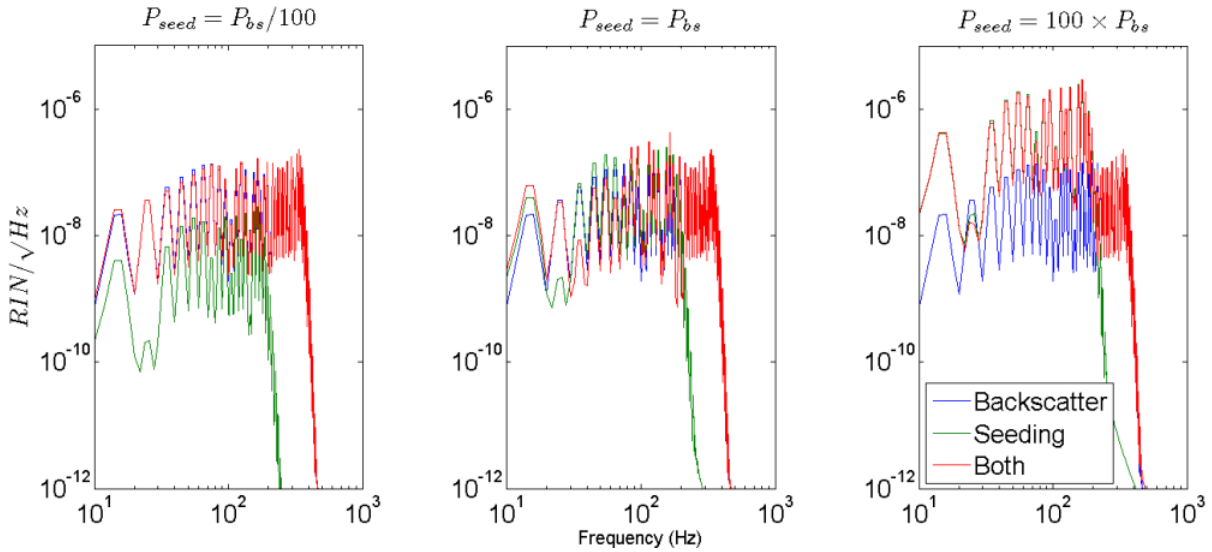

Figure 6-7: In the frequency domain, the fringe wrapping feature is dominated by backscattered light, unless the power due to direct seeding from the squeezer table is much larger.

wrapping measurement is only sensitive to backscattered power. If seeding was dominant, two shelves would appear, the one from seeding adding a second lower frequency shelf.

In the final configuration of the squeezing experiment a fringe wrapping measurement indicates that the power due to backscatter at the output mode cleaner photo-detectors is 260 fW in the normal operating condition with a parametric amplification of 6.2 and squeezing injected. The results for both squeezing and anti-squeezing at different nonlinear gains are presented in 6.5. The backscatter for anti-squeezing is always larger than the result for squeezing, more evidence that the dominant scatter source is inside the OPO. We saw that the squeezing angle phase noise could change dramatically with small changes in alignment, so some of the variation in these measurements could be due to changes in the phase noise. In the final columns of 6.5 the estimate for incident power on the OPO found in the next section is used, along with the detection efficiency, to find an estimate for the reflectivity of the OPO in each of these measurements.

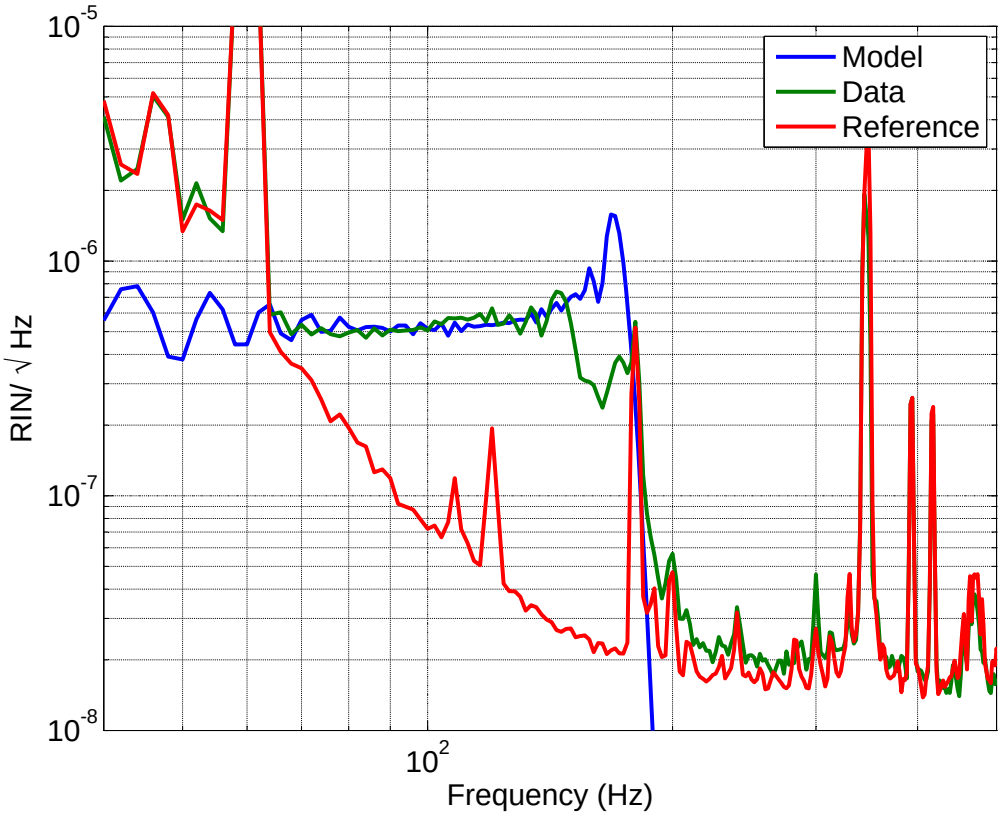

Figure 6-8: Fringe wrapping result with squeezing in final configuration. The blue trace is a fit to the part of the spectrum which is dominated by fringe wrapping only. The green trace is the relative intensity noise measured while the injection path length was modulated by many wavelengths and the squeezing angle kept locked, and the red trace is a reference. The suppression of the differential arm control loop is removed from the data.

Nonlinear gain	$P_{out,bs}$(fW) Squeezing	$P_{out,bs}$ (fW) Anti-squeezing	R_{OPO}(dB) Squeezing	R_{OPO}(dB) Anti Squeezing	η_{det}
6.2	260	2000	-47	-38	35 %
10.8	620	5100	-43	-34	28%
16.7	34	NA	-56	NA	35%
22.5	52	500	-54	-44	14%
28.8	240	4500	-48	-35	31 %

Table 6.5: Power at OMC PDs due to backscatter, in femtoWatts. Since exciting the PZT caused misalignment, the detection efficiency was measured after each pair of measurements, and the scattered powers listed are all rescaled for a detection efficiency of 35%.

6.3.5 Factors that influence the amount of back scattered power

To interpret our measurements of the backscattered power at the photo-detectors, we would like to know the amount of scattered power incident on the OPO, $P_{sc,inc}$ which is in the correct frequency, polarization and spatial modes to couple into the OPO and interfere with the carrier light after backscattering. Figure 6-9 illustrates several of the factors that contribute to the power incident on the OPO and to P_{bs}, the power on the readout detectors.

$$P_{sc,inc} = P_{as} \left| \frac{P_{carr}}{P_{tot}} \right|_{as} R_{OF} T_{SF} M_{OPO} \tag{6.37}$$

The scattered power is proportional to the power in the anti-symmetric port beam, the fraction of that power that is at the carrier frequency will be the same in the anti-symmetric beam as in the scattered beam. The next terms describe the fraction of the anti-symmetric beam carrier that will reach the squeezer table. The fraction of the anti-asymmetric beam that is reflected towards the squeezing injection path , R_{OF}, was measured before installation to be -23 dB [3], and the isolation of the Faraday in the squeezing injection path T_{SF} was measured to be -37.6 dB. Once these two Faradays were installed in vacuum we measured 3.6 uW of light incident on the squeezer table when the anti-symmetric port beam had 300mW, so the total isolation was 11.4 dB less than expected [14]. Of the carrier power incident on the squeezer table, the fraction M_{OPO} is in the correct polarization and spatial mode to couple into the OPO and be transmitted back into the interferometer. In our test the scattered

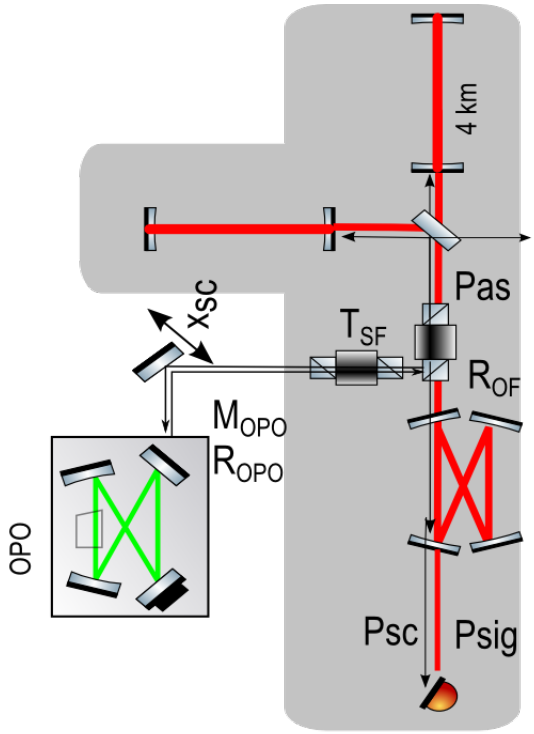

Figure 6-9: Factors that contribute to amount of scattered power: P_{as} is the amount of power heading towards the anti-symmetric port from the interferometer, R_{OF} is the power reflectivity of the output Faraday towards the squeezing injection path, T_{SF} is the transmission in reverse of the squeezing injection Faraday, M_{OPO} is the fraction of power in the AS beam that is in the right polarization and spatial mode to cause backscatter, R_{OPO} is the fraction of the power that enters the OPO that will be scattered into the direction propagating towards the interferometer.

light was almost all in the correct polarization [14]. A photo-detector was installed on the scattered beam reflecting off of the OPO, in an effort to measure the fraction of the scattered beam in the 00 spatial mode. The resulting scan is shown in Figure 6-10. Although it is not clear which peak is the correct spatial mode, the two most likely peaks contain 14% and 7.8% of the power, so we can assume that M_{OPO} is roughly $11 \pm 3\%$. This gives us a value of 79 ± 21nW for the incident power on the OPO which could potentially cause backscatter.

The amount of backscattered power that reaches the output photo-detectors will be:

$$P_{bs} = P_{sc,inc} R_{OPO} \eta_{loss} \tag{6.38}$$

P_{as}	$300mW$
$\left\|\frac{P_{carr}}{P_{tot}}\right\|_{as}$	$\frac{1}{5}$ [5]
R_{OF}	23 dB [4] measured in lab
T_{SF}	37.6 dB [4] measured in lab
$R_{OF}T_{SF}$	49.2 dB installed
M_{OPO}	10%
η_{loss}	38%

Table 6.6: Factors that contribute to P_{sc}.

Using this estimate of $P_{sc,inc}$, the inferred value of the backscattered power incident on the readout detectors without nonlinear gain in the OPO from the frequency offset measurements in Table 6.4, the estimated reflectivity of the OPO without nonlinear gain is -50.6 ± 1 dB. Using Equation 6.15, T_{bs} is $9.5 \pm 3 \times 10^{-9}$. Using our waist size of 34 um in the crystal, the BSDF is $6.5 \pm 3.5 \times 10^{-5}$. The large uncertainty is due to the uncertainty in the match of the spatial mode of the scattered beam into the OPO. We can compare this to the measurement of the backscattered light suppression of 41 dB for a traveling wave cavity OPO measured in [12]. This OPO had a finesse of 35.3 and a waist size in the crystal of $34\mu m$, using 6.15 and 6.2.3 we have $T_{bs} = 1.3 \times 10^{-7}$ and a BSDF of 4.2×10^{-4} attributing all of the scatter to the crystal. The OPO used in [12] used off the shelf optics without super-polishing and a non super-polished crystal, we would expect our OPO, which has both super-polished optics and a super-polished crystal to have lower scatter.

6.4 Summary

Of the three technical noise coupling mechanisms we have investigated, backscatter is of most concern, but we have seen that the level of backscatter noise does not degrade the interferometer sensitivity at any frequency. We estimated that the level of backscatter noise in the critical region between 100-300 Hz is at least a factor of 10 below the limiting noise. Fringe wrapping measurements and frequency offset measurements are useful for characterizing the amount of backscattered power. Spurious interferometers created by light at the carrier frequency that originates from the squeezer table could also add noise, but the frequency

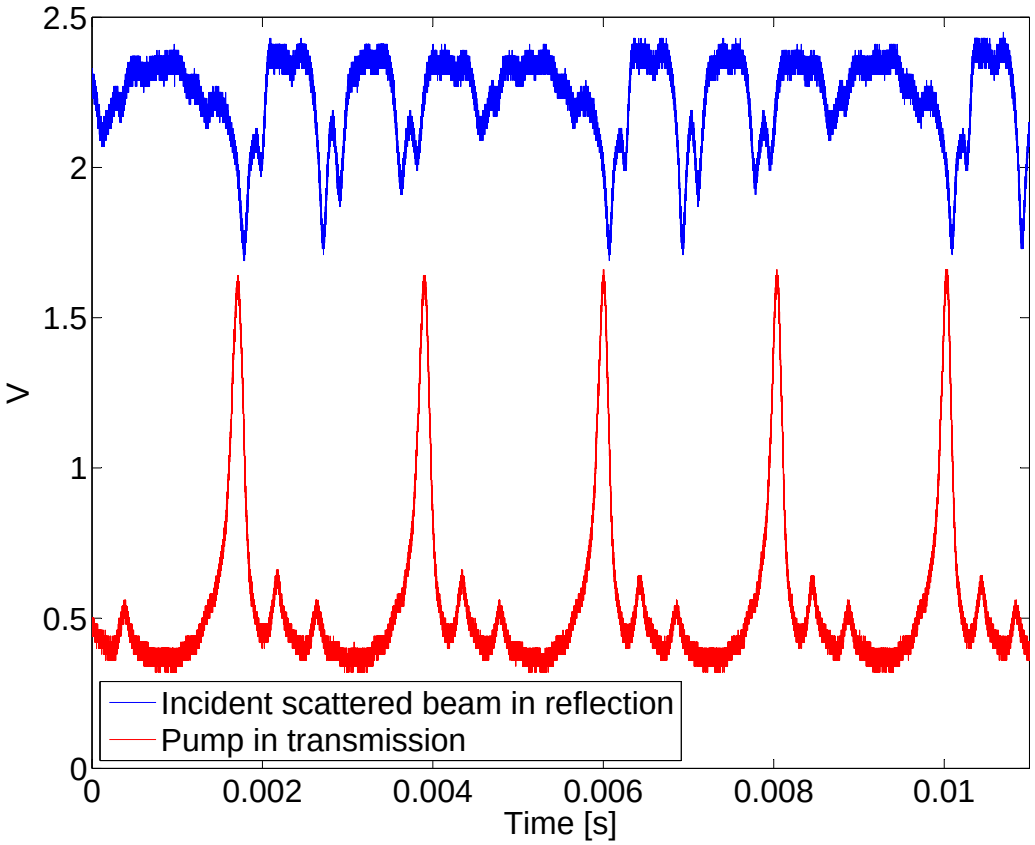

Figure 6-10: The blue trace shows a mode scan of the scattered beam in reflection off of the OPO, while the red trace is the transmitted second harmonic pump power [14]. The infrared cavity line-width is 12.7 MHz, and the interferometer control sidebands are 24.5 MHz away from the carrier. With the squeezing angle unlocked, the pump laser is a few kHz away from the interferometer carrier frequency. By integrating the total area of the reflection dips, and comparing to the area of the two dips most nearly coinciding with peaks in the transmitted green power the estimated mode matching is 14% and 7.8%

offset measurement provides a useful tool to identify seeding at the level of femtoWatts, which can then be eliminated. Lastly, amplitude noise from the coherent squeezing angle locking sidebands is not a concern with the currently used scheme of sensing the squeezing angle before the OMC, but could become important if the transmission of these sidebands is increased so that the error signal can be sensed in transmission from the OMC.

Chapter 7

Implications for Advanced LIGO

One important goal of this experiment was to learn enough about squeezing with a full scale interferometer to plan for implementation of squeezing in Advanced LIGO. We have shown that squeezing could improve the sensitivity of Enhanced LIGO, without adding excess noise anywhere in the spectrum. The better sensitivity of Advanced LIGO will change the requirements for squeezing in two important ways: the backscatter requirements will be more stringent and quantum radiation pressure noise will limit the sensitivity at low frequencies.

The goal of characterizing the technical noise that we added to Enhanced LIGO, which was all below the interferometer sensitivity, was to allow us to plan confidently for installing a squeezer on Advanced LIGO without adding technical noise. The amplitude noise from the coherent locking field will only become a concern for Advanced LIGO if the squeezing angle error signal is derived in transmission of the OMC. If the amount of coherent power in transmission is increased by a factor of a thousand and the OPO is out of vacuum, an intensity stabilization may be needed on the coherent field. Noise added by light originating from the squeezer can be reduced to levels too small to measure by carefully eliminating any seeding paths on the squeezer table. The remaining noise mechanism of most concern for Advanced LIGO is backscatter.

7.1 Backscatter requirements for Advanced LIGO

We would like the noise introduced by backscatter from the squeezer to be a factor of ten below the interferometer sensitivity at all frequencies. Shot noise will be the dominant noise in Advanced LIGO down to 100 Hz, so we will compare the backscattering noise to the shot noise level. The amplitude spectral density of RIN due to shot noise will be:

$$RIN_{shot}(f) = 10^{S/20}\sqrt{\frac{2hc}{\eta_{PD}P_{sig}\lambda}} \tag{7.1}$$

where S is the level of noise reduction due to squeezing in decibels, and η_{PD} is the photodetector quantum efficiency. Using Equations 6.4 and 7.1 the requirement for backscattering noise a factor of ten below the shot noise becomes:

$$\frac{RIN_{sc}}{RIN_{shot}} = \sqrt{\frac{\eta_{PD}P_{sc}}{\lambda hc}}\frac{4\pi\delta x_{sc}(f)}{10^{S/20}} \leq \frac{1}{10}$$

Since the level of noise reduction will be frequency dependent, this is a frequency dependent requirement. From 100 to 50 Hz, Advanced LIGO will be limited by a combination of coating thermal noise and quantum noise, so squeezing injection will reduce the interferometer noise by a smaller factor than at frequencies above 100 Hz. Although P_{leak}, the power in the DC offset field used as a local oscillator, cancels out of this equation, the amount of scattered power P_{sc} will depend on the amount of power at the AS port, so the increased power in Advanced LIGO could increase the level of backscatter noise.

Our measurements in Figure 6-5 showed that the scatter noise was a factor between 2 and 12 below the non squeezed shot noise level in the final configuration of our experiment at the specific frequencies where we measured. Our results from Chapter 3 show that there are no frequencies where the scattering noise was larger than the interferometer noise. For Advanced LIGO, we should plan to reduce the noise by a factor of at least a factor of 5, preferably a factor of 10, above 100 Hz to have a safety factor of 10.

Assuming that Advanced LIGO will want 6 dB of noise reduction above 100Hz, the

requirement 7.1 can be written as:

$$\frac{\sqrt{P_{sc}}\delta x_{sc}(f)_{aLIGO}}{\sqrt{P_{sc}}\delta x_{sc}(f)_{eLIGO}} \leq \begin{cases} \frac{1}{10} & f > 100 \text{ Hz} \\ \frac{1}{5} & \text{f=50 Hz} \end{cases}$$

There are two approaches to reducing backscatter noise, the first is to reduce the motion of the scattering source and the second is to reduce the amount of backscattered power.

7.1.1 Reduction of motion

Depending on the level of ambient noise, seismic noise transmitted through the table legs dominates optic motion at frequencies below 100 Hz, while acoustic noise drives motion at higher frequencies. Our squeezed vacuum source was on an in air table with no acoustic enclosure, and our measurements were taken at a time when the ambient acoustic noise was above the normal science running level. The Advanced LIGO pre-stabilized laser is housed in an acoustic enclosure that has been shown to reduce acoustic noise above 100 Hz by a factor of 10 or more [71]. Adding an enclosure of this type should satisfy the requirement above 100 Hz. Carefully designed tables can also reduce the motion at lower frequencies, although by a smaller factor. Figure 7-1 shows the table motion measured by accelerometers on the squeezer table during our measurement compared to the Initial and Advanced LIGO pre-stabilized laser table during quiet times. The table leg resonances have been moved to a higher frequency for Advanced LIGO, reducing the total RMS table motion, but slightly increasing the motion compared to the Inital LIGO table at the frequencies relevant to backscatter. Assuming that we use an Inital LIGO table the table motion is reduced by about a factor of 2 from 25-200 Hz. Further reduction in the motion might also be achieved through careful mechanical design of the OPO and mounting of optics in the injection path.

If the OPO were moved inside a vacuum chamber, we could expect a much greater reduction in the noise, about a factor of 100 reduction for an OPO resting on a seismic isolation table and a factor of 10,000 reduction for a suspended OPO, even down to 10 Hz. It is possible that by suspending the OPO inside of a vacuum chamber the injection

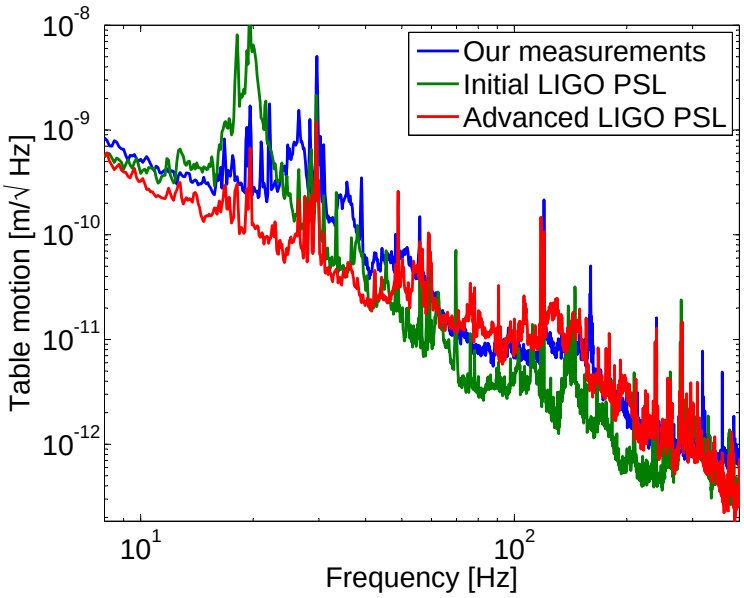

Figure 7-1: Measurements of table motion from accelerometers on our table during our measurement, and the Initial and Advanced LIGO pre- stabilized laser (PSL) tables during quiet time similar to normal interferometer operating conditions. Data for PSL tables from Robert Schofield.

path Faraday could be eliminated, reducing the losses. This may be a solution for a third generation interferometer with either more stringent loss requirements or more stringent backscatter requirements.

Another approach to reducing the motion would be to use active feedback to keep the length constant. If the path length fluctuations between the OPO and the interferometer were the dominant source of noise in the squeezing angle control loop, then a length actuator in the injection path would reduce the relative motion. In our experiment the dominant noise for the squeezing angle control loop was length fluctuations inside the OPO, so feeding back to a path length actuator would actually increase the relative motion.

7.1.2 Predicted scattered power for Advanced LIGO

We also need an estimate of how the amount of backscattered power will change in Advanced LIGO. We can expect the amount of carrier power in the anti-symmetric port beam to

Parameter	Shaker Test	Advanced LIGO prediction
P_{as}	$300mW$	-
$\left\lvert\frac{P_{carr}}{P_{tot}}\right\rvert_{as}$	$\frac{1}{5}$ [5]	-
$P_{as}\left\lvert\frac{P_{carr}}{P_{tot}}\right\rvert_{as}$	60 mW	100 mW upper limit [1]
R_{OF}	-23 dB [4] measured in lab	-23 dB
T_{SF}	-37.6 dB [4] measured in lab	-37.6 dB
$R_{OF}T_{SF}$	-49.2 dB installed	-60.6 dB
M_{OPO}	10%	$10-40\%$
$R_{OPO}(x=0)$	-50.6 dB	-57 dB
η_{det}	38%	80%
$P_{sc}(x=0)$	120fW	$7-29$ fW

Table 7.1: Factors that contribute to P_{sc} for Advanced LIGO.

increase to a maximum carrier power at the AS port of 100mW [1]. The isolation achieved by the combination of the two Faradays installed during our experiment was 11.4 dB worse than the expected performance based on measurements in the lab, we can assume that Advanced LIGO will achieve the performance measured in the lab. The crystal scatter will remain approximately the same, but the OPO output coupler will need to have higher transmission in order to reach 98% escape efficiency and 6dB of measured squeezing. With the current cavity losses, the input coupler transmission will need to double, meaning that the reflectivity of the OPO will be reduced by a factor of 4. These predicted changes are summarized in Table 7.1. If instead we had assumed that the matching of the scattered light into the OPO will stay the same in Advanced LIGO, the backscattered power would be reduced by a factor of 16.

7.1.3 Conclusion for Advanced LIGO backscatter noise

An acoustic enclosure alone would probably reduce the backscatter noise to a level acceptable to Advanced LIGO. If we also include improved Faraday isolation, reduced OPO finesse, reduced seismic motion of the table, and allow for increased power at the AS port, better detection efficiency and better modematching of the scattered beam into the OPO, we can expect a reduction in backscatter noise by factor of 20-40 above 100 Hz, and a factor of 4-8

at lower frequencies. Backscatter alone does not require the OPO to move in vacuum for Advanced LIGO, although it may well become necessary in a third generation detector.

7.2 Squeezing as an alternative to high power operation

Injection of squeezing with a frequency independent squeezing angle, as was done in this experiment, has a similar impact on the interferometer's quantum noise as a change in the laser power. The Advanced LIGO design includes a factor of four increase in the laser power used, which may prove difficult to implement. In the early days of Advanced LIGO science running, the interferometer will operate at less than full power, a configuration in which the squeezing demonstrated in this experiment could significantly improve the range, as shown in Figure 7-2. In this section the range for binary neutron stars is calculated using the same assumptions that were used in 3.3.2 while the black hole inspiral range assumes 30 $M_{\odot}$ black holes.

Loss	η
OPO escape efficiency	0.98
Injection optics	0.997
Vacuum window	0.998
Squeezing injection Faraday	0.97
Output Faraday in reverse	0.97
Injection Losses	0.918
Interferometer losses	Frequency dependent
Output Faraday	0.97
AS table pick off	0.99
OMC transmission	0.97
OMC mode matching	0.96
PD quantum efficiency	0.99
Injection and detection losses	0.81

Table 7.2: Losses assumed for Advanced LIGO, excluding interferometer losses

Because the quantum radiation pressure noise will limit the sensitivity of Advanced LIGO, frequency independent squeezing will degrade the low frequency sensitivity somewhat. The

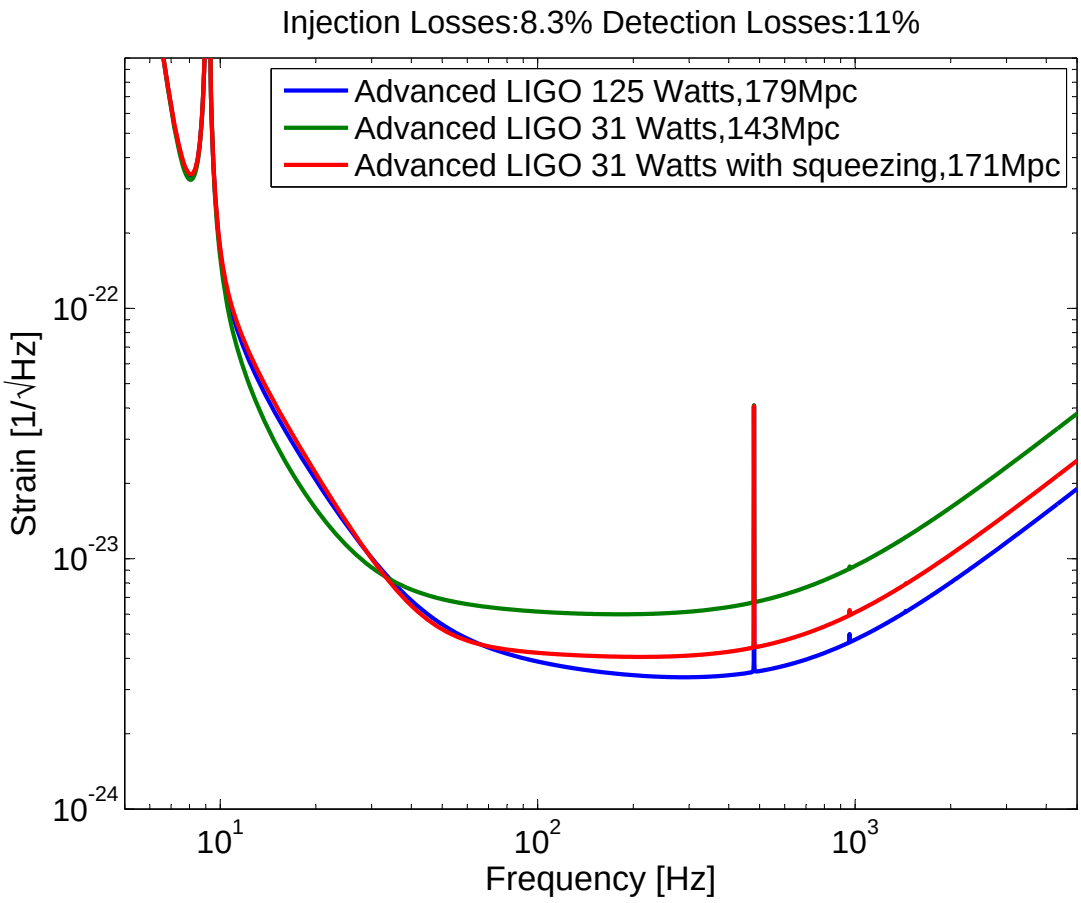

Figure 7-2: Squeezing as an alternative to high power in Advanced LIGO. Dashed lines show quantum noise only, while solid lines show the total noise. Advanced LIGO operated with one fourth of the ultimately planned laser power would have a neutron star inspiral range of 143 Mpc, but with modest squeezing the range could be increased to 171 Mpc, approaching the range at the design sensitivity, and increasing the volume of the universe surveyed by 70%.

differential amplitude noise in the arm cavities determines the radiation pressure noise, so only losses between the OPO and the arm cavities effect the radiation pressure noise. The frequency independent losses assumed in this calculation are summarized in Table 7.2; the frequency dependent losses of the nested interferometer cavities are also included using the simulation program GWINC [53]. When both radiation pressure noise and shot noise limit the interferometer sensitivity, the benefit of squeezing at one frequency needs to be balanced against the degradation at another frequency. The level of squeezing injected and the squeezing angle could be chosen to optimize sensitivity to different sources, or after a first detection to improve measurements of certain parameters. Binary neutron star inspirals are a leading candidate for a first detection of gravitational waves, so optimization of the binary neutron star inspiral range is commonly used as a figure of merit for the sensitivity of a gravitational wave detector. The example shown in Figure 7-3 shows how the range for binary neutron star inspirals varies with the squeezing level and squeezing angle.

The level of measured squeezing required to improve the volume of the universe surveyed for binary neutron star inspirals by 70% is modest, as shown in Figure 7-4. Although the level of squeezing is similar to that observed during the Enhanced LIGO squeezing experiment, the assumed losses are significantly lower which will be necessary to avoid degrading the low frequency sensitivity.

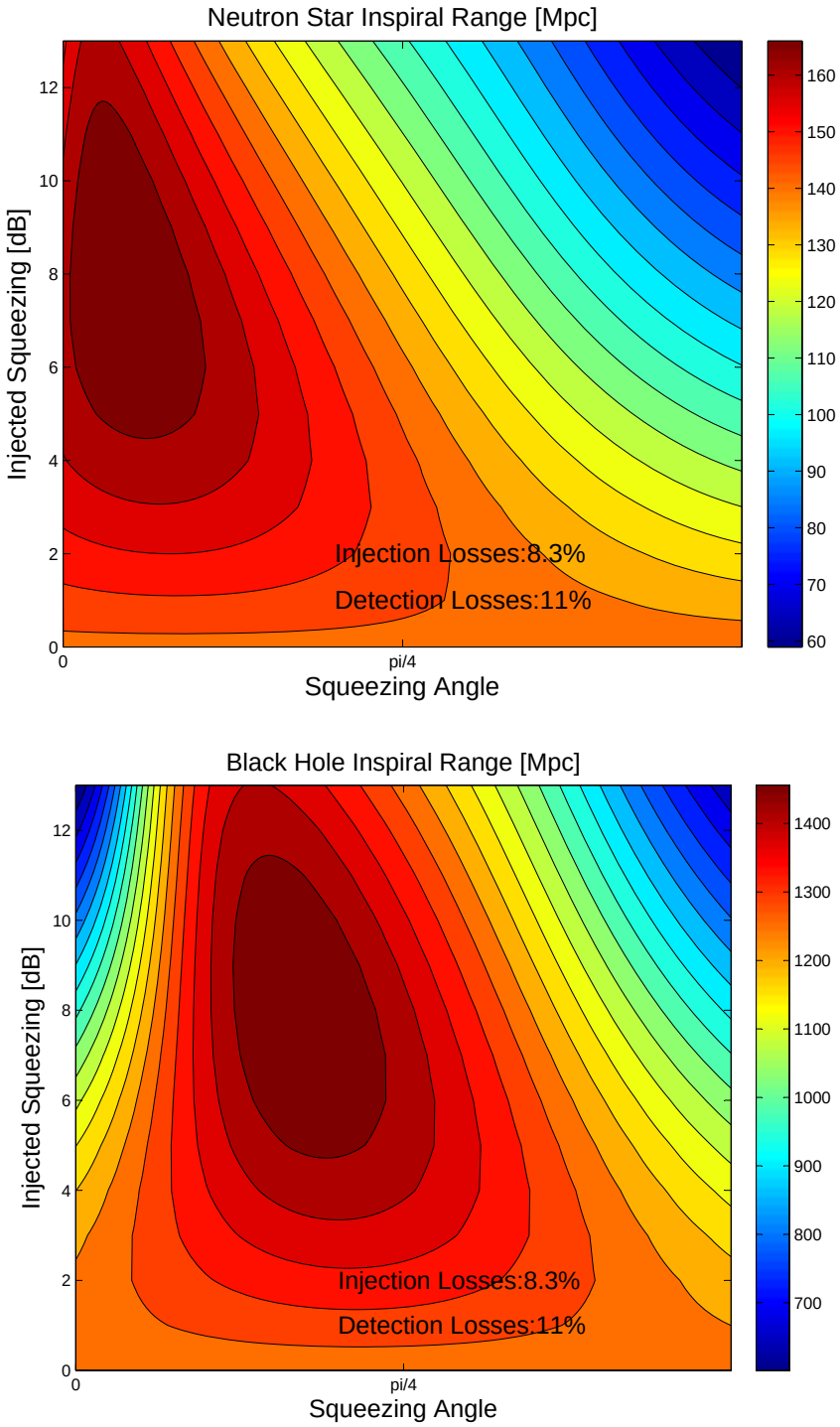

Figure 7-3: Range of Advanced LIGO with 31 Watts input power as a function of level of injected squeezing and squeezing angle, assuming losses from Table 7.2.

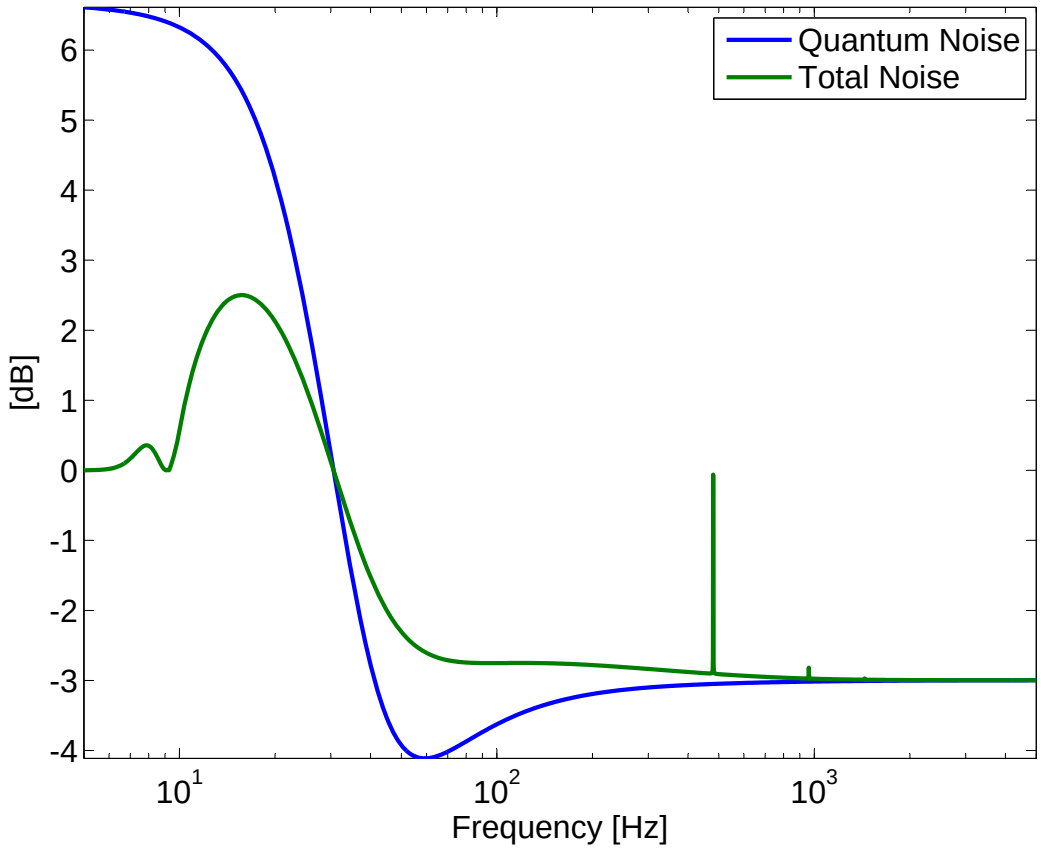

Figure 7-4: Ratio (in dB) of interferometer noise with squeezing to noise without squeezing, both with with 31 Watts input power. The level of squeezing needed to improve the range from 139 Mpc to 163 Mpc is similar to the level of squeezing observed during the Enhanced LIGO squeezing experiment, although the assumed losses are significantly lower.

7.3 Frequency independent squeezing in Advanced LIGO at full power

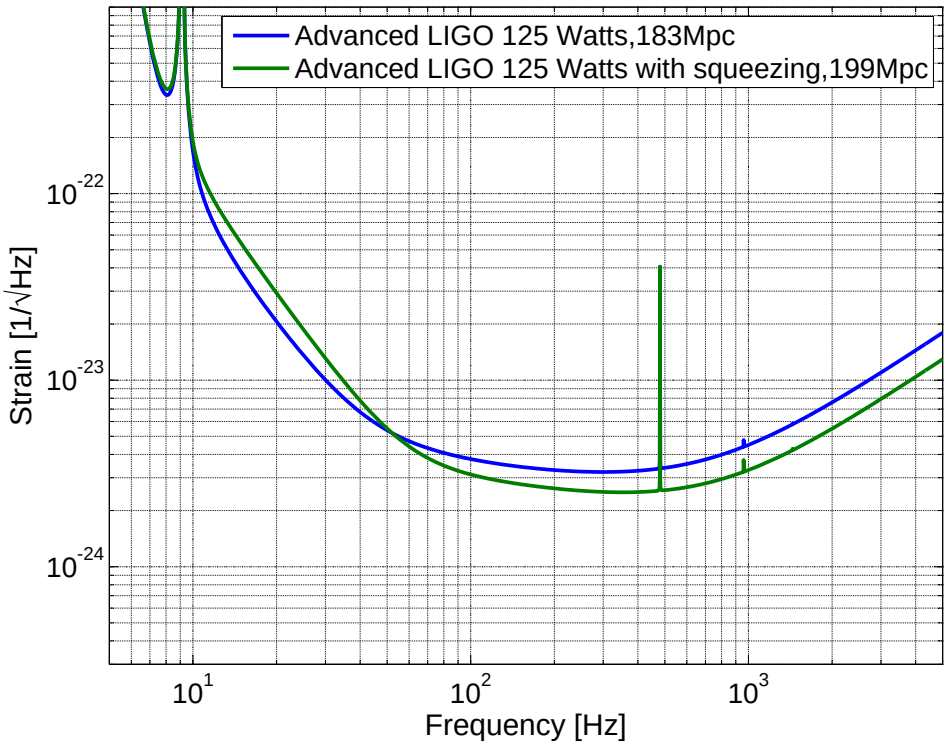

Figure 7-5: Frequency independent squeezing in Advanced LIGO at full power, optimized for binary neutron star inspirals assuming losses from Table 7.2.

Figures 7-5 and 7-6 show the benefits possible from frequency independent squeezing in Advanced LIGO once it is operating at full power. Squeezing could extend the volume of the universe that is surveyed for binary neutron star inspirals by 28%. The black hole binary range can be increased from 1 Gpc to 1.5 Gpc, with squeezing, increasing the volume of the universe surveyed by nearly a factor of 3. Frequency dependent squeezing will be needed to realize the full potential of squeezing in a gravitational wave interferometer.

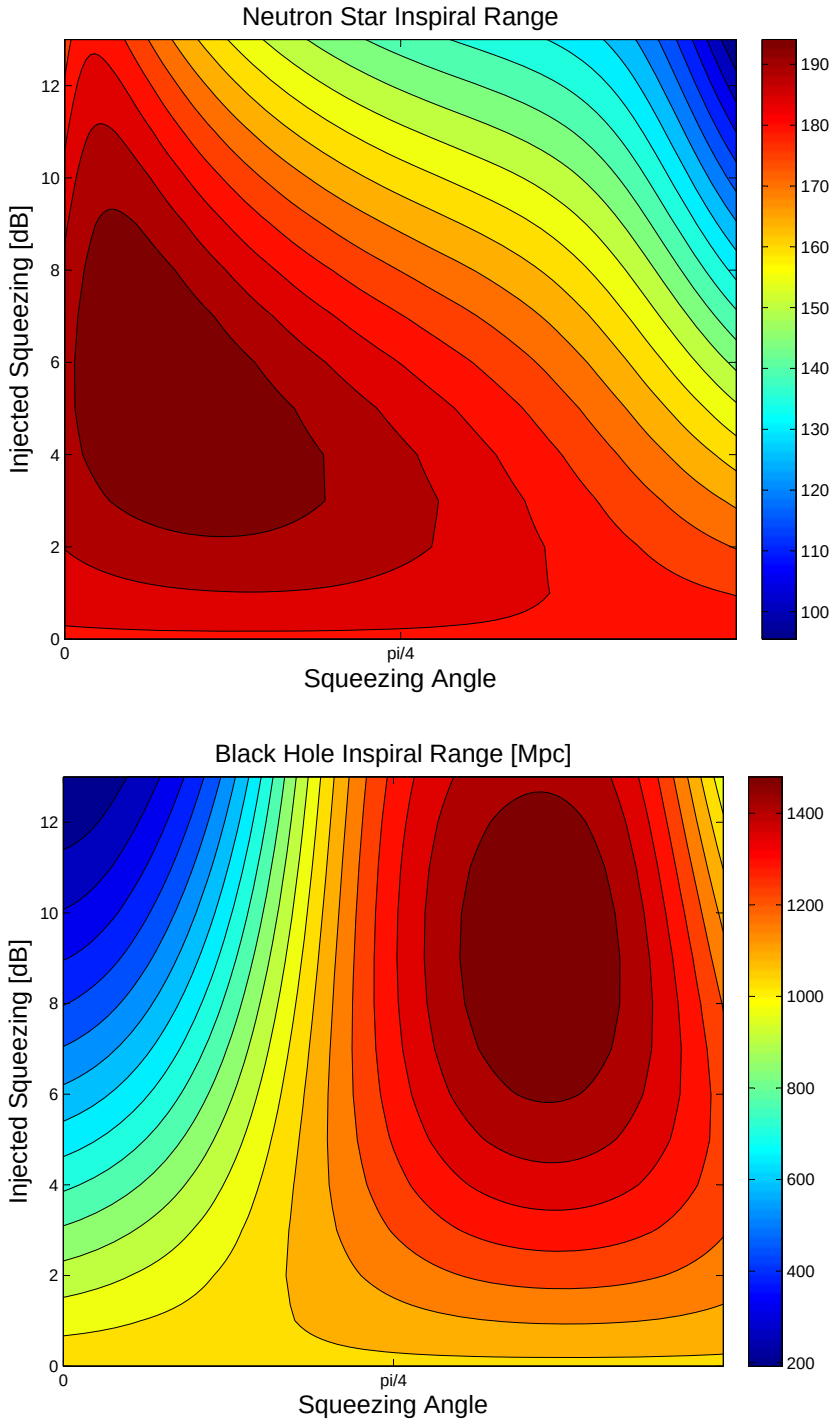

Figure 7-6: Range of Advanced LIGO with 125 Watts input power as a function of level of injected squeezing and squeezing angle, assuming 8.25% injection losses and 11.5% detection losses.

7.4 Frequency Dependent Squeezing

Once advanced gravitational wave interferometers are operating at their full sensitivity, and both shot noise and radiation pressure noise are dominant noise sources, frequency independent squeezing will be of limited use. However, it is possible to inject frequency dependent squeezing, in which the squeezing angle or level of squeezing varies with the sideband frequency [52]. Currently the most feasible way to achieve frequency dependent squeezing is with the use of filter cavities, although other options like electromagnetically or optomechanically induced transparency have been considered [63]. The original proposals for frequency dependent squeezing aimed to achieve an improvement at all frequencies, but required long filter cavities the same lengths as arm cavities with very low losses. More recently filter cavity designs have been proposed that use higher loss cavities which transmit low frequency squeezing, and reflect high frequency squeezing [18, 20]. This would preserve the benefits of squeezing in the shot noise limited region but reduce the anti-squeezing of radiation pressure noise at low frequencies. Research programs at MIT and Caltech are investigating squeezing filter cavities as an early upgrade to Advanced LIGO. With the use of a filter cavity that attenuates the low frequency squeezing, higher levels of squeezing become useful at the high frequencies.

7.5 Higher levels of squeezing in Advanced LIGO and beyond

The maximum level of squeezing that can be measured in an interferometer is determined by the losses and squeezing angle noise. The nonlinear gain can be optimized for the level of squeezing angle noise, as shown in Figure 4-6b. At frequencies were the sensitivity is limited

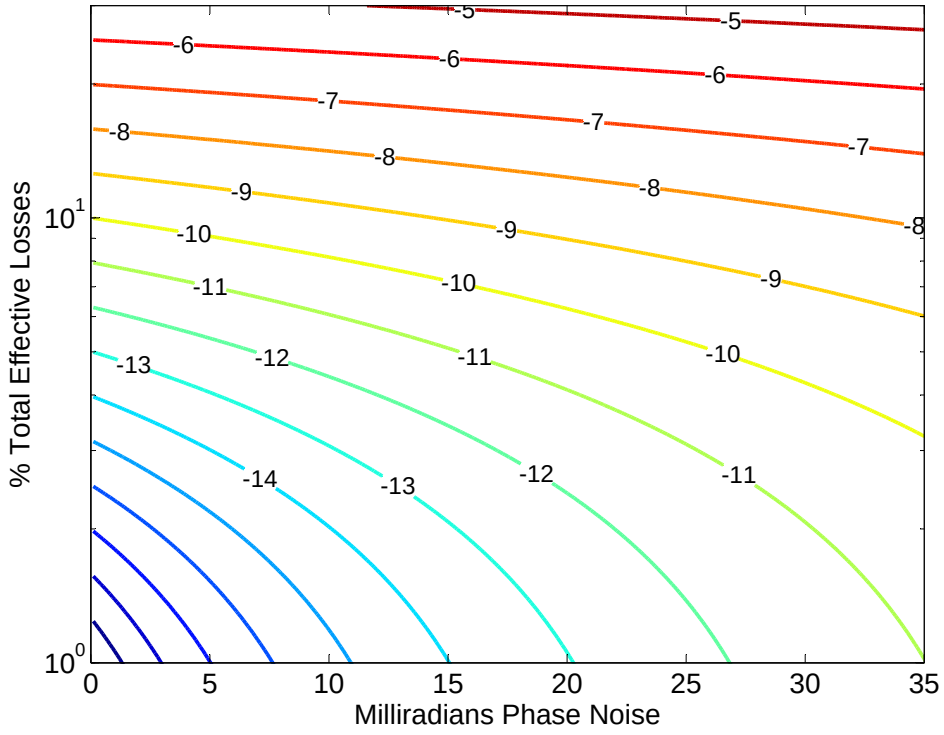

Figure 7-7: Shot noise reduction, with nonlinear gain optimized for the RMS squeezing angle fluctuations. The nonlinear gain is capped so that the OPO pump power is always 80% or less of the threshold power, which does not change the result significantly.

by shot noise, the variance and its derivatives are given by:

$$V = 1 - 4\eta_{tot}x\left(\frac{\cos^2\widetilde{\theta}_{sqz}}{(1+x)^2} - \frac{\sin^2\widetilde{\theta}_{sqz}}{(1-x)^2}\right) \tag{7.2}$$

$$\frac{dV}{dx} = \frac{4\eta_{tot}}{(1-x^2)^3}\left((1+6x^2+x^4)\cos 2\widetilde{\theta}_{sqz} - 4x(1+x^2)\right) \tag{7.3}$$

To second order in the RMS squeezing angle fluctuations $\widetilde{\theta}_{sqz}$, the best shot noise limited sensitivity will be measured when:

$$x = 1 - 2\sqrt{\widetilde{\theta}_{sqz}} + 2\widetilde{\theta}_{sqz} - 2\widetilde{\theta}_{sqz}^{3/2} + 2\widetilde{\theta}_{sqz} \tag{7.4}$$

Figure 7-7 shows the reduction in shot noise possible for a given level of losses and

squeezing angle noise. Reduction of losses is clearly the most important task to improve the level of squeezing. The most important ways to reduce losses are to improve the transmission of Faraday isolators and the OMC, and to improve the mode matching of the squeezed beam to the OMC. Once total losses are reduced to levels around 20%, phase noise also becomes an important limit. To reach 6 dB of squeezing in Advanced LIGO a reduction of the total phase noise from 37 mrad to 10 mrad would increase the allowable loss from 19% to 24.6%, more comfortably within the expected range of 28-20% losses based on the losses in 7.2 and the interferometer losses at 100 Hz. To realize the full potential of squeezing in a third generation detector with total losses below 10%, phase noise should be kept below 5 mrad, and in the rather optimistic scenario of a detector with total losses of 3% a total phase noise of 1 mrad would allow for 15 dB of shot noise reduction.

7.6 Summary

The Enhanced LIGO squeezing experiment has demonstrated that squeezing is compatible with the low frequency sensitivity of a full scale gravitational wave detector, and characterized the limits to the level of squeezing observed. The results indicate that backscatter from an out of vacuum squeezer is compatible with Advanced LIGO's sensitivity, although in a third generation detector the OPO will probably need to move inside the vacuum system to reduce the backscatter noise. Frequency independent squeezing is a viable alternative to high power operation for Advanced LIGO, and frequency dependent squeezing provides a promising early upgrade path to improve the sensitivity beyond the Advanced LIGO design. Optical losses are the most important limit to the level of squeezing, and reducing losses will be one of the main challenges of any implementation of squeezing in a gravitational wave detector. We have also understood that higher order modes couple alignment changes to squeezing angle fluctuations, which was the dominant source of squeezing angle fluctuations in our experiment. Although this would not limit the use of squeezing as an alternative to high power operation, reducing the squeezing angle fluctuations will be helpful in any effort to observe 6 dB or more of squeezing.

Appendix A

List of LIGO documents relevant to this thesis

This thesis has the LIGO document number LIGO-P1300006. More information, including specifications for optics, electronics board layouts and assemblies, and documentation of the table layout can be found at maz.mit.edu/sqwiki/H1Squeezer

These documents are available in the LIGO document control center (dcc.ligo.org):

Proposal	T070265-D
Noise Model	T0900325-v2
Summary of loss measurements	T1200023-v1
Electronics	
Delay line phase shifter	D050339-A
IQ demodulator	D1000181-v2
Common mode board	D040180
Table Top Frequency Stabilization Servo (TTFSS)	D040105-C
TTFSS Interface	D0902048-C
PZT Driver	D1001203-v2
Cable plan	1000737-v2

Appendix B

Acronyms, symbols and terminology

B.1 Acronyms

CLF	coherent locking field
DARM	differential arm degree of freedom
EOM	electro optic modulator
KTP	potassium titanyl phosphate
LO-	local oscillator
OMC	output mode cleaner
OPO	optical parametric oscillator
PDH	Pound Drever Hall
PPTKTP	periodical poled KTP
PSL	prestabilized laser
PZT	piezo electric transducer
SHG	second harmonic generator

B.2 Symbols used in this thesis

Latin Symbols	
$a(t), \tilde{a}(\Omega)$	annihilation operator for fundamental field in cavity
$A_{in,j}(\omega)$	annihilation operator for bath modes incident on coupler j at the fundamental frequency
$A_{out,j}(\omega)$	annihilation operator for bath modes incident on coupler j at the fundamental frequency
b	annihilation operator for second harmonic field in cavity (except in Chapter 1)
$\|b_{th}\|$	amplitude of circulating second harmonic field at threshold
$B_j(\omega)$	annihilation operator for bath modes incident on coupler j at the second harmonic frequency
c	speed of light
$D(\alpha)$	displacement operator that generates a coherent state $\|\alpha\rangle$
$\mathcal{F}_{r,g}$	cavity finesse in infrared (r) or green (g)
$G(x,\theta)$	parametric amplification or amplification
g	nonlinear gain (maximum parametric amplification)
h	gravitational wave strain
L_c	length of nonlinear interaction in crystal (poled length of crystal)
$L_{c,0}$	poled length of crystal at $25°C$
$L_{c,tot}$	total crystal length
$L_{x,y}$	Length of x and y arms of interferometer
$L_+ = (L_x + L_y)/2$	common arm degree of freedom
$L_- = (L_x - L_y)/2$	differential arm degree of freedom
$\mathbf{M}$	matrix describing OPO given by Equation 2.30
P_{th}	power in incident second harmonic field at threshold
$\mathbf{R}$	transformation from annihilation and creation operators to quadrature operators
$\mathcal{R}$	transimpedance gain of photodetector
$S(\theta,\Omega)$	Power spectral density at frequency Ω measured in quadrature θ
$S_n(f)$	power spectral density of total interferometer noise
T_0	phase matching temperature
$V(\theta,\Omega)$	variance of arbitrary quadrature operator at frequency Ω
V_+	variance in anti-squeezed quadrature
V_-	variance in squeezed quadrature
$\mathbf{V_{vac}}, \mathbf{V_c}, \mathbf{V_{out}}$	vector of quadrature variances for vacuum fluctuations, circulating cavity field, and field leaving front coupler respectively
$X_{1,2}$	Quadrature operators for electric field
$X(\theta)$	arbitrary quadrature operator
$x = \|\epsilon\|\|\beta\|/\gamma_r^{tot}$	normalized nonlinear interaction strength
y_{cr}	optimal crystal position

Greek Symbols	
$\|\alpha\rangle, \alpha$	coherent state and its eigenvalue
α_{shg}	ratio of SHG conversion to loss, defined by Equation 3.8
α_{KTP}	thermal expansion coefficient for KTP
β	eigenvalue of second harmonic field coherent state (except in Chapter 1)
β_{KTP}	second order thermal expansion coefficient for KTP
Γ	modulation depth
$\gamma_{r,g}^{j}$	field decay rate for fundamental (r) or second harmonic (g) field at coupler j
$\gamma_{r,g}^{tot}$	total cavity field decay rate for fundamental (r) or second harmonic (g) field
$\Delta_a = \Delta$	cavity detuning at fundamental frequency
$\Delta_b = 2\Delta$	cavity detuning at fundamental frequency
Δ_{dc}	interferometer DC offset
Δk_q	effective difference in refractive indexes in quasi-phase matching
$\Delta X_{1,2}$	uncertainty in $X_{1,2}$
$\Delta\phi_{rt}$	dispersion mismatch
$\delta\mathbf{a}$	vector of time dependent parts of annihilation and creation operators for field circulating in cavity
$\delta\mathbf{A_{l,in}}$	vector of time dependent parts of annihilation and creation operators for vacuum fluctuations incident on lossy coupler
$\delta\mathbf{A_{f,in}}$	vector of time dependent parts of annihilation and creation operators for vacuum fluctuations incident on front coupler
$\delta\mathbf{A_{f,out}}$	vector of time dependent parts of annihilation and creation operators for vacuum fluctuations leaving front coupler
$\delta\mathbf{X_{l,in}}$	vector of time dependent parts of quadrature operators for vacuum fluctuations incident on lossy coupler
$\delta\mathbf{X_{f,in}}$	vector of time dependent parts of quadrature operators for vacuum fluctuations incident on front coupler
$\delta\mathbf{X_{f,out}}$	vector of time dependent parts of quadrature operators for vacuum fluctuations leaving on front coupler
ϵ	nonlinear coupling parameter
ε_0	normalization factor relating electric field to quadrature operators and annihilation and creation operators

$\eta_{esc} = \gamma_r^f / \gamma_r^{tot}$	OPO escape efficiency
η_{loss}	power transmission of a series of lossy optical elements
η_{PD}	photodetector quantum efficiency
η_{SHG}	SHG conversion efficiency
θ_b	phase of circulating second harmonic field
θ_{sqz}	squeezing angle
$\widetilde{\theta}_{sqz}$	RMS squeezing angle fluctuations
θ_w	crystal wedge angle
Λ	poling period for quasi-phase matching
$\lambda_{r,g}$	wavelength of fundamental infrared field (r) and green second harmonic field (g) in a vacuum
τ	OPO round trip time
τ_{shg}	SHG round trip time
$\phi_{g,m}, \phi_{r,m}$	phase acquired by green and infrared fields respectively from dispersive elements in the cavity, other than the crystal
ω	laser carrier frequency
Ω	measurement frequency, audio sideband frequency

B.3 Terminology

Optical parametric amplifier/ optical parametric oscillator:

Some texts use OPO to refer to above threshold operation, and OPA when the crystal is single passed and not in a cavity or when the cavity is below threshold [6, 40, p486]. Sometimes OPA is used to refer to operation of a parametric down-converter in a cavity, below threshold when a seed beam is injected [56].

Degenerate OPO- An OPO in which the signal and idler frequencies are the same or nearly the same. (as in OPO's used for quadrature squeezing)

Doubly resonant OPO- In nonlinear optics literature this normally refers to an OPO which is resonant for both the signal and ilder fields [6]. It has also sometimes been used to refer to a degenerate OPO which is resonant for the fundamental and harmonic fields [82].

Appendix C

Procedure for optimizing crystal position

This is a procedure taught to me by Michael Stefszky, for optimizing the crystal position. This should allow you to acheive dispersion compensation at the phase matching temperature, as described in 3.2.6.

Set the crystal temperature to a temperature approximately near the phase matching temperature, and scan the cavity with both green and seed field injected.

1) Adjust the crystal position so that the green and red cavity resonances occur at the same cavity length. This temperature is used as a reference for the crystal position. Try to make sure that the cavity stays well aligned as the crystal is moved. The crystal position needs to be accurately adjusted to the position where the two fields are co-resonant so that the measurement will be repeatable.

2)Lock the cavity with the green field, check the level of transmitted green power to make sure that it stays the same for each cavity lock. This will cause localized heating in the crystal so that the two fields are no longer co-resonant. Scan a longitudinal PZT in the seed path and measure the nonlinear gain, adjust the crystal temperature to maximize the nonlinear gain. Write down the scanning temperature, the nonlinear gain, locked temperature, transmitted green power and an approximate position of the translation stage if possible.

3) Scan the cavity again, and set the temperature setting to a new scanning temperature, and go back to step 1.

Eventually this will trace out the curve shown in 3-12 as the projection of the nonlinear gain along the position axis. The crystal position (for which a scanning temperature is used as a reference) that maximizes the nonlinear gain is the one to use.

Bibliography

[1] Rich Abbott, Rana Adhikari, Stefan Balmer, Lisa Barsotti, Matt Evans, Peter Fritschel, Valera Frolov, Guido Mueller, Bram Slagmolen, and Sam Waldman. AdvLIGO Interferometer Sensing and Control Conceptual Design. Technical Report LIGO-T070247-010-I, LIGO DCC, 2008. Available at dcc.ligo.org.

[2] T. Aoki, G. Takahashi, and A. Furasawa. Squeezing at 946nm with periodically poled ktiopo4. *Optics Express*, 14(15):6930–6935, 2006.

[3] Lisa Barsotti. aLIGO Faraday: t=96%, Isolation 40 dB, but only 23 dB backscatter isolation. LHO ilog found at http://ilog.ligo-wa.caltech.edu/ilog/pub/ilog.cgi, For readonly access use username: reader Password: readonly, June 9th 2011.

[4] Lisa Barsotti. IFO light back to the squeezer (Expected). August 30th 2011.

[5] Lisa Barsotti. Sideband/carrier power @ 8W. LHO ilog found at http://ilog.ligo-wa.caltech.edu/ilog/pub/ilog.cgi, For readonly access use username: reader Password: readonly, November 29th 2011.

[6] Robert W. Boyd. *Nonlinear Optics*. Elsevier, Academic Press, Burlington, MA, 2008.

[7] Benjamin Buchler. *Electro-Optic Control of Quantum Measurements*. PhD thesis, Australian National University, September 2001.

[8] Carlton M. Caves. Quantum-mechanical noise in an interferometer. *Phys. Rev. D*, 23:1693–1708, Apr 1981.

[9] Carlton M. Caves and Bonny L. Schumaker. New formalism for two-photon quantum optics. i. quadrature phases and squeezed states. *Phys. Rev. A*, 31:3068–3092, May 1985.

[10] Simon Chelkowski. *Squeezed Light and Laser Interferometeric Gravitational Wave Detectors*. PhD thesis, Gottfried Wilhelm Leibniz Universitat Hannover, September 2007.

[11] Simon Chelkowski, Henning Vahlbruch, Karsten Danzmann, and Roman Schnabel. Coherent control of broadband vacuum squeezing. *Phys. Rev. A*, 75:043814, Apr 2007.

[12] S Chua, M Stefszky, C Mow-Lowry, B Buchler, S Dwyer, D Shaddock, P K Lam, and D McClelland. Backscatter tolerant squeezed light source for advanced gravitational-wave detectors. *Optics Letters*, 36(23):4680–4682, 2011.

[13] Sheon Chua. H1 Squeezing vs CLF input power. LHO ilog, October 10th 2011.

[14] Sheon Chua. Power returning back from HAM4 +polarization. LHO ilog, December 3rd 2011.

[15] LIGO Scientific Collaboration. A gravitational wave observatory operating beyond the quantum shot-noise limit. *Nature Physics*, volume(number):pages, September 2011.

[16] LIGO Scientific Collaboration. Official ligo sensitivity curves. https://www.lsc-group.phys.uwm.edu/ppcomm/graphics.html, December 19th 2012.

[17] M. J. Collett and C. W. Gardiner. Squeezing of intracavity and traveling-wave light fields produced in parametric amplification. *Phys. Rev. A*, 30:1386–1391, Sep 1984.

[18] Thomas Corbitt. *Quantum Noise and Radiation Pressure Effects in High Power Optical Interferometers*. PhD thesis, Massachusetts Institute of Technology, 2008.

[19] Thomas Corbitt, Yanbei Chen, Farid Khalili, David Ottaway, Sergey Vyatchanin, Stan Whitcomb, and Nergis Mavalvala. Squeezed-state source using radiation-pressure-induced rigidity. *Phys. Rev. A*, 73:023801, Feb 2006.

[20] Thomas Corbitt, Nergis Mavalvala, and Stan Whitcomb. Optical cavities as amplitude filters for squeezed fields. *Phys. Rev. D*, 70:022002, Jul 2004.

[21] David D. Crouch and Samuel L. Braunstein. Limitations to squeezing in a parametric amplifier due to pump quantum fluctuations. *Phys. Rev. A*, 38:4696–4711, Nov 1988.

[22] Katherine Dooley. *Design and performance of high laser power interferometers for gravitational-wave detection*. PhD thesis, Louisiana State University, 2011.

[23] P.D. Drummond, K.J. McNeil, and D.F. Walls. Non-equilibrium transitions in sub/second harmonic generation. *Optica Acta: International Journal of Optics*, 27(3):321–335, 1980.

[24] Réjean J. Dupuis and Graham Woan. Bayesian estimation of pulsar parameters from gravitational wave data. *Phys. Rev. D*, 72:102002, Nov 2005.

[25] Sheila Dwyer. CLF noise gone. LHO ilog, November 21st 2011.

[26] Sheila Dwyer. Noise in darm proportional to CLF power. LHO ilog, October 24th 2011.

[27] Sheila Dwyer. Summary of Loss Measurements for H1 Squeezing Test. Technical Report LIGO-T1200023-v1, LIGO DCC, January 2012.

[28] Shai Emanueli and Ady Arie. Temperature-dependent dispersion equations for ktiopo4 and ktioaso4. *Appl. Opt.*, 42(33):6661–6665, Nov 2003.

[29] Stephen Fairhurst. Triangulation of gravitational wave sources with a network of detectors. *New Journal of Physics*, 11(12):123006, 2009.

[30] M.M. Fejer, G.A. Magel, D.H. Jundt, and R.L. Byer. Quasi-phase-matched second harmonic generation: tuning and tolerances. *Quantum Electronics, IEEE Journal of*, 28(11):2631 –2654, nov 1992.

[31] B. P. Abbott for the LIGO Scientific Collaboration. Searches for gravitational waves from known pulsars with science run 5 ligo data. *The Astrophysical Journal*, 713(1):671, 2010.

[32] B P Abbott for the LSC. Ligo: the laser interferometer gravitational-wave observatory. *Reports on Progress in Physics*, 72(7):076901, 2009.

[33] Alexander Franzen, Boris Hage, James DiGuglielmo, Jaromir Fiurasek, and Roman Schnabel. Experimental demonstration of continuous variable purification of squeezed states. *Phys. Rev. Lett.*, 97:150505, Oct 2006.

[34] Tobin Fricke. *Homodyne Detection for Laser Interferometric Gravitational Wave Detectors*. PhD thesis, Louisiana State University, 2011. http://etd.lsu.edu/docs/available/etd-11082011-115541/unrestricted/frickediss.pdf.

[35] Tobin Fricke. L1, H1 S6 shot noise estimates. LLO ilog, April 13th 2011.

[36] Tobin T Fricke, Nicols D Smith-Lefebvre, Richard Abbott, Rana Adhikari, Katherine L Dooley, Matthew Evans, Peter Fritschel, Valery V Frolov, Keita Kawabe, Jeffrey S Kissel, Bram J J Slagmolen, and Sam J Waldman. Dc readout experiment in enhanced ligo. *Classical and Quantum Gravity*, 29(6):065005, 2012.

[37] R. Friedberg. The squeezing operator in quasinormal form. *Laser Physics*, 12(8):1171–1176, 2002.

[38] Peter Fritschel. Backscattering from the AS port:Enhanced and Advanced LIGO. Technical Report T060303-00, LIGO DCC, 2006.

[39] C. W. Gardiner and M. J. Collett. Input and output in damped quantum systems: Quantum stochastic differential equations and the master equation. *Phys. Rev. A*, 31:3761–3774, Jun 1985.

[40] J. C. Garrison and R. Y. Chiao. *Quantum Optics*. Oxford University Press, Oxford, 2008.

[41] J. Gea-Banacloche and M. S. Zubairy. Influence of pump-phase fluctuations on the squeezing in a degenerate parametric oscillator. *Phys. Rev. A*, 42:1742–1751, Aug 1990.

[42] Christopher C. Gerry and Peter L. Knight. *Introductory Quantum Optics*. Cambridge University Press, Cambridge, 2005.

[43] K. Goda, O. Miyakawa, E. E. Mikhailov, S. Saraf, R. Adhikari, K. McKenzie, R. Ward, S. Vass, A. J. Weinstein, and N. Mavalvala. A gravitational wave observatory operating beyond the quantum shot-noise limit. *Nature Physics*, 2008.

[44] Keisuke Goda. *Development of Techniques for Quantum Enhanced Laser-Interferometric Gravitational-Wave Detectors*. PhD thesis, Massachusetts Institute of Technology, 2007.

[45] Keisuke Goda, Kirk McKenzie, Eugeniy E. Mikhailov, Ping Koy Lam, David E. McClelland, and Nergis Mavalvala. Photothermal fluctuations as a fundamental limit to low-frequency squeezing in a degenerate optical parametric oscillator. *Phys. Rev. A*, 72:043819, Oct 2005.

[46] Richard W. Henry and Sharon C. Glotzer. A squeezed-state primer. *American Journal of Physics*, 56(4):318–328, 1988.

[47] Kissel Jeffrey. *Calibrating and Improving the Sensitivity of the LIGO Detectors*. PhD thesis, Louisianan State University, 2010.

[48] I. Juwiler, A. Arie, A. Skliar, and G. Rosenman. Efficient quasi-phase-matched frequency doubling with phase compensation by a wedged crystal in a standing-wave external cavity. *Opt. Lett.*, 24(17):1236–1238, Sep 1999.

[49] Kiyoshi Kato and Eiko Takaoka. Sellmeier and thermo-optic dispersion formulas for ktp. *Appl. Opt.*, 41(24):5040–5044, Aug 2002.

[50] Keita Kawabe, Luca Matone, and Joseph Betzwieser. Excess noise mechanism in ligo output mode cleaner. Technical Report LIGO-T040158-00-D, LIGO DCC, 2004.

[51] Alexander Khalaidovski, Henning Vahlbruch, Nico Lastzka, Christian Grf, Karsten Danzmann, Hartmut Grote, and Roman Schnabel. Long-term stable squeezed vacuum state of light for gravitational wave detectors. *Classical and Quantum Gravity*, 29(7):075001, 2012.

[52] H. J. Kimble, Yuri Levin, Andrey B. Matsko, Kip S. Thorne, and Sergey P. Vyatchanin. Conversion of conventional gravitational-wave interferometers into quantum nondemolition interferometers by modifying their input and/or output optics. *Phys. Rev. D*, 65:022002, Dec 2001.

[53] LIGO Laboratory. Gravitational wave interferometer noise calculator, version 3. August 2012.

[54] Michele Maggiore. *Gravitational Waves Volume 1:Theory and Experiment*. Oxford University Press, Oxford, UK, 2008.

[55] Genta Masada, Tsuyoshi Suzudo, Yasuhiro Satoh, Hideki Ishizuki, Takunori Taira, and Akira Furusawa. Efficient generation of highly squeezed light with periodically poled mgo:linbo3. *Opt. Express*, 18(12):13114–13121, Jun 2010.

[56] Kirk McKenzie. *Squeezing in the Audio Gravitational Wave Detection Band*. PhD thesis, Australian National University, February 2008.

[57] Kirk McKenzie, Malcolm B. Gray, Ping Koy Lam, and David E. McClelland. Nonlinear phase matching locking via optical readout. *Opt. Express*, 14(23):11256–11264, Nov 2006.

[58] Kirk McKenzie, Nicolai Grosse, Warwick P. Bowen, Stanley E. Whitcomb, Malcolm B. Gray, David E. McClelland, and Ping Koy Lam. Squeezing in the audio gravitational-wave detection band. *Phys. Rev. Lett.*, 93:161105, Oct 2004.

[59] Kirk McKenzie, Daniel A. Shaddock, David E. McClelland, Ben C. Buchler, and Ping Koy Lam. Experimental demonstration of a squeezing-enhanced power-recycled michelson interferometer for gravitational wave detection. *Phys. Rev. Lett.*, 88:231102, May 2002.

[60] Grant Meadors. Plots/graphs/figures of range and range integrand. LHO ilog, November 23rd 2011.

[61] Moritz Mehmet, Sebastian Steinlechner, Tobias Eberle, Henning Vahlbruch, André Thüring, Karsten Danzmann, and Roman Schnabel. Observation of cw squeezed light at 1550 nm. *Opt. Lett.*, 34(7):1060–1062, Apr 2009.

[62] Moritz Mehmet, Henning Vahlbruch, Nico Lastzka, Karsten Danzmann, and Roman Schnabel. Observation of squeezed states with strong photon-number oscillations. *Phys. Rev. A*, 81:013814, Jan 2010.

[63] Eugeniy E. Mikhailov, Keisuke Goda, Thomas Corbitt, and Nergis Mavalvala. Frequency-dependent squeeze-amplitude attenuation and squeeze-angle rotation by electromagnetically induced transparency for gravitational-wave interferometers. *Phys. Rev. A*, 73:053810, May 2006.

[64] Miguel Orszag. *Quantum Optics: Including Noise Reduction, Trapped Ions, Quantum Trajectories, and Decoherence*. Springer, Berlin Heidelberg New York, 2008.

[65] David J Ottaway, Peter Fritschel, and Samuel J. Waldman. Impact of upconverted scattered light on advanced interferometric gravitational wave detectors. *Optics Express*, 20(8):8329–8336, 2012.

[66] E. S. Polzik, J. Carri, and H. J. Kimble. Atomic spectroscopy with squeezed light for sensitivity beyond the vacuum-state limit. *Applied Physics B: Lasers and Optics*, 55:279–290, 1992. 10.1007/BF00325016.

[67] E. S. Polzik and H. J. Kimble. Frequency doubling with KNbO3 in an external cavity. *Opt. Lett.*, 16(18):1400–1402, Sep 1991.

[68] Sudhakar Prasad. Quantum noise and squeezing in an optical parametric oscillator with arbitrary output-mirror coupling. iii. effect of pump amplitude and phase fluctuations. *Phys. Rev. A*, 49:1406–1426, Feb 1994.

[69] F J Raab and S E Whitcomb. Estimation of special optical properties of a triangular ring cavity. Technical Report T920004-00, LIGO DCC, February 1992.

[70] Robert Schofield. The impact of squeezing on vibration coupling to H1. LHO ilog, October 23rd 2011.

[71] Robert Schofield. Status of acoustic isolation of the H2 PSL enclosure. LHO alog available at alog.ligo-wa.caltech.edu/aLOG, September 19 2011.

[72] Bonny L. Schumaker and Carlton M. Caves. New formalism for two-photon quantum optics. ii. mathematical foundation and compact notation. *Phys. Rev. A*, 31:3093–3111, May 1985.

[73] Marlan O. Scully and M. Suhail Zubairy. *Quantum Optics*. Cambridge University Press, Cambridge, UK, 1997.

[74] Anthony E Siegman. *Lasers*. University Science Books, Mill Valley, CA, 1986.

[75] Daniel Sigg. Measurements today. LASTI ilog available at http://www.ligo.mit.edu/ilog/pub/ilog.cgi, October 17th 2010.

[76] R. E. Slusher, L. W. Hollberg, B. Yurke, J. C. Mertz, and J. F. Valley. Observation of squeezed states generated by four-wave mixing in an optical cavity. *Phys. Rev. Lett.*, 55:2409–2412, Nov 1985.

[77] Nicolas Smith-Lefebvre, 2012. Personal Communication.

[78] Nicolas Smith-Lefebvre. *Techniques for Improving the Readout Sensitivity of Gravitational Wave Antennae*. PhD thesis, Massachusetts Institute of Technology, June 2012.

[79] Daniel A. Steck. Quantum and Atom Optics. available online at http://steck.us/teaching, (revision 0.8.3) 25 May 2012.

[80] M S Stefszky, C M Mow-Lowry, S S Y Chua, D A Shaddock, B C Buchler, H Vahlbruch, A Khalaidovski, R Schnabel, P K Lam, and D E McClelland. Balanced homodyne detection of optical quantum states at audio-band frequencies and below. *Classical and Quantum Gravity*, 29(14):145015, 2012.

[81] Michael Stefszky. New SHG characterization. LASTI ilog available at http://www.ligo.mit.edu/ilog/pub/ilog.cgi, July 9 2010.

[82] Michael Stefszky, Conor M Mow-Lowry, Kirk McKenzie, Sheon Chua, Ben C Buchler, Thomas Symul, David E McClelland, and Ping Koy Lam. An investigation of doubly-resonant optical parametric oscillators and nonlinear crystals for squeezing. *Journal of Physics B: Atomic, Molecular and Optical Physics*, 44(1):015502, 2011.

[83] John C Stover, editor. *Optical Scattering: Measurement and Analysis*. SPIE Optical Engineering Press, Bellingham Washington, 1995.

[84] Yuishi Takeno, Mitsuyoshi Yukawa, Hidehiro Yonezawa, and Akira Furusawa. Observation of -9 db quadrature squeezing with improvement of phasestability in homodyne measurement. *Opt. Express*, 15(7):4321–4327, Apr 2007.

[85] Henning Vahlbruch. *Squeezed Light for Gravitational Wave Astronomy*. PhD thesis, Gottfried Wilhelm Leibniz Universitt Hannover, 2008.

[86] Henning Vahlbruch, Simon Chelkowski, Boris Hage, Alexander Franzen, Karsten Danzmann, and Roman Schnabel. Demonstration of a squeezed-light-enhanced power- and signal-recycled michelson interferometer. *Phys. Rev. Lett.*, 95:211102, Nov 2005.

[87] Henning Vahlbruch, Simon Chelkowski, Boris Hage, Alexander Franzen, Karsten Danzmann, and Roman Schnabel. Coherent control of vacuum squeezing in the gravitational-wave detection band. *Phys. Rev. Lett.*, 97:011101, Jul 2006.

[88] Henning Vahlbruch, Alexander Khalaidovski, Nico Lastzka, Christian Grf, Karsten Danzmann, and Roman Schnabel. The geo600 squeezed light source. *Classical and Quantum Gravity*, 27(8):084027, 2010.

[89] D F Walls and Gerard J Milburn. *Quantum Optics*. Springer, Berlin, 2008.

[90] Wódkiewicz, K., and M. S. Zubairy. Effect of laser fluctuations on squeezed states in a degenerate parametric amplifier. *Phys. Rev. A*, 27:2003–2007, Apr 1983.

[91] Min Xiao, Ling-An Wu, and H. J. Kimble. Precision measurement beyond the shot-noise limit. *Phys. Rev. Lett.*, 59:278–281, Jul 1987.

[92] Horace P. Yuen. Two-photon coherent states of the radiation field. *Phys. Rev. A*, 13:2226–2243, Jun 1976.